RANGE-SELECTIVE DIGITAL HOLOGRAPHY FOR ON-AXIS GEOMETRIES AND VIBRATING OUTDOOR OBJECTS

by

Cole Hammond

A dissertation submitted in partial fulfillment
of the requirements for the degree

of

Doctor of Philosophy

in

Electrical Engineering

MONTANA STATE UNIVERSITY
Bozeman, Montana

December 2025

©COPYRIGHT

by

Cole Hammond

2026

All Rights Reserved

DEDICATION

"There's a fine line between clever and stupid."
— Spinal Tap

ACKNOWLEDGEMENTS

I would like to thank my research advisors, Dr. Wm Randall Babbitt and Dr. R.Krishna Mohan, for their continual support, and for consistently challenging me. I am also incredibly grateful to Dr. Joe Shaw and Dr. Brad Whitaker for the many class hours we have shared and for their encouragement in my academic pursuits.

This work would not have been possible without the encouragement and support from the students and faculty of Spectrum Lab. A special thanks goes to Zachery Lakin, Corey Pearson, and Matt Goodman for their invaluable assistance and friendship throughout this endeavor.

We gratefully acknowledge funding from the Office of Naval Research. The United States Government has a royalty-free license throughout the world in all copyrightable material contained herein. Any opinions, findings, and conclusions or recommendations expressed in this material are those of the author(s) and do not necessarily reflect the views of the Office of Naval Research. This work was funded under Department of Navy award N00014-20-1-2260 issued by the Office of Naval Research.

VITA

Cole Hammond was born in Jackson, WY in 1996. Raised on both sides of the Tetons, Cole graduated from Jackson Hole High School. After high school, Cole attended Whitman College in Walla Walla Washington where he graduated with a BA in Physics and Astronomy. After which, Cole moved back to the mountains and received his masters in Optics and Photonics from Montana State university in 2023.

TABLE OF CONTENTS

1. INTRODUCTION 1

Optical Imaging Systems in Adverse Conditions 1
Imaging Through Extreme Environments 2
FMCW Lidar and Range Selective Holographic Imaging 4
Imaging Vibrating Objects with Coherent Systems 6
Objectives and Overview 7

2. BACKGROUND 10

Lidar 10
Pulsed Lidar 11
Frequency Modulated Continuous Wave Lidar 12
Optical Frequency Modulation 20
Range-Doppler Ambiguity 29
Digital Holography 35
Propagation of Optical Fields (Fresnel and Fraunhofer Approximations) 35
Mathematical Framework of Digital Holography 39
Holographic Recording Planes 41
Image-Plane 41
Pupil-Plane 42
Recording Geometries 42
Spatial-Heterodyne Digital Holography 44
Spatial-Heterodyne: Image-plane 45
Spatial-Heterodyne: Pupil-plane 48
On-Axis Phase-shifting Digital Holography 51
Phase-Shifting: Image-plane 53
Phase-Shifting: Pupil-plane 55
Range Selective Digital Holography 57
Depth of Field 61
Time of Flight Detectors 64

3. RANGE SELECTIVE PHASE-SHIFTING FREQUENCY-MODULATED DIGITAL HOLOGRAPHY WITH TEMPORAL-HETERODYNING 72

Manuscript Introduction 72
Contribution of Authors and Co-Authors 72
Manuscript Information 73

TABLE OF CONTENTS – CONTINUED

4. FREQUENCY DETUNING ANALYSIS IN MULTI-CHIRP RANGE-SELECTIVE DIGITAL HOLOGRAPHY WITH TEMPORAL HETERODYNING 85

Manuscript Introduction 85
Contribution of Authors and Co-Authors 85
Manuscript Information 87
Additional Material 105

5. CONSTRUCTION OF DUAL FMCW LIDAR AND RANGE SELECTIVE DIGITAL HOLOGRAPHIC SYSTEM 111

Chirp Generation 111
Scanning Lidar System 116
Range-Selective Digital Holographic System 123
Holographic Stabilization System 127
Integration of Lidar and stabilized Holographic Systems 133

6. FMCW LIDAR STABILIZED RANGE SELECTIVE DIGITAL HOLOGRAPHY FOR IMAGING VIBRATING OBJECTS 136

Manuscript Introduction 136
Contribution of Authors and Co-Authors 136
Manuscript Information 138

7. ADDITIONAL MATERIAL 152

FMCW Lidar Vibrometry 152
Lidar Point Clouds with Doppler Information 157

8. CONCLUSION 159

REFERENCES CITED 164

APPENDIX: Experimental Setups and Components 173

Temporal-Heterodyne Holographic System 174
Combined Lidar and RSDH imaging System 174

LIST OF TABLES

Table Page

1. Table 1 Key components used in the Temporal-Heterodyne RSDH System. 174

2. Table 2 Key components used in the Chirped-RSDH System. 175

LIST OF FIGURES

Figure Page

1. Figure 1 Pulsed lidar system cartoon. The transmitted signals are shown in red while the time-delayed returns are shown in blue. 12

2. Figure 2 Basic FMCW Lidar Schematic. A laser source is linearly chirped and split into a TX and LO path. The RX signal is mixed with the LO on a coherent balanced photodetector (assumed incorporated into "detector"), and the resulting beat signal is digitized. A Fast Fourier Transform (FFT) is applied in post-processing to extract the beat frequency, which is used to determine the object distance. This figure is not to scale and is for illustrating purposes only. 16

3. Figure 3 The top plot depicts Interference between the LO and RX FMCW chirps with a chirp bandwidth B_c, chirp duration τ_c, and round-trip delay τ_R. The center plot shows temporal windowing of the resulting time-domain beat signal. The bottom plot presents the frequency-domain representation, computed as the Fourier transform of the windowed signal. The gaps between the noisy sinusoidal signals in the Time-Domain Beat Signal plot are caused by the beat being outside of the detector bandwidth. 17

4. Figure 4 Resolution limit for a chirp bandwidth of 1 GHz, corresponding to a range resolution of $\Delta R_{res} \approx 0.15$ m. Two objects with approximately zero separation (top left). Two objects that are separated in distance by less than the range resolution of the system (top right). Two objects spaced exactly ΔR_{res}, meeting the Rayleigh resolution criterion (bottom left). Two objects separated by more than ΔR_{res}, clearly resolved as distinct peaks (bottom right). 19

LIST OF FIGURES – CONTINUED

Figure Page

5. Figure 5 Electro-optic phase modulator (top) and electro-optic intensity modulator (bottom). The entire structure represents the electro-optic crystal. The red lines represent the input and output optical waveguides. The active region indicates where the RF drive voltage is applied. The intensity modulator forms a Mach–Zehnder interferometer, in which an additional bias voltage controls the relative phase between the two arms. 21

6. Figure 6 Sidebands of a chirped signal where f_L is the laser frequency (carrier), f_0 is the starting frequency of the chirp, and f_1 is the end frequency of the chirp. 23

7. Figure 7 Simulation illustrating the output of an electro-optic modulator modeled as the phase-modulated signal $e^{i2\pi f_1 t} e^{i\beta \sin(2\pi f_2 t)}$ for three different modulation indices β. The left column shows the spectrum while the right column displays the corresponding Bessel functions of the first kind, which predict the amplitudes of the generated sidebands. The zeroth through third order Bessel functions are plotted to demonstrate how sideband amplitudes vary with modulation depth. 24

8. Figure 8 Simulated spectrograms of the baseband optical field output from a Mach-Zehnder intensity modulator under varying modulation index $\beta \in \{0.39,\ 1.84,\ 3.05\}$ V and DC bias voltages $V_b \in \{0,\ 1,\ 2\}$ V. Modulation depth values were chosen to show maximum power in the first and second sidebands. The modulator has a half-wave voltage of $V_\pi = 2\,\mathrm{V}$. The RF drive is a linearly chirped sinusoid starting at 1 MHz with a bandwidth of 2 MHz and chirp duration of $\tau_c = 500\,\mu$s. Each subplot shows the spectrogram of the modulated baseband field shifted down to DC. At $V_b = 0\,\mathrm{V}$, the modulator's cosine transfer function is symmetric, producing predominantly even harmonics whereas when $V_b = V_\pi$, the response is antisymmetric, yielding mostly odd harmonics. At intermediate bias voltages, both even and odd sidebands are present. 26

LIST OF FIGURES – CONTINUED

Figure Page

9. Figure 9 RF chirp spectrum measured by the an RF spectrum analyzer (RFSA), showing a 1.8 GHz bandwidth chirp from approximately 6 to 7.8 GHz (Top Left). Optical spectrum of the unmodulated continuous-wave 1550 nm laser source, displaying a single narrow peak at the carrier wavelength (Top Right). Optical spectrum of the laser under modulation with an electro-optical intensity modulator, exhibiting multiple sidebands symmetrically spaced around the carrier frequency (Bottom Left). Optical spectrum of the modulated laser with carrier suppression achieved by biasing the EOM, showing reduced carrier power and enhanced sideband visibility, highlighting the importance of biasing for effective optical carrier suppression (Bottom Right). 28

10. Figure 10 Illustration of how single-sideband up-chirps and down-chirps consecutively can be used to separate the doppler frequency shift from the range-dependent component..... 30

11. Figure 11 Illustration of double-sideband modulation interference, where the LO and TX/RX are shifted from one another by f_{AOFS}. 32

12. Figure 12 Double-sideband modulation interference without shifting the LO or TX with an AOFS. IQ detection is used to remove the undesired frequency components. 34

13. Figure 13 Fresnel Propagation Coordinates. 37

14. Figure 14 Fresnel Propagation of an Air Force Target digitally. The intensity is plotted at propagation distances of $z = 0.33, 0.66, 1$ meters. 38

15. Figure 15 Interference between the LO and RX fields. 40

16. Figure 16 Schematic of both image plane and pupil plane holographic recordings for when the LO and RX beams are angled relative to one another ($\Delta\vec{k} \neq 0$)..... 43

LIST OF FIGURES – CONTINUED

Figure Page

17. Figure 17 Simulation results for an off-axis recording geometry. Image of the object (top left). Intensity of the complex LO (top right). Recorded intensity calculated from the interference between the object and LO (center left). 2D FFT of the recorded intensity showing how the DC terms are separated from both the image terms and conjugate image terms in the Fourier domain (center right). Masking of image terms (bottom left). Hologram intensity obtained by taking the squared magnitude of the inverse 2D Fourier transform of the masked image (bottom right). 47

18. Figure 18 Simulation results for a pupil-plane off-axis recording geometry. Target object (top left). intensity of propagated object field (top right). Intensity of the LO (middle left). Recorded intensity of the interference of both fields (middle right). Quadratic phase correction applied (bottom left). Reconstructed target intensity (bottom right). 50

19. Figure 19 Simulation results for on-axis image-plane digital holography. Recorded intensities with known phase shifts of the LO (top left, top right, middle left, and middle right). Original object (bottom left). Reconstructed intensity (bottom right). 54

20. Figure 20 Simulation results for on-axis pupil-plane digital holography. Recorded intensities with known phase shifts of the LO (top left, top right, middle left, and middle right). Original object (bottom left). Reconstructed object intensity (bottom right). 56

21. Figure 21 Range-selective imaging schematic. Shifting f_s allows for the construction of holograms at different distances where the range resolution ΔR_{res} is the range window. This is shown for three cases where no hologram is formed ($f_s \neq f_{R_1} \neq f_{R_2}$), a hologram of the object at R_1 is formed ($f_s \approx f_{R_1} \neq f_{R_2}$), and a hologram of the object at R_2 is formed ($f_s \approx f_{R_2} \neq f_{R_1}$). 60

22. Figure 22 Frequency shifts for RSDH. RSDH in a traditional off-axis recording geometry (left). RSDH using an on-axis Temporal Heterodyne recording geometry (Right). 61

LIST OF FIGURES – CONTINUED

Figure Page

23. Figure 23 DOF_{NDL} of a single lens imaging system. With a fixed pixel size, varying the aperture diameter is the primary factor controlling DOF_{NDL}. 63

24. Figure 24 Schematic of the modulation and demodulation process in a time-of-flight camera. The emitted signal is modulated at a known frequency, and is also used mixed phase shifts of the returned signal are used to compute both intensity and distance for each pixel. 65

25. Figure 25 Images of Sentis M100 ToF detectors (left). Example intensity and range maps of two different objects (right). The range is mapped from red being close to blue being far. 66

26. Figure 26 Simulated illustration of the four reference signals with phase shifts of 0°, 90°, 180°, and 270° used to sample the reflected Time-of-Flight signal. Each subplot depicts the corresponding reference waveform, the measured reflected signal, and their point-wise product, which represents the correlation needed for phase demodulation. The distinct phase shifts enable separation of in-phase and quadrature components, forming the foundation for accurate phase recovery in TOF systems. 67

27. Figure 27 Presentation of the demodulated in-phase (I) and quadrature (Q) components derived by subtracting the mixed signals corresponding to opposing phase shifts (A - C and B - D, respectively). The shaded areas indicate the individual mixed signals contributing to each component. These I and Q values constitute the orthogonal components of the complex baseband signal used for computing pixel wise distance. 68

LIST OF FIGURES – CONTINUED

Figure Page

28. Figure 28 Phasor representation of the demodulated TOF signal, plotting the normalized I-Q vector on the complex unit circle. The vector's angle corresponds directly to the measured phase shift of the reflected signal, which relates to the time delay and thus the distance to the object. The magnitude provides insight into signal quality and strength. This visualization offers an intuitive understanding of TOF phase demodulation in the complex plane, facilitating interpretation of the measurement's precision. 69

29. Figure 29 Simulated illustration of the four reference signals with phase shifts of 0°, 90°, 180°, and 270° used to sample the reflected Time-of-Flight signal. Both the LO and RX signals are sinusoidal with no added noise. Under these conditions, the phase angle reconstruction is more accurate than when using a square-wave LO due to the absence of harmonic distortion. 71

30. Figure 30 Timing diagram of the four recordings required for temporal-heterodyne RSDH. 105

31. Figure 31 Individual components that make up the detuning profiles for image-plane, pupil-plane image, and pupil-plane conjugate image temporal-heterodyne RSDH (top left, middle left, and bottom left). The observed detuning profiles for the subsequent geometries which are the product of all components (top right, middle right, and bottom right). 107

32. Figure 32 Image-plane simulation results showing the effect of averaging over increasing numbers of pixels. The top subplot corresponds to a single pixel (highly fluctuating), and subsequent subplots show averages over more pixels, with the bottom subplot demonstrating convergence to the analytical detuning profile. 108

33. Figure 33 Pupil-plane image simulation result showing the simulation results for a single pixel. The complex exponential representation produces the expected detuning profile without averaging, in contrast to the image-plane simulation. 110

LIST OF FIGURES – CONTINUED

Figure Page

34. Figure 34 Time-domain trigger signal and output chirp from the Euvis (left). Spectrogram of the Euvis chirp in a dB scale (right). 112

35. Figure 35 Schematic of the chirp multiplication and amplification chain. Output A is used to modulate the lidar TX/LO and DH TX arm while output B is used to modulate the DH LO optical signal. 114

36. Figure 36 Output chirps as a function of TPI signal generator frequency. The data was recorded on a radio-frequency spectrum analyzer with a resolution bandwidth (RBW) of 0.5 MHz.....115

37. Figure 37 The two output channels of the chirp generator are shifted from one another by changing the relative input frquencies between f_A and f_B.....116

38. Figure 38 Schematic of the constructed FMCW lidar system (top). Lidar free space optics and fast scanning mirror (bottom). 117

39. Figure 39 Upper sideband of the amplitude spectrum, $10\log_{10}(\mathbf{A}[n,i]^2)$, for 10 randomly selected mirror positions n before background subtraction and thresholding. The example background spectrum, $10\log_{10}(\mathbf{B}[i]^2)$, is also shown for reference. 120

40. Figure 40 3D lidar point cloud of the scanned object scene, shown from the front (top), top (middle), and side (bottom) views. The units are in meters. 122

41. Figure 41 Cartoon of the Digital holography transmit system, the imaging system, and the holographic recording geometry.....123

42. Figure 42 RSDH of a speaker with retroreflective tape taken at 90 meters. Raw intensity captured by detector (top left). 2D FFT of the recorded intensity (top right). Masking of the hologram (bottom left). Reconstructed hologram (bottom right). 126

43. Figure 43 Phase-frequency detector output voltage when input R is less than inout V by 10 kHz (left) and when input R is greater than input V by 10 kHz (right).....128

LIST OF FIGURES – CONTINUED

Figure Page

44. Figure 44 Phase-frequency detector output voltage when input R is equal in frequency to V but V is frequency modulated at 1 kHz with 10 kHz deviation. 129

45. Figure 45 Schematic of the combined FMCW lidar and RSDH system when performing stabilized RSDH of a vibrating speaker. 134

46. Figure 46 Illustration of the combined FMCW lidar and RSDH system. 135

47. Figure 47 Segmented time-domain data where each segment is shown as a different color and is the recorded beat signal over a single chirp (top). Doppler velocity computed for each segment (bottom). The doppler frequency color is computed from the matching time domain data. Only the real time-domain spectrum is shown even though the complex spectrum is used to compute the doppler. 154

48. Figure 48 Doppler frequency vs time for 101 Hz speaker (top). Frequency spectrum of the target vibrations (bottom). 155

49. Figure 49 Doppler frequency vs time (top) and position vs time (bottom) of the speaker data when playing a song. 156

50. Figure 50 3D lidar point cloud depicting two people, a vehicle, and trees (top). The same data processed for Doppler information (bottom) shows the two people rotating in opposite directions, while the vehicle and trees remain stationary. The color bars indicate signal strength (top) and object velocity (bottom), with red and blue chosen to represent red and blue shifts, respectively. 158

51. Figure 51 Range-Selective Temporal Heterodyne Digital Holography System. 174

52. Figure 52 Internal components of the combined lidar and RSDH system. 175

53. Figure 53 Lidar and RSDH tower. 176

ABSTRACT

Optical imaging systems often experience significant performance degradation in turbulent or scattering environments such as fog or dust. To address these challenges, coherent range-selective imaging techniques inspired by frequency-modulated continuous-wave (FMCW) lidar have been developed. These approaches enable holographic imaging of closely spaced objects while suppressing backscatter from objects outside the system's range resolution by reconstructing only those located at specific, tunable ranges.

Traditionally, range-selective digital holography has been demonstrated only in off-axis geometries, which limit spatial resolution. This work advances the field through the development of a novel on-axis temporal heterodyne technique that achieves range selectivity without compromising spatial resolution. Experimental results are shown at distances of a few meters, although the method is applicable to longer distances. A corresponding mathematical framework was established to analyze range-selective temporal heterodyne digital holography, which operates by coherently integrating over multiple FMCW chirps to reconstruct a hologram. The developed theoretical formulation is broadly applicable to other holographic systems that employ multi-chirp integration.

To enhance outdoor range-selective digital holographic operation, where object motion, vibration, and atmospheric turbulence present major challenges, two additional techniques were developed. First, long-range holographic capability was achieved by combining a scanning lidar system with a telescope-based digital holography platform, enabling imaging at distances exceeding one kilometer. Second, a stabilization subassembly was implemented to mitigate turbulence and motion-induced phase distortions. This system successfully demonstrated coherent holographic imaging of strongly vibrating objects that exhibited displacement greater than 18 optical wavelengths during an integration at 90 meters, thereby confirming the system's ability to maintain coherence and support reliable outdoor imaging under adverse conditions.

1

INTRODUCTION

Optical Imaging Systems in Adverse Conditions

Optical imaging systems face significant challenges when operating under adverse conditions such as turbulence, scattering media, or fog. These factors distort and attenuate optical signals, degrading image quality. Long-range active imaging systems face even greater challenges, as weak return signals must traverse fluctuating and scattering media.

Developing imaging techniques that remain effective under such degraded and dynamic conditions is increasingly critical, given society's growing reliance on optical systems for safety and autonomous decision-making. Such applications include autonomous vehicles navigating complex environments, maritime and aerial platforms operating through turbulence or fog, and long-range remote sensing and surveillance [1–5]. In all cases, robust imaging under adverse and time-varying conditions is essential for reliable operation.

Traditional intensity-based ranging approaches, such as time-of-flight cameras or gated imaging, can provide depth information but are fundamentally limited in sensitivity and in their ability to recover the phase of the optical field. Coherent ranging techniques, such as frequency-modulated continuous-wave (FMCW) lidar, overcome these limitations. By mixing the received field with a strong local oscillator, coherent detection enables phase-sensitive measurements and coherent gain, significantly improving the signal-to-noise ratio while preserving both range and phase information. These properties make coherent detection a promising pathway for extending reliable optical imaging into adverse environments and for long ranges.

While coherent lidar provides robust range information, it reconstructs a scene as a collection of discrete points, since scanning is used to sample the object scene. The transverse

resolution is largely determined by the beam scanning technique, which is susceptible to pointing errors, including wobble. Furthermore, the delay between the transmitted and returned beam directions (beam lag) limit the achievable scanning speeds.

In contrast, digital holography captures the full amplitude and phase of the optical field, producing a continuous, phase-resolved image of the scene with all transverse points captured simultaneously and without the issues associated with scanning beams. Conventional digital holography, however, reconstructs all objects within the depth of field, which can introduce unwanted contributions from scatterers or surfaces outside the region of interest. This limitation motivates the development of holographic techniques that combine the full-field phase sensitivity of holography with range selectivity, while also addressing stability challenges caused by object motion and environmental factors such as turbulence.

This thesis explores novel on-axis digital holography techniques developed in a laboratory setting to enable range-selective holographic imaging. In addition, lidar-enabled stabilization techniques are developed and demonstrated for outdoor operation, compensating for object motion to achieve stable range-selective digital holographic reconstructions. Together, these developments extend the capabilities of coherent optical imaging systems for operation in adverse and dynamically varying environments, including scenarios affected by turbulence and other phase-distorting phenomena.

Imaging Through Extreme Environments

Range-resolved imaging in challenging environments, such as over long distances, through turbulent or scattering media, or of vibrating and moving objects, remains a significant technical problem. Various approaches have been developed to address these difficulties, including time-of flight detectors, lidar-based scanning techniques, and holographic methods that rely heavily on post-processing. While these methods can partially correct distortions, strongly turbulent or scattering media severely attenuate reflected signals

and limit coherent integration times, limiting the fidelity of reconstructed images.

Time-of-flight (ToF) systems, which can measure both intensity and pixel-wise distance to objects, offer rapid three-dimensional reconstructions of scenes. However, they are highly susceptible to backscatter, which degrades accuracy and contrast and they do not record the optical field of the object. Modifications such as time-gating have improved imaging through fog, but ToF detectors remain constrained to short ranges of only a few meters before aliasing, insufficient for most real-world long-range applications [6].

These limitations have motivated the development of lidar-based imaging systems, including point-cloud methods and synthetic aperture or aperture-synthesis techniques [7–10]. While laser illumination extends imaging range, it introduces challenges such as speckle, which can reduce image quality. Techniques such as digital shearing interferometry have shown some success in mitigating speckle effects, but environmental perturbations and phase distortions still limit reliable performance in outdoor conditions [11–13].

Environmental instabilities, including atmospheric turbulence and mechanical vibration, introduce time-varying phase distortions that degrade coherent imaging. While turbulence has been extensively studied, vibration-induced phase fluctuations remain a critical challenge for stable holographic imaging, especially in field conditions.

Turbulence degrades coherent imaging primarily through wavefront phase distortions, including piston shifts (uniform phase changes across the aperture), and amplitude fluctuations. Phase distortions blur the reconstructed image and reduce spatial coherence, while amplitude fluctuations cause scintillation and signal washout [13–15].

A variety of strategies have been explored to address turbulence-related distortions in digital holograms [16]. These include phase correction approaches such as Zernike polynomial fitting and Bayesian algorithms, which have shown success in improved image contrast in laboratory tests [17–20]. Other methods employ multi-plane or spectral diversity, including wavelength-scanning holography and multi-plane iterative reconstruction (MIR), to improve

robustness against phase distortions. More recently, machine-learning approaches have been introduced, with coherent plug-and-play (CPnP) frameworks and neural-network-based reconstructions demonstrating promising results for turbulence mitigation and coherent image recovery [21–26]. However, all these phase-correction techniques rely on high signal-to-noise ratio (SNR) captures of the coherent object field, and piston phase shifts caused by atmospheric turbulence and object vibrations are a major limitation for obtaining high-SNR coherent images, particularly at long ranges. This thesis addresses long range coherent imaging through turbulent media, enabling capture of phase fronts that can be operated on by the above distortion compensating techniques.

Despite these advances, most demonstrations remain confined to short ranges and controlled laboratory environments. Few techniques simultaneously address the requirements of long-range operation, full-field phase reconstruction, range selectivity, and robustness to vibration-induced phase instabilities. This persistent gap motivates the work presented in this thesis, which develops a technique to stabilize range-selective digital holograms recorded under realistic outdoor conditions from time-dependent phase shifts causes by movement or piston phase shifts.

FMCW Lidar and Range Selective Holographic Imaging

Coherent lidar techniques provide both phase and amplitude information, making them important tools for imaging in challenging conditions, due in part to the benefits of coherent gain. Among these, frequency-modulated continuous wave (FMCW) lidar has emerged as an effective ranging technique. By transmitting and receiving linearly chirped optical signals, FMCW lidar encodes distance information as a beat frequency between the received signal and a local oscillator. This allows for fine range resolution to be achieved without the need for ultrafast detector bandwidths, in contrast to a pulsed lidar with similar specifications [27]. One advantage that FMCW lidar has over pulsed lidar systems is the achievable range

resolution. This is demonstrated by Roos et al., who achieved linear chirp bandwidths of up to 5 THz, resulting in a range resolution of approximately 30 micrometers [28].

FMCW lidar systems have been used extensively to compute 3D point clouds, where a scanning beam is used to sweep across the observed scene and distance calculations are performed at each stop. While effective at mapping, point-cloud images only provide distance information at the scanned locations, not a full-field wavefront reconstruction of the object scene. Additionally, scanning systems are limited by both the achievable spatial resolution and pointing instability (wobble) of the scanning mechanism, as well as by the lag between the transmitted and return beams, which restrict scan speed. This occurs because the receiver may no longer be aligned with the transmitted beam when the return signal arrives, impacting the coupling efficiency. While continuous-wave (CW) digital holography records both the amplitude and phase of the object field, it lacks range information so reconstructions include all objects within the depth of field of the imaging system.

By combining FMCW modulation with digital holographic recording techniques, the complex optical field can be reconstructed, yielding holographic imaging of an object scene with intrinsic range information, which represents a powerful advancement to coherent imaging systems.

Linear FMCW signals have been integrated into digital holography to perform range profiling in two distinct ways. The first approach, often referred to as FMCW digital holography, employs long broadband chirps in combination with high speed detectors, enabling multiple short integrations during each chirp. Post-processing the recorded frames using a Fourier transform across the temporal dimension allows the reconstruction of pixel wise range profiles [29–32]. More complicated configurations have allowed for the polarization analysis of a object, as well as the implementation of wavelength multiplexing techniques to perform spatial profiles of metallic blocks [33, 34]. On the microscale, in a similar manner, Crouch et al. demonstrated synthetic aperture ladar using an ultrabroadband ($>$ 3 THz)

linear chirp to capture topographical images of a coin [35].

The other technique, known as range-selective digital holography (RSDH), enables objects at tunable distances within the range resolution of the FCMW chirp to be reconstructed. This is performed by frequency shifting the reference beam by an amount set by the object distance, and has been demonstrated in an off-axis recording geometry which has allowed for the distinction of closely spaced objects that are within the depth of field of the imaging system [36, 37].

Stabilized RSDH, capable of compensating for phase shifts caused by object vibrations and uniform piston phase variations, while suppressing light from unwanted object ranges, will greatly enhance all previously discussed techniques. Furthermore, stabilization techniques will enables digital holography to function in practical real-world conditions outside of the laboratory setting.

Imaging Vibrating Objects with Coherent Systems

One limitation to digital holography is its extreme sensitivity to the vibrations of the object being captured. Since holography is an interferometric imaging technique, if the object's displacement along the optical axis approaches half the wavelength of the illuminating light within the camera's exposure time, the interference fringes in the digital hologram become blurred, effectively reducing their visibility to zero. Additionally, atmospheric turbulence can further disturb this phase relationship, leading to degraded reconstructions that worsen over longer distances due to piston phase fluctuations. This sensitivity is especially problematic for phase-shifting holographic techniques, which require phase stability across four separate integrations to successfully reconstruct a hologram.

Coherent imaging systems struggle to accurately capture images of vibrating objects due to the rapid phase fluctuations introduced by motion, which can distort the reconstructed image and reduce clarity. One approach to mitigate this issue is to use shorter exposure times,

minimizing movement during a single integration [38]. However, in outdoor applications where longer exposure times are necessary due to limited return light, this solution becomes less practical. Modulating the phase of the local oscillator beam can enhance the detection of both low and high vibration amplitudes which has been previously demonstrated by reflecting the local oscillator beam off a mirror mounted on the vibrating object of interest [39–41]. Unfortunately, this is impractical in real-world applications. Methods for focusing the illumination signal onto the object to use as a reference have also been explored, which has led to shearing interferometry approaches where the spatial displacement between the reference and object beams are used to detect small changes [42, 43].

A stabilization technique where the lidar beat frequency is used to modulate the holographic system to correct for an unknown vibration has recently been achieved in an off-axis image plane holographic recording geometry [44]. This experiment was conducted in a laboratory setting at a maximum range of only a meter with a depth of field of less than a centimeter. While this technique has only been demonstrated in controlled environments, it is anticipated that similar approaches could be beneficial for coherent imaging over long distances or through turbulent conditions in outdoor settings, as well as applicable to other recording geometries.

Despite these table-top successes, several challenges remain, including the realization of on-axis range-selective holographic geometries using more exotic modulation schemes, the development of long-range outdoor capabilities that can correct for vibration and turbulence, and the characterization of multi-chirp integration. Addressing these issues is central to the work presented in this thesis.

Objectives and Overview

The objective of this thesis is to develop novel range-selective digital holography (RSDH) techniques and to advance both the methodology and practical implementation

of outdoor range-selective holographic imaging. The research is organized along two main directions. The first direction explores on-axis, range-selective digital holography in laboratory environments, including experimental demonstrations and the development of the underlying theory for temporal-heterodyne range-selective imaging. Additionally, theoretical models for multi-chirp integration are developed, which are essential for phase-shifting techniques that require multiple integrations. On-axis geometries are particularly advantageous for holographic recordings due to their simplified configuration and improved spatial resolution.

The second direction focuses on long-range outdoor holographic imaging. A dual lidar and range-selective digital holographic system is constructed for outdoor operation at distances over a kilometer, with demonstrated operation up to a quarter of a kilometer. In addition, a lidar-enabled stabilization method is developed that preserves holographic fidelity under vibration, enabling coherent imaging of vibrating objects in realistic outdoor conditions. The novel contributions of this thesis are:

- Demonstration of on-axis temporal heterodyne range-selective digital holography using time-of-flight detectors.

- Theoretical and experimental analysis of detuning outcomes in multi-chirp temporal heterodyne range-selective holography, with implications for other range-selective holographic methods that integrate over multiple chirps.

- Design and construction of a long-range outdoor dual-lidar and holography platform capable of operation at distances over a kilometer, with demonstrations at 90 meters.

- Demonstration of lidar-enabled stabilization of digital holography, achieving coherent imaging at 90 meters under vibrations exceeding 18 optical wavelengths within a single integration period.

Outline of the Document

This thesis is organized into eight main chapters. Chapter 2 provides the necessary background, introducing the physical principles that form the foundation of this work. Topics include coherent lidar, optical modulation, holographic imaging, range-selective holography, and time-of-flight detectors. Chapter 3 presents a published manuscript on temporal-heterodyne on-axis range-selective digital holography, a novel holographic technique that leverages time-of-flight detectors to perform phase shifting. Chapter 4 contains an additional publication examining the effects of detuning in temporal heterodyne range-selective digital holography when integration occurs over multiple frequency chirps. These results have broader implications for range-selective holography methods beyond temporal heterodyning which rely on integrating the hologram over multiple chirps. Chapter 5 details the design and construction of an outdoor, long-range lidar and range-selective digital holography system capable of operating in both modalities. Chapter 6 introduces a manuscript prepared for submission that demonstrates how the lidar system can stabilize digital holograms under adverse conditions, such as vibration, which would normally preclude coherent imaging. Chapter 7 presents supplementary material not included in the manuscripts. This includes vibrometry results showing how the lidar system can reconstruct audio signals from vibrating objects, as well as demonstrations of Doppler point cloud reconstruction, providing velocity-resolved imaging. Finally, Chapter 8 summarizes the key contributions of this work and outlines directions for future research.

10

BACKGROUND

In this section, a concise overview of the essential background topics required to understand the completed work will be provided. Key methods and concepts will be introduced, including lidar, frequency-modulated continuous-wave signals, digital holography and its various recording geometries, hologram reconstruction, range-selective digital holography, and Time-of-Flight detectors. This is done to ensure a comprehensive foundation for understanding the published work that is included in the following chapters.

Lidar

Lidar (Light Detection and Ranging) is a remote sensing technique that measures the distance to objects by illuminating an object and detecting the reflected signal. The time delay between the transmit field (TX) and return field (RX), combined with the known speed of light c, allows precise measurement of object range. In addition to range, lidar can provide information on object reflectivity, polarization, velocity and, when scanning is applied, 3D spatial profiles known as point cloud images.

Lidar techniques are generally classified into two main categories. The first is pulsed lidar, which encodes information in short, amplitude-modulated light pulses. The second is Frequency-Modulated Continuous-Wave (FMCW) Lidar, which uses continuous illumination from a frequency-modulated laser source to extract range information. Each approach has distinct advantages, as well as relative disadvantages, and is widely employed across a variety of applications.

An additional distinction can be made between incoherent and coherent detection schemes. Incoherent lidar directly measures the intensity of the returned optical field, providing information on range and reflectivity. Coherent lidar, by contrast, mixes the return signal with a local oscillator (LO) in a heterodyne or homodyne receiver. This enables

measurement of both amplitude and phase, allowing for higher sensitivity and improved rejection of background noise. The majority of FMCW lidar systems rely on coherent detection, whereas pulsed lidar is commonly implemented using either coherent or incoherent detection schemes.

Pulsed Lidar

Pulsed lidar systems generate short, discrete light pulses ("flashes"), which are used to illuminate an object. Some of the light is reflected off of the object back to the detector. The round-trip time of each pulse (from transmission to detection) is measured at the detector to determine the object distance using the speed of light. The range to the object is then calculated using

$$R = \frac{c\,\tau_R}{2}, \tag{1}$$

where c is the speed of light in air and τ_R is the time delay between the transmitted and received signals [45]. One consequence of shortening the pulse duration is improved range resolution, but this comes at the cost of higher peak power requirements and the need for faster detectors. The range resolution can be expressed as a function of the pulse width τ_p as

$$\Delta R_{res} = \frac{c\,\tau_p}{2}. \tag{2}$$

Figure 1 illustrates the working principle by showing the transmit and time-delayed return optical signals. The time between TX pulses is the pulse repetition interval τ_{PRI}.

Pulsed lidar is widely used in applications such as three-dimensional imaging and time-of-flight cameras because of its simplicity, but its sensitivity and resolution are generally lower than those achievable with coherent detection methods like FMCW lidar. Moreover,

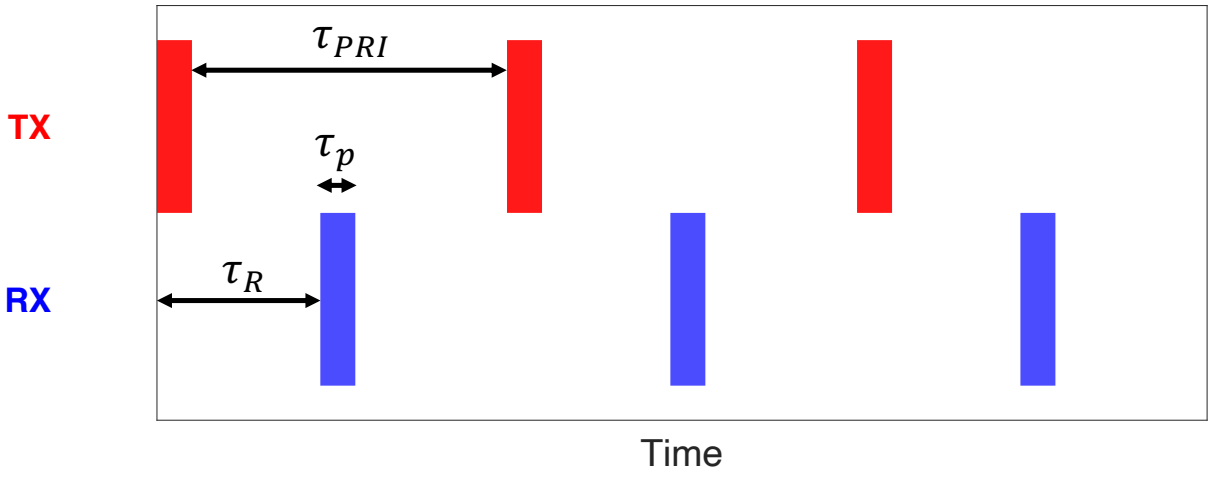


Figure 1: Pulsed lidar system cartoon. The transmitted signals are shown in red while the time-delayed returns are shown in blue.

pulsed lidar systems require higher-bandwidth detectors than coherent systems to accurately capture the short-duration pulsed signals and achieve comparable resolution, which can complicate design and increase cost.

Frequency Modulated Continuous Wave Lidar

Frequency-Modulated Continuous-Wave Lidar is a coherent ranging technique that uses the frequency modulation of a laser to perform high-resolution distance measurements, typically through linear frequency sweeps, also known as "chirps". In a coherent FMCW lidar system the TX signal is split into two paths forming a TX and LO signal. The LO is mixed with the received RX field scattered from the object, producing a beat frequency proportional to the object's range. Measuring this beat frequency enables precise range calculation, with range resolution inversely proportional to the chirp bandwidth, rather than the pulse duration. This technology is widely used in applications requiring precise distance measurements, such as in autonomous vehicles sensors and advanced surveying and mapping systems. While more complex modulation schemes exist, in this document, any reference

to FMCW lidar or FMCW digital holography will specifically pertain to linear frequency-modulated signals (chirps) and not to more complicated waveforms that also use frequency modulation techniques.

For FMCW lidar, both the LO and TX beams are modulated with a linear chirp that is applied before the laser is split into the two channels. The chirp is characterized by a chirp rate, κ, which is defined as

$$\kappa = \frac{B_c}{\tau_c}, \tag{3}$$

where B_c is the chirp bandwidth and τ_c is the chirp duration. The optical fields for both the LO and the RX signal, where the RX is a time-delayed copy of the TX signal delayed by τ_R, can be expressed as

$$E_{\mathrm{LO}}(t) = A_{\mathrm{LO}} e^{i(2\pi f_L t + \pi\kappa t^2 + \phi_{\mathrm{LO}})} \tag{4}$$

$$E_{\mathrm{RX}}(t, \tau_R) = A_{\mathrm{RX}} e^{i(2\pi f_L (t-\tau_R) + \pi\kappa (t-\tau_R)^2 + \phi_{\mathrm{RX}})} \tag{5}$$

where A_{LO} and A_{RX} are the amplitudes of the LO and RX field, ϕ_{LO} and ϕ_{RX} are the initial phases of the LO and RX field, and f_L is the laser frequency. The intensity of the two interfering waves, as observed through a photodetector with bandwidth BW_{det}, is given by:

$$
\begin{aligned}
I(t,\tau_R) &= \left\langle \left| E_{\mathrm{LO}}(t) + E_{\mathrm{RX}}(t,\tau_R) \right|^2 \right\rangle_{\frac{1}{BW_{\mathrm{det}}}} \\
&= \left\langle |E_{\mathrm{LO}}(t)|^2 + |E_{\mathrm{RX}}(t,\tau_R)|^2 + E_{\mathrm{LO}}(t)E^*_{\mathrm{RX}}(t,\tau_R) + E_{\mathrm{RX}}(t,\tau_R)E^*_{\mathrm{LO}}(t) \right\rangle_{\frac{1}{BW_{\mathrm{det}}}} \\
&= A^2_{\mathrm{LO}} + A^2_{\mathrm{RX}} + 2A_{\mathrm{LO}}A_{\mathrm{RX}} \cos\!\big(2\pi\kappa\tau_R\, t + 2\pi f_L \tau_R - \pi\kappa\tau_R^2 + \phi_{\mathrm{LO}} - \phi_{\mathrm{RX}}\big) \\
&= A^2_{\mathrm{LO}} + A^2_{\mathrm{RX}} + 2A_{\mathrm{LO}}A_{\mathrm{RX}} \cos\!\big(2\pi f_b\, t + \phi_b\big),
\end{aligned}
\tag{6}
$$

The interference between the LO and RX signals produce a beat frequency, f_b, which is proportional to the object distance by,

$$
f_b = \frac{2\kappa R}{c} = \kappa\tau_R \tag{7}
$$

where R is the distance to the object and c is the speed of light. The phase of the beat frequency, ϕ_b, is defined as $\phi_b = (2\pi f_L \tau_R - \pi\kappa\tau_R^2 + \phi_{\mathrm{LO}} - \phi_{\mathrm{RX}})$ [46, 47]. Higher frequency phase terms are suppressed because of the finite bandwidth of the detector. The distance to the object can then be calculated from the beat frequency using the following equation,

$$
R = \frac{f_b c}{2\kappa}. \tag{8}
$$

In FMCW lidar, balanced photodetection is commonly employed to improve sensitivity and suppress common-mode noise [48]. In this case, the optical signals from the LO and RX channels are combined in a beam splitter, producing two paths in which the beat signals are 180° out of phase. The two paths are directed onto two photodiodes, generating photocurrents that contain the same beat frequency but interference terms of opposite phase. Subtracting these photocurrents cancels the large DC components that do not carry range information while preserving the relative phase, thereby enabling more accurate measurement

of the beat signal. Mathematically, the photocurrents at the two diodes can be expressed as:

$$i_1(t) \propto |E_{\mathrm{LO}}(t) + E_{\mathrm{RX}}(t)|^2 = A_{\mathrm{LO}}^2 + A_{\mathrm{RX}}^2 + 2A_{\mathrm{LO}}A_{\mathrm{RX}}\cos(2\pi f_b t + \phi_b) \tag{9}$$

$$i_2(t) \propto |E_{\mathrm{LO}}(t) - E_{\mathrm{RX}}(t)|^2 = A_{\mathrm{LO}}^2 + A_{\mathrm{RX}}^2 - 2A_{\mathrm{LO}}A_{\mathrm{RX}}\cos(2\pi f_b t + \phi_b) \tag{10}$$

Subtracting the two currents yields the balanced output:

$$i_{\mathrm{diff}}(t) = i_1(t) - i_2(t) = 4A_{\mathrm{LO}}A_{\mathrm{RX}}\cos(2\pi f_b t + \phi_b) \tag{11}$$

Notice that the large DC terms $A_{\mathrm{LO}}^2 + A_{\mathrm{RX}}^2$ cancel exactly, leaving only the interference term at the beat frequency f_b, which encodes the object range along with the phase difference between the LO and RX channels. If multiple returns are present, and provided that $A_{\mathrm{RX}} \ll A_{\mathrm{LO}}$ for all objects, the differential detector output $i_{\mathrm{diff}}(t)$ consists of the sum of sinusoidal components, each with a beat frequency corresponding to the range of a particular object.

After the signal is detected on the photodetector, it is digitized using an analogue-to-digital converter (ADC), which enables post-processing of the signal on a computer to recover the frequency spectrum using algorithms such as the FFT. A more thorough discussion of post processing techniques will be discussed in chapter 5.

A schematic of a simplified FMCW lidar system is shown in Figure 2. The laser source is first modulated with a linear chirp and is then split into both the LO and TX paths. The TX signal passes through an optical circulator (a type of optical directional coupler) and is emitted into free space to illuminate the object. The reflected RX field is collected back into

the transmit port of the circulator and directed to the detector, where it mixes with the LO signal, preferably with a coherent balanced detector as described above. Post-processing of the recorded time-domain signal yields a frequency spectrum, where the beat frequency will be proportional to the object distance.

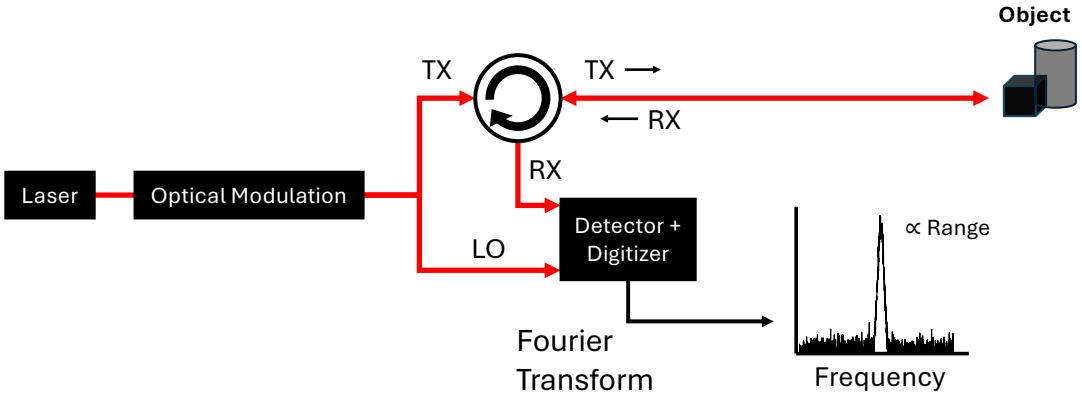


Figure 2: Basic FMCW Lidar Schematic. A laser source is linearly chirped and split into a TX and LO path. The RX signal is mixed with the LO on a coherent balanced photodetector (assumed incorporated into "detector"), and the resulting beat signal is digitized. A Fast Fourier Transform (FFT) is applied in post-processing to extract the beat frequency, which is used to determine the object distance. This figure is not to scale and is for illustrating purposes only.

Figure 3 illustrates the chirped LO and RX signals delayed from one another by τ_R using a positive chirp rate ($\kappa > 0$). Also shown is the windowed time-domain beat signal resulting from their overlap, as detected by a photodetector, and the corresponding frequency-domain representation obtained by applying a Fast Fourier Transform to the windowed data.

It should be noted that the previously introduced range equations for both pulsed and FMCW lidar assume a constant and known speed of light. However, during long-range operations, variations in the air's refractive index caused by turbulence, temperature fluctuations, humidity, and other factors can degrade the ranging accuracy of both techniques. Extensive research has been conducted to account for these refractive index changes [49–51].

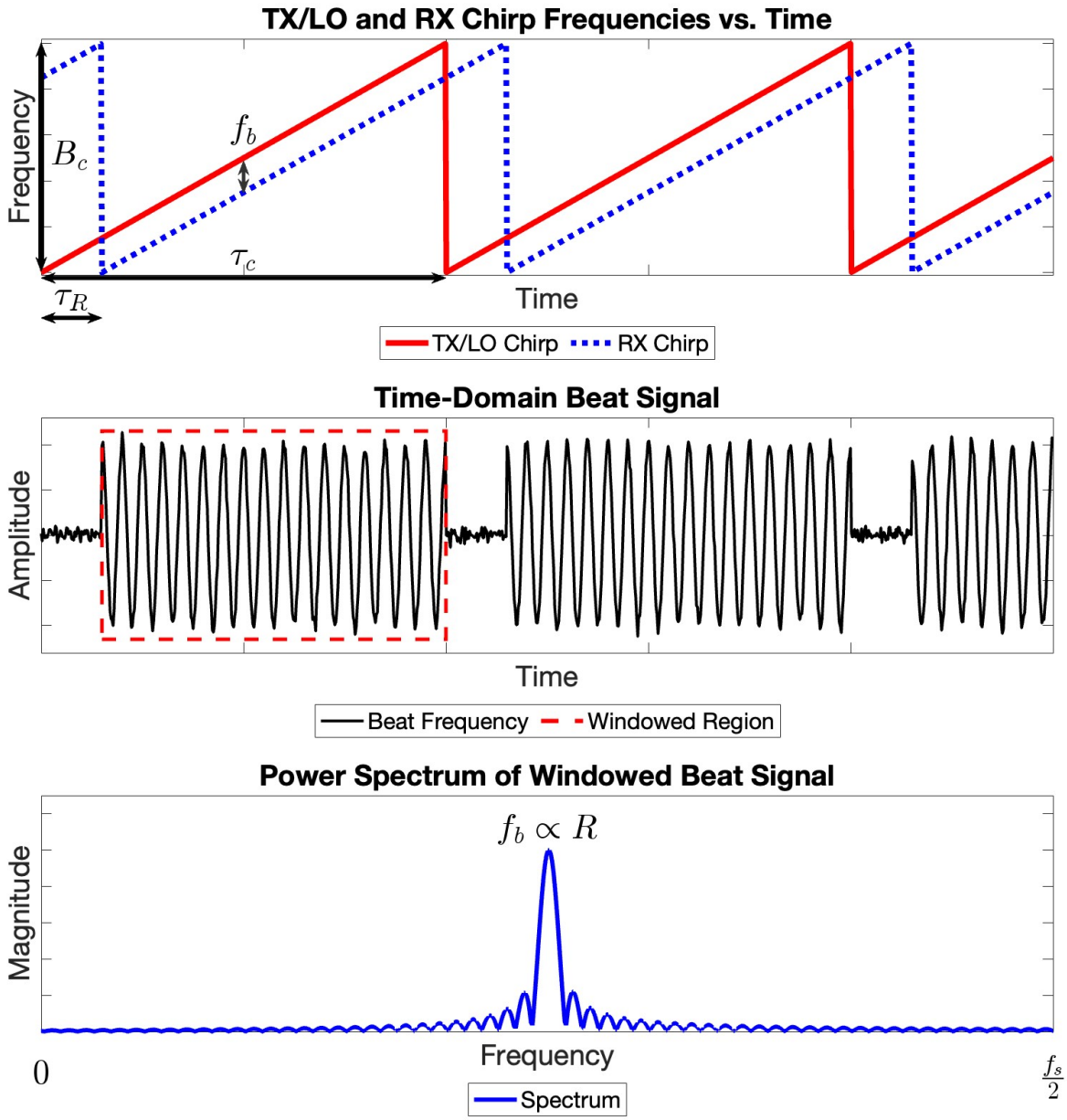


Figure 3: The top plot depicts Interference between the LO and RX FMCW chirps with a chirp bandwidth B_c, chirp duration τ_c, and round-trip delay τ_R. The center plot shows temporal windowing of the resulting time-domain beat signal. The bottom plot presents the frequency-domain representation, computed as the Fourier transform of the windowed signal. The gaps between the noisy sinusoidal signals in the Time-Domain Beat Signal plot are caused by the beat being outside of the detector bandwidth.

Range Resolution

Range resolution is a critical parameter in FMCW lidar systems as it determines the ability to distinguish between two closely spaced objects. It is defined as the minimum radial distance, ΔR_{res}, at which two targets can still be resolved as distinct objects by the system. The range resolution is given by

$$\Delta R_{res} = \frac{c}{2B_c}, \tag{12}$$

where c is the speed of light and B_c is the chirp bandwidth. A larger chirp bandwidth leads to a finer range resolution, allowing the system to distinguish objects that are more closely spaced. Notably, the range resolution is inversely proportional to the chirp bandwidth and is independent of chirp duration. Figure 4 illustrates how the system's ability to resolve two objects depends on their separation relative to ΔR_{res}. When two objects are separated by exactly ΔR_{res}, the peak of one object's response coincides with the first null of the other. At this separation, the objects are just resolvable according to the Rayleigh criterion. For smaller separations, they can no longer be distinguished. The responses in both the range and frequency domains follow a sinc^2 pattern, which is due to the rectangular time-domain window imposed by the integration period. This sinc^2 profile arises from taking the squared magnitude of the Fourier transform of the rectangular time-domain window defined by the integration time τ_{int}, which is often equal to or shorter than the chirp duration τ_c. Note that amplitude modulating the chirp can implement different windowing functions, resulting in corresponding changes to the range response.

Two objects can only be resolved when their separation is greater than or equal to ΔR_{res}. However, several practical factors can degrade the effective range resolution of an FMCW lidar system. These include laser phase noise, chirp nonlinearity, and laser decoherence (particularly when the round-trip path length approaches or exceeds the laser's coherence

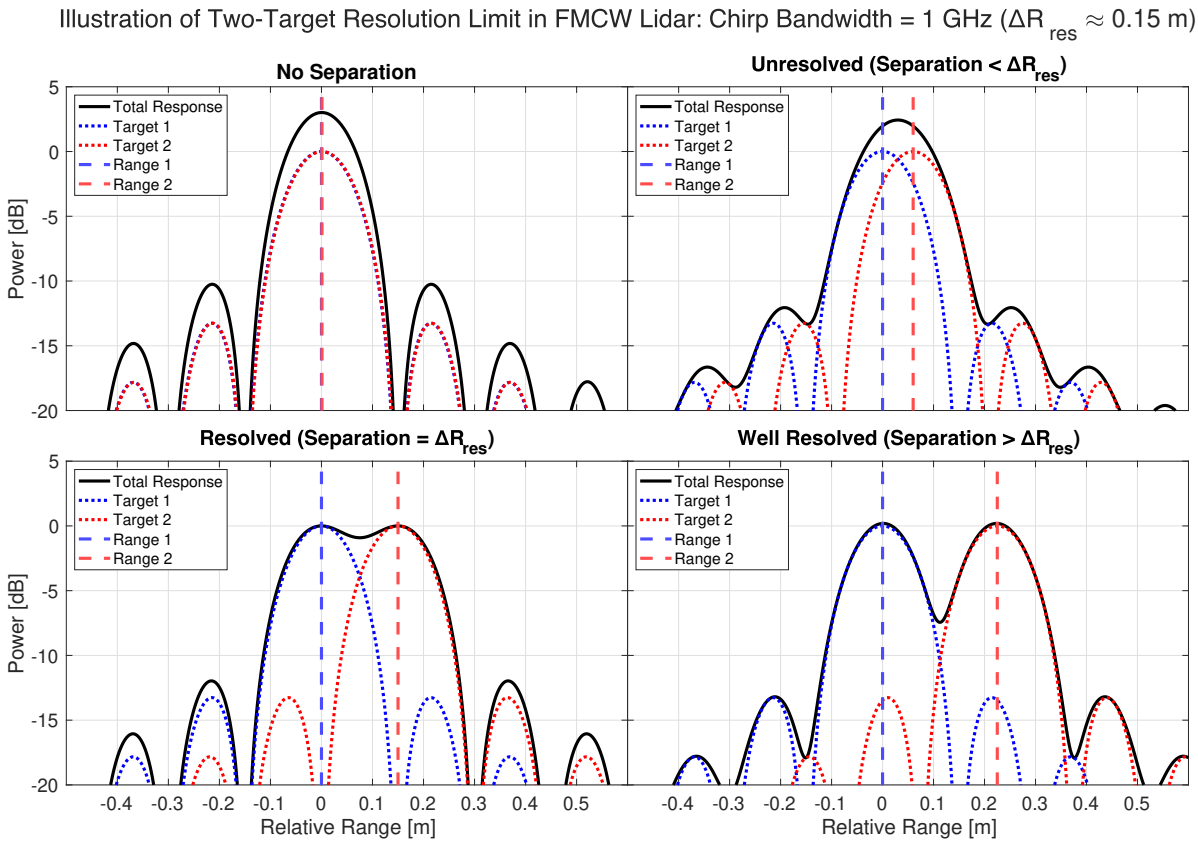


Figure 4: Resolution limit for a chirp bandwidth of 1 GHz, corresponding to a range resolution of $\Delta R_{res} \approx 0.15$ m. Two objects with approximately zero separation (top left). Two objects that are separated in distance by less than the range resolution of the system (top right). Two objects spaced exactly ΔR_{res}, meeting the Rayleigh resolution criterion (bottom left). Two objects separated by more than ΔR_{res}, clearly resolved as distinct peaks (bottom right).

length). Such impairments can cause object responses to broaden or shift in the frequency domain, reducing the system's ability to distinguish closely spaced objects.

Optical Frequency Modulation

To enable FMCW lidar, the laser source must be modulated with a highly repeatable controlled frequency chirp. One effective method to achieve optical frequency modulation is through the use of electro-optical modulators (EOMs). These devices exploit the electro-optic effect, where the refractive index of a material changes in response to an applied electric field. This change in refractive index modifies the optical path length, allowing controlled modulation of the light's phase and, by extension, its instantaneous frequency. In a typical setup, the laser beam travels through an EOM before being split into the LO and TX beams. The EOM consists of a crystal with a high electro-optic coefficient, such as lithium niobate ($LiNbO_3$). When a time-varying voltage is applied across the crystal, it induces a periodic change in the refractive index, resulting in a frequency modulation of the passing laser beam [52].

EOMs are commonly implemented as either electro-optic phase modulators (EOPMs) or electro-optic intensity modulators (EOIMs). An EOPM uses a single RF input to directly change the optical phase of the light as it passes through the crystal. An EOIM is based on a Mach-Zehnder interferometer in which the RF drive signal changes the phase in one or both arms to control the output intensity through interference, and an additional DC bias sets the relative phase between the two arms. An illustration of both an EOPM and EOIM is shown in Figure 5.

Mathematically, this frequency modulation can be illustrated using the simpler case of an EOPM by considering a laser beam entering the modulator, described as:

$$E(t) = Ae^{i\omega_L t} \tag{13}$$

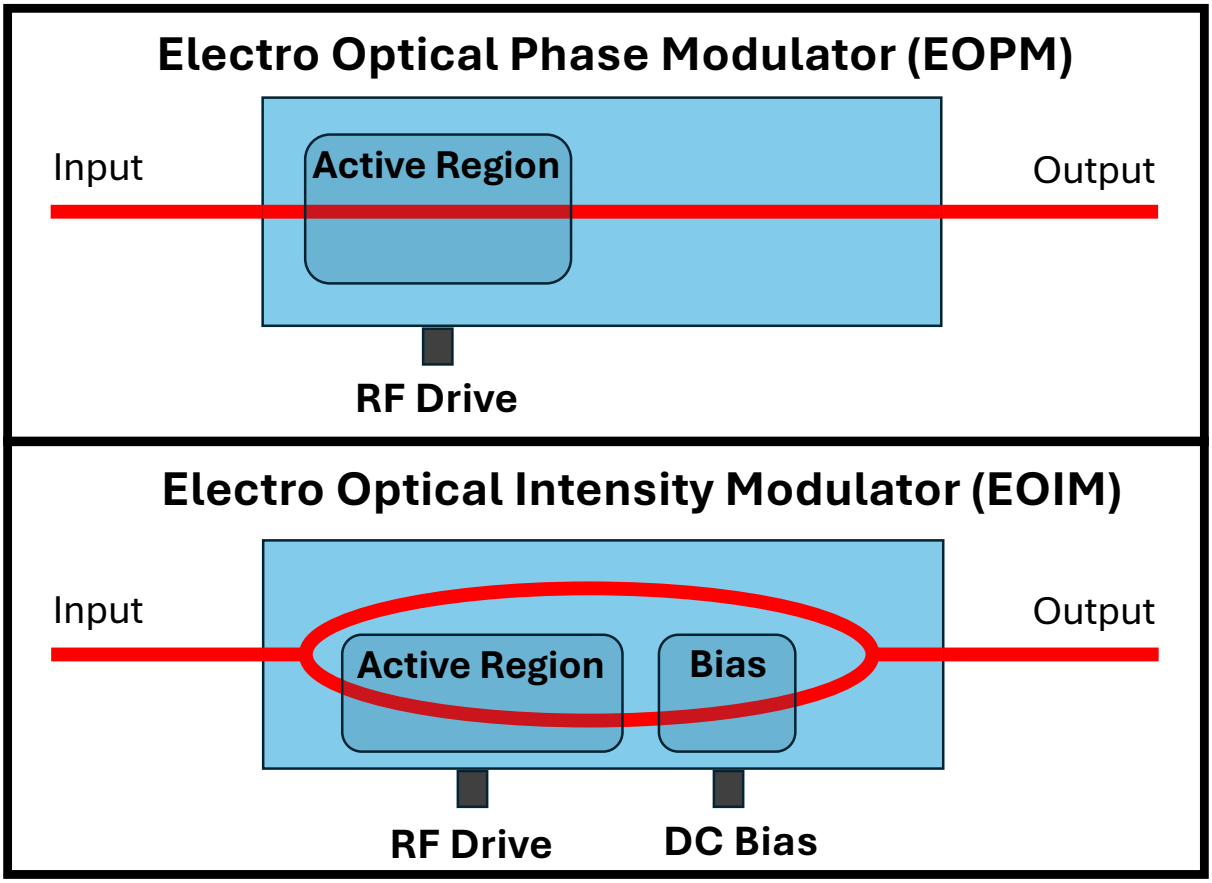


Figure 5: Electro-optic phase modulator (top) and electro-optic intensity modulator (bottom). The entire structure represents the electro-optic crystal. The red lines represent the input and output optical waveguides. The active region indicates where the RF drive voltage is applied. The intensity modulator forms a Mach–Zehnder interferometer, in which an additional bias voltage controls the relative phase between the two arms.

where A is the amplitude of the laser and ω_L is the angular frequency of the optical carrier. If a chirped voltage is applied to the EOM with modulation index β, and chirp rate κ, a time-dependent phase will be imparted to the optical field. The modulated beam can be expressed as,

$$E_{\text{mod}}(t) = Ae^{i\omega_L t}e^{i\beta\sin(2\pi(f_o t+\frac{1}{2}\kappa t^2))} \tag{14}$$

where f_o is the initial frequency of the chirp. To analyze the frequency content of this modulated signal, the Jacobi-Anger expansion is applied:

$$e^{i\beta\sin\theta} = \sum_{n=-\infty}^{\infty} J_n(\beta)e^{in\theta} \tag{15}$$

Using this identity, the modulated optical field can be rewritten as:

$$E_{\text{mod}}(t) = Ae^{i\omega_L t}\sum_{n=-\infty}^{\infty} J_n(\beta)e^{in(2\pi(f_o t+\frac{1}{2}\kappa t^2))} \tag{16}$$

This representation reveals that the modulated signal can be expressed as a sum of time-varying spectral components, whose amplitudes are governed by Bessel functions of the first kind, $J_n(\beta)$, with integer order $n \in \mathbb{Z}$, and whose frequencies evolve according to the chirped phase term. Unlike the case of sinusoidal modulation, these components do not form evenly spaced sidebands in the frequency domain since higher order sidebands will have a larger frequency bandwidth than the original RF chirp modulation. A cartoon of this principle is shown in Figure 6.

The role of the Bessel functions can be most intuitively understood by examining the power spectrum of Equation 14 for two sinusoidal signals (when $\kappa = 0$) at frequencies $f_1 = 2400$ Hz and $f_2 = 369$ Hz. Figure 7 illustrates how the Bessel functions of the first kind determine the relative amplitudes of the resulting sidebands for three different values

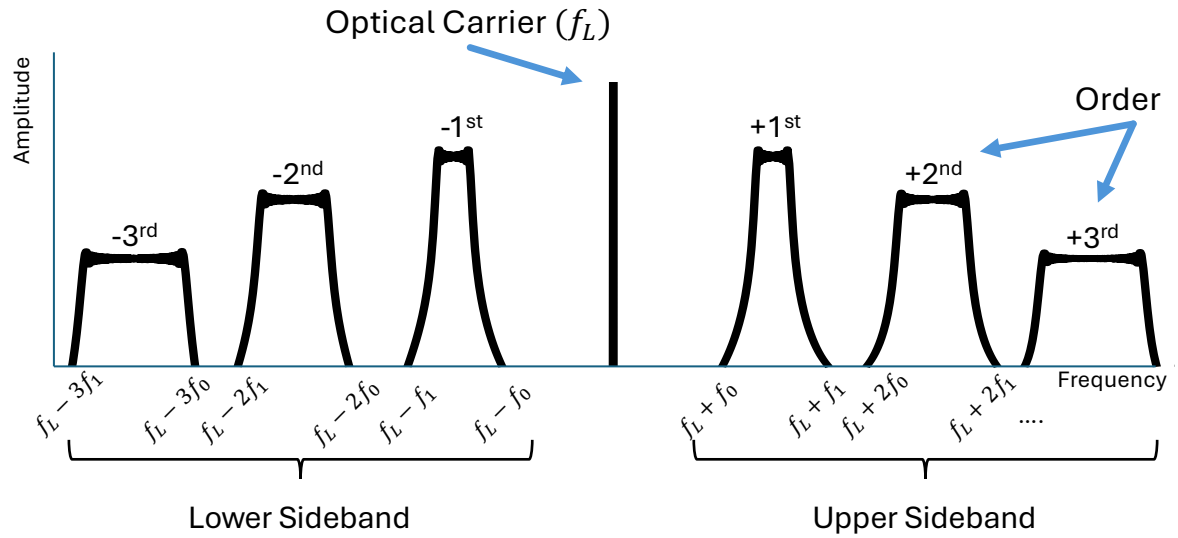


Figure 6: Sidebands of a chirped signal where f_L is the laser frequency (carrier), f_0 is the starting frequency of the chirp, and f_1 is the end frequency of the chirp.

of the modulation index β. While this example is presented at audio frequencies for ease of simulation, the same principles hold at optical frequencies (albeit harder to simulate on a computer). This example illustrates sinusoidal modulation for simplicity, but the Jacobi-Anger expansion remains valid for chirped modulation. In this case, however, the spectral amplitudes are not determined directly by Bessel functions, since the energy is distributed continuously across the chirp bandwidth.

EOMs are characterized by their half-wave voltage, V_π, which is the voltage required to induce a π-radian phase shift on the incoming optical signal. The modulation index β is related to the applied peak-to-peak voltage V_{PP} and V_π through the following expression:

$$\beta = \frac{\pi V_{\mathrm{PP}}}{2V_\pi}. \tag{17}$$

Higher-order sidebands, although occasionally useful because of the increased band-

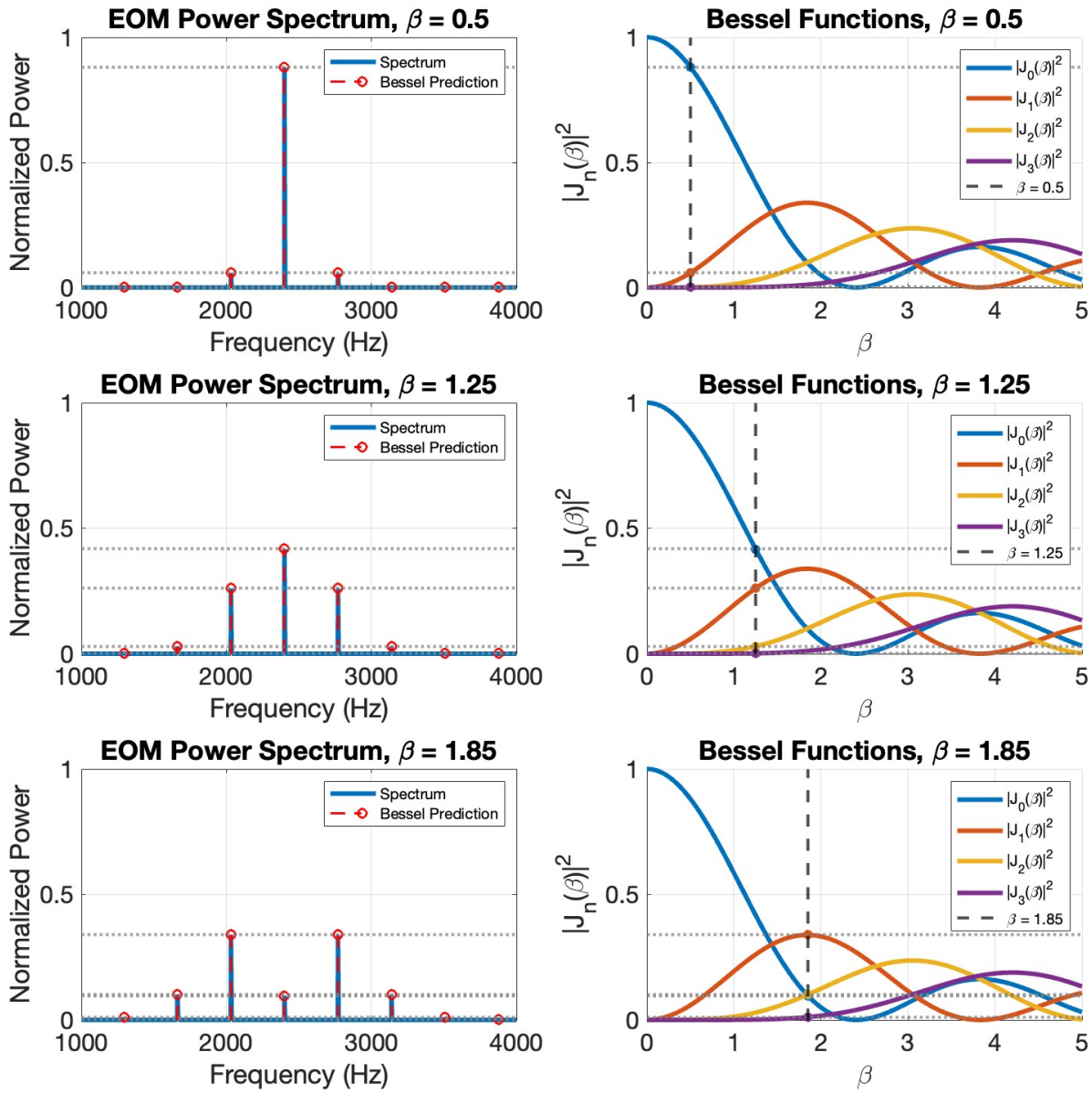


Figure 7: Simulation illustrating the output of an electro-optic modulator modeled as the phase-modulated signal $e^{i2\pi f_1 t}e^{i\beta\sin(2\pi f_2 t)}$ for three different modulation indices β. The left column shows the spectrum while the right column displays the corresponding Bessel functions of the first kind, which predict the amplitudes of the generated sidebands. The zeroth through third order Bessel functions are plotted to demonstrate how sideband amplitudes vary with modulation depth.

width, are often undesirable in optical modulation because they correspond to unwanted frequency components that reduce the optical power concentrated in the desired harmonic, potentially degrading signal quality. To control the spectral content, the modulation depth (or modulation index) is commonly chosen to maximize the first-order Bessel function coefficient $J_1(\beta)$, while minimizing contributions from the carrier and higher-order sidebands.

To further suppress unwanted components, various types of electro-optic modulator configurations have been developed. These include intensity modulators based on Mach-Zehnder interferometers, which enable suppression of the optical carrier by destructive interference between the two interferometer arms. This is typically achieved by applying a DC bias voltage that introduces a π-phase shift between the arms, nullifying the zeroth-order outputs.

In push-pull intensity modulators, equal and opposite voltages are applied to the two arms of a Mach-Zehnder interferometer, producing a differential phase shift that modulates the output intensity. The shape of the transfer function depends on the bias voltage, which determines whether even or odd harmonics are suppressed. This allows the user to control the harmonic content of the optical signal by simply adjusting the bias voltage. Single sideband modulation techniques that also achieve carrier suppression have been demonstrated, although their implementation is more complex [53, 54]. Additionally, optical filtering is often employed to isolate a single sideband and further improve spectral purity.

Figure 8 shows simulation results illustrating the impact of varying both the modulation index and the bias voltage on the spectral output of a Mach-Zehnder intensity modulator. By changing these parameters, the figure shows how the harmonic content and sidebands change, and how modulation depth and bias voltage affect the optical spectrum.

Figure 9 presents optical and electrical spectra illustrating the effects of modulation on a real laser source. The unmodulated laser spectrum shows a single sharp peak at the center wavelength, representing the continuous-wave source. When the laser is driven by the

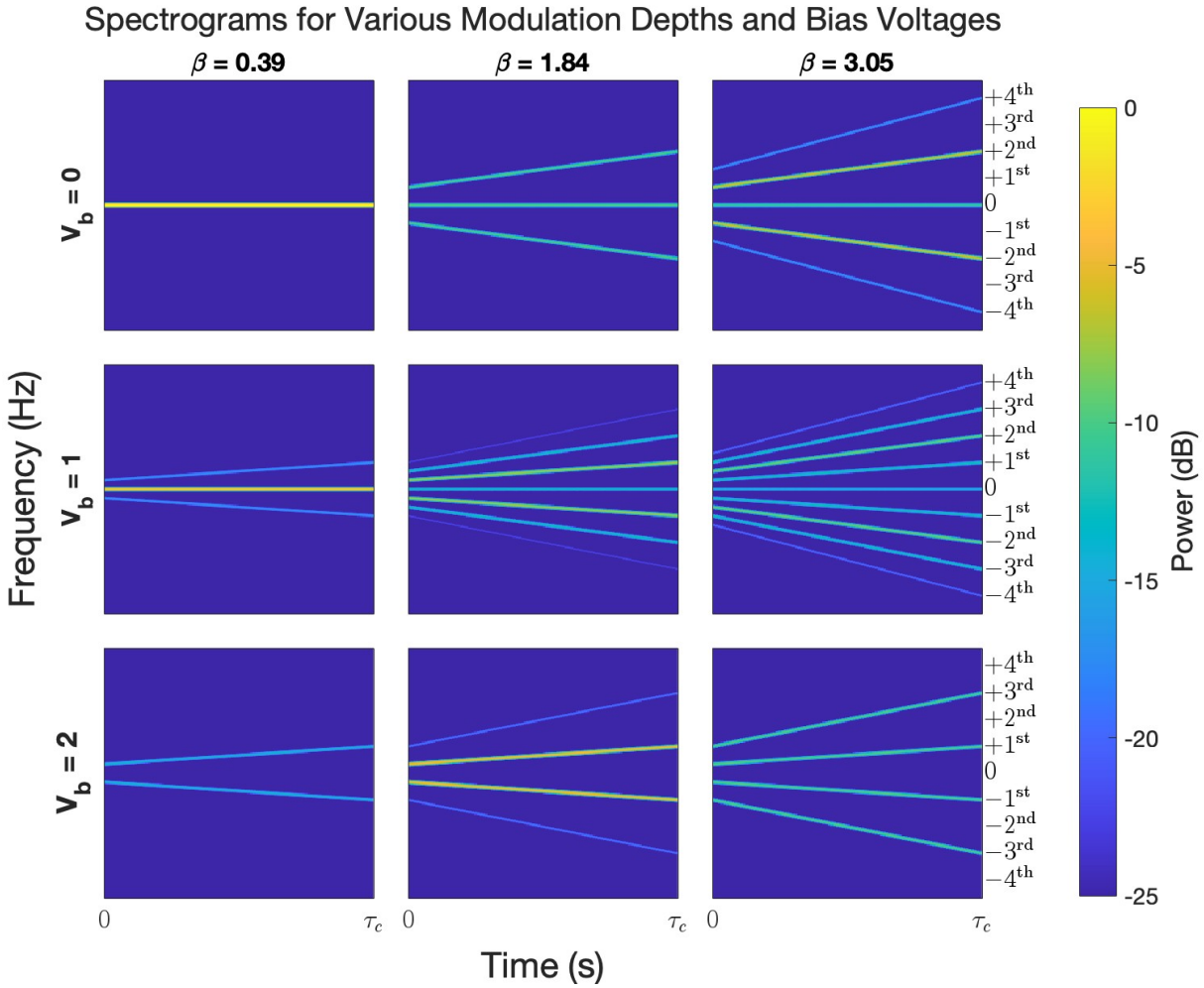


Figure 8: Simulated spectrograms of the baseband optical field output from a Mach-Zehnder intensity modulator under varying modulation index $\beta \in \{0.39,\, 1.84,\, 3.05\}$ V and DC bias voltages $V_b \in \{0,\, 1,\, 2\}$ V. Modulation depth values were chosen to show maximum power in the first and second sidebands. The modulator has a half-wave voltage of $V_\pi = 2\,\text{V}$. The RF drive is a linearly chirped sinusoid starting at 1 MHz with a bandwidth of 2 MHz and chirp duration of $\tau_c = 500\,\mu\text{s}$. Each subplot shows the spectrogram of the modulated baseband field shifted down to DC. At $V_b = 0\,\text{V}$, the modulator's cosine transfer function is symmetric, producing predominantly even harmonics whereas when $V_b = V_\pi$, the response is antisymmetric, yielding mostly odd harmonics. At intermediate bias voltages, both even and odd sidebands are present.

chirped RF signal, multiple sidebands appear symmetrically around the carrier frequency in the optical spectrum, visible on the optical spectrum analyzer (OSA) trace. These sidebands correspond to the frequency components generated by the modulation process. The accompanying RF spectrum of the chirp signal demonstrates the broadband nature of the modulation waveform, which directly influences the spacing and amplitude of the optical sidebands. The combined optical and electrical spectra highlight how the modulation waveform shapes the optical signal's spectral content.

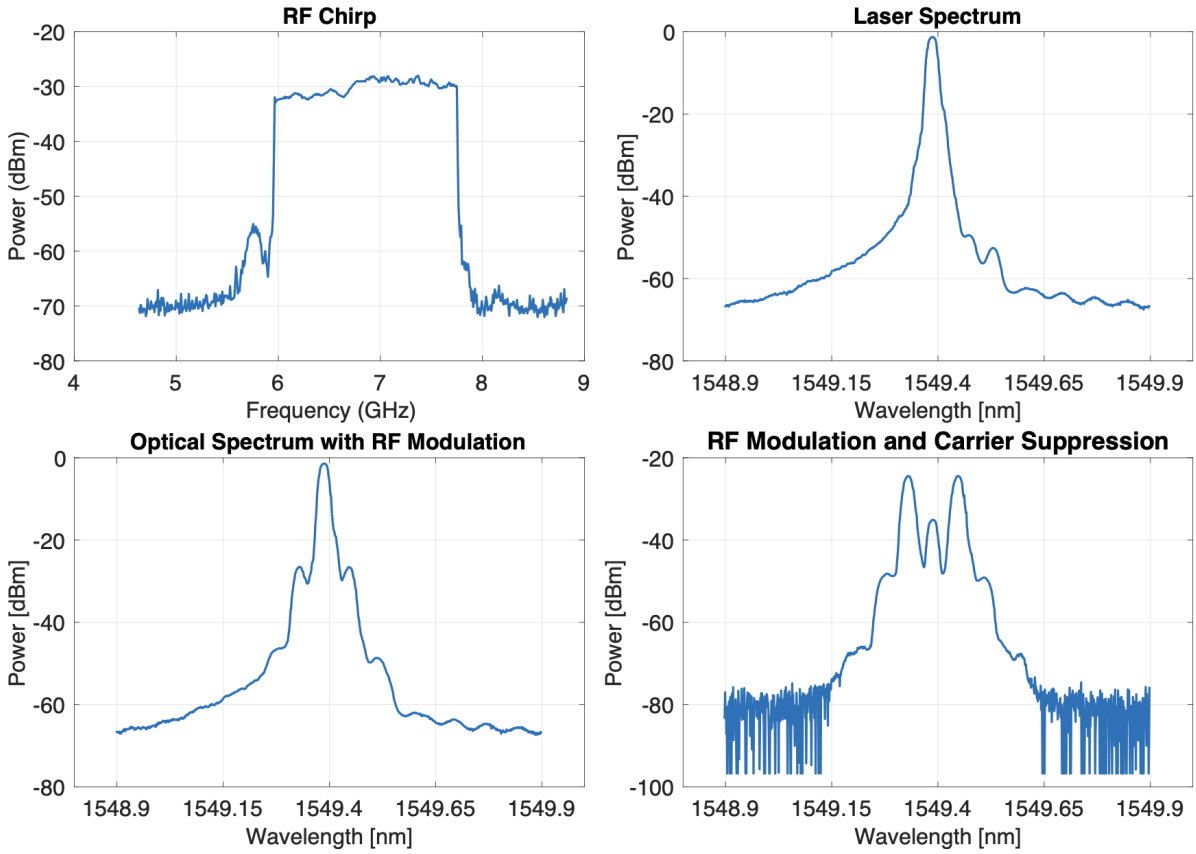


Figure 9: RF chirp spectrum measured by the an RF spectrum analyzer (RFSA), showing a 1.8 GHz bandwidth chirp from approximately 6 to 7.8 GHz (Top Left). Optical spectrum of the unmodulated continuous-wave 1550 nm laser source, displaying a single narrow peak at the carrier wavelength (Top Right). Optical spectrum of the laser under modulation with an electro-optical intensity modulator, exhibiting multiple sidebands symmetrically spaced around the carrier frequency (Bottom Left). Optical spectrum of the modulated laser with carrier suppression achieved by biasing the EOM, showing reduced carrier power and enhanced sideband visibility, highlighting the importance of biasing for effective optical carrier suppression (Bottom Right).

Range-Doppler Ambiguity

In FMCW lidar, when a target is in motion, the recorded beat frequency, f_b, includes contributions from both the range and radial velocity of the target. Specifically, for a positive chirp ($\kappa > 0$) the total beat frequency can be expressed as:

$$f_b = f_R + f_D = \frac{2\kappa R}{c} + \frac{2v_D}{\lambda} \tag{18}$$

Here, f_R is the range-dependent frequency component, f_D is the Doppler shift due to target motion, κ is the chirp rate of the transmitted signal, R is the target distance, v_D is the target's instantaneous radial velocity, c is the speed of light, and λ is the optical wavelength. In this example, the object is moving towards the detector (positive shift). A positive Doppler frequency represents a "blue shift" of the received signal (increase in the frequency) and indicates motion towards the lidar system while a negative Doppler frequency represents a "red shift" of the received signal (decrease in frequency), which corresponds to motion away from the lidar system.

A critical consequence of this relationship is the Range-Doppler ambiguity, where different combinations of range and velocity can result in the same beat frequency. For example, an increase in range can be offset by a corresponding change in radial velocity such that f_b remains constant. Without further processing, it becomes impossible to uniquely determine the object's range and velocity from a single measurement.

To resolve this ambiguity, three common techniques are used. Each method separates the range and Doppler components of the beat frequency using different modulation or detection strategies.

Single sideband Up-down chirps

The first approach is to alternate between up-chirps and down-chirps using single-sideband (SSB) modulation. Because Doppler shifts affect up-chirps and down-chirps in

opposite ways, comparing the beat frequencies between both presents an effective way to separate f_D from f_R [55]. During an up-chirp, a positive Doppler frequency shift causes the return signal to be shifted upward in frequency, reducing the total range-dependent beat frequency. Conversely, during a down-chirp, the Doppler shift increases the beat frequency. Using precise timing across chirps, the difference between the up-chirp and down-chirp beats

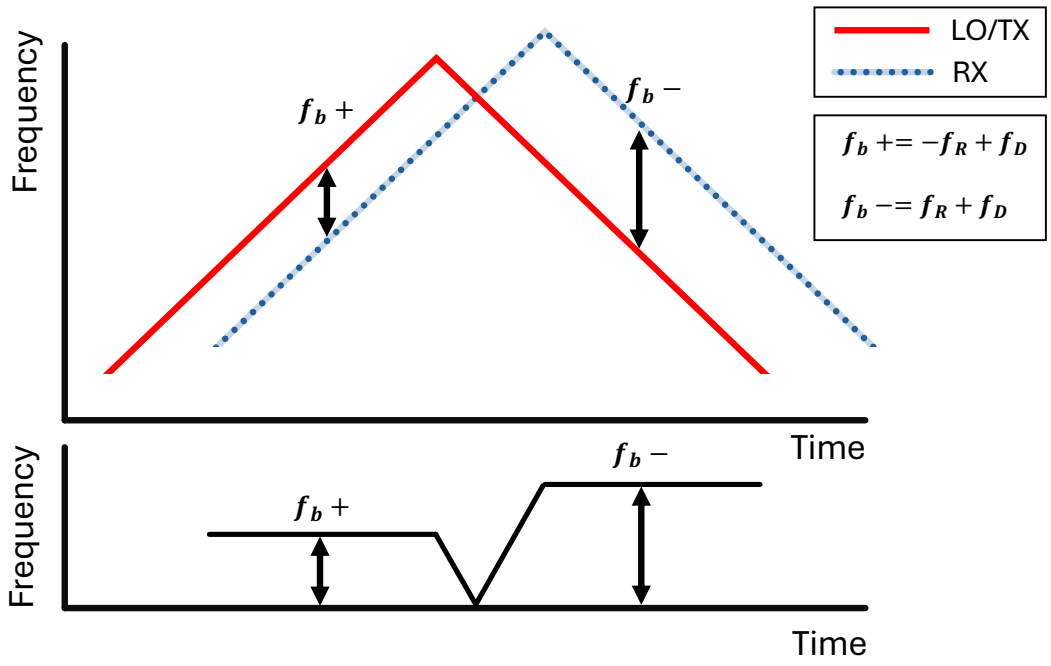


Figure 10: Illustration of how single-sideband up-chirps and down-chirps consecutively can be used to separate the doppler frequency shift from the range-dependent component.

can be compared to determine both f_D and f_R. This is achieved with the following equations where f_b^+ is the beat between the up-chirps with $\kappa > 0$ and f_b^- is the beat between the down-chirps with $\kappa < 0$.

$$f_R = \frac{f_b^- + f_b^+}{2} \tag{19}$$

$$f_D = \frac{f_b^- - f_b^+}{2} \tag{20}$$

This method, while conceptually straightforward, requires comparing the current beat signal with the past beat signal so changes in object velocity from one chirp to the next will reduce the accuracy of the reconstruction. Additionally, the beat frequencies from the up-and down-chirps have opposite signs, with one effectively appearing as a "negative" frequency depending on the chosen interference convention (LO-RX or RX-LO). However, since the signal is digitized and its spectrum is symmetric, this sign difference doesn't cause problems in analysis.

Double sideband AOFS

The second method utilizes double-sideband modulation in conjunction with an acousto-optic frequency shifter (AOFS). In this setup, either the transmitted (TX) or local oscillator (LO) beams are frequency-shifted by a fixed amount f_{AOFS}, such that $f_{\text{AOFS}} \gg f_b$. The optical modulator inherently creates upper and lower sidebands, and the beat frequencies after detection appear as symmetric sidebands around f_{AOFS} if there is no object velocity. For a moving object each sideband will be shifted in the same direction. This technique is particularly useful because Doppler can be recorded over a single chirp when using both the positive and negative optical sidebands. An illustration of this technique is shown in Figure 11 for an object moving towards the detector.

In this case, the frequency components are separated as,

$$f_R = \frac{f_b^- - f_b^+}{2} \tag{21}$$

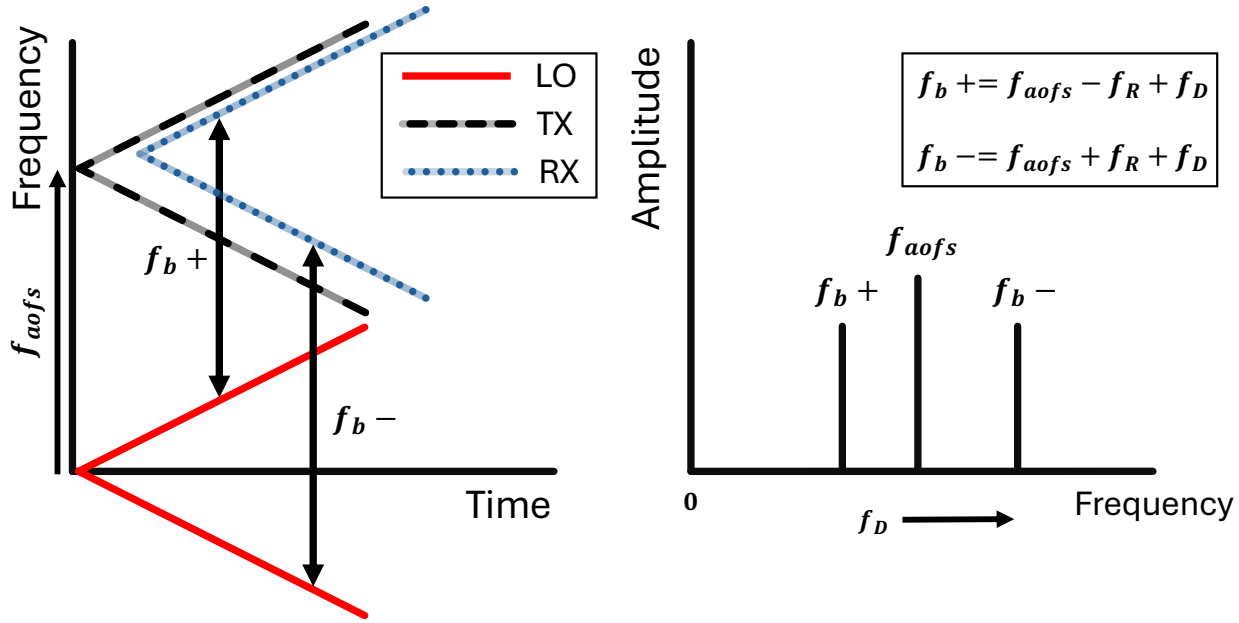


Figure 11: Illustration of double-sideband modulation interference, where the LO and TX/RX are shifted from one another by f_{AOFS}.

$$f_D = \frac{f_b^+ + f_b^- - 2f_{AOFS}}{2} \tag{22}$$

where f_b^+ and f_b^- are the beats between the upper and lower sidebands of each field.

Double sideband IQ detection

The third technique also exploits double-sideband modulation, but instead of frequency shifting one of the optical signals with an AOFS, it relies on IQ detection. For this method a 90-degree optical hybrid is used to split the interference between the LO and RX signals into in-phase (I) and quadrature (Q) components, which are detected on separate photodiodes [56, 57].

The I and Q signals are then combined in post-processing to form a complex-valued time-domain signal:

$$x(t) = I(t) + iQ(t).$$

This representation captures both the amplitude and phase evolution of the signal, allowing for unambiguous separation of positive and negative frequency components resulting in a spectrum of $x(t)$ with frequency peaks at $f_b^+ = -f_R + f_D$ and $f_b^- = f_R + f_D$. The range-dependent beat and doppler frequency are then separated and calculated as,

$$f_R = \frac{f_b^- - f_b^+}{2} \tag{23}$$

$$f_D = \frac{f_b^+ + f_b^-}{2} \tag{24}$$

Without IQ detection, the detected spectrum would show peaks at $\pm f_B^+$ and $\pm f_B^-$, which overlap and create ambiguity between the positive and negative components. IQ detection removes the mirror terms, preserving only one positive and one negative frequency component that can be algebraically separated into range and Doppler. This represents an important distinction from the first example, which did not depend on the sign of the beat frequency (negative or positive) because it relied on a symmetric real-valued spectrum.

This technique requires more complex optical hardware (e.g., optical hybrids and balanced photodetection), but offers a powerful way to resolve the range-Doppler ambiguity in coherent detection systems. It does so without the need of slowing down the measurement to be over two different chirps (as is the case for method one), and without using AOFS, which have limited bandwidth (as is the case in method two).

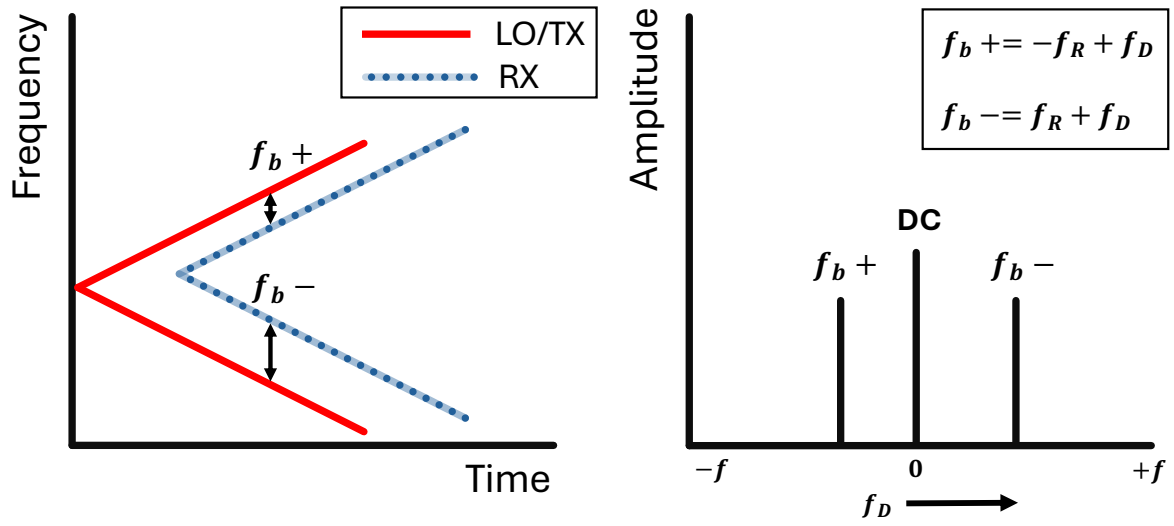


Figure 12: Double-sideband modulation interference without shifting the LO or TX with an AOFS. IQ detection is used to remove the undesired frequency components.

Velocity Resolution

The velocity resolution Δv of an FMCW lidar system is determined by the ability to resolve small Doppler-induced frequency shifts in the received signal. For a carrier frequency f_L and an observation duration τ, the minimum resolvable Doppler frequency shift is approximately $1/\tau$, which corresponds to a velocity resolution

$$\Delta v = \frac{\lambda}{2\tau} = \frac{c}{2\tau f_L}, \tag{25}$$

where c is the speed of light and λ is the optical wavelength. Typically, τ is equal to the chirp duration, but it can also be set by the processing window used in digital signal analysis.

Digital Holography

Digital holography is an advanced coherent imaging technique that enables the reconstruction of holograms through digital post-processing [58]. In this approach, the electromagnetic field from an object (RX), whose phase is initially unknown, interferes with a well-defined reference LO field, producing an interference pattern. The recorded intensity at the detector can then be post-processed to recover both the amplitude and phase of the object field [59]. This ability to retrieve the full complex optical field represents a key advantage over conventional photography, which captures only intensity.

The following sections introduce the field propagation, the mathematical framework of digital holography, the different recording planes, and discusses the recording geometries used for hologram acquisition. The subsequent chapter will demonstrate how FMCW signals can be combined with digital holography to achieve range-selective digital holographic recordings, forming a central contribution of this thesis.

Propagation of Optical Fields (Fresnel and Fraunhofer Approximations)

Before introducing digital holography, the focus of this thesis, it is first necessary to consider how optical fields propagate through free space, as this determines the nature of the wavefront at the detector plane. Since digital holography aims to recover not only the intensity but also the full complex field of the object, a clear understanding of propagation is fundamental for establishing how the recorded hologram is reconstructed to recover the object field.

At the detector plane, the received optical field from some object may appear either as a scaled image of the object, produced by an imaging system, or as the result of free-space propagation of the object field over a distance z [60–62]. Consequently, its structure depends on the object itself, the properties of the imaging system, and the effects of free-

space diffraction. Field propagation can be expressed using the Fresnel diffraction integral, given by

$$U(x_2, y_2, z) = \frac{e^{ikz}}{i\lambda z} \iint_{-\infty}^{\infty} U(x_1, y_1) e^{\frac{ik}{2z}\left((x_1-x_2)^2+(y_1-y_2)^2\right)} dx_1\, dy_1 \tag{26}$$

or expanded to,

$$U(x_2, y_2, z) = \frac{e^{ikz}}{i\lambda z} e^{\frac{ik}{2z}(x_2^2+y_2^2)} \iint_{-\infty}^{\infty} U(x_1, y_1) e^{\frac{ik}{2z}(x_1^2+y_1^2)} e^{-\frac{ik}{z}(x_1x_2+y_1y_2)} dx_1\, dy_1. \tag{27}$$

Here, $U(x_1, y_1)$ is the complex amplitude at the input (object) plane, $U(x_2, y_2, z)$ is the complex amplitude at the output (detector) plane, $k = 2\pi/\lambda$ is the wave number, λ is the wavelength of light, and z is the propagation distance. The coordinate system is shown in Figure 13, where (x_1, y_1) are the input-plane coordinates and (x_2, y_2) are the output plane coordinates. An annotated form of Eq. 27 indicates the contribution of each term to the propagated field

$$\begin{aligned} U(x_2, y_2, z) = {} & \underbrace{\frac{e^{ikz}}{i\lambda z}}_{\text{A}} \underbrace{e^{\frac{ik}{2z}(x_2^2+y_2^2)}}_{\text{B}} \\ & \times \iint_{-\infty}^{\infty} U(x_1, y_1)\, \underbrace{e^{\frac{ik}{2z}(x_1^2+y_1^2)}}_{\text{C}} \underbrace{e^{-\frac{ik}{z}(x_1x_2+y_1y_2)}}_{\text{D}}\, dx_1\, dy_1. \end{aligned} \tag{28}$$

Here, A is an amplitude scaling term, B is a quadratic phase term at the output plane, C is a quadratic phase term at the input plane, and D is Fourier-like kernel. Expressing the Fresnel integral in this form emphasizes its structure as a scaled Fourier transform:

$$U_{\text{Fresnel}}(x_2, y_2, z) = \frac{e^{ikz}}{i\lambda z} e^{\frac{ik}{2z}(x_2^2+y_2^2)}\, \mathcal{F}\left\{ U(x_1, y_1)\, e^{\frac{ik}{2z}(x_1^2+y_1^2)} \right\} (f_x, f_y), \tag{29}$$

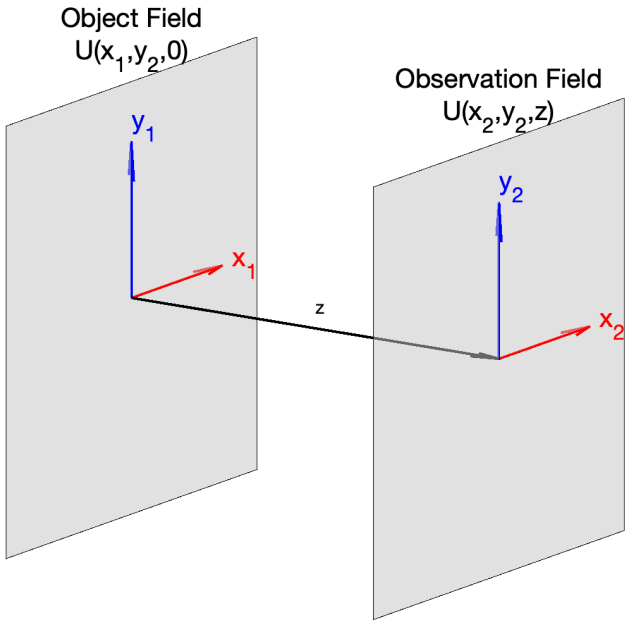


Figure 13: Fresnel Propagation Coordinates.

where the spatial frequencies are defined as

$$f_x = \frac{x_2}{\lambda z}, \qquad f_y = \frac{y_2}{\lambda z}.$$

Here, the propagated field is expressed as the product of an amplitude scaling factor, a quadratic phase term at the output plane, and the Fourier transform of the input field multiplied by a quadratic phase term at the input plane. Figure 14 shows simulated intensity patterns of an Air Force target after Fresnel propagation, illustrating how the field evolves with distance and can appear very different from the original object. For sufficiently large propagation distances, $z \gg W^2/\lambda$ where W is the characteristic size of the object (or size of diffracting aperture), the quadratic phase term inside the Fourier transform becomes nearly planar and can be neglected, leading to the Fraunhofer approximation, denoted $U_{\text{Fraunhofer}}$.

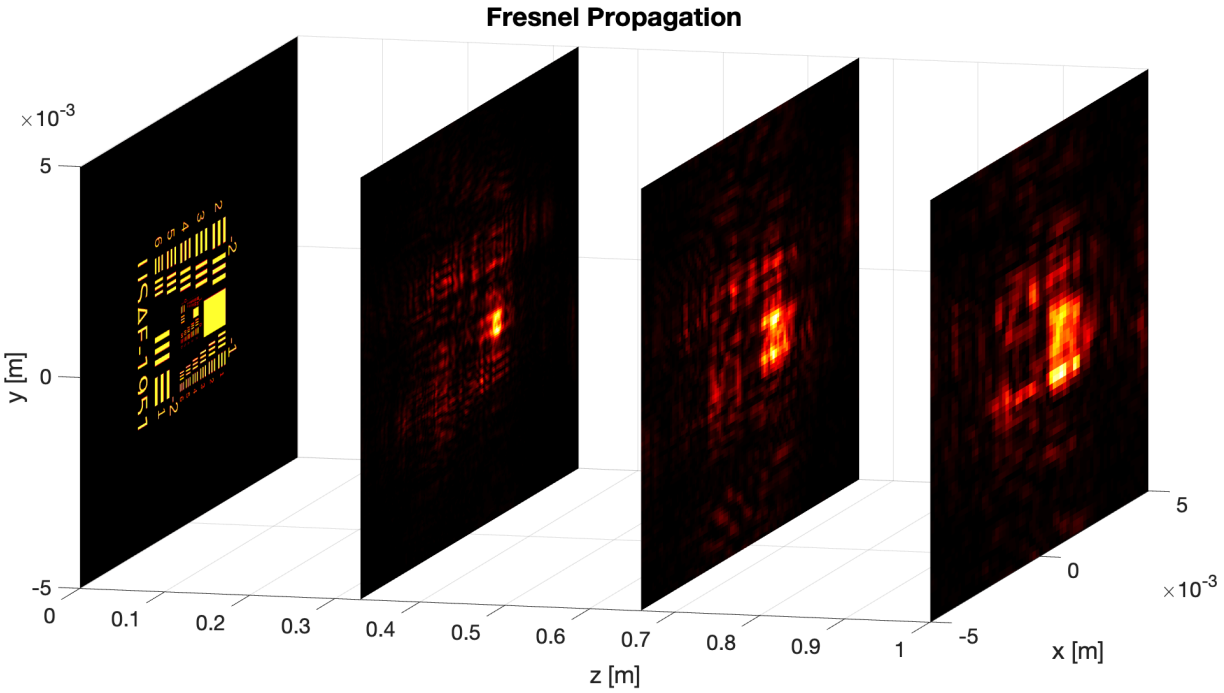


Figure 14: Fresnel Propagation of an Air Force Target digitally. The intensity is plotted at propagation distances of $z = 0.33, 0.66, 1$ meters.

In this regime, the propagated field reduces to a scaled Fourier transform of the input field, multiplied by a global quadratic phase factor.

$$U_{\text{Fraunhofer}}(x_2, y_2, z) = \frac{e^{ikz}}{i\lambda z} e^{\frac{ik}{2z}(x_2^2+y_2^2)} \mathcal{F}\{U(x_1, y_1)\}(f_x, f_y), \tag{30}$$

It is worth noting that the Fresnel integral in Eq. 27 can also be expressed as a convolution. Defining the impulse response

$$H(x, y, z) = \frac{e^{ikz}}{i\lambda z} \exp\left(\frac{ik}{2z}(x^2 + y^2)\right), \tag{31}$$

the propagated field can be written compactly as a two-dimensional convolution:

$$U(x_2, y_2, z) = U(x_1, y_1, 0) * H(x_2, y_2, z). \tag{32}$$

In conclusion, the propagation of an optical field can be approximated using the Fresnel diffraction integral, which under suitable conditions reduces to a scaled Fourier transform of the object field (the Fraunhofer approximation) or a scaled Fourier transform of the object field multiplied by an additional phase factor (the Fresnel approximation). These formulations describe how the object wavefront evolves during free-space propagation and thereby establish the foundation for digital holography, in which reconstruction frequently involves inverting this process to recover the object field from the recorded hologram.

Mathematical Framework of Digital Holography

We begin by considering interference between the RX object field and the LO field, both modeled as plane waves. These optical fields overlap at the detector, arriving with a small angular offset θ, which corresponds to distinct wavevectors $\vec{k}_{\mathrm{RX}}$ and $\vec{k}_{\mathrm{LO}}$. This angular separation introduces a spatial carrier frequency into the interference pattern, which is shown in Figure 15, determined by the difference vector

$$\Delta\vec{k} = \vec{k}_{\mathrm{RX}} - \vec{k}_{\mathrm{LO}}. \tag{33}$$

At the detector plane, with position vector $\vec{r} = (x, y)$, this wavevector mismatch produces oscillatory terms of the form $e^{i\Delta\vec{k}\cdot\vec{r}}$. These terms manifest as interference fringes

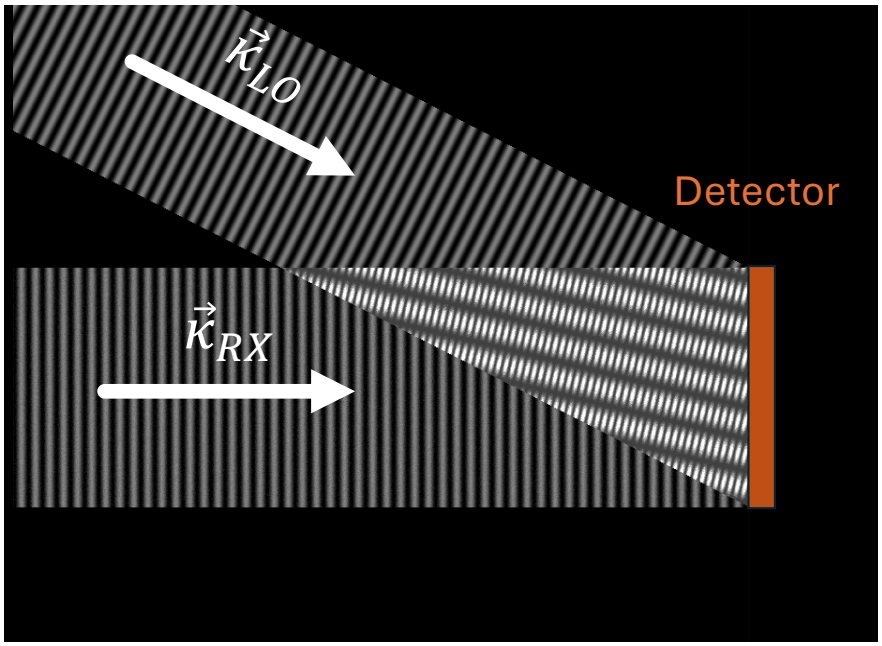


Figure 15: Interference between the LO and RX fields.

oriented perpendicular to $\Delta\vec{k}$, with fringe spacing (or fringe period) given by

$$\Lambda = \frac{2\pi}{|\Delta\vec{k}|} = \frac{\lambda}{\sin\theta}. \tag{34}$$

To describe this mathematically, we express the RX and LO fields in complex phasor notation as

$$E_{\mathrm{RX}}(x, y, t) = E_{\mathrm{RX}}(x, y)\, e^{i\omega_L t}\, e^{i\vec{k}_{\mathrm{RX}}\cdot\vec{r}}, \tag{35}$$

$$E_{\mathrm{LO}}(x, y, t) = E_{\mathrm{LO}}\, e^{i\omega_L t}\, e^{i\vec{k}_{\mathrm{LO}}\cdot\vec{r}}. \tag{36}$$

where $E_{\mathrm{RX}}(x, y)$ and E_{LO} are the complex phasors (encoding amplitude and phase) of the object and LO fields, respectively, and $\omega_L = 2\pi f_L$ is the optical angular carrier frequency. The LO field is generally assumed to be spatially uniform across the detector. If both fields

share the same polarization, the detector measures the time-averaged intensity

$$I(x,y) \;\propto\; \left\langle \left| E_{\mathrm{RX}}(x,y,t) + E_{\mathrm{LO}}(x,y,t) \right|^2 \right\rangle_{\frac{1}{BW_{det}}}. \tag{37}$$

Expanding Eq. 37, we obtain

$$\begin{aligned} I(x,y) \propto\; & \underbrace{|E_{\mathrm{RX}}(x,y)|^2}_{I_{\mathrm{RX}}(x,y)} + \underbrace{|E_{\mathrm{LO}}|^2}_{I_{\mathrm{LO}}} \\ & + \underbrace{E_{\mathrm{RX}}(x,y)E^*_{\mathrm{LO}}e^{i\Delta\vec{k}\cdot\vec{r}}}_{\text{image}} + \underbrace{E^*_{\mathrm{RX}}(x,y)E_{\mathrm{LO}}e^{-i\Delta\vec{k}\cdot\vec{r}}}_{\text{conjugate image}}. \end{aligned} \tag{38}$$

Here, the first two terms represent the individual field intensities of the object and LO, while the last two are the interference cross-terms that encode the complex amplitude and phase information of the object into a real-valued intensity pattern. In digital holography, these cross-terms give rise to the reconstructed image and its conjugate (or "twin") image during the reconstruction process.

Holographic Recording Planes

In digital holography, two primary planes are used to record holograms: the image plane and the pupil plane (Fourier plane), which are distinguished by the form of the RX field at the detector.

Image-Plane In an image plane recording geometry, the propagated field is projected onto the detector by a lens or imaging optics system. When the detector is positioned at the image-plane of the lens, the received field, $E_{\mathrm{RX}}(x,y)$, closely resembles a scaled replica of the object field before propagation, with magnification determined by the optics. This configuration effectively compensates for Fresnel or Fraunhofer propagation effects, so that recording in this plane produces an image-plane hologram.

Pupil-Plane The second recording plane is the pupil-plane (sometimes referred to as the Fourier-plane), where the $E_{\mathrm{RX}}(x, y)$ field at the detector is the object field after Fresnel or Fraunhofer propagation to the detector. In this plane, the RX field generally does not resemble the original object and must be further processed to reconstruct a hologram of the object.

Thus, depending on the recording plane, the received field at the detector may either resemble a scaled image of the object (image plane) or a diffracted version of the object field (pupil plane). This distinction, shown in Figure 16, is crucial in digital holography, as it determines the reconstruction steps required to retrieve the object field.

Recording Geometries

To reconstruct a digital hologram, it is necessary to isolate the object field $E_{\mathrm{RX}}(x, y)$ from both the DC intensity terms, $I_{\mathrm{RX}}(x, y)$ and I_{LO}, as well as from the conjugate (twin) image term in Eq. 38. Although the conjugate term contains the same information as the image, and can, in principle, be used for reconstruction, its spatial overlap with the image term and the DC components introduces artifacts that degrade the reconstruction quality, and in some cases can prevent recovery altogether.

To achieve sufficient separations of terms, two holographic recording geometries are commonly used. The first is spatial-heterodyne (off-axis) digital holography, and the second is on-axis (Gabor) holography, which employs phase-shifting techniques to resolve the object field. Both recording geometries can be used to reconstruct image plane or pupil plane holograms, provided that the appropriate post-processing steps are performed to isolate the desired cross-term and reconstruct the complex object field. In practice, the choice of geometry depends on experimental constraints, including the available reference beam angle and detector resolution.

The following section will introduce the required post-processing steps for each geometry

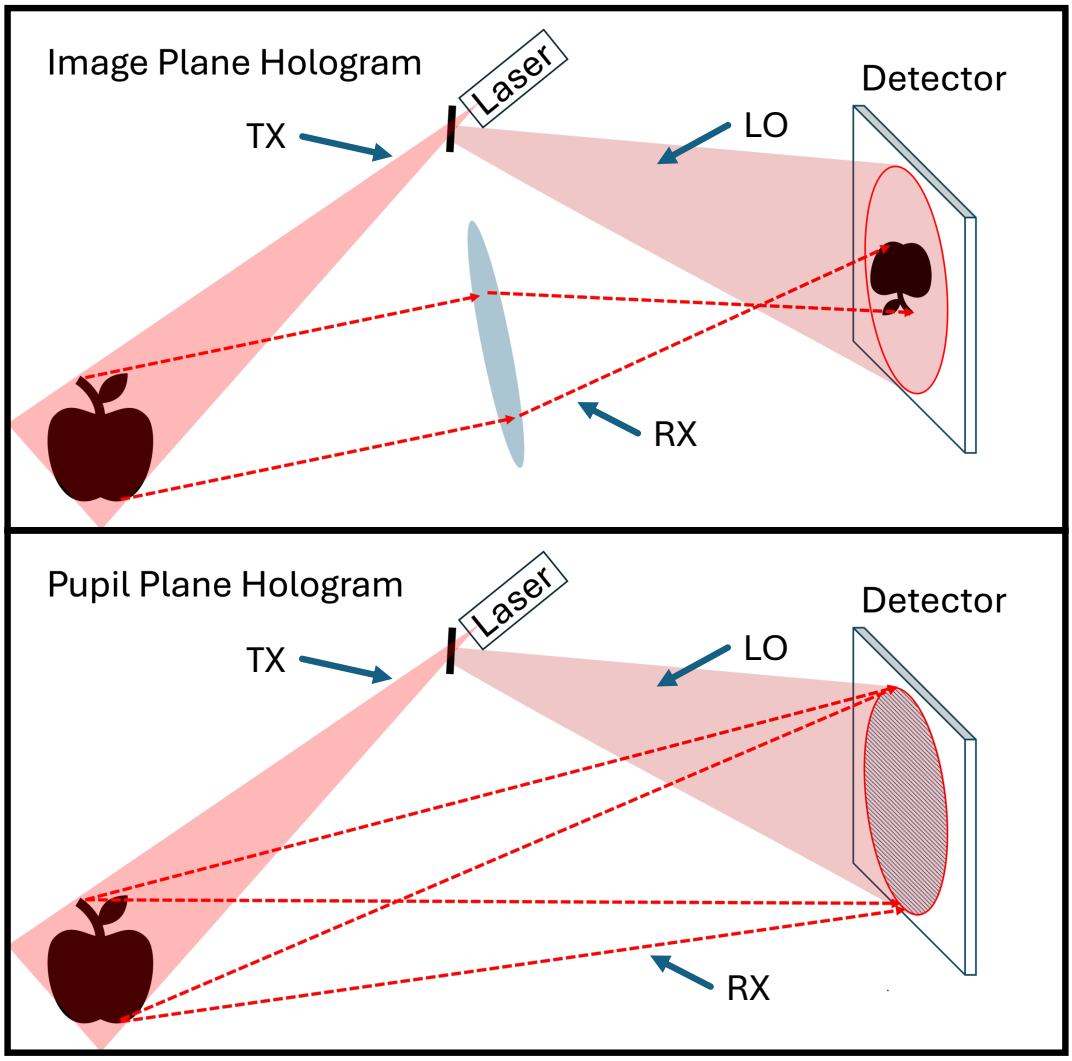


Figure 16: Schematic of both image plane and pupil plane holographic recordings for when the LO and RX beams are angled relative to one another ($\Delta\vec{k} \neq 0$).

when recording both image plane and pupil plane holograms starting from the results of Eq. 38.

Spatial-Heterodyne Digital Holography

Spatial-Heterodyne (or off-axis) digital holography, first introduced by Leith and Upatnieks [63, 64], exploits a deliberate angular tilt of the LO beam relative to the RX beam, as described in the preceding mathematical discussion, to separate the various terms in the hologram. According to the Fourier shift theorem, a linear phase ramp in the detector plane produces a spatial frequency shift in Fourier space. As a result, the image-related cross-term is shifted by the spatial carrier, while the conjugate (twin) image cross-term, with an opposite-sign exponential phase factor, is shifted in the opposite direction. The magnitude of the spatial frequency shift in the recorded interference pattern is determined by the angle between the LO and RX beams, as given by Equation 34. To avoid aliasing, the detector must satisfy the Nyquist sampling criterion, which requires at least two pixels per fringe period, i.e.,

$$\Lambda \geq 2w, \tag{39}$$

where w is the detector pixel pitch. Substituting the expression for Λ into this inequality yields

$$\sin\theta \leq \frac{\lambda}{2w}. \tag{40}$$

Thus, the maximum allowable off-axis angle is

$$\theta_{\max} = \arcsin\left(\frac{\lambda}{2w}\right). \tag{41}$$

To illustrate how this spatial carrier enables separation of terms in the Fourier domain, we take the two-dimensional Fourier transform of Eq. 38:

$$\begin{aligned}\mathcal{F}\{I(x,y)\} \;=\; & \underbrace{\mathcal{F}\{|E_{\mathrm{RX}}|^2\}+\mathcal{F}\{|E_{\mathrm{LO}}|^2\}}_{\text{DC terms at } (k_x,k_y)=(0,0)} \\ & + \underbrace{\mathcal{F}\{E_{\mathrm{RX}}E_{\mathrm{LO}}^*\} * \delta(k_x-\Delta k_x,\, k_y-\Delta k_y)}_{\text{image term centered at } (+\Delta k_x,+\Delta k_y)} \\ & + \underbrace{\mathcal{F}\{E_{\mathrm{RX}}^*E_{\mathrm{LO}}\} * \delta(k_x+\Delta k_x,\, k_y+\Delta k_y)}_{\text{conjugate term centered at } (-\Delta k_x,-\Delta k_y)}.\end{aligned} \tag{42}$$

Here, the low-spatial-frequency DC terms remain centered at the origin of the Fourier domain, while the two cross terms are shifted to opposite locations determined by $\Delta\vec{k}$. This separation enables spatial filtering to isolate the desired image term and suppress the unwanted contributions.

Spatial-Heterodyne: Image-plane To exploit this principle for when the RX field is an image of the object, a 2D spatial Fourier transform is performed digitally to the recorded intensity during post-processing, separating the hologram into distinct components due to the spatial carrier shifts introduced by the angular tilt of the LO. Taking the inverse 2D Fourier transform of a masked region of Fourier space, containing only the desired cross-term, reconstructs a complex object field proportional to the object assuming the LO is uniform. Mathematically, the steps are summarized here for the image field and intensity where the mask is performed in the Fourier domain:

$$E_{\mathrm{RX}}(x,y)_{\mathrm{IP}} \;\propto\; \mathcal{F}^{-1}\{\mathrm{Mask}(f_x,f_y)\cdot\mathcal{F}\{I(x,y)\}\} \tag{43}$$

$$I_{\mathrm{RX}}(x,y)_{\mathrm{IP}} \;\propto\; \left|\mathcal{F}^{-1}\{\mathrm{Mask}(f_x,f_y)\cdot\mathcal{F}\{I(x,y)\}\}\right|^2 \tag{44}$$

Figure 17 shows the results of an off-axis image plane digital holography simulation in which a section of an Air Force target is used as the object. The object field interferes at a small angle with a LO field, producing an intensity pattern that is recorded by the detector. The recorded intensity is then processed to reconstruct the object field, which provides both amplitude and phase information about the target.

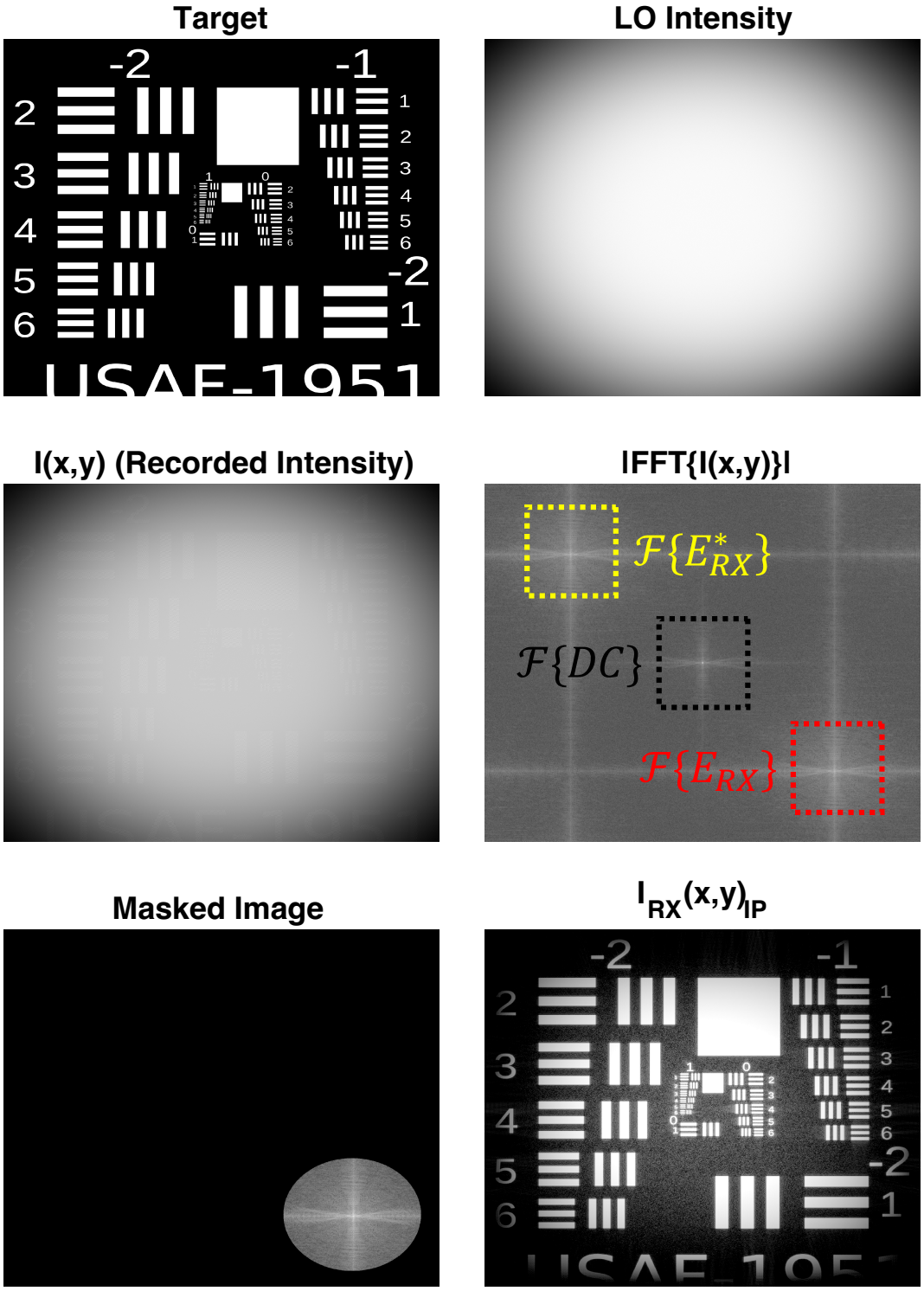


Figure 17: Simulation results for an off-axis recording geometry. Image of the object (top left). Intensity of the complex LO (top right). Recorded intensity calculated from the interference between the object and LO (center left). 2D FFT of the recorded intensity showing how the DC terms are separated from both the image terms and conjugate image terms in the Fourier domain (center right). Masking of image terms (bottom left). Hologram intensity obtained by taking the squared magnitude of the inverse 2D Fourier transform of the masked image (bottom right).

Spatial-Heterodyne: Pupil-plane When the RX field is the object field after propagation, the reconstruction is slightly different than the image plane example. In this case, the RX field at the detector is related to the field at the object by Eq. 29 or Eq. 30, depending on what assumptions are being made about the propagation distance (Fresnel or Fraunhofer approximations). Annotated versions of both equations are included here to clarify the distinction between phase terms.

$$U_{\text{Fresnel}}(x_2, y_2, z) = \frac{e^{ikz}}{i\lambda z} \underbrace{e^{\frac{ik}{2z}(x_2^2+y_2^2)}}_{e^{i\phi_P(x,y)}} \mathcal{F}\Big\{ U(x_1, y_1) \underbrace{e^{\frac{ik}{2z}(x_1^2+y_1^2)}}_{e^{i\phi_{F(x,y)}}} \Big\} \tag{45}$$

$$U_{\text{Fraunhofer}}(x_2, y_2, z) = \frac{e^{ikz}}{i\lambda z} \underbrace{e^{\frac{ik}{2z}(x_2^2+y_2^2)}}_{e^{i\phi_P(x,y)}} \mathcal{F}\{U(x_1, y_1)\} \tag{46}$$

To reconstruct the holographic field of the object, the recorded intensity $I(x, y)$, containing the propagated RX field, is multiplied by a quadratic phase correction, $e^{i\phi_P(x,y)}$, selected to cancel the curvature due to propagation. If the Fresnel approximation is applicable, an additional phase correction is required to cancel the Fresnel phase from the source plane $e^{i\phi_F(x,y)}$. The RX field is therefor given as

$$E_{\text{RX}}(x, y)_{\text{PP(Fresnel)}} \propto \text{Mask}(x, y) \cdot e^{-i\phi_F(x,y)} \cdot \mathcal{F}^{-1}\big\{ e^{-i\phi_P(x,y)} \cdot I(x, y) \big\} \tag{47}$$

when using Fresnel Propagation and

$$E_{\text{RX}}(x, y)_{\text{PP(Fraunhofer)}} \propto \text{Mask}(x, y) \cdot \mathcal{F}^{-1}\big\{ e^{-i\phi_P(x,y)} \cdot I(x, y) \big\} \tag{48}$$

when using the simplified Fraunhofer approximation, ignoring the amplitude scaling term. The mask is used to filter out components of the conjugate image and DC terms. The

intensity of the object is calculated as

$$I_{\mathrm{RX}}(x,y)_{\mathrm{PP}} \;\propto\; \mathrm{Mask}(x,y) \cdot \left|\mathcal{F}^{-1}\left\{e^{-i\phi_P(x,y)} \cdot I(x,y)\right\}\right|^2 \tag{49}$$

for both propagation methods as constant phase terms will be removed when taking the magnitude square of the field. Figure 18 shows simulation results constructing an off-axis hologram in the pupil plane.

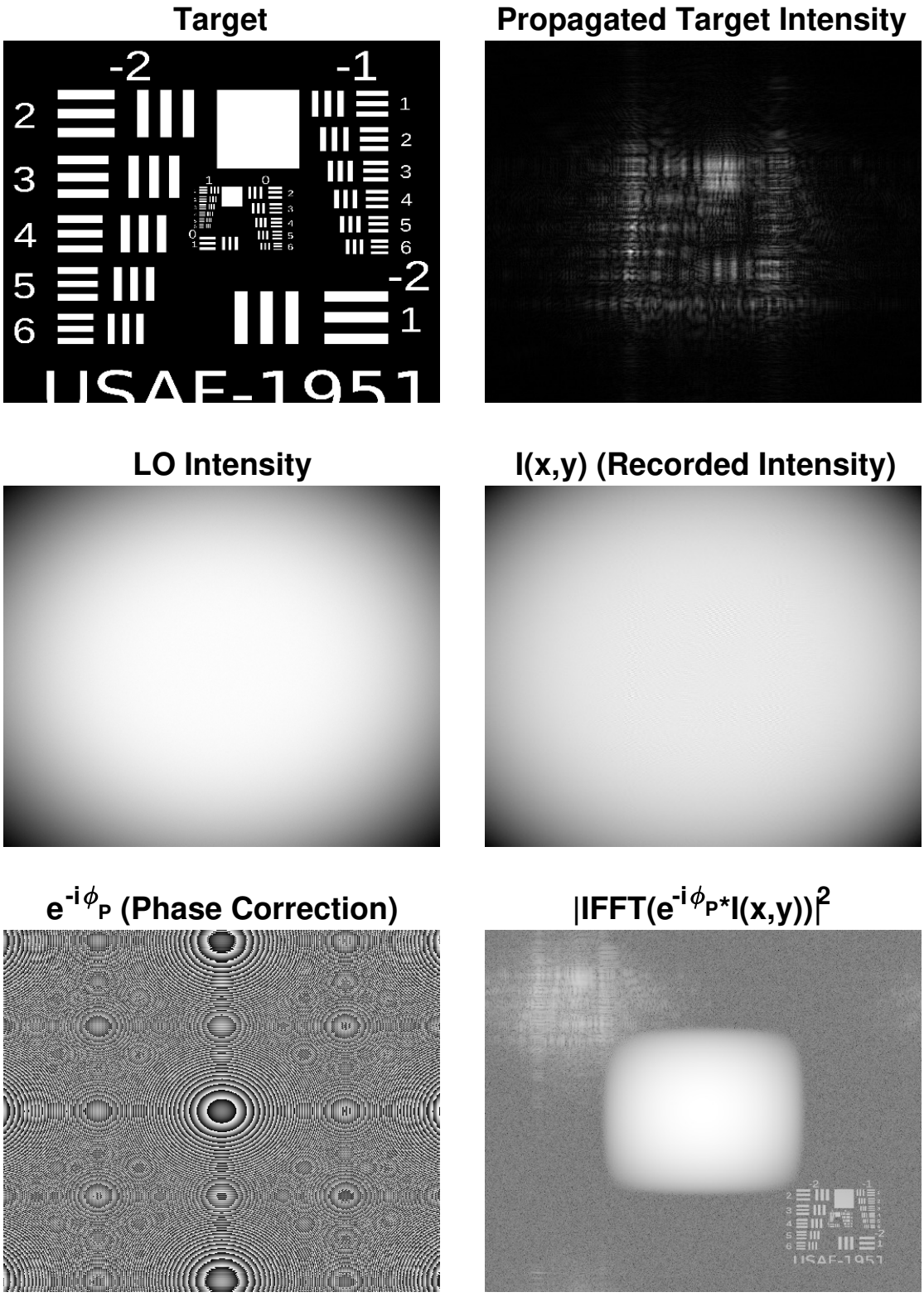


Figure 18: Simulation results for a pupil-plane off-axis recording geometry. Target object (top left). intensity of propagated object field (top right). Intensity of the LO (middle left). Recorded intensity of the interference of both fields (middle right). Quadratic phase correction applied (bottom left). Reconstructed target intensity (bottom right).

On-Axis Phase-shifting Digital Holography

On-axis holograms, originally proposed by Dennis Gabor the inventor of the hologram, involve the direct alignment of the LO and RX beams such that they overlap directly on the recording medium with no angular separation, sharing the same optical axis [65]. In this configuration, the beams are not angled relative to each other, which makes the geometry straightforward and simple to implement. However, it also leads to the well known twin image problem, where the real and conjugate images overlap, complicating the reconstruction process.

To overcome this limitation, phase-shifting holography techniques have been developed, which rely on recording multiple (typically four) holograms of the same scene while introducing controlled phase shifts in the LO field between captures. Post-processing of the recorded phase shifted intensity measurements suppress the unwanted conjugate and zero-order terms. While phase-shifting can also be applied to off-axis holograms, its main advantage is that no angular separation between the LO and RX fields is required, allowing for clean on-axis reconstruction of the complex object field without relying on a spatial carrier [66].

An important advantage to an on-axis geometry is that the reconstructed image utilizes the full resolution of the detector array, unlike off-axis spatial-heterodyne holography where masking in the Fourier domain typically limits the effective resolution to about one quarter of the detector. However, phase-shifting holography does have its own drawbacks. For starters, it is generally much slower, since multiple exposures of the object are required. Additionally, the requirement of several acquisitions for a single reconstruction increases sensitivity to motion or vibration, as holographic stability must be maintained over a longer period of time.

The reconstruction process for an on-axis digital hologram using phase-shifting techniques is summarized here for the fundamental four-step method. In this approach,

four holograms are sequentially recorded while introducing controlled phase shifts in the LO field. For the n^{th} hologram, the LO phase is shifted by $\Phi_n = \frac{n\pi}{2}$, with $n = 0, 1, 2, 3$. At each step, the intensity is measured, and the process is repeated until all four phase-shifted holograms are recorded. Assuming that the LO and RX are co-propagating along the same optical axis ($\Delta\vec{k} = 0$), and again ignoring the rapid temporal factor $e^{i2\pi f_L t}$ because of finite detector bandwidth, the recorded intensity for the n^{th} hologram is

$$I_n(x,y) = \left\langle \left| E_{\text{RX}}(x,y,t) + E_{\text{LO}}(x,y,t)e^{-i\Phi_n} \right| \right\rangle_t^2 \tag{50}$$

which can similarly be expanded to

$$I_n(x,y) \propto I_{\text{RX}}(x,y) + I_{\text{LO}}(x,y) + E_{\text{RX}}(x,y)E^*_{\text{LO}}(x,y)e^{i\Phi_n} + E^*_{\text{RX}}(x,y)E_{\text{LO}}(x,y)e^{-i\Phi_n} \tag{51}$$

The resulting four intensity recordings can be expressed as

$$I_0(x,y) = I_{\text{RX}}(x,y) + I_{\text{LO}}(x,y) + \big(E_{\text{RX}}(x,y)E^*_{\text{LO}}(x,y) + \text{c.c.}\big), \tag{52}$$

$$I_{\frac{\pi}{2}}(x,y) = I_{\text{RX}}(x,y) + I_{\text{LO}}(x,y) + i\big(E_{\text{RX}}(x,y)E^*_{\text{LO}}(x,y) - \text{c.c.}\big), \tag{53}$$

$$I_{\pi}(x,y) = I_{\text{RX}}(x,y) + I_{\text{LO}}(x,y) - \big(E_{\text{RX}}(x,y)E^*_{\text{LO}}(x,y) + \text{c.c.}\big), \tag{54}$$

$$I_{\frac{3\pi}{2}}(x,y) = I_{\text{RX}}(x,y) + I_{\text{LO}}(x,y) - i\big(E_{\text{RX}}(x,y)E^*_{\text{LO}}(x,y) - \text{c.c.}\big). \tag{55}$$

Next, by appropriately combining the recorded intensities in post-processing, the desired cross-term containing the object field can be isolated. This is achieved by multiplying the difference $I_{\frac{\pi}{2}}(x,y) - I_{\frac{3\pi}{2}}(x,y)$ by the imaginary unit i and adding it to $I_0(x,y) - I_{\pi}(x,y)$, which yields

$$4E_{\text{RX}}(x,y)E^*_{\text{LO}}(x,y) = (I_0(x,y) - I_{\pi}(x,y)) + i(I_{\frac{\pi}{2}}(x,y) - I_{\frac{3\pi}{2}}(x,y)). \tag{56}$$

If the LO field is closely approximated as a uniform plane wave, its spatial dependencies will factor out, resulting in a reconstructed field, $E_{recon}(x, y)$, that is directly proportional to the unknown object field.

$$E_{recon}(x, y) = 4E_{\mathrm{RX}}(x, y)E^{*}_{\mathrm{LO}}(x, y) \propto E_{\mathrm{RX}}(x, y) \tag{57}$$

Phase-Shifting: Image-plane If the four intensities were recorded in an image-plane configuration, the reconstruction field is simply a scaled version of the field at the object

$$E_{\mathrm{RX}}(x, y)_{\mathrm{IP}} \ \propto \ E_{recon}(x, y) \tag{58}$$

and the intensity is similarly,

$$I_{\mathrm{RX}}(x, y)_{\mathrm{IP}} \ \propto \ |E_{recon}(x, y)|^2 \tag{59}$$

Notice that explicit spatial filtering in the Fourier domain is not required, since the separation of terms is achieved numerically through phase shifting, which functions analogously to IQ detection. Example phase-shifted intensities for the same Air Force target as before with an on-axis LO are shown in Figure 19. The intensity of the reconstructed field is also included. Although the reconstructed intensity closely approximates the original object, the process relies on interferometric reconstruction. Without the LO, no image could be recovered.

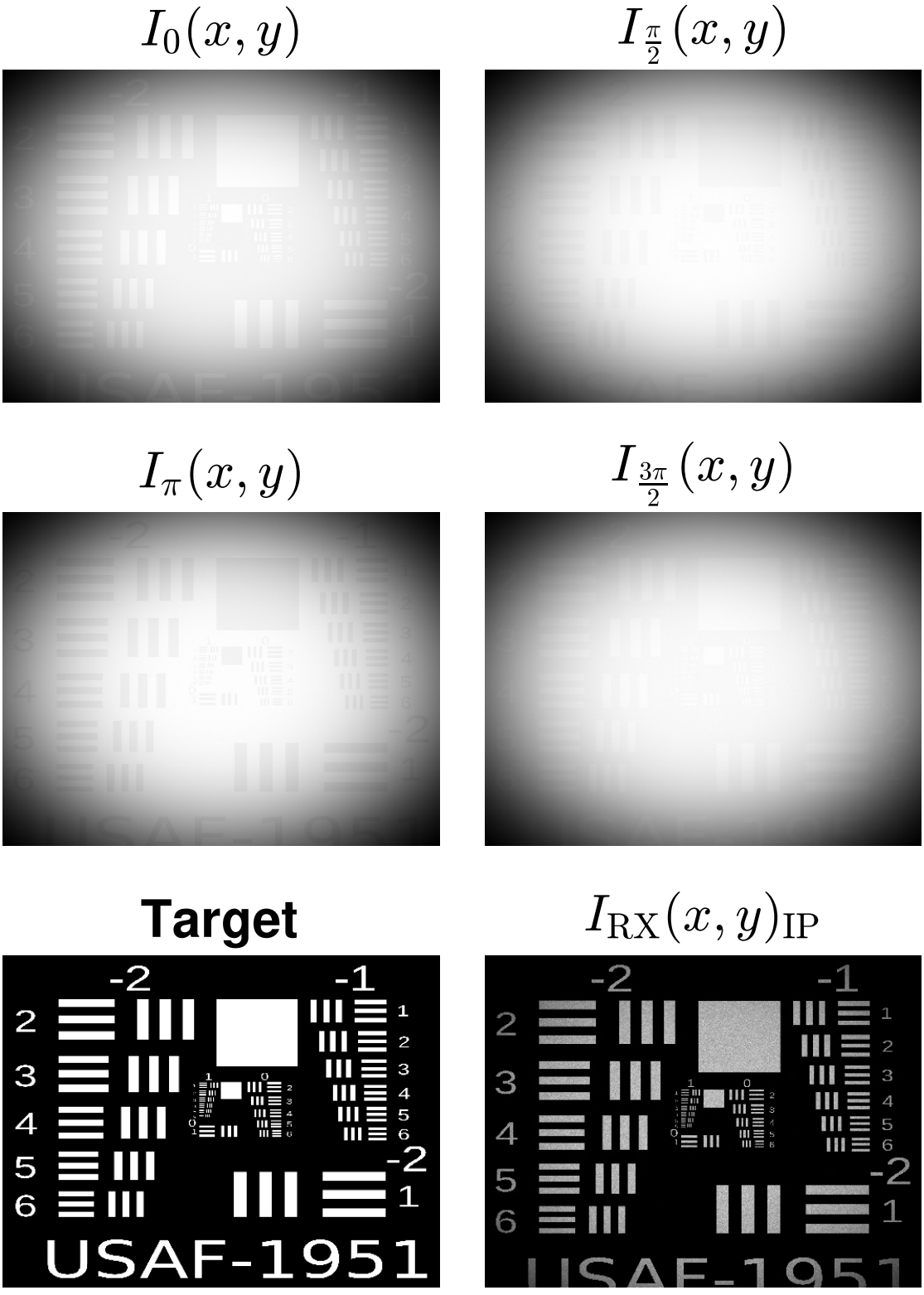


Figure 19: Simulation results for on-axis image-plane digital holography. Recorded intensities with known phase shifts of the LO (top left, top right, middle left, and middle right). Original object (bottom left). Reconstructed intensity (bottom right).

Phase-Shifting: Pupil-plane When the four intensity images are recorded in a lensless system with the RX field being the propagated field from the object, the field is computed, depending on the propagation assumptions as,

$$E_{\mathrm{RX}}(x,y)_{\mathrm{IP(Fresnel)}} \;\propto\; e^{-i\phi_F(x,y)} \cdot \mathcal{F}^{-1}\big\{e^{-i\phi_B(x,y)} \;\cdot\; I(x,y)\big\} \tag{60}$$

when using Fresnel Propagation or

$$E_{\mathrm{RX}}(x,y)_{\mathrm{IP(Fraunhofer)}} \;\propto\; \mathcal{F}^{-1}\big\{e^{-i\phi_B(x,y)} \;\cdot\; I(x,y)\big\} \tag{61}$$

when using the simplified Fraunhofer approximation, ignoring the amplitude scaling term. The intensity for the pupil-plane recording is then computed as

$$I_{\mathrm{RX}}(x,y)_{\mathrm{PP}} \;\propto\; \Big|\mathcal{F}^{-1}\big\{e^{-i\phi_B(x,y)} \;\cdot\; I(x,y)\big\}\Big|^2 \tag{62}$$

Simulated results are shown in Fig. 20 where the object was numerically propagated. No masking is required to separate terms since the conjugate and DC terms were removed from phase shifting.

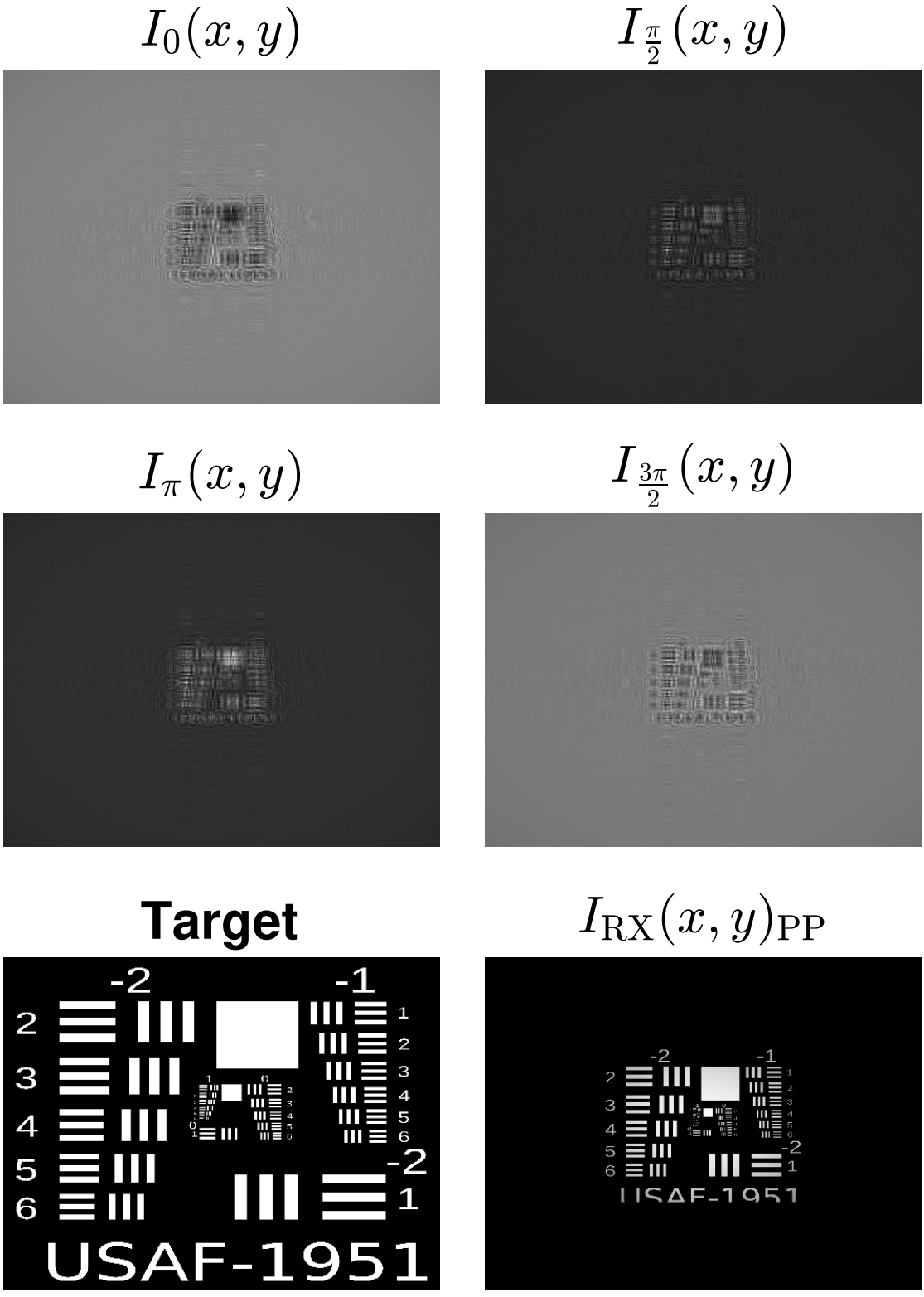


Figure 20: Simulation results for on-axis pupil-plane digital holography. Recorded intensities with known phase shifts of the LO (top left, top right, middle left, and middle right). Original object (bottom left). Reconstructed object intensity (bottom right).

Range Selective Digital Holography

While digital holography provides three-dimensional information through the phase of the recorded wavefront, light from all object distances is captured simultaneously on the detector, which can lead to blurring in the reconstructed image. To overcome this limitation and obtain large-scale distance information rather than only phase-based depth (which requires unwrapping), FMCW signals have been combined with digital holographic recording techniques. This enables the reconstruction of distance profiles using two distinct approaches. The first approach, often referred to as FMCW digital holography, employs broadband chirps and high-speed detectors that record multiple frames at high frame rates over a single chirp period [67–70]. A Fourier transform performed across frames for each pixel yields a pixel-wise distance profile, since each pixel records an oscillating intensity whose beat frequency is proportional to the object range. The second approach, known as range-selective digital holography (RSDH), enables the recording and reconstruction of holograms at tunable distances, with range resolution determined by the chirp bandwidth [36, 71, 72]. This method relies on much shorter chirp durations and can even be performed within a single integration period. RSDH achieves range selectivity by introducing an additional frequency shift to the LO, which acts as a tuning parameter that allows manual selection of the desired recording distance.

RSDH has been demonstrated for both image-plane and pupil-plane holograms in an off-axis spatial heterodyne digital holographic geometry, as well as image-plane and pupil-plane holograms in an on-axis recording geometry using temporal-heterodyning [36, 71, 72]. The latter is one of the accomplishments of this thesis, and will be discussed in further detail in a following chapters.

RSDH is achieved in a very similar manner to FMCW lidar with a delayed LO. First, a laser source is modulated with a linear chirp and is then split into an LO and TX beam that

illuminates the object. The LO field is shifted by an additional frequency offset f_s, which acts as the tuning knob selecting the distance at which to image. The received RX signal from the object is mixed with the frequency shifted LO on a detector, which records the interference intensity. The round-trip delay τ_R between the two chirped fields produces a beat frequency at the detector proportional to the object distance. This can be demonstrated by starting from the expressions for the LO and RX fields introduced in Equations 36 and 35. The modulated fields are then given as,

$$E_{\mathrm{LO}}(x,y,t) = E_{\mathrm{LO}}\, e^{i\left(2\pi(f_L - f_s)\,t + \pi\kappa t^2\right)}\, e^{i\vec{k}_{\mathrm{LO}}\cdot\vec{r}}, \tag{63}$$

and

$$E_{\mathrm{RX}}(x,y,t) = E_{\mathrm{RX}}(x,y)\, e^{i\left(2\pi f_L(t-\tau_R) + \pi\kappa(t-\tau_R)^2\right)}\, e^{i\vec{k}_{\mathrm{RX}}\cdot\vec{r}}. \tag{64}$$

The intensity can be calculated as,

$$\begin{aligned} I(x,y) \propto\ & |E_{\mathrm{RX}}(x,y)|^2 + |E_{\mathrm{LO}}|^2 \\ & + E_{\mathrm{RX}}(x,y) E^*_{\mathrm{LO}} e^{i2\pi(f_s - f_R)t}\, e^{i\Delta\vec{k}\cdot\vec{r}} \\ & + E^*_{\mathrm{RX}}(x,y) E_{\mathrm{LO}} e^{-i2\pi(f_s - f_R)t}\, e^{-i\Delta\vec{k}\cdot\vec{r}}, \end{aligned} \tag{65}$$

Here, the cross terms are shown temporally modulated by an amount set by the difference between f_s and f_R. In FMCW lidar, this beat frequency is desirable because it is used to calculate range. In RSDH, however, the beat is undesirable because a temporally modulated hologram at the range-dependent beat frequency, f_R, will wash out during integration. To counter this, the LO frequency shift f_s is set by the desired object range to image. The applied frequency shift, f_s, is defined as,

$$f_s = \frac{2\kappa R_s}{c}, \tag{66}$$

which produces a stable hologram for objects located at range R_s. An object at some other range R will instead produce a range-dependent beat frequency of

$$f_s - f_R = \frac{2\kappa(R_s - R)}{c}. \tag{67}$$

By adjusting the LO frequency shift, the selected range R_s can be tuned. A stable hologram recordings can be made for an object at distance R when the residual frequency difference satisfies

$$|f_s - f_R| < \frac{1}{\tau_{int}} \tag{68}$$

where τ_{int} is the integration time of the detector. If $\tau_{int} = \tau_c$, this expression can be rewritten as $|R - R_s| < \Delta R$. If A schematic showing how RSDH is performed is shown in Figure 21 for two different objects at range R_1 and R_2.

The advantage of range-selective imaging is that light from objects outside the system's range resolution around the selected distance integrates to zero, suppressing unwanted object contributions. In RSDH with an off-axis recording geometry and a CCD detector, the frequency shift, f_s, must be set close to the range dependent beat, f_R, for an object at range R. This will bring the hologram's temporal modulation to DC, allowing it to be integrated on the detector, as shown on the left image of Figure 22.

In temporal heterodyne RSDH (TH RSDH), implemented with a Time-of-Flight camera (ToF), the LO frequency shift is again chosen to cancel the range dependent beat, f_R, for the object at range R. However, in this case, the residual hologram modulation frequency must match the ToF camera's internal modulation frequency, rather than DC. This requirement arises because ToF cameras rely on lock-in detection, where the recorded signal is mixed with the camera's internal reference frequency. This is shown in the right image of Figure 22. An introduction to ToF-based detection, including published work on TH RSDH from

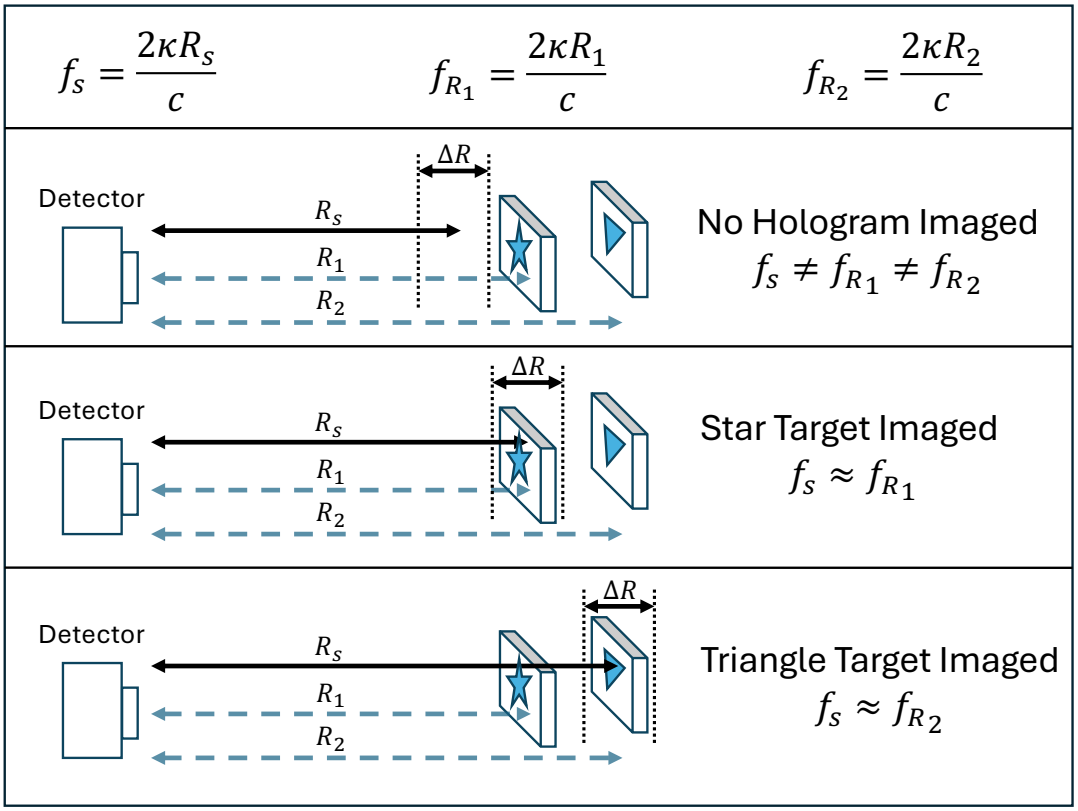


Figure 21: Range-selective imaging schematic. Shifting f_s allows for the construction of holograms at different distances where the range resolution ΔR_{res} is the range window. This is shown for three cases where no hologram is formed ($f_s \neq f_{R_1} \neq f_{R_2}$), a hologram of the object at R_1 is formed ($f_s \approx f_{R_1} \neq f_{R_2}$), and a hologram of the object at R_2 is formed ($f_s \approx f_{R_2} \neq f_{R_1}$).

this thesis, will be revisited in detail after first considering the role of depth of field in digital holography.

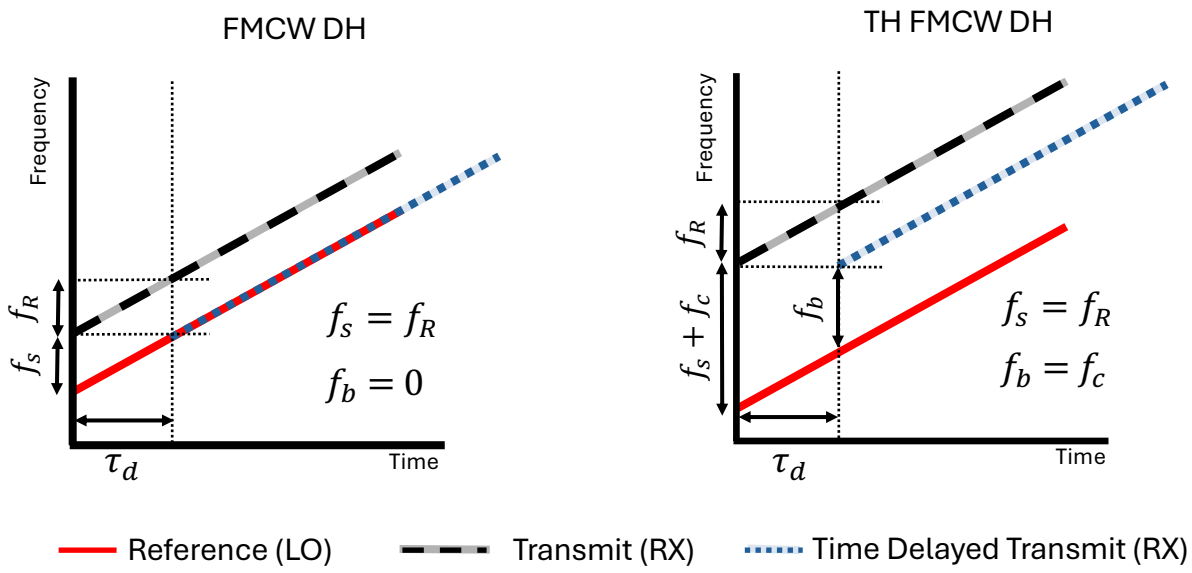


Figure 22: Frequency shifts for RSDH. RSDH in a traditional off-axis recording geometry (left). RSDH using an on-axis Temporal Heterodyne recording geometry (Right).

Depth of Field

In digital holography, the concept of depth of field (DOF) plays a central role in determining how well objects at different distances can be resolved. Because digital holography inherently records information from the entire three-dimensional scene, light from all object depths contributes to the recorded interference pattern. It is therefore important to verify that the range selectivity achieved by RSDH is significantly finer than conventional defocus effects, in which only one plane appears sharp but includes all other frames as blurred. Without this verification, one cannot confirm that RSDH improves the ability to distinguish between different objects in the object scene beyond what simple focusing or defocusing techniques can achieve.

The depth of field (DOF) of an imaging system defines the spatial region around the focal plane within which objects appear acceptably 'in focus'. For a holographic system, the diffraction-limited depth of field is given by

$$\mathrm{DOF} = 2\lambda \left(\frac{R}{D}\right)^2 \tag{69}$$

where R is the object distance, λ is the wavelength, and D is the diameter of the entrance pupil. Objects located outside of this range around the focal range will begin to blur [73].

In many practical cases, the diffraction-limited criteria is overly restrictive. Instead, a non-diffraction-limited depth of field (DOF_{NDL}), based on geometric optics, can be used. If δ denotes the maximum feature size (tolerable blur), then the DOF_{NDL} can be calculated from ray-tracing [74] as,

$$\mathrm{DOF}_{NDL} = 2\delta \left(\frac{R}{D}\right). \tag{70}$$

While the optical depth of field is determined purely by aperture and wavelength, in a digital implementation the effective DOF is also influenced by the detector pixel size, which sets a practical limit on resolvable blur, hence the motivation for a DOF_{NDL}.

The necessary feature of RSDH is that it can distinguish between multiple objects that would all fall within the DOF_{NDL} of the optical system. In this case, the limiting factor to distinguish objects is the range resolution of the system, which is inversely proportional to the chirp bandwidth. An illustration of the Depth of Field for a single lens imaging system is shown in Figure. 23.

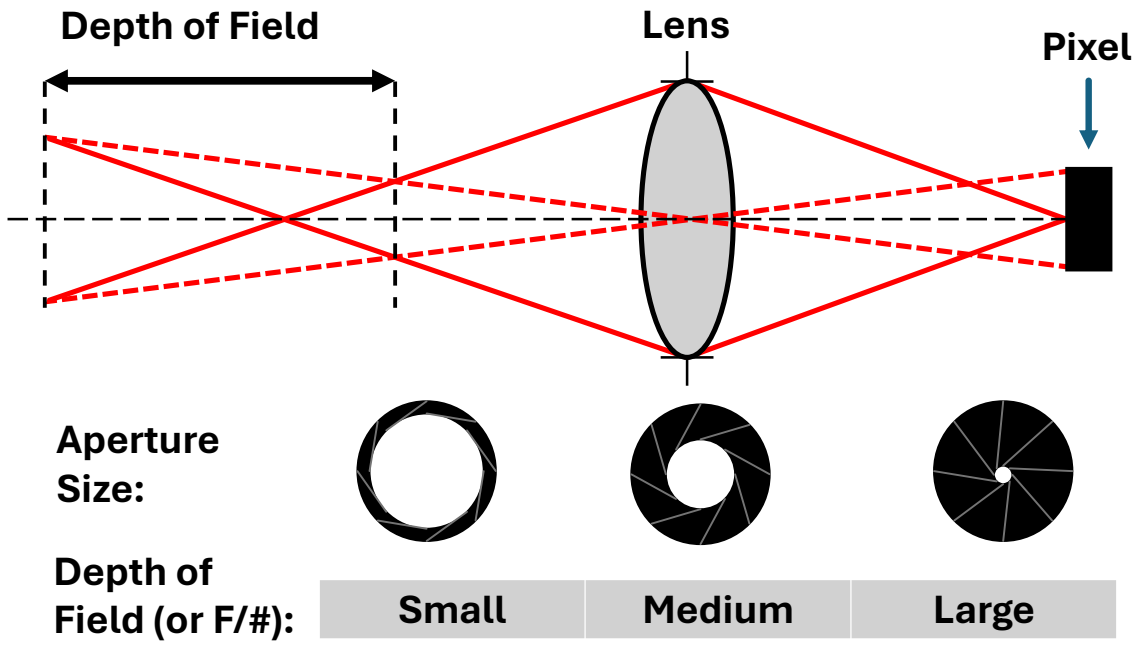


Figure 23: DOF_{NDL} of a single lens imaging system. With a fixed pixel size, varying the aperture diameter is the primary factor controlling DOF_{NDL}.

Time of Flight Detectors

The final background topic to cover is Time-of-Flight (ToF) detectors, a class of sensors in which each pixel acts as a photonic mixer, correlating incoming modulated light with a locally generated reference signal. These detectors operate by illuminating a scene with temporally modulated light and measuring the phase delay of the reflected signal to estimate object distance on a pixel-by-pixel basis.

There are two primary methods for ToF sensing: pulsed illumination and continuous-wave (CW) modulation. In the pulsed illumination approach, a short-duration light pulse is emitted toward the scene. The reflected light is detected at each pixel using two time gates that are offset in phase. By comparing the charge collected in each gate, the system can estimate the time delay of the return pulse and compute the distance to the object.

In the continuous-wave method, the light source is modulated using a sinusoidal or square-wave waveform, and the reflected signal is demodulated at each pixel by mixing it with a reference signal of the same frequency. Four correlation signals are captured at phase offsets of the reference LO of 0°, 90°, 180°, and 270°, which are denoted as A, B, C, and D. These signals represent the results of mixing the modulated reflected optical signal with the in-pixel local oscillator and then integrating over a set period [75]. The advantage of ToF detectors from intensity only detectors is that ToF detectors measure both the intensity and pixel wise distance of objects in an object scene. This is achieved by computing the phase angle of the return signal from the four phase shifted measurements. Owing to this unique capability, ToF detectors were investigated extensively in this thesis and formed the basis of several resulting publications, which will be discussed in the following chapters. A schematic showing a typically ToF detector is shown in Figure 24.

The phase angle is computed from the four recordings using the four-quadrant inverse

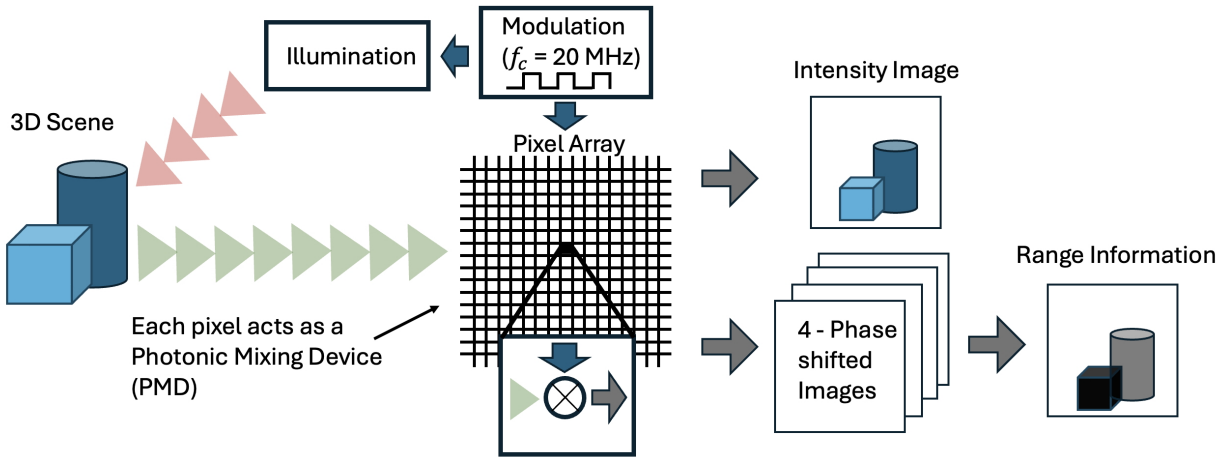


Figure 24: Schematic of the modulation and demodulation process in a time-of-flight camera. The emitted signal is modulated at a known frequency, and is also used mixed phase shifts of the returned signal are used to compute both intensity and distance for each pixel.

tangent function:

$$\Phi(x,y) = \texttt{atan2}\left(\frac{B(x,y) - D(x,y)}{A(x,y) - C(x,y)}\right) \tag{71}$$

The `atan2` function resolves the quadrant ambiguity of `arctan`, producing a unique angle in the range $-\pi$ to π. Once the phase angle is computed for all pixels, the pixel wise distance can then be calculated using:

$$R(x,y) = \frac{c}{4\pi f_c}\Phi(x,y) \tag{72}$$

where c is the speed of light and f_c is the modulation frequency of the illumination, which is synchronized with the reference oscillator in the sensor. The end result is an intensity image, similar to the imaged produced by a conventional camera, alongside a depth map that provides pixel-wise distance measurements based on the phase angle of the return signal. An example of both types of images is shown in Figure 25.

ToF enabled real-time three-dimensional imaging is widely used in applications such as gesture recognition, robotics, 3D mapping, and autonomous navigation. One limitation of ToF systems is the ambiguity distance d_{amb}, which arises because the measured phase wraps

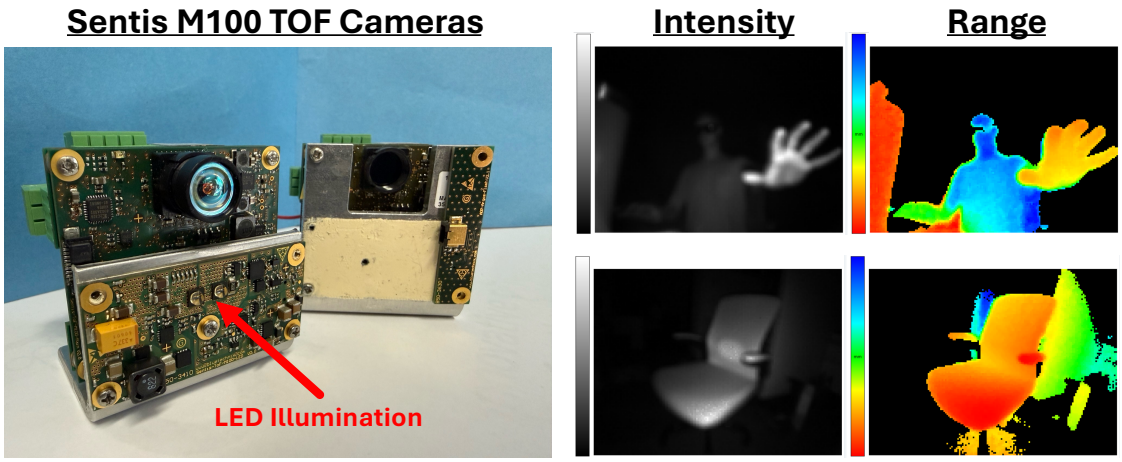


Figure 25: Images of Sentis M100 ToF detectors (left). Example intensity and range maps of two different objects (right). The range is mapped from red being close to blue being far.

around every 2π. This means that distances greater than

$$d_{\text{amb}} = \frac{c}{2f_{\text{mod}}} \tag{73}$$

will produce aliased or ambiguous results. Commercially available ToF detectors are typically constrained to modulation frequencies between 10 and 100 MHz, resulting in an unambiguous measurement range of approximately 1.5 to 15 meters. They also feature significantly fewer pixels than conventional CCD or CMOS sensors, which substantially limits spatial resolution [76–78]. Even the most advanced devices available as of 2025 remain restricted, offering maximum resolutions of only 640 x 480 pixels and maximum ranges of less than 10 meters [79].

Figure 26 illustrates how A, B, C and D are recorded for a single pixel. In this simulation, a noisy sinusoidal return signal is delayed by 37° from a square reference LO signal. Four recordings are performed with phase shifts of the reference LO of 0°, 90°, 180°, and 270°. The shaded region in each of the figures represents the recorded signal from charge accumulation integrated over the same integration time for each measurement.

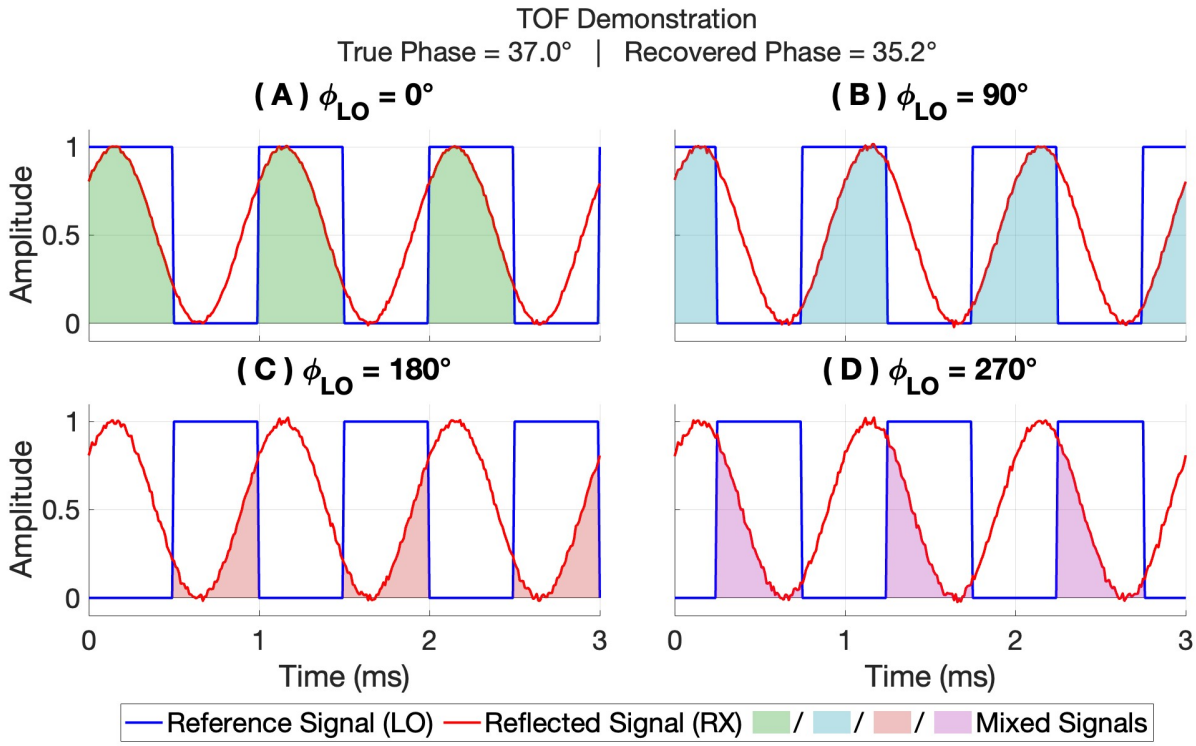


Figure 26: Simulated illustration of the four reference signals with phase shifts of 0°, 90°, 180°, and 270° used to sample the reflected Time-of-Flight signal. Each subplot depicts the corresponding reference waveform, the measured reflected signal, and their point-wise product, which represents the correlation needed for phase demodulation. The distinct phase shifts enable separation of in-phase and quadrature components, forming the foundation for accurate phase recovery in TOF systems.

After the four images are recorded by integrating the return signal with the phase shifted reference LOs, which is usually done in quick succession with four different integrations, the difference between the in phase a quadrature signals is computed to construct I and Q signals. This process for a single pixel is illustrated in Figure 27.

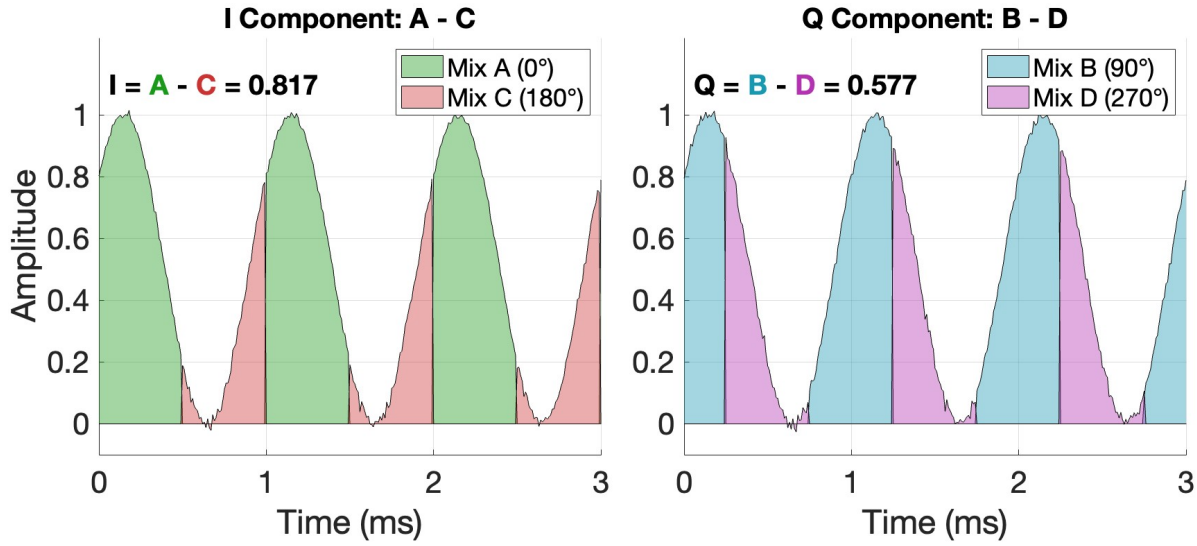


Figure 27: Presentation of the demodulated in-phase (I) and quadrature (Q) components derived by subtracting the mixed signals corresponding to opposing phase shifts (A - C and B - D, respectively). The shaded areas indicate the individual mixed signals contributing to each component. These I and Q values constitute the orthogonal components of the complex baseband signal used for computing pixel wise distance.

The phase angle for the return signal shown in Figure 27 are presented in Figure 28 as a vector on the unit circle for a single pixel.

Phase reconstruction accuracy is strongly influenced by the shape of the reference and return waveforms. In Figure 26, the reference signal is a square wave while the return signal is a noisy sinusoid. This mismatch introduces error in the recovered phase. A square wave contains not only the fundamental frequency but also higher-order harmonics, which can corrupt the demodulation process by contributing unwanted frequency components to the mixing result. In contrast, using a sinusoidal reference signal ensures that both the emitted and mixed signals share a single frequency component, resulting in more accurate phase

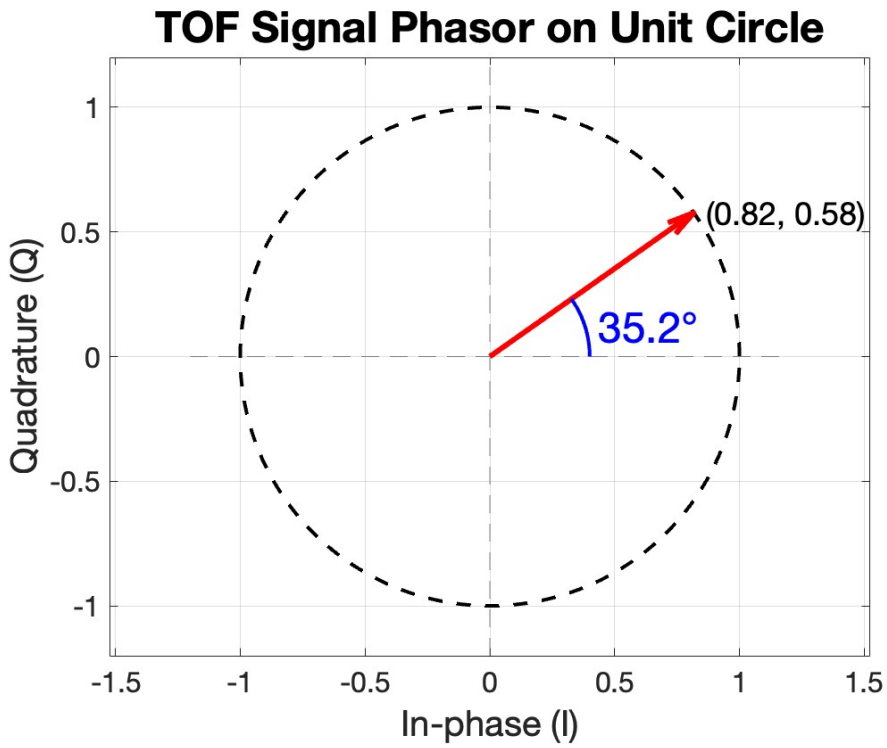


Figure 28: Phasor representation of the demodulated TOF signal, plotting the normalized I-Q vector on the complex unit circle. The vector's angle corresponds directly to the measured phase shift of the reflected signal, which relates to the time delay and thus the distance to the object. The magnitude provides insight into signal quality and strength. This visualization offers an intuitive understanding of TOF phase demodulation in the complex plane, facilitating interpretation of the measurement's precision.

estimation. However, in practice, results are often sufficiently accurate even when only one of the signals, either the reference or the return, is sinusoidal.

Many commercial ToF cameras, such as the Sentis M100, use square waves for modulation and demodulation because of their practical advantages. Square waves are easier to generate using digital logic, require less complex hardware, and allow efficient control of optical emitters by fully switching them on and off. In CMOS-based TOF sensors, square-wave modulation aligns well with the underlying pixel circuitry, which typically uses gated photodiodes or switched integrators. Although this introduces some phase error, the error is often within acceptable limits for the sensor's intended resolution and operating range. Figure 29 shows simulated phase angle reconstruction using both sinusoidal LO and transmit signals, with no added noise, resulting in significantly lower phase error.

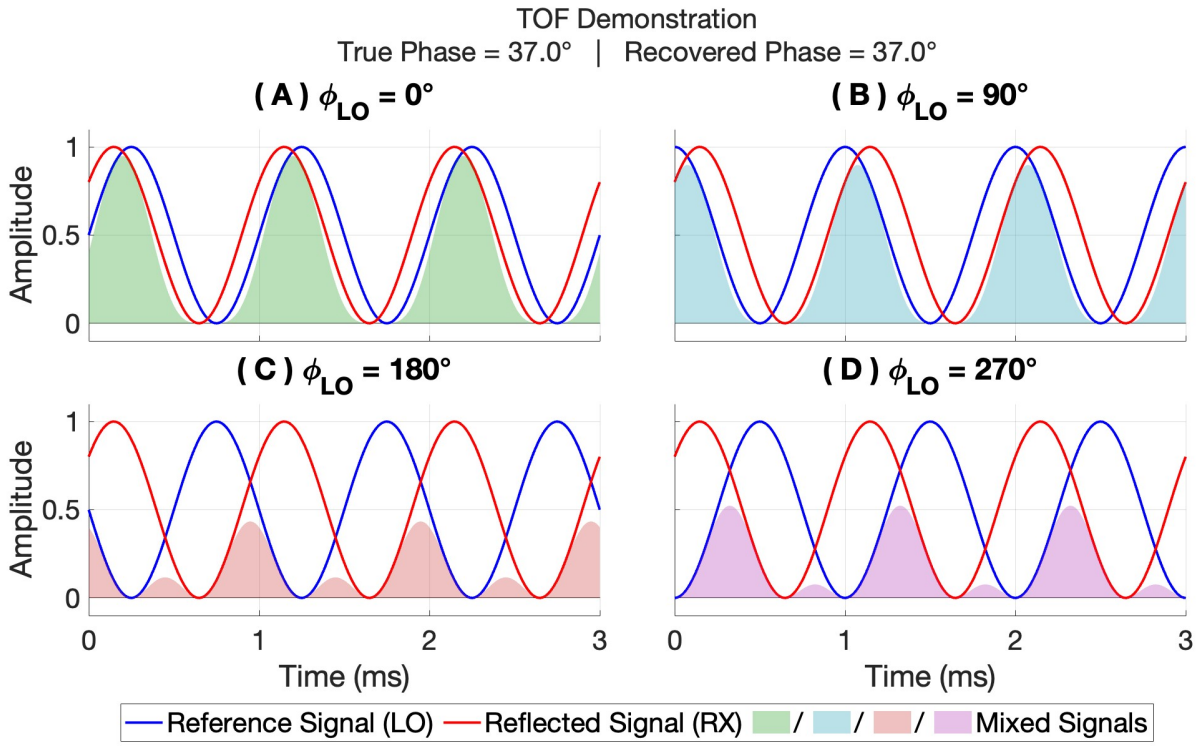


Figure 29: Simulated illustration of the four reference signals with phase shifts of 0°, 90°, 180°, and 270° used to sample the reflected Time-of-Flight signal. Both the LO and RX signals are sinusoidal with no added noise. Under these conditions, the phase angle reconstruction is more accurate than when using a square-wave LO due to the absence of harmonic distortion.

RANGE SELECTIVE PHASE-SHIFTING FREQUENCY-MODULATED DIGITAL HOLOGRAPHY WITH TEMPORAL-HETERODYNING

Manuscript Introduction

Time-of-flight detectors, which are capable of recording four phase-shifted images in rapid succession, present an attractive platform for implementing on-axis range-selective holographic techniques. This advantage arises, in part, from the detector's ability to perform phase shifting automatically and at high speeds, significantly simplifying the experimental setup. Range-selective holographic results were demonstrated in a tabletop laboratory environment and are presented in the following publication.

Contribution of Authors and Co-Authors

Manuscript in following chapter

Author: Cole Hammond

Contributions: Data Collection, Initial Analysis, Software and post processing, Writing - original draft.

Author: Wm. Randall Babbitt

Contributions: Conceptualization, Funding, Methodology, Resources, Supervision, Writing - review and editing

Author: R. Krishna Mohan

Contributions: Conceptualization, Funding, Methodology, Resources, Supervision, Writing - review and editing

Manuscript Information

Cole Hammond, Wm Randall Babbitt, R. Krishna Mohan

Applied Optics

Status of Manuscript:
____ Prepared for submission to a peer-reviewed journal
____ Officially submitted to a peer-reviewed journal
____Accepted by a peer-reviewed journal
_X_ Published in a peer-reviewed journal

OSA (Optical Society of America)
Submitted: 17 October 2022
Published: 22 February 2023
Vol. 62, Issue 10, pp. D157-D162 (2023)
https://doi.org/10.1364/AO.478525

Range Selective Phase-Shifting Frequency-Modulated Digital Holography with Temporal-Heterodyning

COLE HAMMOND,[1,*] WM RANDALL BABBITT,[1] AND R.KRISHNA MOHAN [1]

[1]*Spectrum Lab, Montana State University, Box 173510, Bozeman, Montana 59717, USA*
[*]*Colehammond2@student.montana.edu*

Abstract: We demonstrate that a time of flight (TOF) camera can be used to perform temporal-heterodyne range-selective frequency modulated continuous wave digital holography (TH FMCW DH). The modulated arrayed detection of a TOF camera allows efficient integration of holograms at a selected range with range resolutions significantly less than the optical system's depth of field. TH FMCW DH also allows for on-axis geometries to be achieved, where background light not at the internal modulation frequency of the camera is filtered out. Range selective TH FMCW DH imaging was achieved for both image holograms (IH) and Fresnel holograms (FH) using on-axis DH geometries. A 2.39 GHz FMCW chirp bandwidth resulted in a DH range resolution of 6.3 cm.

© 2025 Optica Publishing Group

1. Introduction

Digital holographic (DH) imaging is a coherent imaging technique that allows for the collection of both intensity and phase information of light scattered off an object by a narrow-band continuous wave (CW) coherent light source [1]. The light scattered from the object is mixed with an optical reference field on a detector array, producing an interference pattern, which is digitally recorded. In off-axis holography, also called spatial heterodyne holography, an angular offset is introduced between the reference beam and the object beam and the object amplitude and phase information is recorded as a real-valued modulated spatial wave. Post processing the digitally recorded interference pattern enables reconstruction of the amplitude and phase of the optical field. Three-dimensional (3D) images of the object(s) can be realized, but with limited field of view. In on-axis holography, where images are generally constructed through phase shifting holography, the reference beam and the object beam have the same optical axis at the detector array. The object amplitude and phase information are obtained by making four holograms, with different phase shifts of the reference field, and post processing the resultant holograms [2]. This on-axis DH geometry has the advantage that the reconstructed image can be recorded from the whole detector array, rather than a fraction (roughly one-quarter) of the detector resolution as is the case with off-axis DH.

DH recorded with traditional detector arrays have three main disadvantages. First, the recorded hologram contains scattered light from all object ranges. Post processing the recorded hologram enables the focusing of objects at a selected range, but all objects within the depth of field (DOF) of the selected range will appear in focus, while all other objects will be out of focus (blurred) [3]. All objects within the DOF will be imaged on top of each other and are indistinguishable. The range resolution of a 3D reconstruction of a scene is thus limited by the DOF. Second, light from objects not within the DOF of the selected range are still recorded and contribute to a blurred background in the reconstruction. Though blurred, this background can have significant spatial structure. If the objects outside the DOF are strong scatterers, the spatial structure of the blurred background can have the effect of obscuring the image of the object(s) at the selected

range. Third, scattering of ambient light into the detector array can create a temporally constant background, which may have spatial components that reduce the contrast of holographic image.

The alternative method for DH recording is to use a temporally modulated detector array. Temporally modulated detector arrays are commonly used in incoherent time-of-flight cameras. Each pixel of the TOF detector array is a photonic mixing device (PMD) with gated integration. A TOF camera has previously been used to demonstrate phase-shifting on-axis temporal heterodyne (TH) DH [4]. In on-axis TH DH, a frequency shift, f_s, is introduced in the CW reference beam equal to the modulation frequency, f_c, of the PMD, as illustrated in Fig. 1 (left), causing the interference pattern at the detector to be temporally modulated at the PMD frequency. Only light modulated at the PMD frequency will integrate constructively and be recorded, other than the unmodulated (DC) background. The complex field of the object light field is obtained by recording four holograms where the phase of the reference beam is shifted by 0, 90, 180, and 270 degrees with respect to the PMD modulation as illustrated in Fig. 2. Post-processing of the recorded holograms reconstructs the amplitude and phase of the object field. The advantage of this type of detector is that whole frames can be captured with relatively high frame rates without the need of cropping images to remove unwanted DC and conjugate terms. However, TH DH has the same blurred background and limited range resolution as traditional CW DH.

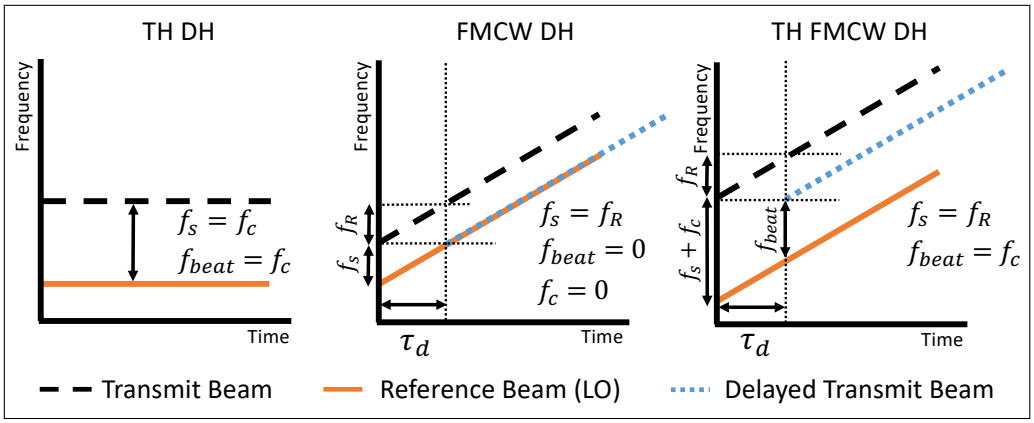


Fig. 1. CW temporal heterodyne digital holography (left), Frequency modulated continuous wave digital holography (center), and Temporal heterodyne frequency modulated digital holography (right)

Frequency modulated continuous wave (FMCW) DH produces range selective coherent imaging by using a broadband frequency chirped coherent light source for both the illumination beam and reference beam [5]. Due to the time delay between the scattered object field and the reference field at the detector array, the interference pattern is temporally modulated at a beat frequency proportional to the time delay. By frequency shifting the reference beam by an amount equal to the beat frequency associated with a selected range, the interference pattern from objects at the selected range will be temporally stable, allowing holograms of objects at the selected range to be recorded much like in traditional DH. The interference patterns associated with objects not at the selected range will have different range-dependent beat frequencies. When these interference patterns are temporally integrated on the detector array, their contribution to the recorded hologram will average toward zero. Thus, FMCW DH removes the spatial background from objects outside the DOF. The range resolution of FMCW DH, which is inversely proportional to the chirp bandwidth, can be significantly less than the optical system's DOF. This allows objects within the DOF of the DH system to be distinguished by their range. By scanning through different shifts of the reference frequency, 3D profiles can be created with much finer

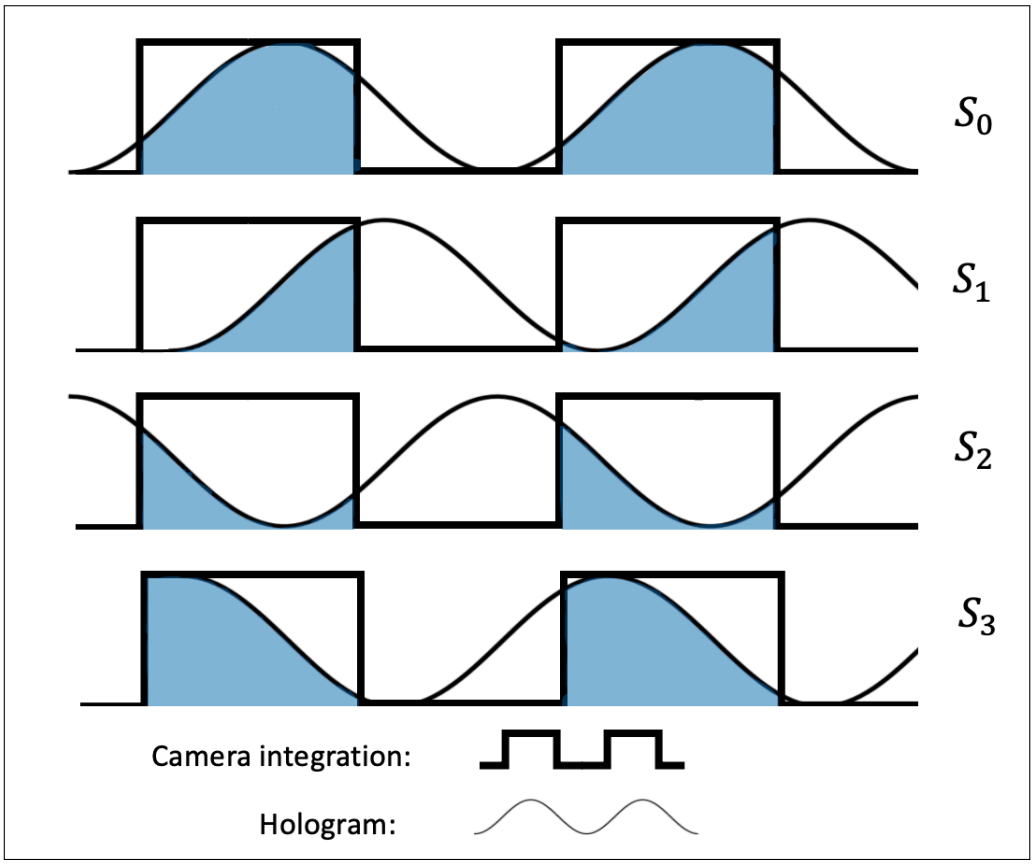


Fig. 2. Graphical depiction of the incident intensity being mixed with the four phase shifted references of the internal camera frequency. The camera's internal reference frequency is depicted as square wave where as the reflected signal from the targets is approximated as sinusoidal.

range resolutions than traditional DH [5].

In this paper, the technique of TH FMCW DH is introduced and demonstrated. Phase-shifting TH FMCW DH combines FMCW DH and TH DH to produce a range-selective on-axis temporally modulated DH image. On-axis TH FMCW DH allows the whole pixel array to be used to image the hologram, as well as providing the desirable range selectivity that has been demonstrated in spatial heterodyne FMCW DH. The heterodyne detection has the advantage of reducing not only ambient DC background interference, but spurious spatial background from scatterers or objects not at the selected range when obscurers or scatterers are present at other ranges.

2. THEORY

2.1. Depth of Field for Digital Holography

Digital interferometric DH imaging for both Fresnel holograms and image holograms is well established [1]. For both geometries, the focal range can be adjusted in post-processing. The diffraction-limited depth of field (DOF) is defined as the axial distance an object can be outside of the selected focal range and still produce a focused diffraction-limited image. The diffraction limited DOF is given by $DOF = 2\lambda(\frac{R}{D})^2$, where λ is the optical wavelength, R is the object range, and D is the diameter of the entrance pupil [3]. Objects located outside of the DOF around

the focal range will start to blur, however non-diffraction-limited features of an object will not appear to blur until the object is far outside the DOF. For a non-diffraction-limited features of size, δ, the depth of field can be calculated using ray tracing as, $DOF_{NDL} = 2\delta R/D$.

2.2. Range Resolution of FMCW DH

The equations for the range resolution of FMCW DH are similar to those of FMCW lidar [6]. In FMCW lidar and FMCW DH, a linear frequency chirp is characterized by the chirp rate $\kappa = B/\tau_c$, where B is the bandwidth of the chirp in frequency and τ_c is the duration of the chirp. The reflected light from an object is delayed from the reference field by $\tau_R = 2R/c$, where R is the object range. The interference of the object and reference fields on the detector produces a beat frequency given by $f_R = 2\kappa R/c$. In practice, the distance to an object is calculated from the measured beat frequency, f_{meas}, as $R = f_{meas}c/(2\kappa)$. The range resolution is given by $\Delta R = c/(2B)$, where c is the speed of light and B is the bandwidth of the chirp and assuming that the frequency resolution is governed by the chirp duration. The linewidth of the light source and non-linearities in the chirp can broaden the beat note and deteriorate the range resolution. FMCW chirp bandwidths in the THz range have been demonstrated with linearization better than 170 kHz, which has allowed range resolutions of 31 um at the 1.5-meter range [7] [8] [9]. The major difference between FMCW LIDAR and FMCW DH is detector bandwidths. In FMCW lidar, the detector bandwidth limits the resolvable beat frequency. In FMCW DH, the detector bandwidth limits the integration time of the detector array, thus the frame rates are in the few tens of Hz range. To remedy this the frequency of the reference is shifted by f_s to cancel the range dependent beat frequency, bringing the resultant beat frequency for objects at the selected range to DC (within the reciprocal of the integration time of the detector), as illustrated in Fig. 1 (center). By scanning the frequency shift of the reference, 3D images of an object or scene can be created with the fine range resolution of c/2B, while background scattered light from other object planes are significantly reduced.

2.3. TH FMCW DH Theory

In TH FMCW DH, the shift of the reference local oscillator (LO), $f_s + f_c$, is chosen such that the beat frequency between the local oscillator and that of the light returning from the target is equal to the TOF camera's modulation frequency, f_c. This only occurs at a single target range, R_s. Targets at other distances will have different range dependent beats, which will wash out during integration. However, by scanning through different values of f_s, targets at different distances are imaged. This allows 3D profiles of the target to be created. In Fig. 1 (right), κ is shown to be positive, requiring a down shift of the LO. For negative κ, the LO would require an up shift. All of the work presented in this paper was done with a repeated up-ramp chirp, sometimes referred to as a sawtooth chirp.

One way to achieve the frequency shift between the LO and transmit beams is to introduce an acousto-optic modulator (AOM) in each beam path with separate driving frequencies. The optical fields for the LO beam and target return arm beam can be written as,

$$E_{lo}(x,y,t) = A_{lo}(x,y)\cos(2\pi(f_L + f_o - f_s - f_c)t + \pi\kappa(t - T_n)^2 + \phi_{lo}(x,y)) \quad (1)$$

$$E_{tar}(x,y,t) = A_{tar}(x,y)\cos(2\pi(f_L + f_o)(t - \tau_R) + \pi\kappa(t - T_n - \tau_R)^2 + \phi_{tar}(x,y)) \quad (2)$$

where f_L is the laser frequency, f_o is the RF center frequency of the AOM, and T_n is the start time of the n^{th} phase measurement as shown in Fig. 3. $A_{lo}(x, y)$ and $A_{tar}(x, y)$ are defined as the spatial amplitudes and $\phi_{lo}(x, y)$ and $\phi_{tar}(x, y)$ are the spatial phases of the LO field and target return fields after propagation to the camera, respectively. $\tau_R = 2R/c$ is the range dependent time delay. The frequency shift f_s, is defined as $f_s = \frac{2\kappa R_s}{c}$, which is tuned to constructively produce a hologram at the selected range, R_s. The intensity incident on the detector will be the interference of the LO field and return target field. Ignoring constant factors,

$$I_n(x, y, t) \propto \left\langle |E_{lo}(x, y, t) + E_{tar}(x, y, t)|^2 \right\rangle_{\frac{1}{f_L}} \tag{3}$$

The terms oscillating as the sum of the laser frequencies will average towards zero over the camera's integration time, yielding a recorded intensity on the camera given by,

$$I_n(x, y, t) = A_{lo}^2 + A_{tar}(x, y)^2 + A_{lo}A_{tar}(x, y)\cos(2\pi(f_c + f_s - f_R)t + \phi_n(x, y)) \tag{4}$$

where f_R is the range dependent beat frequency proportional to the target distance and $\phi_n(x, y)$ is now the sum of all phase terms for the n^{th} quadrature measurement ($\phi_n(x, y) = \phi_{tar}(x, y) - \phi_{lo}(x, y) - 2\pi(f_L + f_o)\tau_R + \pi\kappa\tau_R^2 + 2\pi f_R T_n$). $A_{lo}(x, y)$ is assumed to be constant.

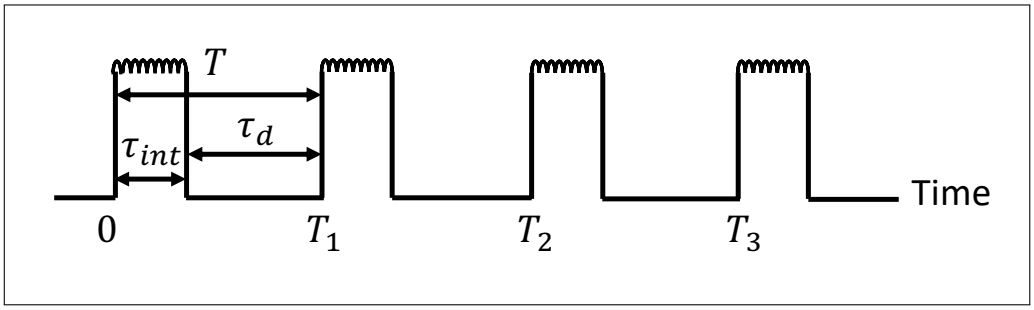


Fig. 3. Timings of the four quadrature measurements.

The holographic image can be recorded with phase-shifting TH techniques as illustrated in Fig. 2. Four successive quadrature measurements are recorded by adjusting the phase of the camera's internal modulation as $\Phi_n = n\pi/2$, where n = 0, 1, 2, 3. The four-quadrature measurements do not all occur at the same time and are instead each separated by $\tau_{int} + \tau_d$, the integration time of the camera with an additional fixed delay. The starting time for the n^{th} integration is given as, $T_n = nT$ for n = 0, 1, 2, 3, where $T = \tau_{int} + \tau_d$. For all results shown, τ_d was equal to 2 ms and τ_{int} was equal to 1 ms. An illustration of the timing between quadrature recordings is shown in Fig. 3. Though the camera's integration is square wave modulated (as illustrated in Fig. 2, the analysis is done assuming that the camera integration is sinusoidal, with no loss in functionality. The resulting signal for the nth phase shift, $S_n(x, y)$, is given as,

$$S_n(x, y) = \int_{T_n}^{T_n+\tau_{int}} I_n(x, y, t)\cos(2\pi f_c t + \Phi_n)dt \tag{5}$$

where the intensity incident on the detector is mixed with a phase shifted reference and integrated over τ_{int}, the integration time of the camera, which is equal to the chirp duration.

The resulting integrations are added in phase and quadrature and the difference is taken to cancel the DC components of the intensity. The complex representation of the reconstructed signal is then calculated as,

$$E_{recon}(x,y) = (S_0(x,y) - S_2(x,y)) + i(S_1(x,y) - S_3(x,y)) \tag{6}$$

For this reconstructed signal to be maximized and produce a stable hologram several conditions must be met. The first is that the hologram must be within the bandwidth of the detector, or $|f_s - f_R| < 1/\tau_{int}$. If outside this limit the hologram will wash out during integration. The second condition is that $|f_s - f_R| \leq 1/2T$ which arises from the fact that f_sT must be an integer value in order to prevent phase discontinuities.

For an image hologram, an image of the target is achieved by taking the magnitude square of $E_{recon}(x,y)$ in post processing. The intensity,

$$I_{recon}(x,y)_{IH} = |E_{recon}(x,y)|^2 \tag{7}$$

is plotted for the image hologram figures in this paper, ignoring amplitude conversion factors.

For a Fresnel hologram, the target field at the detector can be described by the Fresnel propagation of the original field at the object. The target field, $E_{tar}(x,y,t)$, will be approximated by the 2D Fourier transform of the field at the target, multiplied by both an amplitude and quadratic phase term [10]. In order to undo the effects of Fresnel propagation, returning to the desired field at the target, $E_{recon}(x,y)$ is first multiplied by a quadratic phase focusing term, $e^{i\phi_f(x,y)}$. This is done in order to remove the parabolic phase terms from both the LO and target field which were acquired from propagation. This phase correction takes the form,

$$e^{i\phi_f(x,y)} = e^{-i\frac{k}{2}(x^2+y^2)(\frac{1}{z_{tar}} - \frac{1}{z_{lo}})} \tag{8}$$

where z_{lo} and z_{tar} are the distances from the local oscillator and target to the camera, and k is the wave number. Finally, to fully undo the effects of Fresnel propagation a 2D inverse Fourier transformed is performed and the magnitude square is taken. The images plotted for Fresnel holograms are of $I_{recon}(x,y)_{FH}$, where

$$I_{recon}(x,y)_{FH} = |\mathcal{F}^{-1}\{e^{i\phi_f(x,y)}E_{recon}(x,y)\}|^2 \tag{9}$$

This is consistent with other holographic image processing techniques [1]. A flow diagram illustrating the methods of data acquisition and hologram processing is shown in Fig. 4.

The introduction of TH FMCW DH removes much of the unwanted light from targets not at the desired distance in question since only light from targets within the range resolution of the chirp will be temporally stable over the camera's integration time. Holograms from targets outside of this distance will integrate towards zero since their beat frequency will not constructively mix with the internal modulation frequency of the camera. Although the amount of light incident on the TOF detector is not changing between CW or FMCW techniques, light from outside of the range resolution of the chirp will only contribute to low temporal frequencies which are naturally filtered by the TOF's IQ detection.

3. Experimental Procedure and Results

3.1. Experimental Setup

A diagram of the experimental setup is shown in Fig. 5. The TOF camera used was a Sentis M100, which has a 160 pixel by 120-pixel detector array. The PMD in the TOF camera is sensitive from 650 to 1200 nm [11]. The laser source used in the experiments was a New Focus 793 nm vortex diode laser. A double sideband electro-optical phase modulator was used to implement the FMCW chirp. This was driven by a digitally produced chirp sent though a home-made multiplication chain to increase the bandwidth to 2.39 GHz. A 1 ms duration up-chirp was used that varied from 11.91 to 14.3 GHz. This provided a range resolution of approximately 6.3 cm, much finer than the $DOF_{NDL} = 26$ cm that was calculated for a feature size of 1.5 mm at a

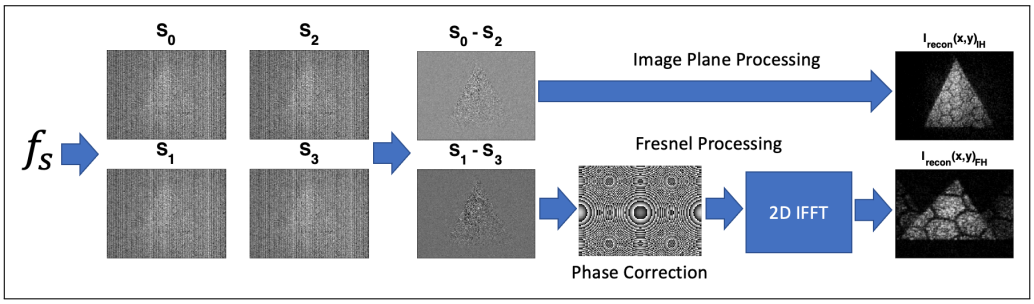


Fig. 4. Flow diagram demonstrating the methods of hologram acquisition for both image and Fresnel holograms. First, the desired target range is selected by adjusting f_s. Second, the four phase shifted signals are recorded as illustrated in Fig. 3 and equation 5. Third, $E_{recon}(x, y)$ is constructed from equation 6. An image hologram is realized by using equation 7 to plot the intensity from the reconstructed field and is shown in the top right figure. For a Fresnel hologram a phase correction is first applied given by equation 8 and a 2D inverse Fourier Transform is performed digitally before taking the magnitude square to form an image. This is shown in equation 9 and is illustrated in the bottom right figure. The images of $S_0(x, y)$ through $S_3(x, y)$ are shown for the image hologram (Top Figure). The images of $S_0(x, y)$ through $S_3(x, y)$ for the Fresnel hologram are not shown (bottom figure). Different targets were used for each recording geometry.

distance between the two targets (R = 87.5 cm). The chirped optical source was amplified by a Toptica BoosTA to increase the optical power. The beam was split with a nonpolarizing beam splitter to create the two arms of our system. The LO arm was frequency shifted with an AOM at 230 MHz. To drive the target arm AOM the electronic internal modulation frequency of the camera (20 MHz) was mixed with a separate 230 MHz RF signal to create a modulated 250 MHz signal. Both signal generators used to generate the two different 230 MHz signals were synced together with a 10 MHz reference to maintain frequency and phase stability. This preserved the relative phases between both AOMs and the camera. When the system is run in CW (without a chirp), the beat note between the two arms is equal to the internal modulation frequency of the camera (20 MHz). When both paths are modulated by an FMCW chirp, the beat note between the arms is shifted away from 20 MHz by f_s, proportional to the distance to the desired target range. By adjusting the frequency of one of the signal generators, the resultant beat note for a selected range can be shifted to 20 MHz where an image is TH recorded. The camera was operated with the factory lens removed. All images for a given geometry were recorded with the same optical and RF powers. A consistent integration time of 1 ms was used in all figures, which matched the chirp duration. Target locations did not change between the different holographic recording geometries, but target size did. Smaller targets were used for Fresnel holograms in order to maintain a similar relative hologram size on the detector. This was needed because of the difference in field of view (FOV) between the two techniques. In the experiment the LO AOM frequency was a constant and the target AOM frequency varied. Although the analysis is done as if the LO was shifted, since the results are the same.

The two targets being imaged were created by attaching retro-reflective tape to glass plates. The first target was attached with a triangle and placed 0.95 m in front of the detector. Using the previously introduced equation for target range the theoretical beat note for an object at this range is calculated as $f_{R1} = 2\kappa R_1/c = 15150$ Hz and was determined experimentally by maximizing the image strength as $f_{R1} = 15130$ Hz . To compare results at different distances, the second target, attached with a star fashioned in the same manner, was placed between the camera and first target. The star target was measured to be 0.815 m in front of the camera. The AOM frequency

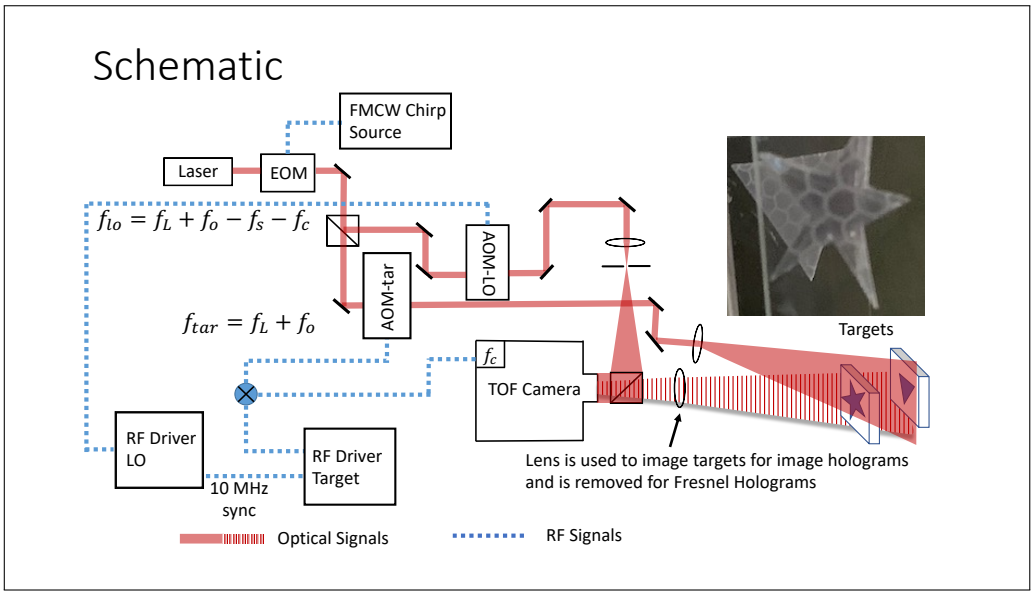


Fig. 5. A schematic of the range selective digital holographic experiment. Direct image of the targets used (Top Right). The lens is used to image the targets onto the TOF sensor array for image holograms. The lens is removed from the system when recording Fresnel holograms.

shift for the star target was calculated to be $f_{R2} = 12990$ Hz and experimentally determined to be $f_{R2} = 12970$ Hz, within the measured error of the target's range. For all images shown in this paper, the star target is the closer of the two with respect to the camera.

The phase correcting term used for all Fresnel hologram results in Fig. 6 was constructed from equation 8 using an LO distance of $z_{lo} = 16.5$ cm and a target distance of $z_{tar} = 87.5$ cm, approximately halfway between each target.

3.2. Results

Both targets were recorded at the same time and their positions were not changed or altered during the experiment. The separation of 13.5 cm was within the theoretical DOF_{NDL} of 26 cm for the target's feature size of a few millimeters. For image holograms, a lens was placed in between the camera and targets and was adjusted to image a spot halfway between the two targets. This was done such that any blurring caused by not being at focus was symmetric between the two targets. Optical power, including that used in both the LO reference arm and the illumination arm was constant for all measurements between each geometry. The target beam size was adjusted between geometries in order to illuminate the different sized targets. All images shown in Fig. 6 are the result of 50 averaged shots. The top row depicts the Fresnel hologram and image hologram results for a CW system when there is no FMCW chirp. Both targets are visible in this case and there is no depth information. The center left image depicts Fresnel hologram TH FMCW imaging system for when f_s is adjusted to be approximately equal to f_{R1}. The center right image similarly shows the TH FMCW system when $f_s \approx f_{R1}$, this time for an image hologram. The bottom left image shows the TH FMCW system, for a Fresnel hologram, when $f_s \approx f_{R2}$. Similarly, the bottom right image depicts $f_s \approx f_{R2}$ for an image hologram.

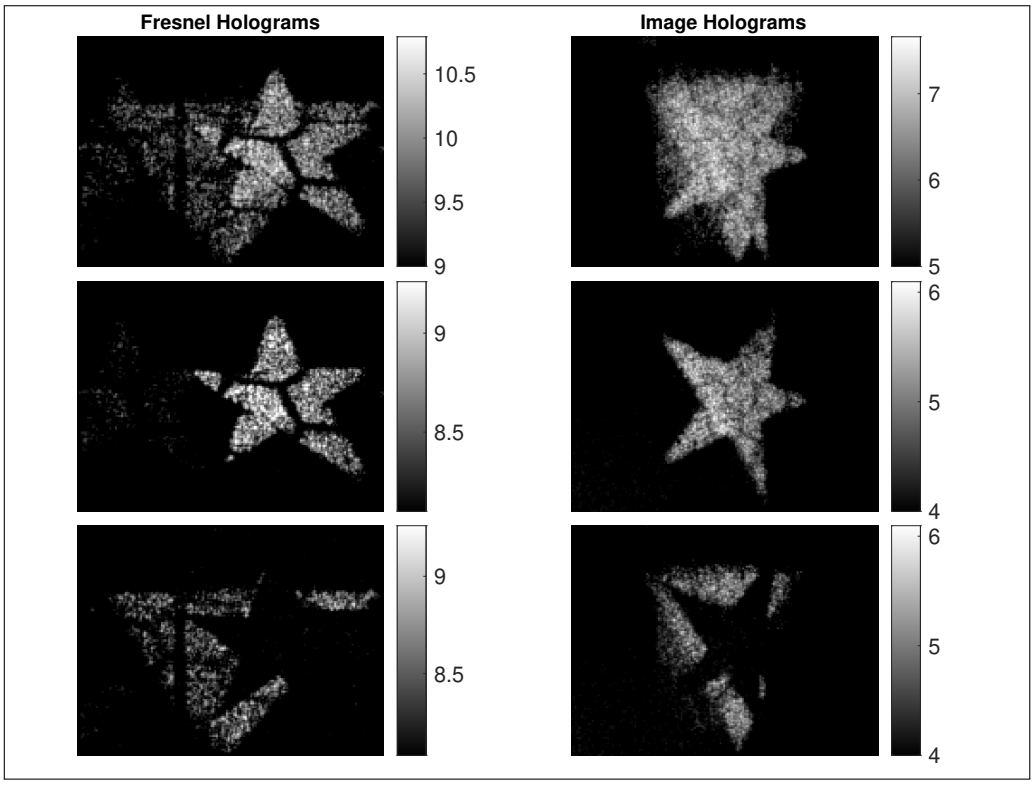


Fig. 6. CW Fresnel hologram recording (top left), CW image hologram recording (top right), TH FMCW Fresnel hologram recording of star target (middle left), TH FMCW image hologram of star target (middle right) ,TH FMCW Fresnel hologram of triangle target (bottom left), TH FMCW image hologram of triangle target (bottom right). Dimensions for each image are 160 X 120 pixels. Images are plotted in a $\log_{10}$ scale to illustrate contrast.

3.3. Extinction Measurements

To quantify the range selective properties of the TH FMCW DH system, extinction percentages for both targets were calculated for each geometry. The extinction percentage is a measure of how well an unselected target that is within the depth of field is filtered out by the range selective imaging. To illustrate the calculation method, Fig. 7 shows the method for calculating the average intensities for the star target for image hologram recordings. Fig. 7 shows TH FMCW recordings when the star target is selected (left) by setting $f_s \approx f_{R1}$ and unselected (right) by setting $f_s \approx f_{R2}$, when the triangle target is selected. $I_{selected}$ and $I_{unselected}$ were calculated by averaging over 50 recordings for each case. $I_{selected}$ is the mean pixel value of the target at Rs, which was calculated by taking the sum of the pixel values in a polygon that roughly matched the observed target (but avoided edge effects) and dividing by the number of pixels in the polygon. The polygon for the star target is shown in Fig. 7. Any constant background in $I_{selected}$ and $I_{unselected}$ was removed by subtracting the mean pixel value computed in an area outside of both targets. A similar process was done for the image holograms of the triangle target and for the Fresnel holograms of both targets. The extinction percentage of a target is defined as,

$$\text{Extinction Percentage} = \frac{I_{selected} - I_{unselected}}{I_{selected}} * 100 \tag{10}$$

If a target is visible and of equal intensity in the selected and unselected cases, similar to the CW TH DH when the two targets are within the depth of field, the extinction percentage would be close to 0%. Complete extinction would be 100%. The results of the extinction calculations can be seen in table 1. The table shows that for both near (star) and far (triangle) targets that are within the depth of field of the optical system, the range selectivity of FMCW TH DH was able to effectively extinguish unselected targets.

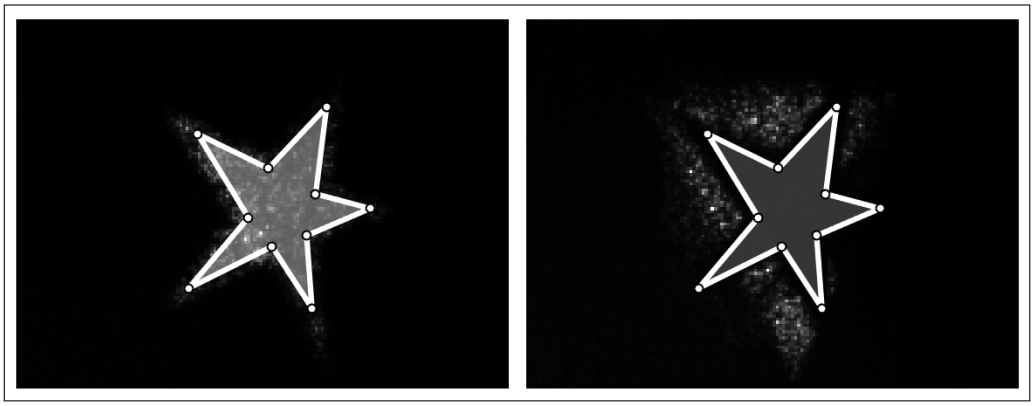


Fig. 7. Method for computing average intensities for TH FMCW recordings of the star target (Image hologram). The mean pixel values $I_{selected}$ and $I_{unselected}$ were computed by averaging the pixel values inside the polygon outlined by the white star when f_s was shifted to select the range of the star target (left) and shifted to select the triangle target (right), respectively. Images are plotted in a linear scale.

	TH FMCW (star)	TH FMCW (Triangle)
Image Holograms	97.6 %	96.3%
Fresnel Holograms	97.2%	98.6%

Table 1. Extinction percentages for recorded image holograms and Fresnel holograms for the star and triangle targets. The percentage represents how much of the target was removed in holograms when the target was not at the selected range.

4. Conclusion

In this paper we proposed and demonstrated a proof of concept of TH FMCW DH using a TOF camera. This technique differed from previous FMCW DH techniques by shifting the hologram away from DC to a beat frequency equal to the internal modulation frequency of the TOF camera. We demonstrate that TH FMCW DH allows for range selective imaging with range resolution less than the DOF_{NDL} of the system. The demonstrated extinction percentages show the significant improvement in range selective imaging of TH FMCW DH over CW techniques. Further experiments are needed to quantify the advantages of TH FMCW DH in reducing interference from ambient and DC backgrounds and spurious spatial backgrounds from scatterers and blurred objects far away from the selected range.

Funding. Office of Naval Research (N00014-20-1-2260)

Acknowledgement. We gratefully acknowledge funding from the Office of Naval Research. This work relates to Department of Navy award N00014-20-1-2260 issued by the Office of Naval Research. The

United States Government has a royalty-free license throughout the world in all copyrightable material contained herein. Any opinions, findings, and conclusions or recommendations expressed in this material are those of the author(s) and do not necessarily reflect the views of the Office of Naval Research.

Disclosures. The authors declare no conflicts of interest.

Data Availability. Data underlying the results presented in this paper are not publicly available at this time but may be obtained from the authors upon reasonable request.

5. References

References

1. T.-C. Poon and J.-P. Liu, *Introduction to Modern Digital Holography with MATLAB* (2014).
2. I. Yamaguchi and T. Zhang, "Phase-shifting digital holography." Opt. letters **22 16**, 1268–70 (1997).
3. R. W. Meier, "Depth of focus and depth of field in holography," J. Opt. Soc. Am. **55**, 1693–1694 (1965).
4. R. Galloway, "Coherent imaging via temporal heterodyne and spatial shearing methods," Master's thesis, Montana State University (2018).
5. M. A. Goodman, R. K. Mohan, and W. R. Babbitt, "Range selective digital holographic imaging using fmcw lidar," Appl. Opt. **61**, B255–B261 (2022).
6. J. Zheng, "Optical frequency-modulated continuous-wave interferometers," Appl. Opt. **45** (2006).
7. Z. W. Barber, C. J. Renner, W. R. Babbitt, *et al.*, "Linearization of ultra-broadband optical chirps for precision length metrology," in *Conference on Lasers and Electro-Optics 2010,* (Optica Publishing Group, 2010), p. JWB1.
8. Z. W. Barber, W. R. Babbitt, B. M. Kaylor, *et al.*, "Accuracy of active chirp linearization for broadband frequency modulated continuous wave ladar." Appl. optics **49 2**, 213–9 (2010).
9. P. A. Roos, R. R. Reibel, T. Berg, *et al.*, "Ultrabroadband optical chirp linearization for precision metrology applications," Opt. Lett. **34**, 3692–3694 (2009).
10. J. W. Goodman, *Introduction to Fourier Optics* (W. H. Freeman, 2017), hardcover ed.
11. K. Uno, L.-J. Burtz, M. HULCELLE, and K. YOSHIDA, "Qualification of a time-of-flight camera as a hazard detection and avoidance sensor for a moon exploration microrover," TRANSACTIONS OF THE JAPAN SOCIETY FOR AERONAUTICAL AND SPACE SCIENCES, AEROSPACE TECHNOLOGY JAPAN **16**, 619–627 (2018).

FREQUENCY DETUNING ANALYSIS IN MULTI-CHIRP RANGE-SELECTIVE DIGITAL HOLOGRAPHY WITH TEMPORAL HETERODYNING

Manuscript Introduction

After demonstrating range-selective digital holography with temporal-heterodyning where f_s is chosen to be approximately equal to f_R, a natural next step is to explore the system's behavior when $f_s \neq f_R$. Specifically, it is of interest to investigate how integrating over multiple chirps influences range resolution and detuning characteristics. Holograms were recorded across a range of frequency shifts for f_s, and a quantitative holographic signal-strength metric was developed to assess the quality of the reconstructions. In addition, target positions were systematically varied, and data were acquired using two closely spaced targets positioned within the system's range resolution limit, which is determined by the chirp bandwidth. This was done to evaluate potential improvements in range resolution and the system's ability to resolve and distinguish multiple targets. A mathematical framework was also developed to explain the observed behavior. These results are not unique to temporally heterodyne systems, but are applicable to any holographic system that integrates over multiple chirps. This work resulted in the following publication:

Contribution of Authors and Co-Authors

Manuscript in following chapter

Author: Cole Hammond

Contributions: Data Collection, Initial Analysis, Software and post processing, Writing - original draft.

Author: Wm. Randall Babbitt

Contributions: Conceptualization, Funding, Methodology, Resources, Supervision, Writing - review and editing

Author: R. Krishna Mohan

Contributions: Conceptualization, Funding, Methodology, Resources, Supervision, Writing - review and editing

Manuscript Information

Cole Hammond, Wm Randall Babbitt, R. Krishna Mohan

Applied Optics

Status of Manuscript:
____ Prepared for submission to a peer-reviewed journal
____ Officially submitted to a peer-reviewed journal
____Accepted by a peer-reviewed journal
_X_ Published in a peer-reviewed journal

OSA (Optical Society of America)
Submitted: 19 June 2025
Published: 16 September 2025
Vol. 64, Issue 27, pp. 8077-8087 (2025)
https://doi.org/10.1364/AO.571313

Frequency Detuning Analysis in Multi-Chirp Range-Selective Digital Holography with Temporal Heterodyning

COLE HAMMOND,[1,*] R.KRISHNA MOHAN,[1] AND WM RANDALL BABBITT [1]

[1] *Spectrum Lab, Montana State University, Box 173510, Bozeman, Montana 59717, USA*
[*] *Colehammond2@montana.edu*

Abstract: Range-selective digital holography (RSDH) is an advanced imaging technique that combines digital holography with the range-selective capabilities of frequency-modulated continuous-wave (FMCW) chirped lidar. Temporal heterodyne FMCW range-selective digital holography (TH FMCW RSDH) further extends this method by incorporating phase-shifting techniques to enable on-axis holographic imaging. In standard implementations, maximum hologram strength is achieved when the local oscillator (LO) frequency shift is set by the target distance, assuming that the hologram integration and chirp duration are aligned. However, in systems where hologram integration spans multiple chirps, this alignment is no longer guaranteed, and the optimal LO frequency shift may deviate from the nominal value. This work develops a theoretical framework to analyze the effects of LO detuning on range resolution and hologram strength in TH FMCW RSDH under multi-chirp integration. The model is experimentally validated using a time-of-flight (ToF) camera to perform phase-shifting and integration. Our results demonstrate that maximum hologram strength can occur at LO frequency shifts that differ from the nominal range-dependent value. These findings provide valuable insights for optimizing the performance of both TH and non-TH FMCW RSDH systems in scenarios where hologram integration spans multiple chirps.

1. Introduction

1.1. Digital Holography

Digital holography is a coherent imaging technique that enables the reconstruction of both the amplitude and phase of an optical field scattered from an object. This is achieved by interfering the scattered field with a coherent reference beam, known as the local oscillator (LO), at a sensor array, where the resulting intensity pattern is recorded as a digital hologram. Post-processing of the recorded hologram enables reconstruction of both the amplitude and phase of the object field [1]. Hologram reconstruction can be performed using either off-axis or on-axis recording geometries. In off-axis digital holography, the LO and scattered fields interfere at an angle, introducing a spatial carrier frequency that shifts the image components in the Fourier domain [1, 2]. This spatial separation enables filtering to isolate the desired image while suppressing the conjugate image and low-spatial-frequency terms. In contrast, on-axis holography relies on phase-shifting techniques, in which multiple intensity patterns are recorded with known phase shifts applied to the LO field, allowing complete reconstruction of the complex object field [3].

Each geometry has inherent trade-offs. Off-axis digital holography enables single-shot acquisition, making it well-suited for real-time or dynamic measurements, but typically sacrifices spatial resolution due to the need to separate overlapping terms in the Fourier domain. On-axis holography, while requiring multiple frames and being more sensitive to environmental instability, can achieve higher spatial resolution and more precise phase recovery, making it preferable for applications prioritizing accuracy over speed [4, 5]. Additionally, the simpler beam combining geometry of on-axis holography is more compact and robust than the off-axis geometry. The choice between these recording geometries depends on system-level performance requirements

such as temporal resolution, spatial fidelity, and robustness to motion.

1.2. Temporal-Heterodyne Digital Holography

Temporal-Heterodyne Digital Holography (TH DH) is an on-axis holographic technique that uses a sensor array in which each pixel functions as a photonic mixing device (PMD) with gated integration. This approach has been demonstrated using time-of-flight (ToF) cameras, where four phase-shifted recordings are captured at different times with temporal phase shifts of the modulation frequency of the sensor array [6, 7]. The object field is reconstructed from these four intensity recordings, each corresponding to a different phase shift of the LO field, following standard phase-shifting holography techniques. TH DH can be implemented using either Continuous-Wave illumination (TH CW DH) or made range-selective using Frequency-Modulated Continuous-Wave (FMCW) signals.

1.3. Range-Selective Digital Holography

FMCW signals have been widely applied in digital holography, particularly in range and surface profiling. One prominent approach employs long broadband chirps in conjunction with high-speed detectors, enabling multiple short integration windows during each chirp. This technique, often referred to as FMCW digital holography, has been demonstrated in various configurations, including single-wavelength scanning systems [8], multi-wavelength setups [9], and configurations incorporating polarized LO fields [10]. In these methods, a slow broadband linear chirp is used to modulate both arms of the holographic system, with a high-speed camera capturing sequential images. Post-processing using a Fourier transform across the temporal dimension of the recorded frames enables the reconstruction of pixel-wise range profiles [11–13]. Other FMCW-based methods have employed aperture synthesis for surface profiling [14]. In contrast, lidar-derived digital holography achieves depth-resolved holographic images from pulsed lidar 3D point clouds, without relying on FMCW techniques [15].

The second application is FMCW Range-Selective Digital Holography (FMCW RSDH), a technique that enables objects to be selectively imaged and holograms recorded at specific, adjustable distances [7, 16, 17]. This is achieved by introducing a frequency shift to the LO, which functions as a tuning mechanism. This method allows for the isolation and capture of distinct objects within the system's non-diffraction-limited depth of field (DOF_{NDL}). The DOF_{NDL} is the range over which objects are imaged in focus at the sensor array [16]. The DOF_{NDL} for an object feature size δ can be computed from ray tracing as $DOF_{NDL} = 2\delta R/D$ where R is the object range and D the diameter of the entrance pupil. FMCW RSDH has been demonstrated in off-axis geometries for Fresnel-plane (FP) holograms and in on-axis geometries for both image-plane (IP) and FP holograms using temporal heterodyning [7, 16]. In FMCW RSDH, illumination of a target at range R by a transmit field (TX) results in a time-delayed return field (RX), whose range-dependent frequency shift is given by

$$f_R = 2\kappa R/c \tag{1}$$

where κ is the chirp rate of the linear FMCW modulation defined as $\kappa = B/\tau_c$, B is the chirp bandwidth, τ_c is the chirp duration, and c is the speed of light.

In FMCW RSDH with a single-sided chirped laser with a positive chirp rate, the LO is shifted down by f_s to cancel the range-dependent frequency shift of the RX field at a selected range, R_s, as shown in Fig. 1 (left). When $f_s \approx f_R$, the hologram for the object at distance R will beat at a frequency $f_b = |f_s - f_R| \approx 0$, and become temporally stable, allowing for constructive integration on a sensor array. For Temporal-Heterodyne (TH) FMCW RSDH, the TX field is shifted up by f_c and the LO is shifted down by f_s which causes the hologram to be temporally modulated at a frequency $f_b = f_c + f_s - f_R$. When $f_s \approx f_R$, the resulting beat frequency is approximately equal to the modulation frequency, f_c, of the photonic mixing device (PMD) detector, as shown in Fig.

1 (right). To prevent the hologram from washing out during integration, the difference between f_s and f_R must be within the bandwidth of sensor array, expressed as $|f_s - f_R| < 1/\tau_{int}$, where τ_{int} is the sensor's integration time, ideally matched to the overlap time between the LO chirp and its delayed replica in the RX path. It should be noted that all frequency shifts are relative, so the way in which shifts are applied to the LO and TX beams is a matter of convention. In practice, for both FMCW lidar and FMCW RSDH, the integration time should be less than or equal to the duration of the chirp ($\tau_{int} \leq \tau_c$).

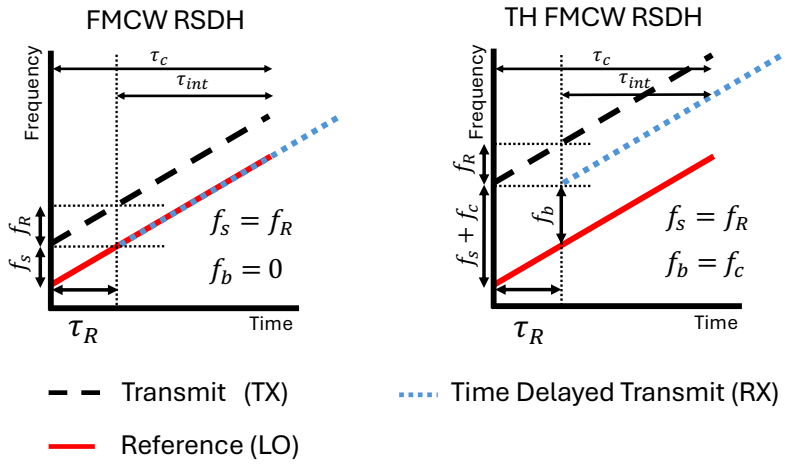


Fig. 1. Frequency vs time plot of the interfering fields for FMCW RSDH (left), and TH FMCW RSDH (right). In FMCW RSDH the LO is shifted down by f_s to cancel the range-dependent beat. For TH FMCW RSDH, the LO is shifted down by f_s and the TX is shifted up by f_c, resulting in a total shift of $f_s + f_c$.

The range resolution of FMCW RSDH and FMCW lidar is limited by the chirp bandwidth, given by $c/2B$, where c denotes the speed of light and B is the chirp bandwidth [18]. High chirp rates are desired because they increase the frequency shift of f_R for a given target distance, helping to reduce the impact of low-frequency noise on the final corrected hologram that could arise from unwanted reflections in the optical system or objects at very close distances. However, practical system constraints introduce a trade-off between achieving high range resolution and maintaining long integration times needed to improve signal-to-noise ratio (SNR). While this balance motivates the use of multi-chirp integration techniques, it is important to note that in some real-time or dynamic imaging scenarios, minimizing acquisition time to reduce the impacts of movement or vibration may take precedence over maximizing SNR. Unfortunately, commercially available visible and SWIR cameras, while having integration options down to the microsecond range, often have frame rates well below 1 kHz, resulting in low duty cycle operation when utilizing short integration times.

Multi-chirp integration is particularly attractive for TH FMCW RSDH, where four measurements are required to construct a single holographic image. By recording each quadrature measurement over a separate chirp, as illustrated in Fig. 2, the system can maintain high chirp rates without sacrificing integration time. However, this approach introduces complex interference effects during hologram reconstruction, caused by phase differences between the LO and RX fields in each quadrature measurement. These misalignments are not limited exclusively to cases where the LO frequency shift f_s deviates from the range-dependent frequency shift f_R, but can also arise from target-dependent phase delays and timing offsets. These phase differences

lead to inconsistencies between quadratures, which introduces interference artifacts and intensity modulation in the reconstructed hologram as a function of both f_s and the object range. Previous work in continuous-wave systems has examined similar quadrature errors in interferometers [19] as well as phase-shifting errors in digital holography [20]. To date, the effects of such detuning for RSDH systems have received little attention despite their potential to affect hologram strength and range resolution.

In this paper, we develop a theoretical framework to analyze detuning outcomes in TH FMCW RSDH when $f_s \neq f_R$. We experimentally demonstrate that the optimal LO frequency shift for achieving the maximum holographic strength may unexpectedly differ from the predicted range-dependent value. The results also apply to non-TH FMCW RSDH systems that employ integration over multiple chirps (versus a single chirp) in order to increase the beat frequency away from low-frequency interference or when the chirp generator has issues with long chirps. The results of this paper are thus essential for optimizing both non-TH and TH FMCW RSDH systems that perform integration over multiple chirps.

2. Theory

The procedure for generating a temporal heterodyne range-selective digital hologram has been previously demonstrated [7], but a concise summary of the key steps is provided here for reference. First, the target object range is selected. Next, the predicted range-dependent frequency shift (f_R) is calculated based on the chirp parameters and the object range using Eq. (1). The LO is then shifted down in frequency by an amount $f_s \approx f_R$, which sets the hologram's beat frequency f_b to be approximately equal to f_c. Four intensity measurements are captured in rapid succession with phase shifts of the internal RF modulation of the ToF camera, enabling phase-shifting holography.

This paper focuses exclusively on TH FMCW RSDH, since single-shot off-axis FMCW RSDH and FMCW lidar share the same range resolution and exhibit expected detuning behavior when integration occurs over a single chirp. However, the results presented here generalize to other FMCW RSDH systems that integrate holograms over multiple chirps.

Although Fig. 1 shows modulation of the LO and TX fields using a single-sideband up chirp with $\kappa > 0$, both FMCW RSDH and TH FMCW RSDH can be implemented just as easily with down chirps ($\kappa < 0$) with equivalent performance. In this case, the LO frequency must be upshifted by f_s (rather than downshifted) to ensure that the interference terms beat at $f_b \approx 0$ for FMCW RSDH or at $f_b \approx f_c$ for TH FMCW RSDH when the TX field includes an additional upshift by f_c.

Double-sideband systems, in which both the upper and lower sidebands are present, offer greater flexibility in selecting the LO frequency shift. In such systems, an LO upshift of f_s results in the correct beat between the lower sidebands of the RX and LO fields, while downshifts of f_s yields the correct beat between the upper sidebands. The direction of the LO frequency shift should be carefully considered if interference between a specific sideband is significant. However, if this is not a concern, the only requirement is that $|f_s| \approx f_R$. The theoretical analysis in this paper assumes single-sideband up chirps for both the LO and TX, but the results apply equally to systems using single-sideband down chirps with the appropriate frequency shifts, or to double-sideband configurations, provided that unwanted beat frequencies, particularly those not near f_c, are filtered out by the detector's limited bandwidth during integration.

The optical fields of the LO and RX beams in a TH FMCW RSDH system, corresponding to Fig. 1 and assuming single-sideband chirps with $\kappa > 0$, where f_c and f_s are positive, can be written as follows:

$$E_{\mathrm{LO}}(x, y, t, T_n) = A_{\mathrm{LO}}(x, y) \cos(2\pi(f_L + f_0 - f_s)t + \pi\kappa(t - T_n)^2 + \phi_{\mathrm{LO}}(x, y)) \tag{2}$$

$$E_{\mathrm{RX}}(x,y,t,\tau_R,T_n) = A_{\mathrm{RX}}(x,y)\cos(2\pi(f_L+f_0+f_c)(t-\tau_R)+\pi\kappa(t-T_n-\tau_R)^2+\phi_{\mathrm{RX}}(x,y)) \quad (3)$$

where f_L is the laser frequency, $f_0 - f_s$ is the RF drive frequency of the LO acousto-optical frequency shifter (AOFS), $f_0 + f_c$ is the RF drive frequency of the TX AOFS, f_0 is the nominal RF operating frequency of the two AOFS, f_c is the internal modulation frequency of the PMD sensor array, and T_n is the start time of the n^{th} phase measurement defined as $T_n = nT$ for $n = 0$, 1, 2, 3, where $T = \tau_d + \tau_{int}$, and τ_d is the delay between integrations, as shown in Fig 2. The spatial amplitudes and phases for the LO and RX fields are defined as $A_{\mathrm{LO}}(x,y)$, $A_{\mathrm{RX}}(x,y)$, and $\phi_{\mathrm{LO}}(x,y)$ and $\phi_{\mathrm{RX}}(x,y)$, respectively. The intensity incident on the detectors will be equal to the interference between the LO and RX fields, which can be calculated as:

$$I_n(x,y,t,\tau_R,T_n) \propto \left\langle \left| E_{\mathrm{LO}}(x,y,t,T_n) + E_{\mathrm{RX}}(x,y,t,\tau_R,T_n) \right|^2 \right\rangle_{\frac{1}{BW_{det}}} \quad (4)$$

for the n^{th} phase measurement, where $\langle\cdot\rangle_{\frac{1}{BW_{det}}}$ represents the filter for high-frequency beating by the detector, or

$$\begin{aligned} I_n(x,y,t,\tau_R,T_n) \propto\ & |A_{\mathrm{LO}}(x,y)|^2 + |A_{\mathrm{RX}}(x,y)|^2 \\ & + A_{\mathrm{LO}}(x,y)A_{\mathrm{RX}}(x,y)\cos(2\pi(f_c+f_s-f_R)t+\phi_n(x,y,\tau_R,T_n)) \end{aligned} \quad (5)$$

where f_R is the range-dependent frequency shift defined in Eq. (1) and $\phi_n(x,y,\tau_R,T_n)$ is the phase term for the n^{th} quadrature given as $\phi_n(x,y,\tau_R,T_n) = \phi_{\mathrm{RX}}(x,y) - \phi_{\mathrm{LO}}(x,y) - 2\pi(f_L+f_0+f_c)\tau_R + \pi\kappa\tau_R^2 + 2\pi f_R T_n$. The phase results from the difference between the interfering fields in Eq. 2 and Eq. 3, after filtering out high-frequency components due to limited detector bandwidth. The intensity incident on the sensor array is then integrated on the PMD pixels of the ToF camera, which have internal modulation frequency f_c. Four images are captured in quick succession with phase shifts of the camera's modulation frequency of $\Phi_n = \frac{n\pi}{2}$ for the n^{th} measurement to reconstruct the hologram using phase-shifting techniques. A diagram showing both the LO and RX chirp timings, the beat frequency between the interfering chirps when $f_s \approx f_R$, and the integration timing of the ToF camera is shown in Fig. 2. The signal recorded by the ToF sensor array, $S_n(x,y)$, at coordinates (x,y) is the incident intensity for the n^{th} measurement, mixed with an internal RF signal at the detector's modulation frequency with distinct phase shifts. After integrating over τ_{int}, the four recorded signals (for $n = 0$, 1, 2, 3) are given by:

$$S_n(x,y) = \int_{T_n}^{T_n+\tau_{int}} I_n(x,y,t,\tau_R,T_n)\cos(2\pi f_c t + \Phi_n)dt \quad (6)$$

Finally, the four recordings are used to reconstruct the object field using phase-shifting holographic principles, assuming a uniform LO field.

$$E_{\mathrm{recon}}(x,y) = S_0(x,y) - S_2(x,y) + i(S_1(x,y) - S_3(x,y)) \quad (7)$$

If configured in an image-plane recording geometry, where the object is imaged onto the sensor array with a lens, the reconstructed image of the object is calculated as the magnitude square of the reconstructed field.

$$I_{\mathrm{recon}}(x,y)_{\mathrm{IP}} = |E_{\mathrm{recon}}(x,y)|^2 \quad (8)$$

When recording Fresnel holograms, the reconstructed field at the detector will be approximated by Fresnel propagation of the original field at the object [2]. In order to undo this, a quadratic phase correction is applied, and a 2-dimensional (2D) inverse Fourier transform (IFFT) is performed digitally in post-processing. The phase correction term is of the form

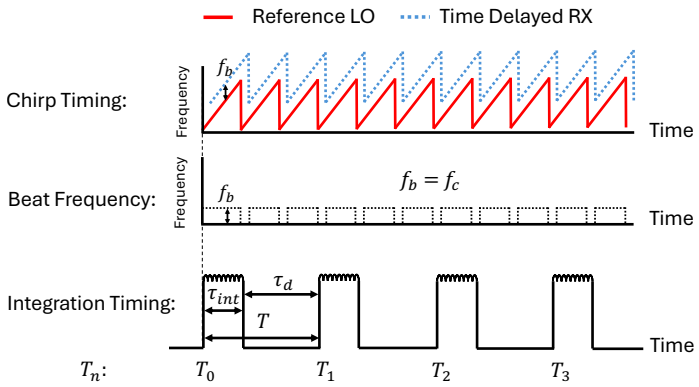


Fig. 2. Timing diagram of the LO and time delayed RX chirps (top), beat frequency between the LO and object RX fields (center). Timing of the ToF camera integration (bottom).

$$e^{-i\phi_c(x,y)} = e^{\frac{-i\pi f_L}{c}(x^2+y^2)\left(\frac{1}{z_{\text{obj}}}-\frac{1}{z_{\text{LO}}}\right)} \tag{9}$$

where z_{obj} and z_{LO} are the distances from the LO and object's effective point source locations to the detector [1]. The phase correction is necessary to eliminate parabolic phase terms introduced by Fresnel propagation, while the inverse Fourier transform (IFFT) effectively reverses the propagation, neglecting constant-amplitude scaling factors. The reconstructed image for Fresnel holograms is calculated as

$$I_{\text{recon}}(x,y)_{\text{FP}} = |\mathcal{F}^{-1}\{e^{-i\phi_c(x,y)}\tilde{E}_{\text{recon}}(x,y)\}|^2 \tag{10}$$

where $\tilde{E}_{\text{recon}}(x,y) \propto \mathcal{F}\{E_{\text{recon}}(x,y)\}$, and $\mathcal{F}$ and $\mathcal{F}^{-1}$ denote the 2D Fourier and inverse Fourier transforms, respectively, with amplitude scaling factors from Fresnel propagation ignored [1]. Changing the sign of the quadratic phase correction will reconstruct the conjugate image.

For an IP system, the wrapped phase map is obtained from the reconstructed complex field:

$$\phi_w(x,y) = \arg\big(E_{\text{recon}}(x,y)\big), \quad \phi_w \in (-\pi,\pi]. \tag{11}$$

Phase-unwrapping algorithms can then be used to recover a continuous phase profile. For FP holograms, the phase is computed in the same manner following the appropriate post-processing steps.

2.1. Detuning

When the object range is unknown, FMCW RSDH is performed by scanning through a series of LO frequency shifts, f_s, and recording holograms at each step. In most cases, no hologram is reconstructed because $f_s \neq f_R$ results in a temporally modulated hologram that is outside the bandwidth of the detector. In an off-axis image-plane FMCW RSDH system, when integrating over a single chirp, it has been shown that the image strength is maximized when $f_s = f_R$, while detuning by an added frequency shift away from f_R results in a sinc pattern for the field and a sinc^2 profile in the intensity [16]. This behavior arises from the detector's finite integration time, which effectively acts as a rectangular temporal window.

In contrast, the four recordings that comprise a single holographic image for TH FMCW RSDH are observed to interfere with one another when each is integrated over a separate chirp. As a result, the detuning behavior becomes more complex: the maximum hologram strength may occur at a frequency shift f_s that does not precisely match the range-dependent frequency shift f_R, and the resulting detuning pattern can be asymmetric. This phenomenon is analyzed in detail using a theoretical model, which is validated by experimental results presented in Section 4. The predicted intensity detuning profile for an image-plane hologram with uniform spatial amplitude is derived in Appendix A and is given as a function of f_s and f_R by:

$$I_{\text{recon}}(f_s, f_R)_{\text{IP}} \propto \text{sinc}^2((f_s - f_R)\tau_{int}) \cos^2(2\pi f_s T) \tag{12}$$

When recording Fresnel-plane holograms, the detuning behavior differs from that observed in image-plane reconstructions and depends on whether the image or conjugate image is being reconstructed. Assuming uniform spatial amplitudes, the theoretical intensity detuning profile for a Fresnel-plane hologram image and conjugate image can be expressed as functions of f_s and f_R. These expressions are derived in Appendix B and given by:

$$I_{\text{recon}}(f_s, f_R)_{\text{FP(Image)}} \propto \text{sinc}^2\left((f_s - f_R)\tau_{int}\right) \cos^2\left(2\pi f_s T\right) \cos^2\left(\pi f_s T\right) \tag{13}$$

when using a quadratic phase correction with a negative-valued exponential, or

$$I_{\text{recon}}(f_s, f_R)_{\text{FP(Conjugate)}} \propto \text{sinc}^2\left((f_s - f_R)\tau_{int}\right) \cos^2\left(2\pi f_s T\right) \sin^2\left(\pi f_s T\right) \tag{14}$$

when using a phase correction with a positive value exponential to reconstruct the conjugate image. Eq. (12) was used to fit all data recorded in an IP configuration, while Eq. (13) and Eq. (14) were used to fit all FP data. Here, $\text{sinc}(x) \equiv \frac{\sin(\pi x)}{\pi x}$.

3. Experimental Procedure

An arbitrary waveform generator (AWG) was used to create a repeating linear up-chirp with a 2 GHz bandwidth and a duration of 1 ms. An output trigger from the AWG (Tektronix AWG70002A) was used to trigger the ToF camera (Sentis M100), which features a 160 x 120 pixel detector array and operates at wavelengths from 650 to 1200 nm [21]. For all results presented, the delay between quadrature recordings was fixed at τ_d = 2 ms. A 793-nm diode laser (New Focus 6017 Vortex) was modulated with the linear chirp using a double-sideband electro-optical phase modulator (EOM) from EOSPACE. The modulated beam was then amplified with a laser amplifier (Toptica BoosTA) to increase optical power, before being split into the LO and TX paths. The LO arm was frequency shifted by f_0 using an AOFS (Crystal Technology Inc./G&H 3200) driven by a signal generator (HP E4433B). An additional offset frequency f_s was introduced by adjusting the signal generator, allowing control over the heterodyne beat frequency. The transmit path was frequency-shifted with a similar AOFS that was driven by the sum of the internal modulation frequency of the camera, f_c, and a second signal generator (TPI 1001-A) operating at a constant frequency of f_0. Both signal generators were phase-locked using a 10 MHz reference frequency to maintain phase stability. A schematic of the holographic experiment is shown in Fig. 3. The objects were constructed using retroreflective tape attached to glass plates and positioned in front of the camera at a starting distance of 65.0 cm. A frequency scan was performed by varying the additional LO frequency shift f_s around the expected range-dependent shift f_R, which was calculated using Eq. 1 based on the current target distance and adjusted to account for differences in path length. The double-sideband EOM allowed the LO to be shifted up or down by f_s, depending on whether interference with the lower or upper sideband was desired. When $|f_s| \approx f_R$, the system was tuned to reconstruct a range-selective holographic image of the object at distance R.

TH FMCW RSDH images were recorded at frequency shifts f_s, ranging from 8 to 12 kHz in 10 Hz increments, using an integration time of 1 ms. These values were chosen to span the expected range-dependent beat frequencies for the various target distances, after accounting for path length differences between the TX and the LO. After each scan, the object was repositioned 5 mm farther from the camera and the frequency scan was repeated. This process was carried out at distances of 65.0 to 75.0 cm. The same procedure was repeated to acquire FP holograms using the same object positions.

For comparison, TH CW DH recordings (i.e., without chirp modulation) were performed at a fixed object distance for IP and FP configurations. In this case, f_s was scanned from –2 kHz to 2 kHz in 10 Hz steps and repeated for integration times of 1 ms, 2 ms, and 3 ms. To streamline the data collection process, the camera recordings and the signal generator frequency shifts were automated, allowing the capture of 10 frames at each 10 Hz frequency step without manual intervention.

For IP recordings, a lens was used to form an image of the object directly onto the detector. In contrast, for FP recordings, the lens was removed and appropriate digital post-processing steps were applied to reconstruct the hologram. Although the objects in both configurations were positioned at the same physical location, their sizes differed. A smaller object was used in the FP configuration to ensure a comparable relative hologram size on the detector across both geometries. This adjustment accounts for differences in the field of view (FOV) between the IP and FP setups.

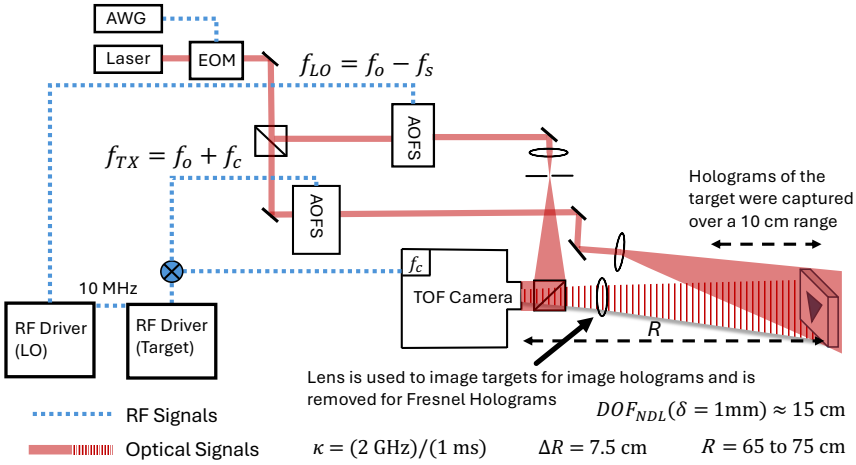


Fig. 3. Schematic of the holographic recording setup. An AWG was used to generate a 2 GHz chirp, providing a range resolution of $\Delta R = 7.5$ cm.

3.1. Hologram Strength Metric

To quantify the hologram strength as a function of the added frequency shift f_s, we define a simple image domain strength metric. This metric computes the difference between the average pixel intensity in a region of interest (ROI) where the hologram is expected to appear and subtracts the average pixel intensity value of a background region, where no holographic signal is expected. This process is illustrated in Fig. 4. For all results presented in this paper, 10 frames were acquired and incoherently averaged at each frequency step prior to computing the strength metric for a given object distance. The strength metric is given by:

$$\text{Strength Metric} = \text{mean}(\text{Region of Interest}) - \text{mean}(\text{Background Region}) \tag{15}$$

The ROI and background region were selected to contain approximately the same number of pixels.

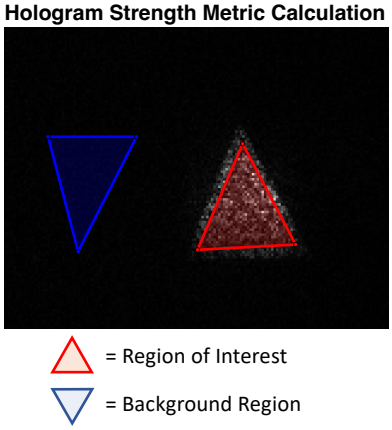


Fig. 4. Hologram strength metric calculated from the average of 10 shots. The red triangle indicates the ROI where the average pixel value was computed for the hologram, while the light blue area denotes the region used for background pixel value computation. The region of interest was reduced in size compared to the hologram to minimize potential edge effects. The hologram is plotted in a linear scale. The ROI differed between recording geometries due to the use of different targets.

3.2. Fits

Least-squares fitting was used to compare the experimental strength metrics with the developed detuning patterns. For IP data, Eq. (12) was applied, while FP data was fit using either Eq. (13) or Eq. (14), depending on whether the image or the conjugate image was reconstructed. To more accurately reflect experimental conditions, the theoretical detuning curves were convolved with a Lorentzian function to account for the system's finite frequency resolution and phase noise.

4. Experimental Results

4.1. TH CW DH Results

Data was collected using a TH CW DH setup without FMCW chirp modulation, with integration times of 1 ms, 2 ms, and 3 ms. This configuration was used to evaluate the theoretical predictions under the condition $f_R = 0$. As shown in Fig. 5, the experimental results closely match the theoretical model for all three integration times and for both IP and FP recording geometries, with each data point representing the average of 10 measurements per frequency step, and error bars indicating the standard deviation of the computed strength metric between shots. The results show a characteristic sinc^2 envelope whose width is inversely proportional to the integration time, with a full-width half-maximum (FWHM) of approximately $1/\tau_{int}$. In contrast, the narrower frequency features have an FWHM proportional to $1/4T$, where $4T$ represents the total duration required to acquire all four phase-shifted images.

An alternative method to calculate the detuning pattern for images recorded in a FP configuration (when $f_R = 0$) is to take the Fourier transform of the temporal integration window shown in Fig. 2, since the frequency resolution is determined by the shape and duration of the integration period.

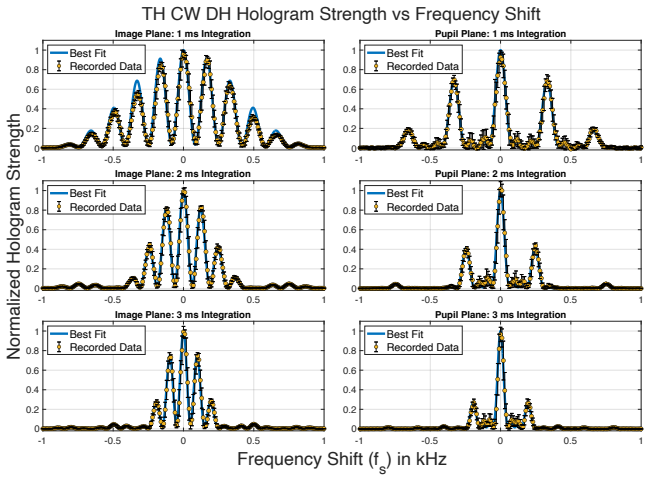


Fig. 5. TH CW DH hologram strength as a function of frequency shift, f_s. IP results are shown in the left column for integration times of 1, 2, and 3 ms. FP results are shown in the right column for the same integration times. All holograms peak at the expected value of $f_s = 0$. The normalized hologram strength is computed using an average of 10 shots and Eq. (15). The frequency plots were then fit to theory and normalized.

4.2. TH FMCW RSDH Results

When modulated with the linear chirp, the center value of the sinc^2 envelope shifts towards the expected value of f_R for a object distance R, in accordance to theory. Interestingly, there are locations where the detuning pattern is asymmetric and the maximum hologram strength does not occur at the expected value of f_R, which is in the center of the sinc^2 envelope. The test was conducted with a 1 ms integration time per quadrature recording that matched the chirp duration. Objects were imaged over a 10 cm range, but only the results from three object positions are shown due to the cyclical nature of the data. Fig. 6 shows the detuning results for an object at 65.0, 66.0, and 67.0 cm with a positional uncertainty of ±0.15 cm which corresponds to a round-trip uncertainty of ±0.30 cm. The expected range-dependent frequency shift for a 1.0 cm displacement is approximately 133 Hz. The accuracy of the chirp rate was confirmed by comparing the range-dependent beats obtained from each fit at different target distances with the expected values. The calculated chirp rate matched the programmed value within the uncertainty of the object distances. The experimental data in Fig. 6 represent the average of 10 measurements for each frequency step. The error bars are computed by taking the standard deviation of the computed strength metric between shots. The range-dependent beat frequencies for the three IP object distances were calculated from the fit parameters as 10.005 ± 0.010 kHz, 10.101 ± 0.013 kHz, and 10.229 ± 0.016 kHz. The corresponding displacements, calculated from the difference between adjacent frequencies using Eq. 1, were 0.72 ± 0.12 cm and 0.96 ± 0.15 cm. Similarly, FP frequencies were calculated as 9.970 ± 0.098 kHz, 10.080 ± 0.078 kHz, and 10.201 ± 0.078 kHz, corresponding to displacements of 0.83 ± 0.94 cm and 0.91 ± 0.83 cm. The range-dependent beats calculated from the fits are shown as vertical dotted lines in Fig. 6. The beats show how the reconstructed hologram strength can be at a null even when $f_s = f_R$. The measured displacements fell within the uncertainty of the target positions in all trials. The notably higher uncertainty in the FP fit parameters compared to the IP parameters is likely due to the significantly lower signal strength in the FP measurements, which results from the smaller aperture size of the ToF detector compared to the larger focusing lens used in the IP geometry. Additionally, the slight discrepancy between the IP and FP beat frequencies is attributed to the different targets

used in each recording geometry.

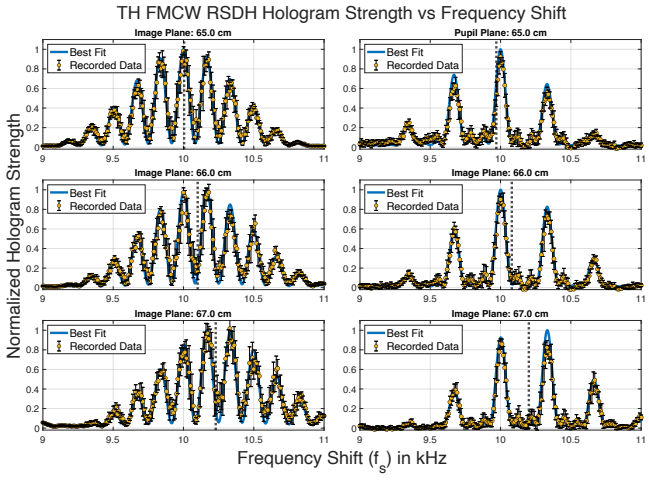


Fig. 6. Detuning patterns for TH FMCW RSDH. The left column displays results for a single object placed at distances of 65.0 cm, 66.0 cm, and 67.0 cm, recorded using an IP geometry. The right column shows the same object distances, but for FP holograms. The dotted vertical line in each plot indicates the value of f_R calculated from the fit. The peak hologram strength often occurs when $f_s \neq f_R$.

4.3. Two objects within the range resolution of the system

An additional experiment was performed in which two objects, spaced within the system's range resolution, were imaged to investigate whether resolution improvements could be achieved by leveraging the higher-frequency grating terms. The two objects were positioned approximately 5 mm apart, which was chosen because if the higher frequency grating shifted with range, it would form a null for one of the objects and a peak for the other. However, consistent with the developed theory, the zeros of the detuning patterns occur at the same frequency shift for both objects. Only the sinc^2 envelope moves as a function of range.

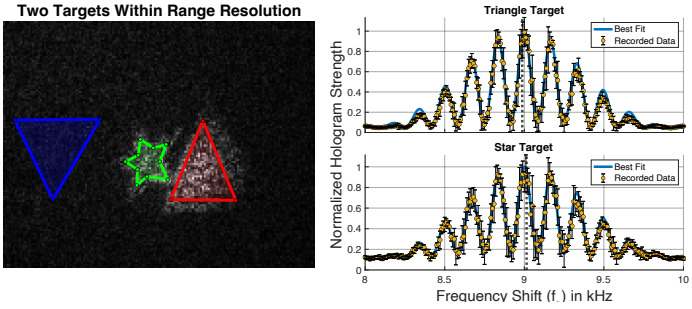


Fig. 7. Detuning plots for two objects within the range resolution of the system in an image-plane configuration. The triangle target was located closer to the detector than the star target. The objects were separated by approximately 5 mm.

4.4. Conjugate Image

For Fresnel-plane holograms, the conjugate image can be computed in one of two ways. First, the conjugate of Eq. (7) can be taken by reversing the sign of the imaginary components, as shown in Eq. (16):

$$E^*_{\text{recon}}(x, y) = S_0(x, y) - S_2(x, y) - i(S_1(x, y) - S_3(x, y)) \tag{16}$$

Alternatively, the sign of the quadratic phase correction can be reversed in Eq. (9). Fig. 8 illustrates the detuning results for the same target after applying different quadratic phase corrections to the TH FMCW RSDH Fresnel-plane data. The results show how the holographic strength metric is maximized for the image data at a frequency null of the conjugate image, and vice versa. This indicates that the image and the conjugate image will reach maximum strength at different frequency shifts of f_s for the same object. Phase maps of the image and its conjugate reveal a speckled target, where coherent scattering produces strong interference patterns in the phase data. These patterns cause the wrapped phase to vary rapidly and appear nearly random, which in turn complicates phase unwrapping.

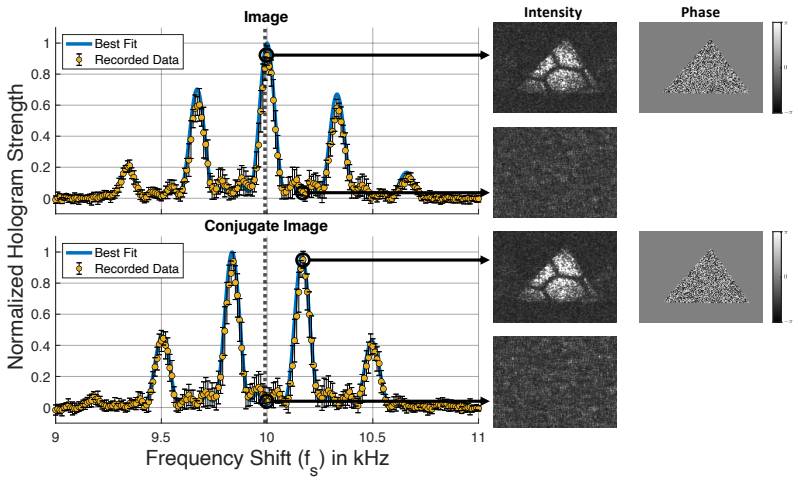


Fig. 8. Fresnel-plane TH FMCW RSDH hologram strength as a function of f_s for a single target. Detuning scans using the phase correction defined in Eq. (9) (Top Left). Detuning scans of the same data but processed with the conjugate of Eq. (9) (Bottom left). Eq. (13) was used to fit the image data while Eq. (14) was used to fit the conjugate data. The center column shows holograms at the maximum and minimum (first null) strength for both image and conjugate image processing. The hologram figures are the incoherent average of 10 shots and are plotted in the same linear scale. The right column shows the phase of the reconstructed field from a single frame for both the image and conjugate image.

5. Conclusion

In conclusion, we have developed a mathematical framework for the range resolution and detuning patterns of TH FMCW RSDH and TH CW DH. Theoretical predictions were found to be consistent with the experimental results for both IP and FP recording geometries. Our analysis reveals the presence of a high-frequency grating pattern that defines the FWHM of the central peak as $1/4T$. However, since this pattern is independent of f_R, the narrower peak does

not contribute to improved object selectivity, which is determined by the chirp bandwidth and the sinc^2 envelope.

The analysis also informs the design of multi-chirp RSDH systems for improved SNR and signal recovery by adjusting f_s near f_R, aligned with the closest peak in the detuning profiles rather than f_R exactly. The maximum hologram strength occurs at discrete frequency shifts given by $f_s = m/(2T)$ for IP recordings, $f_s = m/T$ for FP image recordings, and $f_s = (2m+1)/(2T)$ for FP conjugate image recordings, where $m \in \mathbb{Z}$, with the additional practical constraint that $|f_s - f_R|$ must be within the detector bandwidth. This strategy also applies to FMCW RSDH systems that integrate multiple chirps without temporal heterodyning. In general, the framework provides practical guidance for selecting the optimal LO frequency shift to maximize holographic reconstruction and improve signal recovery in multi-chirp holographic systems.

Funding. Office of Naval Research (N00014-20-1-2260)

Acknowledgments. We gratefully acknowledge funding from the Office of Naval Research. This work relates to Department of Navy award N00014-20-1-2260 issued by the Office of Naval Research. The United States Government has a royalty-free license throughout the world in all copyrightable material contained herein. Any opinions, findings, and conclusions or recommendations expressed in this material are those of the author(s) and do not necessarily reflect the views of the Office of Naval Research.

Disclosures. The authors declare no conflicts of interest.

Data Availability. Data underlying the results presented in this paper are not publicly available at this time but may be obtained from the authors upon reasonable request.

A. Image-plane Detuning Formulation

Starting with Eq. (6), we introduce a substitution defined as

$$t' = t - \left(T_n + \frac{\tau_{int}}{2}\right) \quad \Rightarrow \quad t = t' + T_n + \frac{\tau_{int}}{2} \tag{17}$$

This change in variable centers the integral around $t' = 0$, simplifying the integration process. The amplitude of the LO field is also assumed to be uniform.

$$S_n(x,y) = A_{\mathrm{LO}} A_{\mathrm{RX}}(x,y) \int_{-\frac{\tau_{int}}{2}}^{\frac{\tau_{int}}{2}} \cos(2\pi(f_c + f_s - f_R)(t' + T_n + \frac{\tau_{int}}{2}) + \phi_n(x,y,\tau_R,T_n)) \\ * \cos(2\pi f_c(t' + T_n + \frac{\tau_{int}}{2}) + \Phi_n)dt' \tag{18}$$

The integrand can be simplified and combined into a single term using the cosine identity $\cos(A)\cos(B) = \frac{1}{2}[\cos(A-B) + \cos(A+B)]$ where only the difference frequency will be considered because of bandwidth limitations of the detector. After filtering out bandwidth-limited terms,

$$S_n(x,y) = \frac{A_{\mathrm{LO}} A_{\mathrm{RX}}(x,y)}{2} \int_{-\frac{\tau_{int}}{2}}^{\frac{\tau_{int}}{2}} \cos(2\pi(f_s - f_R)t' + 2\pi(f_s - f_R)(T_n + \frac{\tau_{int}}{2}) \\ + \phi_n(x,y,\tau_R,T_n) - \Phi_n)dt' \tag{19}$$

Substituting $\phi_n(x,y,\tau_R,T_n)$ back in,

$$S_n(x,y) = \frac{A_{\mathrm{LO}} A_{\mathrm{RX}}(x,y)}{2} \int_{-\frac{\tau_{int}}{2}}^{\frac{\tau_{int}}{2}} \cos(2\pi(f_s - f_R)t' + 2\pi f_s T_n + \pi(f_s - f_R)\tau_{int} + \pi\kappa\tau_R^2 \\ - 2\pi(f_L + f_0 + f_c)\tau_R + \phi_{\mathrm{RX}}(x,y) - \phi_{\mathrm{LO}}(x,y) - \Phi_n)dt' \tag{20}$$

The integrand can be separated into its dependent and independent components using an additional cosine identity $\cos(A+B) = \cos(A)\cos(B) - \sin(A)\sin(B)$. Once again, the odd terms are ignored since they will integrate to zero.

$$S_n(x,y) = \frac{A_{\mathrm{LO}} A_{\mathrm{RX}}(x,y)}{2} \int_{-\frac{\tau_{int}}{2}}^{\frac{\tau_{int}}{2}} \cos(2\pi(f_s - f_R))t' \cos(2\pi f_s T_n + \pi(f_s - f_R)\tau_{int} \\ + \pi\kappa\tau_R^2 - 2\pi(f_L + f_0 + f_c)\tau_R + \phi_{\mathrm{RX}}(x,y) - \phi_{\mathrm{LO}}(x,y) - \Phi_n)dt' \tag{21}$$

The signal strength for the n^{th} recordings can be calculated as,

$$S_n(x,y) = \frac{A_{\mathrm{LO}} A_{\mathrm{RX}}(x,y)}{2} \left[\mathrm{sinc}\left((f_s - f_R)\tau_{int}\right) \cos(2\pi f_s T_n + \frac{2\pi(f_s - f_R)\tau_{int}}{2} \right. \\ \left. + \pi\kappa\tau_R^2 - 2\pi(f_L + f_0 + f_c)\tau_R + \phi_{\mathrm{RX}}(x,y) - \phi_{\mathrm{LO}}(x,y) - \Phi_n) \right] \tag{22}$$

Next, letting $\phi_{xy} = \pi\kappa\tau_R^2 - 2\pi(f_L + f_0 + f_c)\tau_R + \phi_{\mathrm{RX}}(x,y) - \phi_{\mathrm{LO}}(x,y)$, and evaluating Eq. (22) for n = 0, 1, 2, 3 results in the following four recorded signals.

$$S_0(x,y) = \frac{A_{\mathrm{LO}}A_{\mathrm{RX}}(x,y)}{2}\left[\mathrm{sinc}((f_s - f_R)\tau_{\mathrm{int}})\cos\left(\frac{2\pi(f_s - f_R)\tau_{\mathrm{int}}}{2} + \phi_{xy}\right)\right] \tag{23}$$

$$S_1(x,y) = \frac{A_{\mathrm{LO}}A_{\mathrm{RX}}(x,y)}{2}\left[\mathrm{sinc}((f_s - f_R)\tau_{\mathrm{int}})\sin\left(\frac{2\pi(f_s - f_R)\tau_{\mathrm{int}}}{2} + 2\pi f_s T_1 + \phi_{xy}\right)\right] \tag{24}$$

$$S_2(x,y) = \frac{-A_{\mathrm{LO}}A_{\mathrm{RX}}(x,y)}{2}\left[\mathrm{sinc}((f_s - f_R)\tau_{\mathrm{int}})\cos\left(\frac{2\pi(f_s - f_R)\tau_{\mathrm{int}}}{2} + 2\pi f_s T_2 + \phi_{xy}\right)\right] \tag{25}$$

$$S_3(x,y) = \frac{-A_{\mathrm{LO}}A_{\mathrm{RX}}(x,y)}{2}\left[\mathrm{sinc}((f_s - f_R)\tau_{\mathrm{int}})\sin\left(\frac{2\pi(f_s - f_R)\tau_{\mathrm{int}}}{2} + 2\pi f_s T_3 + \phi_{xy}\right)\right] \tag{26}$$

$S_0(x,y)$ and $S_2(x,y)$ are combined using the identity

$$\cos(A) + \cos(B) = 2\cos\left(\frac{A-B}{2}\right)\cos\left(\frac{A+B}{2}\right) \tag{27}$$

resulting in

$$S_0(x,y) - S_2(x,y) = A_{\mathrm{LO}}A_{\mathrm{RX}}(x,y)\left[\mathrm{sinc}\left((f_s - f_R)\tau_{int}\right)\right] * \left[\cos(2\pi f_s T)\right]\cos(2\pi f_s T + \frac{2\pi(f_s - f_R)\tau_{int}}{2} + \phi_{xy}) \tag{28}$$

The difference between $S_1(x,y)$ and $S_3(x,y)$ can be calculated similarly from the identity,

$$\sin(A) + \sin(B) = 2\cos\left(\frac{A-B}{2}\right)\sin\left(\frac{A+B}{2}\right) \tag{29}$$

resulting in,

$$S_1(x,y) - S_3(x,y) = A_{\mathrm{LO}}A_{\mathrm{RX}}(x,y)\left[\mathrm{sinc}\left((f_s - f_R)\tau_{int}\right)\right] * \left[\cos(2\pi f_s T)\right]\sin\left(4\pi f_s T + \frac{2\pi(f_s - f_R)\tau_{int}}{2} + \phi_{xy}\right) \tag{30}$$

Finally, an expression for $E_{recon}(x,y)$ can be computed by combining both of these equations and multiplying $S_1(x,y) - S_3(x,y)$ by i as shown in equation 7.

$$E_{\mathrm{recon}}(x,y) = A_{\mathrm{LO}}A_{\mathrm{RX}}(x,y)\left[\mathrm{sinc}\left((f_s - f_R)\tau_{int}\right)\right]\left[\cos(2\pi f_s T)\right] * \left[\cos(2\pi f_s T + \frac{2\pi(f_s - f_R)\tau_{int}}{2} + \phi_{xy}) + i\sin(4\pi f_s T + \frac{2\pi(f_s - f_R)\tau_{int}}{2} + \phi_{xy})\right] \tag{31}$$

Since the predominant factor of ϕ_{xy} will be the spatial phase variations of the speckled object, an expression for the hologram strength as a function of only f_s and f_R can be calculated by averaging over ϕ_{xy} which represents an average hologram strength over many pixels which have uniform amplitude for both A_{LO} and $A_{\mathrm{RX}}(x,y)$. The magnitude squared of Eq. (31) when averaged over ϕ_{xy}, ignoring the amplitude conversion factors, is given as

$$I_{\mathrm{recon}}(f_s, f_R)_{\mathrm{IP}} = \left\langle |E_{recon}(x,y)|^2 \right\rangle_{\phi_{xy}} \propto \mathrm{sinc}^2((f_s - f_R)\tau_{int})\cos^2(2\pi f_s T) \tag{32}$$

B. Fresnel-plane Detuning Formulation

When recording Fresnel holograms, the reconstructed field at the detector is approximated by Fresnel propagation of the original field at the object to the detector plane [2]. To get back to an approximation of the reconstructed field at the object, ignoring the amplitude scaling factors, a phase correction is applied, and a 2D IFFT is performed digitally. The phase correction applied is given by Eq. (9) and is selected to correct for propagation, as well as curvature differences between the LO field and propagated field wave fronts. The sign of the phase correction will cause either the image or the conjugate image to become prominent, while blurring the other.

Consider a modified version of Eq. (31) recorded in a Fresnel-plane geometry such that $\tilde{E}_{\text{recon}}(x, y)$ is reconstructed.

$$\tilde{E}_{\text{recon}}(x, y) = A_{\text{LO}} A_{\text{RX}}(x, y)\left[\text{sinc}\left((f_s - f_R)\tau_{int}\right)\right]\left[\cos(2\pi f_s T)\right] * \left[\cos(2\pi f_s T + \frac{2\pi(f_s - f_R)\tau_{int}}{2} + \phi_{xy}) + i\sin(4\pi f_s T + \frac{2\pi(f_s - f_R)\tau_{int}}{2} + \phi_{xy})\right] \quad (33)$$

Starting with Eq. (33), and letting $C = A_{\text{LO}} A_{\text{RX}}(x, y)\left[\text{sinc}\left((f_s - f_R)\tau_{int}\right)\right]\left[\cos(2\pi f_s T)\right]$ and defining the new variables, $\xi = 2\pi f_s T + \frac{2\pi(f_s - f_R)\tau_{int}}{2} + \phi_{xy}$ and $\gamma = 4\pi f_s T + \frac{2\pi(f_s - f_R)\tau_{int}}{2} + \phi_{xy}$, allows for the following simplification since $\xi = \gamma + 2\pi f_s T$.

$$\tilde{E}_{\text{recon}}(x, y) = C\left(\cos(\xi) + i\sin(\gamma)\right) = \frac{C}{2}\left(e^{-i\xi} + e^{i\xi} + e^{i(\xi + 2\pi f_s T)} - e^{-i(\xi + 2\pi f_s T)}\right) \quad (34)$$

$$= \frac{C}{2}\left(e^{-i\xi} + e^{i\xi} + e^{i\xi} e^{i2\pi f_s T} - e^{-i\xi} e^{-i2\pi f_s T}\right) \quad (35)$$

$$= \frac{C}{2}\left(e^{i\xi}\left[1 + e^{i2\pi f_s T}\right] + e^{-i\xi}\left[1 - e^{-i2\pi f_s T}\right]\right) \quad (36)$$

$$= \frac{C}{2}\left(e^{i\xi} e^{\frac{i2\pi f_s T}{2}}\left(e^{\frac{-i2\pi f_s T}{2}} + e^{\frac{i2\pi f_s T}{2}}\right) + e^{-i\xi} e^{\frac{-i2\pi f_s T}{2}}\left(e^{\frac{i2\pi f_s T}{2}} - e^{\frac{-i2\pi f_s T}{2}}\right)\right) \quad (37)$$

$$= C\left(\cos\left(\frac{2\pi f_s T}{2}\right) e^{i\phi_{xy}} e^{i\phi_{fs}} + i\sin\left(\frac{2\pi f_s T}{2}\right) e^{-i\phi_{xy}} e^{-i\phi_{fs}}\right) \quad (38)$$

where $e^{i\phi_{fs}} = e^{i\left(\frac{2\pi f_s T}{2} + \frac{2\pi(f_s - f_R)}{2} + 2\pi f_s T\right)}$ is a temporal phase with no x-y dependency. Referencing Eq. (10), an expression for the intensity can be be computed by applying the quadratic phase correction and applying a spatial inverse 2D Fourier transform. Once again, assuming uniform amplitude for both A_{LO} and $A_{\text{RX}}(x, y)$, the Fourier transform will only act upon the spatial phase terms (in both the quadratic phase correction as well as the phase curvature term from propagation). The following expression can then be obtained for the intensity,

$$I_{\text{recon}}(f_s, f_R)_{\text{FP}} = \left\langle \left| \mathcal{F}^{-1}\left\{ e^{-i\phi_c(x,y)} \tilde{E}_{\text{recon}}(x, y) \right\} \right|^2 \right\rangle_{\phi_{xy}} \propto \left\langle \left| C\left(\cos\left(\frac{2\pi f_s T}{2}\right) e^{i(\phi_{xy} - \phi_c(x,y) + \phi_{fs})} + i\sin\left(\frac{2\pi f_s T}{2}\right) e^{-i(\phi_{xy} + \phi_c(x,y) - \phi_{fs})}\right) \right|^2 \right\rangle_{\phi_{xy}} \quad (39)$$

When the phase correction, $e^{-i\phi_c(x,y)}$, is correctly adjusted to be opposite to the curvature of $e^{i\phi_{xy}}$, the phase factor in the cosine term simplifies to a constant (i.e., becomes independent of

ϕ_{xy}), so it remains after averaging the random spatial phase variations. In contrast, the sine term retains an (x,y) dependent phase term, which fluctuates randomly and averages out. As a result, the cosine term dominates, while the sine term is suppressed.

If instead the phase correction is applied with the opposite sign, i.e. $e^{i\phi_c(x,y)}$, then the sine term becomes independent of ϕ_{xy} and survives the averaging, while the cosine term is averaged out, which results in the sine term dominating the reconstruction. Therefore, the sign of the phase correction determines whether the image or the conjugate image term survives after averaging. The resulting detuning behavior corresponds to Eq. (40) (image reconstruction in which the cosine survives) or Eq. (41) (conjugate image where the sine survives), depending on the phase correction used.

$$I_{\text{recon}}(f_s, f_R)_{\text{FP(Image)}} \propto \text{sinc}^2\left((f_s - f_R)\tau_{int}\right)\cos^2\left(2\pi f_s T\right)\cos^2\left(\pi f_s T\right) \tag{40}$$

$$I_{\text{recon}}(f_s, f_R)_{\text{FP(Conjugate)}} \propto \text{sinc}^2\left((f_s - f_R)\tau_{int}\right)\cos^2\left(2\pi f_s T\right)\sin^2\left(\pi f_s T\right) \tag{41}$$

References

1. T.-C. Poon and J.-P. Liu, *Introduction to Modern Digital Holography: With Matlab* (Cambridge University Press, 2014).
2. J. W. Goodman, *Introduction to Fourier Optics* (W. H. Freeman, 2017), hardcover ed.
3. I. Yamaguchi and T. Zhang, "Phase-shifting digital holography." Opt. letters **22 16**, 1268–70 (1997).
4. U. Schnars and W. P. O. Jüptner, "Digital recording and numerical reconstruction of holograms," Meas. Sci. Technol. **13**, R85 (2002).
5. E. Cuche, P. Marquet, and C. Depeursinge, "Spatial filtering for zero-order and twin-image elimination in digital off-axis holography," Appl. Opt. **39**, 4070–4075 (2000).
6. R. Galloway, "Coherent imaging via temporal heterodyne and spatial shearing methods," Master's thesis, Montana State University (2018).
7. C. Hammond, W. R. Babbitt, and R. K. Mohan, "Range selective phase-shifting frequency-modulated digital holography with temporal-heterodyning," Appl. Opt. **62**, D157–D162 (2023).
8. L. Yu and M. K. Kim, "Wavelength-scanning digital interference holography for tomographic three-dimensional imaging by use of the angular spectrum method," Opt. Lett. **30**, 2092–2094 (2005).
9. A. Wada, M. Kato, and Y. Ishii, "Multiple-wavelength digital holographic interferometry using tunable laser diodes," Appl. Opt. **47**, 2053–2060 (2008).
10. M. Yokota, T. Ishikawa, and N. Aoki, "Polarization analysis of the object wave using fmcw-digital holography," in *Optical Metrology,* (2019).
11. L. Cuellar, S. Shakir, D. Voelz, *et al.*, "Digital holography three-dimensional imaging using frequency chirping of a laser," (2020), p. 16.
12. W. Atsushi and M. Yoko, "Wavelength scanning digital holography using temporal fourier transform," 2015 14th Workshop on Inf. Opt. (WIO) (2015).
13. B. W. Krause, B. G. Tiemann, and P. Gatt, "Motion compensated frequency modulated continuous wave 3d coherent imaging ladar with scannerless architecture," Appl. Opt. **51**, 8745–8761 (2012).
14. S. Crouch, B. M. Kaylor, Z. W. Barber, and R. R. Reibel, "Three dimensional digital holographic aperture synthesis," Opt. Express **23**, 23811–23816 (2015).
15. J. Skirnewskaja, Y. Montelongo, P. Wilkes, and T. Wilkinson, "Lidar-derived digital holograms for automotive head-up displays," Opt. Express **29**, 13681–13695 (2021).
16. M. A. Goodman, R. K. Mohan, and W. R. Babbitt, "Range selective digital holographic imaging using fmcw lidar," Appl. Opt. **61**, B255–B261 (2022).
17. H. Hamada, V. Kumar, and M. Yokota, "Spatiotemporal heterodyne multiplexing in digital holography for realizing broad recordable bandwidth," Opt. Lett. **50**, 2808–2811 (2025).
18. J. Zheng, "Optical frequency-modulated continuous-wave interferometers," Appl. Opt. **45** (2006).
19. P. L. M. Heydemann, "Determination and correction of quadrature fringe measurement errors in interferometers," Appl. Opt. **20**, 3382–3384 (1981).
20. C.-S. Guo, L. Zhang, H.-T. Wang, *et al.*, "Phase-shifting error and its elimination in phase-shifting digital holography," Opt. Lett. **27**, 1687–1689 (2002).
21. K. Uno, L.-J. Burtz, M. HULCELLE, and K. YOSHIDA, "Qualification of a time-of-flight camera as a hazard detection and avoidance sensor for a moon exploration microrover," Trans. Jpn. Soc. for Aeronaut. Space Sci. Aerosp. Technol. Jpn. **16**, 619–627 (2018).

Additional Material

Additional material relating to the detuning analysis of multi-chirp integration which was not included in the publications is discussed in the following section. Key results from the publication are summarized to emphasize the contributions to the field. Figure 30 illustrates the timing of the four quadrature recordings used in temporal-heterodyne digital holography with a ToF detector.

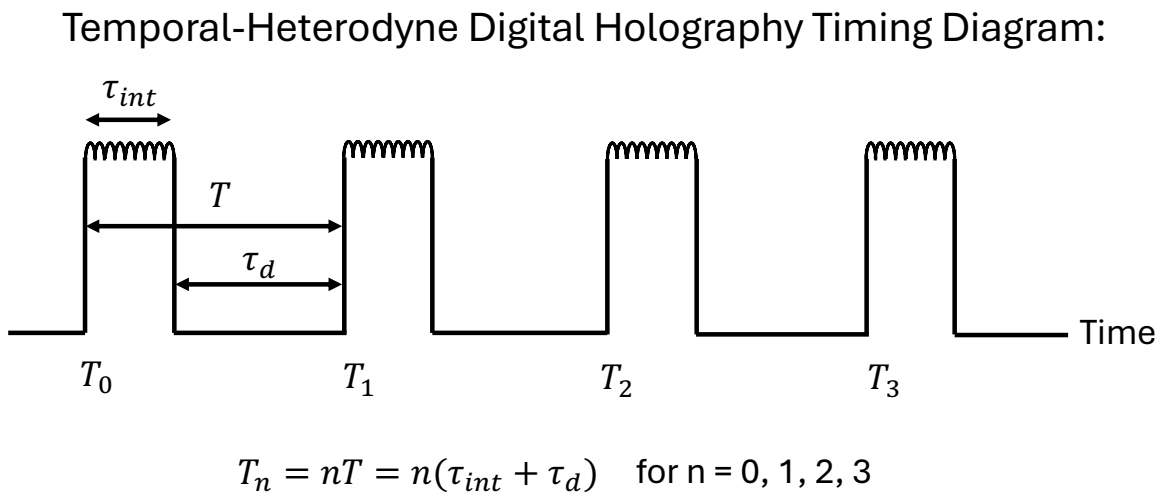


Figure 30: Timing diagram of the four recordings required for temporal-heterodyne RSDH.

It was found that the maximum hologram strength in image-plane recording geometries occurs at discrete frequency shifts given by

$$f_s = \frac{m}{2T}, \tag{74}$$

while in pupil-plane geometries the maxima appear at

$$f_s = \frac{m}{T} \quad \text{(image)}, \qquad f_s = \frac{2m+1}{2T} \quad \text{(conjugate image)}, \tag{75}$$

with $m \in \mathbb{Z}$. An additional constraint is that the detuning $|f_s - f_R|$ must remain within the detector bandwidth. Figure 31 illustrates these results, showing the peak frequencies as red dots, the high-frequency terms in blue, and the sinc^2 envelope in orange for both image-plane and pupil-plane temporal heterodyne digital holographic recording for a hypothetical target with range-dependent beat of $f_R = 3900$ Hz. The final detuning profile is the product of the high-frequency grating with the sinc^2 envelope.

Simulation Results

While the detuning profiles in the publication were derived analytically, the same results can be reproduced by numerically simulating the integrated signal and averaging over multiple pixels:

$$S_n(f_s) = \frac{1}{N_{\text{pix}}} \sum_{\text{pixels}} \int_{T_n}^{T_n+\tau_{\text{int}}} I_n(t, \tau_R, T_n) \cos(2\pi f_c t + \Phi_n)\, dt \tag{76}$$

Here,

$$I_n(t, \tau_R, T_n) = \cos\big(2\pi(f_c + f_s - f_R)t + \phi_n(\tau_R, T_n)\big) \tag{77}$$

represents the local intensity at a single pixel, with a random phase $\phi_n(\tau_R, T_n)$. The modulation phase is $\Phi_n = \frac{n\pi}{2}$ for $n = 0, 1, 2, 3$. Averaging over pixels recovers the expected analytical detuning profile.

Image-Plane Simulation Results The integrated signal in Eq. 76 can be computed for multiple pixels, each with a random phase $\phi_n(\tau_R, T_n)$. While the single-pixel signal fluctuates due to the random phase, averaging over multiple pixels reproduces the smooth detuning profile predicted analytically. Figure 32 shows the evolution of the simulated spectrum as the number of pixels included in the average is increased, illustrating convergence to the expected analytical envelope.

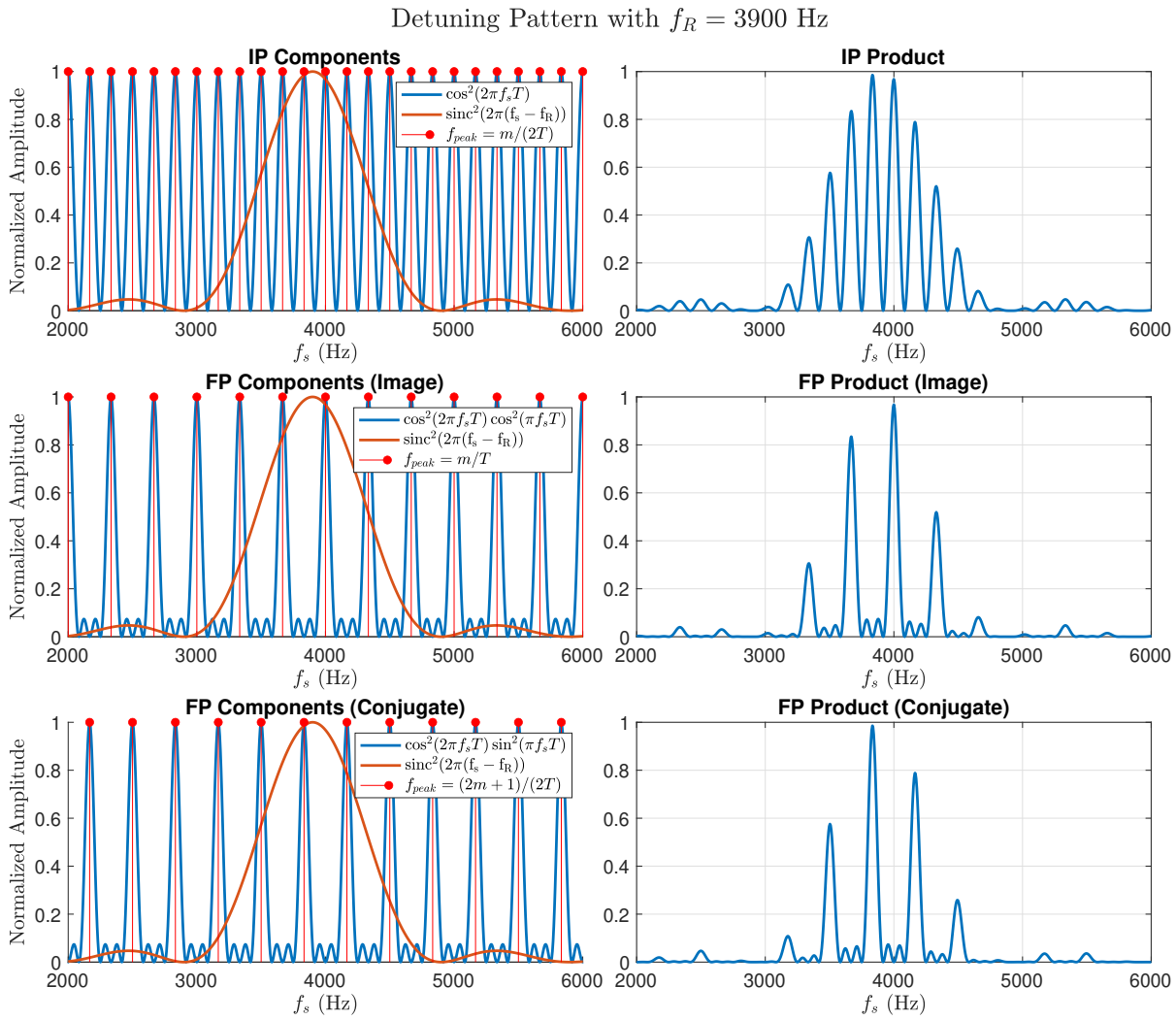


Figure 31: Individual components that make up the detuning profiles for image-plane, pupil-plane image, and pupil-plane conjugate image temporal-heterodyne RSDH (top left, middle left, and bottom left). The observed detuning profiles for the subsequent geometries which are the product of all components (top right, middle right, and bottom right).

Figure 32 shows the evolution of the simulated spectrum as the number of averaged pixels is increased. Each subplot corresponds to a different number of pixels, illustrating how the random phase contributions are progressively averaged out. This demonstrates that the image-plane simulation reproduces the analytical detuning profiles once sufficient averaging over independent pixel phases is performed.

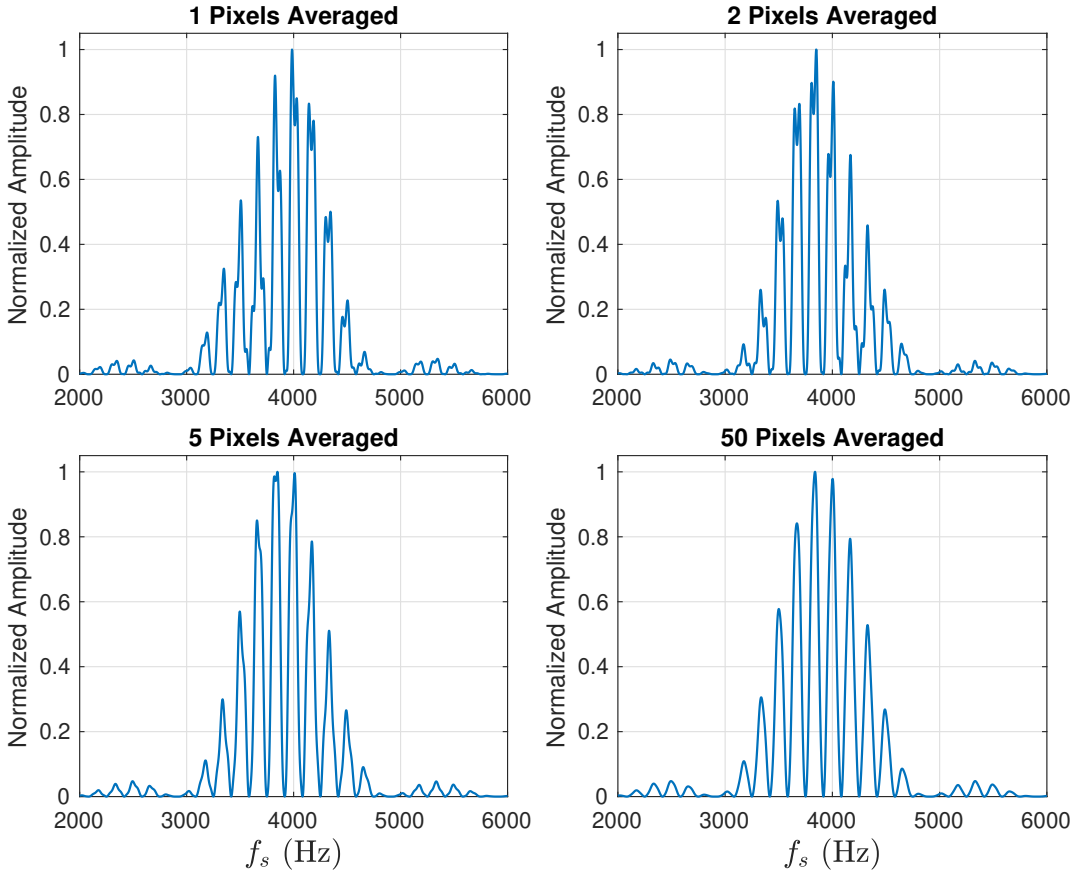


Figure 32: Image-plane simulation results showing the effect of averaging over increasing numbers of pixels. The top subplot corresponds to a single pixel (highly fluctuating), and subsequent subplots show averages over more pixels, with the bottom subplot demonstrating convergence to the analytical detuning profile.

Pupil-Plane Simulation Results In pupil-plane reconstruction, either the image or the conjugate image is brought into focus while the other remains blurred. If we are only

interested in the detuning pattern for the image that is brought into focus via the quadratic phase correction and inverse Fourier transform (which undoes the effects of propagation), the blurred conjugate can be ignored. Because only one of the two images is reconstructed at a time, the negative-frequency component of a real cosine is physically irrelevant in this geometry. Conversely, if the conjugate image were reconstructed instead, the positive-frequency component would be irrelevant. This justifies modeling the pupil-plane integrand using only the positive-frequency analytic signal, as shown in Eq. 76.

The pupil-plane integral can therefore be expressed as

$$S_n(f_s) = \frac{1}{N_{\text{pix}}} \sum_{\text{pixels}} \int_{T_n}^{T_n+\tau_{\text{int}}} e^{i\left(2\pi(f_c+f_s-f_R)t+\phi_n(\tau_R,T_n)\right)}\, dt, \tag{78}$$

where $\phi_n(\tau_R, T_n)$ represents the random phase at a single pixel. Since the negative-frequency component of a real cosine corresponds to the conjugate image, which is not reconstructed, integrating the positive-frequency analytic signal is sufficient to reproduce the expected detuning profile. Consequently, averaging over multiple pixels is actually unnecessary in this geometry.

Figure 33 illustrates this point by showing that the detuning pattern computed from a single pupil-plane pixel already matches the analytical detuning envelope, demonstrating that the pupil-plane measurement directly captures the coherent field response.

If, instead, the detuning pattern for the conjugate image were to be simulated, this could be achieved by changing the sign of the integrand to select the negative-frequency components corresponding to the conjugate image.

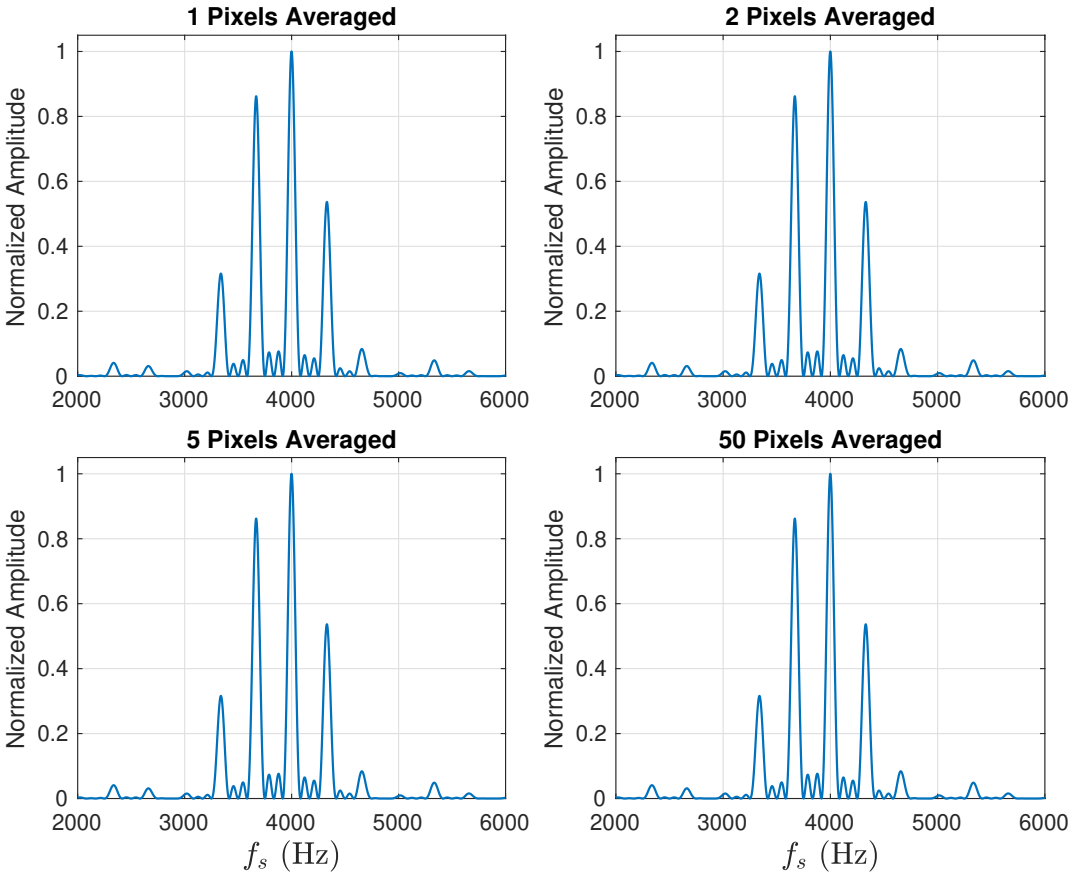


Figure 33: Pupil-plane image simulation result showing the simulation results for a single pixel. The complex exponential representation produces the expected detuning profile without averaging, in contrast to the image-plane simulation.

CONSTRUCTION OF DUAL FMCW LIDAR AND RANGE SELECTIVE DIGITAL HOLOGRAPHIC SYSTEM

A second project was undertaken to develop a combined scanning FMCW lidar and RSDH system. The primary objective was to generate lidar point cloud images and RSDH recordings at distances of up to several hundred meters. The lidar and RSDH subsystems were designed to function either independently, or in an integrated configuration, in which the lidar system detected vibrations of the object and modulated the DH LO with a proportional signal, thereby stabilizing the holograms for long-range measurements.

The following chapter introduces the key components of the system including the chirp generation module, the scanning lidar subassembly, the range-selective holography subassembly, and the stabilization module. Finally, the overall operation of the integrated system is discussed.

Chirp Generation

Chirp generation for FMCW lidar and RSDH is a nontrivial task that requires balancing several key design parameters. Three of the most critical parameters are the chirp duration (including its ability to be externally triggered), the chirp bandwidth, and, for RSDH, its tunability.

For scanning FMCW lidar systems, short chirp durations on the order of tens of microseconds are advantageous because they enable rapid data acquisition across many scan points. However, shorter chirps reduce the amount of return signal reaching the detector, creating an inherent trade-off between fast scanning and sufficient signal strength. For RSDH, longer chirps enable longer integration times, thereby improving the SNR in holographic reconstructions.

The second major factor is chirp bandwidth. As discussed in the background section,

the range resolution of an FMCW lidar and RSDH system is inversely proportional to the chirp bandwidth. While larger bandwidths improve range resolution, they are also more difficult and costly to implement. The third factor is tunability, which enables RSDH to image objects at variable distances.

The design goal of this work was to construct a tunable chirp generation system in which both chirp duration and bandwidth could be adjusted while maintaining external triggering capability. To achieve this, a Euvis DSM-309 chirping module was employed [80]. While this module is easily triggered and allows adjustable chirp durations and bandwidths, its native bandwidth is limited. To overcome this constraint, a custom frequency multiplication and amplification chain was developed, extending the effective bandwidth to approximately 1.8 GHz. This corresponds to a range resolution of around 8.3 cm, which is sufficient for a scanning FMCW lidar system. The Euvis module also supports chirp durations from tens of microseconds to several milliseconds, making it well-suited for flexible operation. The output of the Euvis signal is shown in Figure 34 when outputting a 40 microseconds chirp that spans from 450 MHz to 900 MHz.

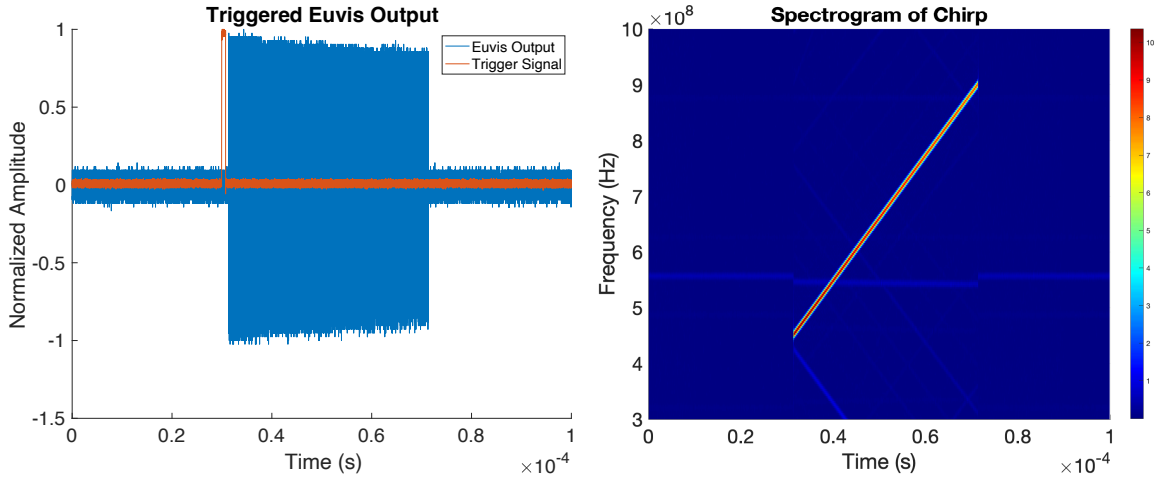


Figure 34: Time-domain trigger signal and output chirp from the Euvis (left). Spectrogram of the Euvis chirp in a dB scale (right).

To enable RSDH, frequency shifts must be applied to the DH LO to cancel the range dependent beat for some object distance. Traditionally, this has been achieved by modulating the laser source and splitting it into the TX and LO fields, which are frequency shifted relative to each other using two separate AOFS. The LO tuning frequency is implemented by shifting one of the AOFS relative to the other.

While effective for short to medium range operations, AOFS have limited bandwidth, which imposes a maximum range-window restriction on the RSDH systems. To overcome this limitation and achieve long-range imaging capabilities at distances up to a kilometer, a novel chirp generation and shifting technique was developed to produce two RF outputs with a controllable frequency offset between channels. In our implementation, one arm of the chirp generator modulates the laser beam used for both the lidar and the RSDH transmit path, while the second arm modulates the digital holography LO path. Tunability of the DH LO chirp is essential, as it enables cancellation of the range-dependent beat frequency and thus allows RSDH operation, as described in the background section. This functionality was realized through a custom frequency multiplication and amplification chain.

A schematic of the system is presented in Figure 35 showing the Euvis chirp generator, the two TPI signal generators that are used to implement frequency shifts between the output chirps, and the various RF components (amplifiers and filters).

The resulting system is a dual-output RF chirp generator that can be externally triggered, configured with adjustable chirp durations, and tuned to provide an adjustable frequency offset between its two arms. The output of a single arm as a function of the TPI signal generator frequency is shown in Figure 36. Here, the chirp is shifted by 4-times the TPI shift (because of the frequency multipliers) allowing for shifts between the two arms of over 500 MHz, far exceeding the capabilities of AOFS based systems.

The two output RF chirps from the chirp generator are shown in Figure 37 illustrating how they can be shifted relative to one another by changing the relative frequency between

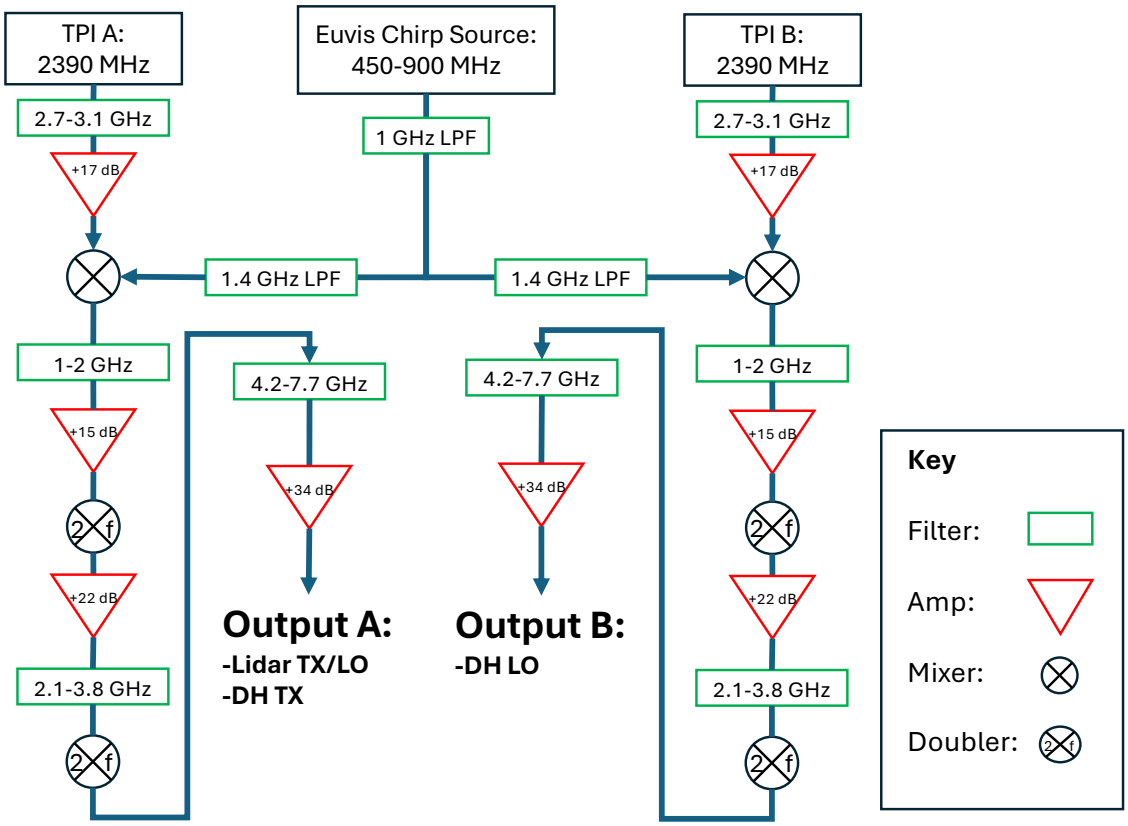


Figure 35: Schematic of the chirp multiplication and amplification chain. Output A is used to modulate the lidar TX/LO and DH TX arm while output B is used to modulate the DH LO optical signal.

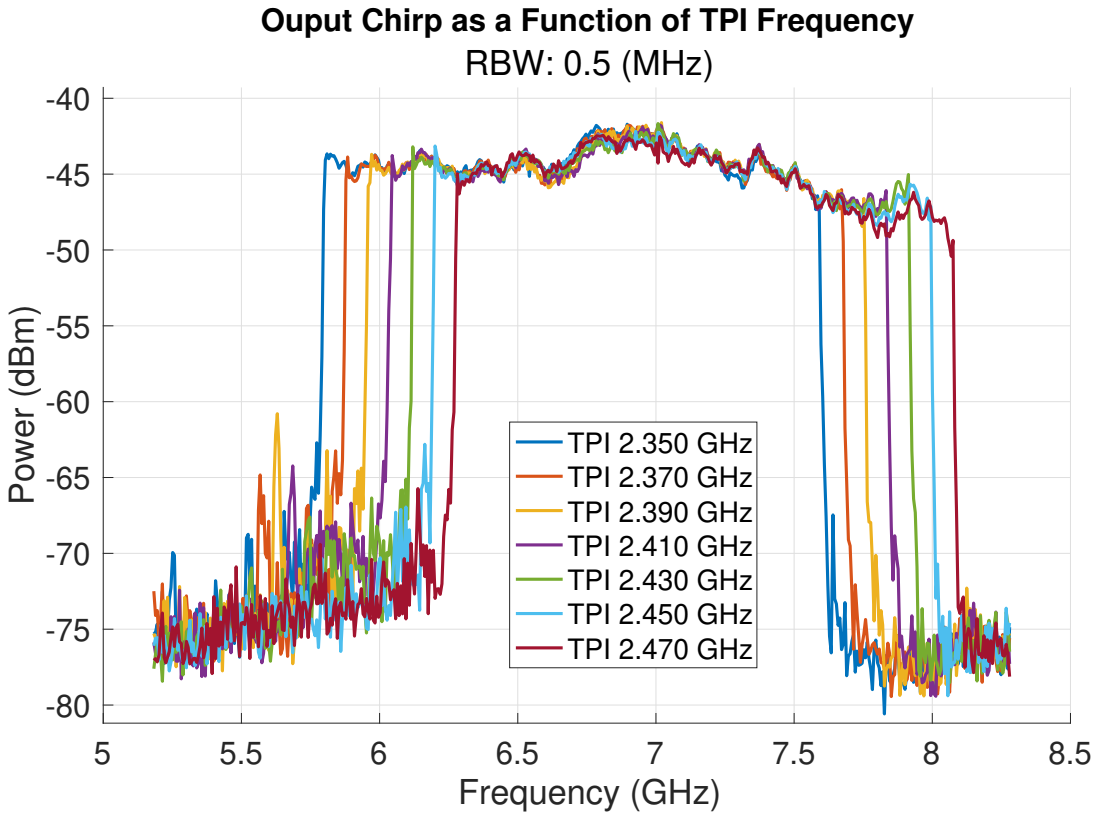


Figure 36: Output chirps as a function of TPI signal generator frequency. The data was recorded on a radio-frequency spectrum analyzer with a resolution bandwidth (RBW) of 0.5 MHz.

the two input signal generators. Unlike other techniques of RSDH which use AOFS, the chirps are frequency shifted from one another in RF before optical modulation.

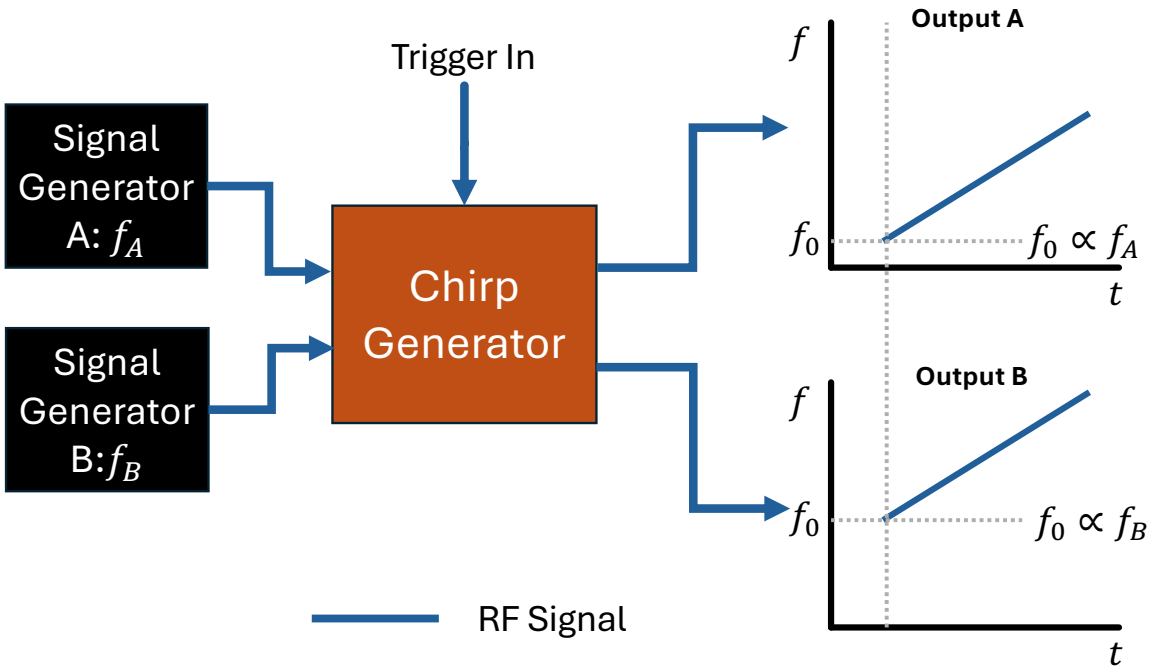


Figure 37: The two output channels of the chirp generator are shifted from one another by changing the relative input frquencies between f_A and f_B.

Scanning Lidar System

A scanning lidar system was constructed by using one of the RF outputs from the chirp generator to modulate a 1550 nm RIO laser with a push-pull electro optical intensity modulator. The laser was split into TX and LO paths using an optical splitter, and the TX path was subsequently amplified with an erbium-doped fiber amplifier (EDFA) to increase the optical power to 100 mW. It was then launched into free space using a custom beam expander [81] and a fast-scanning mirror (FSM) which could be controlled by a computer. The FSM allowed for fine tune beam steering with angular resolution of $< 2\,\mu$rad [82].

The RX signal reflected from the object couples back into the transmit optics and travels in the opposite direction through an optical circulator, where it combines with the

LO at a Kylia 90-degree optical hybrid.The hybrid splits the optical signal into differential I and differential Q optical signals that are detected on two differential photodetectors. The output of the photodetectors was then recorded on two channels of an analogue to digital converter (ADC) resulting in a signal that could be stored for post processing on a computer. Figure 38

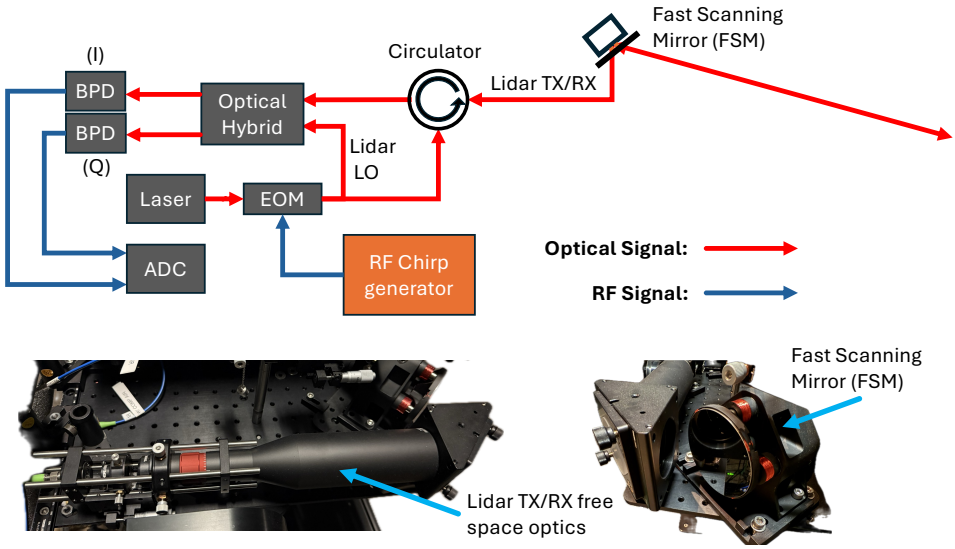


Figure 38: Schematic of the constructed FMCW lidar system (top). Lidar free space optics and fast scanning mirror (bottom).

To create 3D point cloud images of a object scene, a scan pattern is first sent to the FSM, specifying the desired number of scan locations, their x and y coordinates, and the dwell time at each location. At each mirror position, the FSM pauses and simultaneously trigger the Euvis chirp generator to produce a chirp and the analog-to-digital converter to record the output of the balanced photodetectors. This process is repeated for a programmable number of mirror positions (up to 180,000), with a single chirp generated at each step and both I and Q data saved for each position.

The measurement data is collected into the complex-valued matrix

$$\mathbf{X} = \begin{bmatrix} x_{1,1} & x_{1,2} & \cdots & x_{1,M} \\ x_{2,1} & x_{2,2} & \cdots & x_{2,M} \\ \vdots & \vdots & \ddots & \vdots \\ x_{N,1} & x_{N,2} & \cdots & x_{N,M} \end{bmatrix} \in \mathbb{C}^{N \times M}$$

Here, N is the number of mirror positions (equal to the number of chirps) and M is the number of samples recorded at each position, determined by the ADC sampling rate and the integration time. Each row of $\mathbf{X}$ corresponds to a single mirror position and contains complex entires, represented as $x_{n,m} = I_{n,m} + iQ_{n,m}$, where $I_{n,m}$ and $Q_{n,m}$ are the in-phase and quadrature components, respectively. This $N \times M$ data set is then processed to generate spectra for each mirror location.

To process each spectrum, each row of the measurement matrix $\mathbf{X}$, denoted by

$$\mathbf{x}_n = \begin{bmatrix} x_{n,1} & x_{n,2} & \cdots & x_{n,M} \end{bmatrix} \in \mathbb{C}^{1 \times M}, \qquad n = 1, \ldots, N \tag{79}$$

is first multiplied element-wise by a window function $\mathbf{w} \in \mathbb{R}^{1 \times M}$ (e.g., Hann). The windowed row is then zero-padded (if $L > M$) and transformed by an L-point FFT:

$$\mathbf{X}_{\mathrm{FFT}}[n, i] = \mathrm{FFT}_L\big(\mathbf{x}_n \odot \mathbf{w}\big)_i, \quad n = 1, \ldots, N,\ i = 1, \ldots, L, \tag{80}$$

where $\odot$ denotes element-wise multiplication. The FFT can be optionally centered so that the zero frequency appears in the middle of the spectrum. For even L, this can be written as

$$\mathbf{X}_{\mathrm{shifted}}[n, i] = \mathbf{X}_{\mathrm{FFT}}\big[n, (i + L/2) \bmod L\big], \quad n = 1, \ldots, N,\ i = 1, \ldots, L, \tag{81}$$

which is equivalent to using `fftshift` in MATLAB or Python (keeping in mind that

MATLAB and Python use different indexing conventions).

The magnitude of each FFT value is then computed to obtain the amplitude:

$$\mathbf{A}[n, i] = |\mathbf{X}_{\text{shifted}}[n, i]|. \tag{82}$$

A background, $\mathbf{B} \in \mathbb{R}^{1\times L}$, can be subtracted from each row to remove fiber tip reflections and system-inherent spectrum components. Values below a threshold τ are set to zero to suppress small fluctuations and remove unwanted signals:

$$\mathbf{A}_{\text{thresh}}[n, i] = \begin{cases} \mathbf{A}[n, i] - \mathbf{B}[i], & \text{if } \mathbf{A}[n, i] - \mathbf{B}[i] \geq \tau \\ 0, & \text{otherwise} \end{cases}, \quad n = 1, \ldots, N,\ i = 1, \ldots, L. \tag{83}$$

Finally, the background-corrected amplitude is converted to power in dB units:

$$\widehat{\mathbf{P}}_{\text{dB}}[n, i] = 10 \log_{10} \left(\mathbf{A}_{\text{thresh}}[n, i]^2 \right). \tag{84}$$

Each row of the matrix $\widehat{P}_{\text{dB}}[n, i]$ represents the two-sided frequency-domain spectrum of the received signal for the n-th mirror position. Figure 39 plots the cropped upper sideband of $10 \log_{10}(\mathbf{A}[n, i]^2)$ for 10 random n values before background subtraction and thresholding, along with a similarly cropped example background $10 \log_{10}(\mathbf{B}[i]^2)$.

To convert the FFT spectrum to physical range, the frequency corresponding to bin i is

$$f_R[i] = \left(i - \frac{L}{2} - 1 \right) \frac{f_s}{L}, \quad i = 1, \ldots, L, \tag{85}$$

where f_s is the ADC sampling rate and L is the FFT length. Each FFT bin corresponds to a frequency increment of

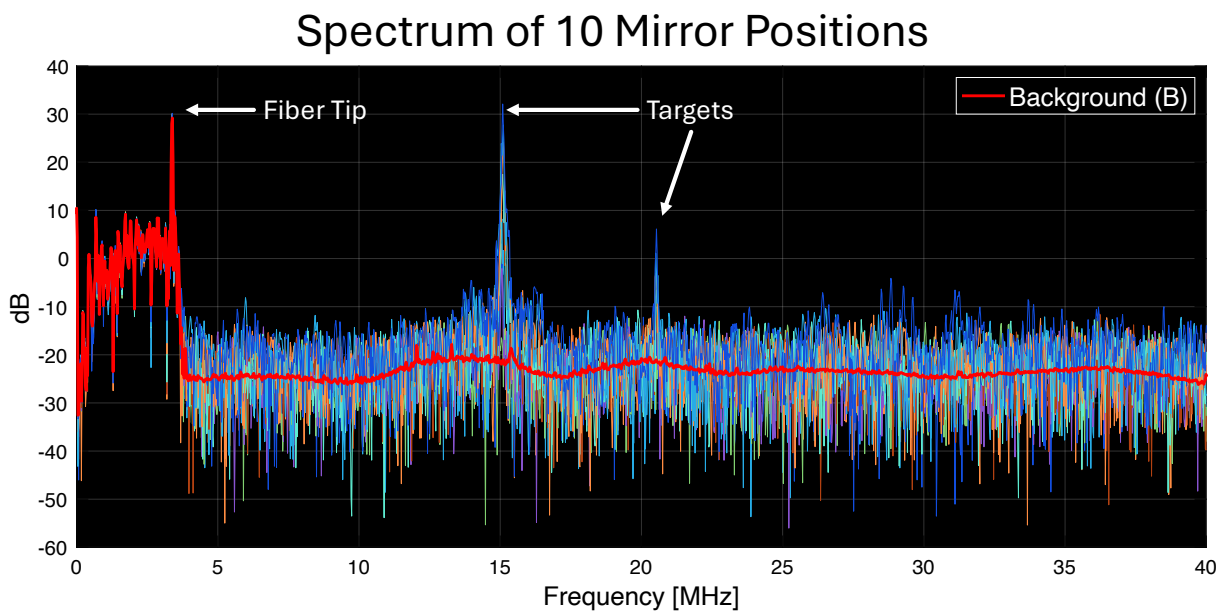


Figure 39: Upper sideband of the amplitude spectrum, $10\log_{10}(\mathbf{A}[n,i]^2)$, for 10 randomly selected mirror positions n before background subtraction and thresholding. The example background spectrum, $10\log_{10}(\mathbf{B}[i]^2)$, is also shown for reference.

$$\Delta f = \frac{f_s}{L}. \tag{86}$$

For a stationary object, this beat frequency is proportional to the round-trip time delay $\Delta t[i]$ via the chirp rate k (Hz/s):

$$f_R[i] = k\,\Delta t[i]. \tag{87}$$

The corresponding range $R[i]$ is then

$$R[i] = \frac{c\,\Delta t[i]}{2} = \frac{c\,|f_R[i]|}{2k}, \tag{88}$$

where c is the speed of light. Each FFT bin i can be mapped to a specific range $R[i]$, allowing the frequency spectrum for each mirror position n to be converted to a range profile. For stationary objects, the positive and negative beats will be exactly mirrored around zero

frequency. This simplifies the computation because only one sideband is required to map frequencies to distance (positive sideband) if the objects are stationary.

The spectrum matrix, now expressed as a function of mirror position n and range $R[n, i]$, can be directly associated with the scanning pattern programmed for the FSM positions. By combining the range information with the corresponding angular positions of the mirror, a three-dimensional point cloud of the scene can be reconstructed. This mapping allows each range measurement to be placed in 3D space according to its mirror angle, providing a complete spatial representation of the object, even if multiple object ranges are above the threshold for a single mirror position. Shifting the range so that it starts at the last system reflection (the fiber tip) is common practice, ensuring that zero range corresponds to the fiber tip and is not affected by path-length differences elsewhere in the system. A reconstructed point cloud from 120,000 mirror positions using a zig-zag scanning pattern is shown in Figure 40. The acquisition used a dwell time of 45 µs, a chirp duration of 40 µs, and a chirp bandwidth of 1.8 GHz. This figure illustrates the 3D nature of the data by showing the front, top, and side profiles of a reconstructed scene.

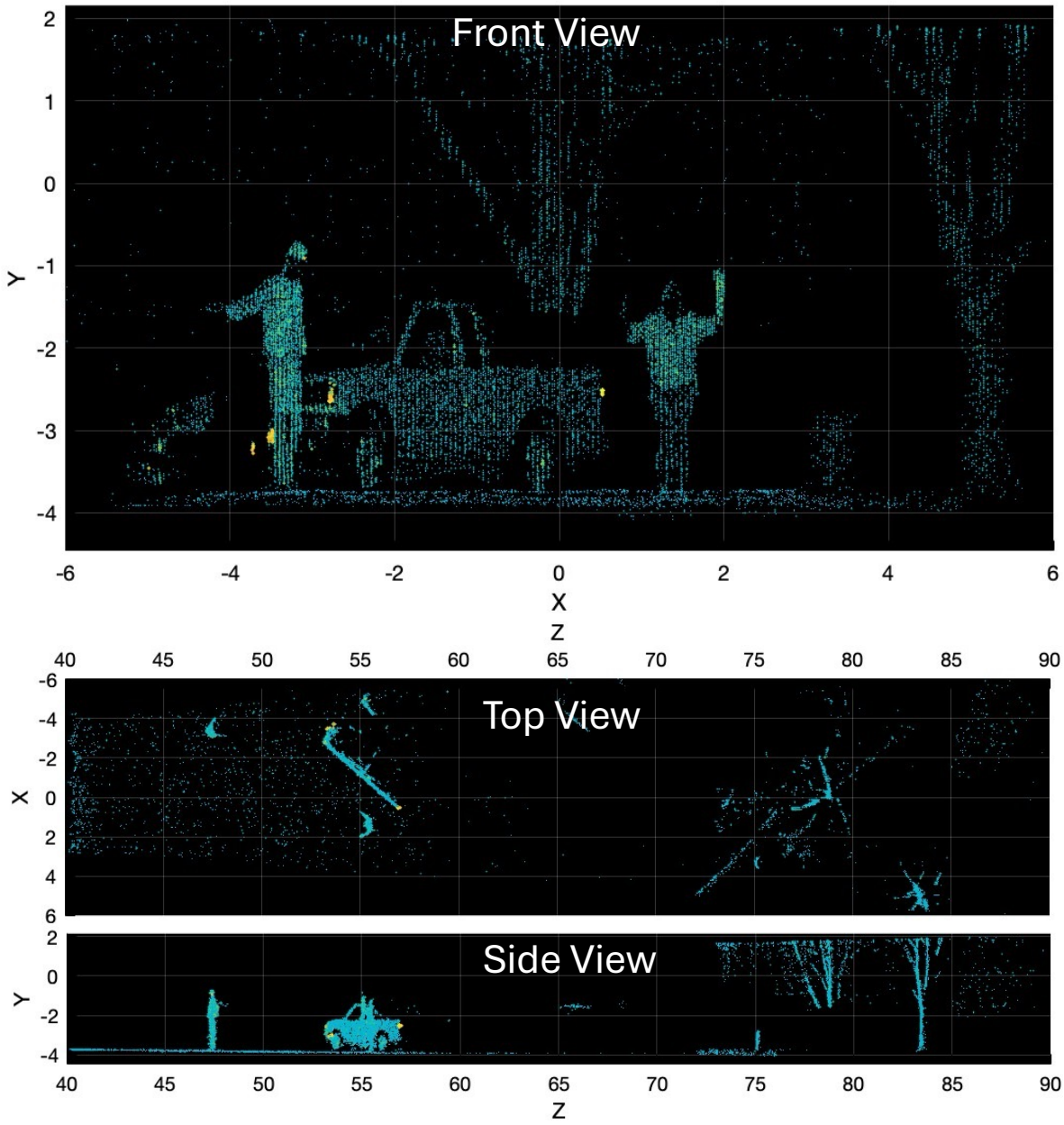


Figure 40: 3D lidar point cloud of the scanned object scene, shown from the front (top), top (middle), and side (bottom) views. The units are in meters.

Range-Selective Digital Holographic System

In order to perform digital holographic recordings at long range, a digital holographic free-space optics (FSO) subsystem was developed with three primary goals. First, the FSO were designed to illuminate the object of interest with a DH TX beam allowing for the beam size to be adjusted. For long range DH operation, it is important that the DH TX beam be aligned with the receive optical axis to avoid the need for active beam steering. Second, the FSO system needed to capture a sufficient amount of the return DH RX signal. Third, the system must perform digital holography by recording the interference between the DH RX signal and the angled DH LO signal.

Digital holography at range is inherently challenging, particularly because the received signal power decreases rapidly with distance, making detection more difficult at hundreds of meters. To maximize collection efficiency, a 6-inch Ritchey-Chrétien telescope was used as the imaging apparatus, imaging the object onto a detector. A schematic of the developed free-space optics system is shown in Figure 41.

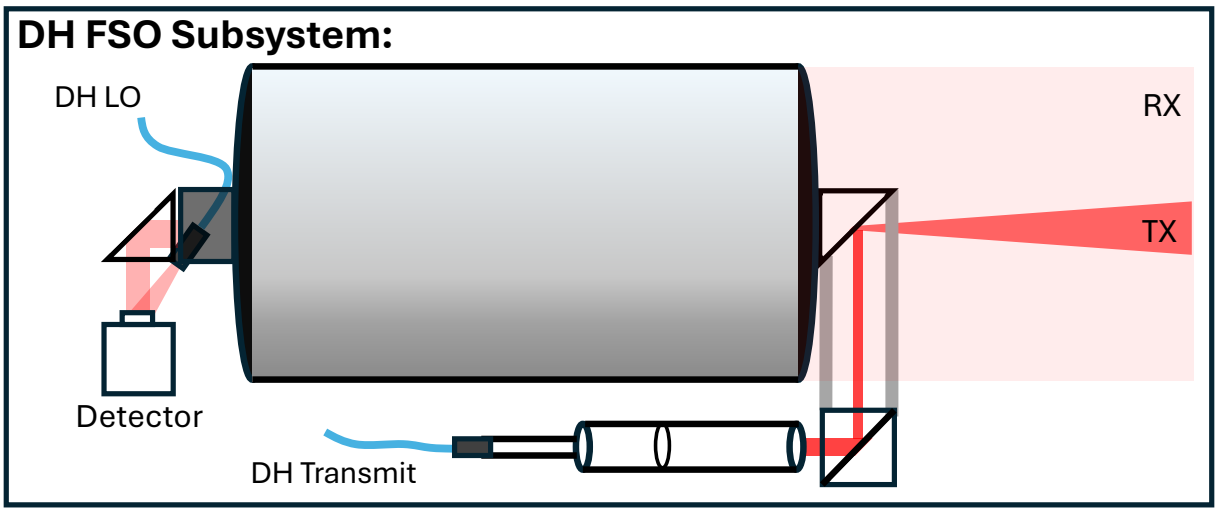


Figure 41: Cartoon of the Digital holography transmit system, the imaging system, and the holographic recording geometry.

After a lidar scan is performed and processed, the telescope, which is mounted on a gimbal, is aimed at a subsection of the point cloud scene or specific object of interest. The DH TX beam, generated by splitting the lidar TX beam and amplifying it with an additional EDFA, was expanded to flood-illuminate the object, enabling holographic recording across the entire telescope field of view. The TX signal was launched from a mirror located in the "blind" spot created by the telescope's secondary mirror, allowing the TX beam to remain co-aligned with the optical axis. The corresponding DH RX signal was imaged onto a detector, forming a scaled image of the object. The optical DH RX signal was mixed with an angled DH LO forming an off-axis image-plane hologram at the detector plane. When the optical signals are modulated with a linear chirp, the interference between the DH LO, which is modulated from output B of the chirp generator, mixes with a time delayed RX signal which is modulated from output A, forming a temporally modulated interference pattern. Shifting the frequency of one of the output chirps relative to the other provides a means to scan over object distances to construct range-selective digital holograms. The means in which the output RF chirps are shifted from one another is shown in Figure 37. The range-dependent beat frequency of the interference will be given by Equation 67, as outlined in the background section.

Selecting the correct frequency shift can be expedited by measuring the object range with the lidar system and appropriately shifting the DH LO by an amount set by the object range, after accounting for path length differences between the lidar system and DH system, the most prominent of which is the extra fiber delay in the DH TX EDFA. This allows range-selective digital holograms to be recorded much quicker than in cases where the object range is unknown or estimated and manually scanning through frequency shift values is required before the the beat is within the detectors bandwidth and the object appears.

The process for recording a range-selective digital hologram is summarized here. First an object is selected. Next, the lidar system is used to calculate the precise range to

the object. The required frequency shift is estimated using Equation 67 remembering to compensate for the path length difference between the lidar and DH system (which is a calibration constant). Based on the lidar's range-dependent beat for the object, the RF chirp that modulates the RSDH LO is frequency-shifted relative to the chirp modulating the DH TX beam by one-fourth of the estimated range-dependent beat, accounting for the frequency multiplication that occurs within the chirp generation system. Finally, fine tuning of the added frequency can help increase signal strength. It is important to note that frequency shifts are relative and shifting the DH LO is only conventional since shifting the transmit will also produce the necessary relative shifts between paths.

Figure 42 shows a single-shot RSDH taken from a distance of 90 meters.

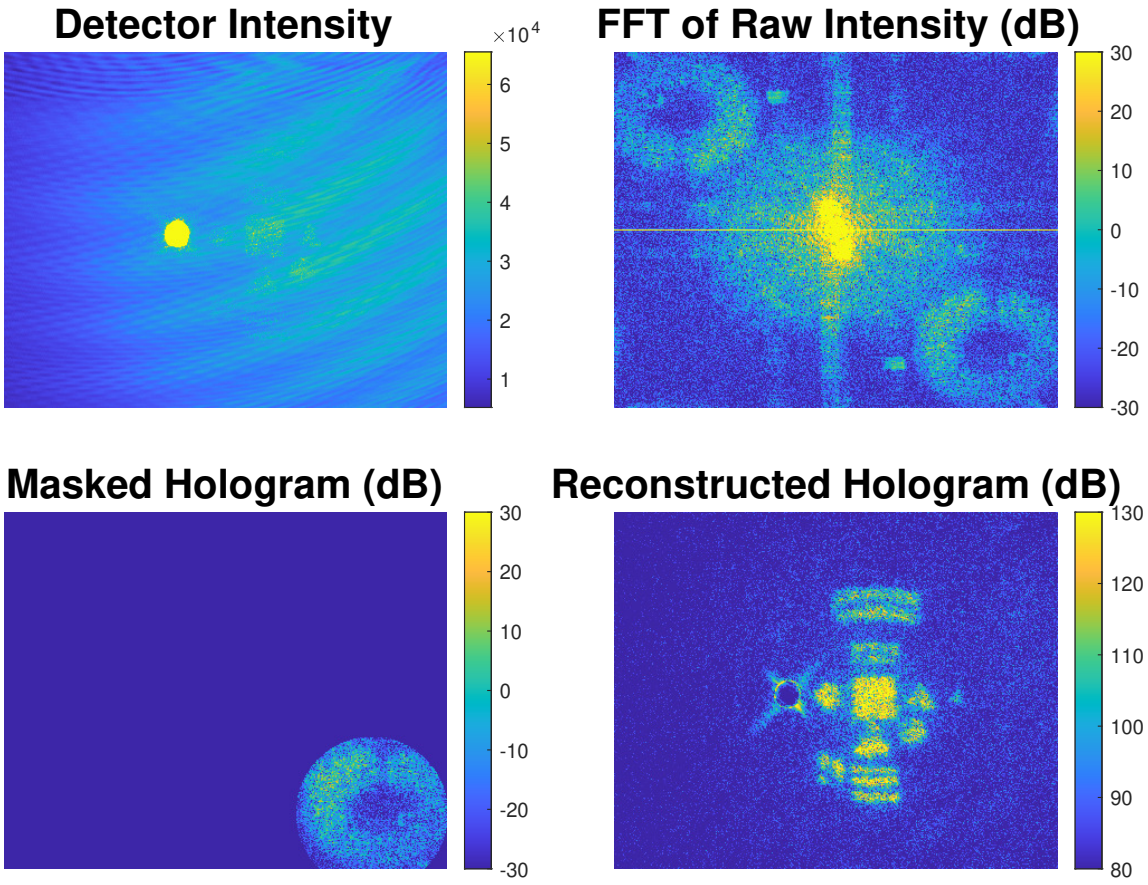


Figure 42: RSDH of a speaker with retroreflective tape taken at 90 meters. Raw intensity captured by detector (top left). 2D FFT of the recorded intensity (top right). Masking of the hologram (bottom left). Reconstructed hologram (bottom right).

Holographic Stabilization System

Holographic recordings are highly susceptible to object vibration, movement, or fluctuations in the index of refraction caused by turbulence. These effects change the phase between the RX and LO beams, causing the interference patterns that form the hologram to wash out during integration, leaving reconstruction severely diminished or, in severe cases, completely impossible. To remedy this for object vibration as well as atmospheric phase degradation an FMCW lidar-enabled stabilization module was constructed with the goal of modulating the DH LO optical signal with an error signal that was proportional to the instantaneous phase difference between the lidar RX and LO which would sufficiently capture both object movement and atmospheric phase changes caused by turbulence. To accomplish this, a novel technique was developed that relied of phase-frequency detectors.

Phase-frequency detectors (PFD) are circuits that are often used in PID controllers and phase-locked loops to create an error signal proportional to the phase and frequency difference between two RF input signals applied to the reference (R) and variable (V) ports [83]. The PFD used in the constructed stabilization system is an HMC439 which is a digital PFD. While internal designs are often proprietary, digital PFD chips generally employ flip-flop logic to detect both the phase and frequency difference [84]. While the chip takes two inputs, it also produces two complementary outputs, NU (up output complement) and ND (down output complement), which are designed to feed a differential loop filter. The loop filter integrates and smooths the pulsed input signals and outputs a continuous control voltage, $V_{\mathrm{PFD}}(t)$, which is proportional to the instantaneous phase difference between the two input signals. Because the signal is derived from the differential of NU and ND, $V_{\mathrm{PFD}}(t)$ is positive when the reference leads the variable input and negative when the variable leads the reference.

Figure 43 illustrates the RF output of an HMC439 digital phase-frequency detector

for two inputs of slightly different frequency after a differential loop filter. In this case, a sawtooth pattern is observed since the instantaneous phase difference between the two inputs will accumulate linearly from 0 to 2π until the signals realign, at which point the pattern resets. The sign of the signal is dependent on the direction of phase accumulation and the repetition rate is given by the frequency difference of the two inputs.

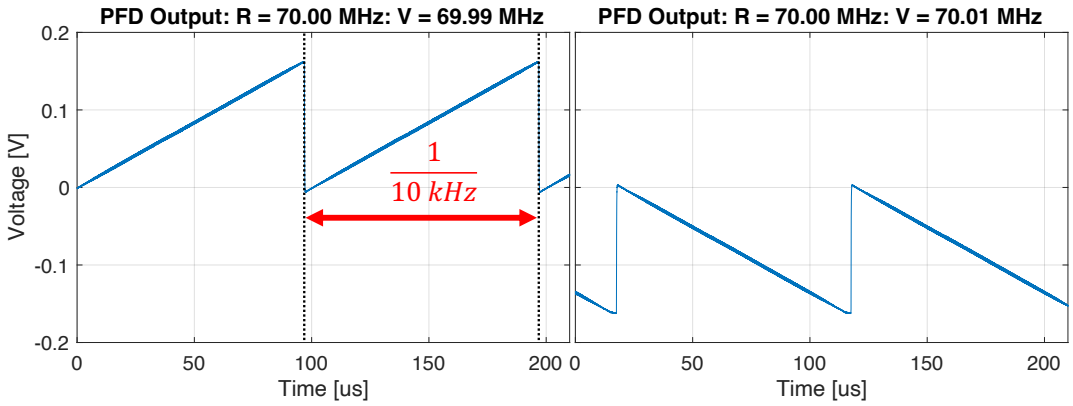


Figure 43: Phase-frequency detector output voltage when input R is less than inout V by 10 kHz (left) and when input R is greater than input V by 10 kHz (right).

If the two inputs are set equal to each other in frequency, the output is a constant voltage where the amplitude is proportional to the initial phase difference. Applying frequency modulation to one channel, emulating what happens to a lidar beat frequency when recording a vibrating object, causes the output to now be sinusoidal similar to the frequency modulation. However, the phase will reset after each 2π and the number of phase "resets" will be given by the frequency deviation Δf. Figure 44 illustrates the PFD output when both inputs are the same frequency but one is frequency modulated by $f_{\text{mod}} = 1\,\text{kHz}$ with a frequency deviation of $\Delta f = 10\,\text{kHz}$. As shown in the figure, a wrapped output voltage is produced for each phase difference between the two signals, ranging from 0 to 2π.

To confirm this behavior, we can estimate the maximum phase deviation directly from

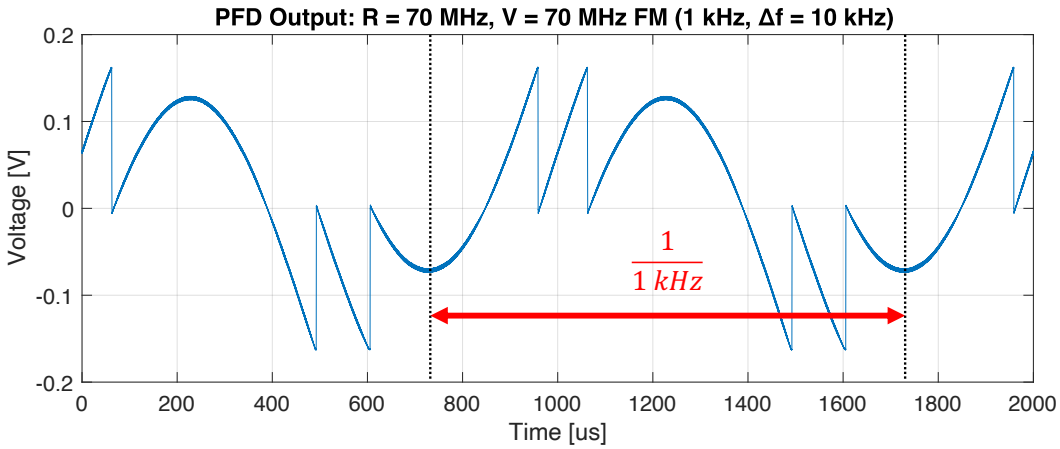


Figure 44: Phase-frequency detector output voltage when input R is equal in frequency to V but V is frequency modulated at 1 kHz with 10 kHz deviation.

the modulation parameters. The peak phase swing is given by

$$\Delta\phi_{\max} = \frac{2\Delta f}{f_{\text{mod}}} = \frac{2 \cdot 10{,}000}{1{,}000} = 20\,\text{rad}. \tag{89}$$

Expressed in cycles, this corresponds to

$$\frac{\Delta\phi_{\max}}{2\pi} = \frac{20}{2\pi} \approx 3.18\,\text{cycles}. \tag{90}$$

Thus, over one modulation period (1000 µs), the phase difference sweeps through approximately 3.2 cycles modulo-2π, but returns to zero at the end of the interval which is consistent with the behavior shown in Figure 44.

One challenge with using a lidar beat signals as one input into the stabilization system is their strong susceptibility to speckle effects, where small variations in the beam position or surface roughness can cause large fluctuations in the return signal amplitude. To mitigate this, an automatic gain control (AGC) amplifier is employed to stabilize the signal level prior to processing. The AGC minimizes the impact of return-signal amplitude variations by dynamically adjusting the gain, ensuring that a consistent signal amplitude is presented

to the PFD input.

Next, let us consider this process by analyzing both the lidar and RSDH signals for vibrating objects. To achieve stabilization, it must be shown that the output of the PFD can be used to modulate the RSDH LO to compensate for object movement or vibration. First the lidar signal and PFD will be analyzed, followed by the RSDH fields for vibrating objects.

Lidar Beat for Vibrating Object

The lidar beat signal (as the output voltage of a photodetector) for a stationary object is given as

$$V_b(t) \propto \cos\big(\varphi_b(t)\big), \qquad \varphi_b(t) = 2\pi\kappa\tau_R t + 2\pi f_L \tau_R - \pi\kappa\tau_R^2, \tag{91}$$

with round-trip delay

$$\tau_R = \frac{2R_0}{c}. \tag{92}$$

If the object is moving, the round-trip delay is now a function of time given as

$$\tau_R(t) = \frac{2\big(R_0 + \Delta R(t)\big)}{c}, \tag{93}$$

where $\Delta R(t)$ is the time-dependent displacement. Here we consider $\Delta R(t)$ with magnitudes up to one half the range resolution so that the deviation from R_0 does not put the object of interest into a new range bin. This is then substituted into the phase $\varphi_b(t)$:

$$\begin{aligned}\varphi_b(t) &= 2\pi\kappa t\,\frac{2\big(R_0 + \Delta R(t)\big)}{c} + 2\pi f_L\,\frac{2\big(R_0 + \Delta R(t)\big)}{c} - \pi\kappa\,\frac{4}{c^2}\Big(R_0^2 + 2R_0\Delta R(t) + \Delta R(t)^2\Big) \\ &= \frac{4\pi}{c}\big(\kappa t R_0 + f_L R_0\big) - \frac{4\pi\kappa R_0^2}{c^2} + \frac{4\pi}{c}\big(\kappa t + f_L\big)\Delta R(t) - \frac{8\pi\kappa R_0}{c^2}\Delta R(t) - \frac{4\pi\kappa}{c^2}\Delta R(t)^2.\end{aligned} \tag{94}$$

Output of the Phase - Frequency Detector

The lidar beat signal $V_b(t)$ forms the variable (V) input into the PFD. The other input is a reference cosine from a signal generator at frequency f_{LO}, and phase ϕ_{LO}:

$$V_{\mathrm{LO}}(t) \propto \cos\big(\varphi_{\mathrm{LO}}(t)\big), \qquad \varphi_{\mathrm{LO}}(t) = 2\pi f_{\mathrm{LO}} t + \phi_{\mathrm{LO}}. \tag{95}$$

The PFD output is proportional (up to a constant scaling factor) to the instantaneous phase difference between its two inputs,

$$\phi_{\mathrm{PFD}}(t) = \varphi_b(t) - \varphi_{\mathrm{LO}}(t). \tag{96}$$

Substituting the expression for $\varphi_b(t)$ gives

$$\phi_{\mathrm{PFD}}(t) = -2\pi f_{\mathrm{LO}}\, t + \varphi_b(t) - \phi_{\mathrm{LO}} \tag{97}$$

Phase of RSDH

Next, we consider the RX and LO fields in range-selective digital holography when the object is undergoing vibration. The corresponding optical fields can be expressed as:

$$E_{\mathrm{LO}}(x,y,t) = A_{\mathrm{LO}}(x,y)\, \cos\big(\, 2\pi(f_L - f_s)t + \pi\kappa t^2 + \phi_{\mathrm{LO}}(x,y)\big)\,, \tag{98}$$

and

$$E_{\mathrm{RX}}(x,y,t) = A_{\mathrm{RX}}(x,y)\, \cos\big(\, 2\pi f_L\,(t - \tilde{\tau}_R(t)) + \pi\kappa\,(t - \tilde{\tau}_R(t))^2 + \phi_{\mathrm{RX}}(x,y)\big)\,. \tag{99}$$

The amplitudes are given as $A_{\mathrm{LO}}(x,y)$ and $A_{\mathrm{RX}}(x,y)$ while the phases are $\phi_{\mathrm{LO}}(x,y)$ and $\phi_{\mathrm{RX}}(x,y)$ for the LO and RX signals. The phase of the difference term retained by the detector is given as

$$\phi_{\mathrm{RSDH}}(x,y,t) = 2\pi f_s t - 2\pi f_L \tilde{\tau}_R(t) - 2\pi\kappa t\, \tilde{\tau}_R(t) + \pi\kappa\, \tilde{\tau}_R(t)^2 + (\phi_{\mathrm{RX}}(x,y) - \phi_{\mathrm{LO}}(x,y))\,. \quad (100)$$

Next, $\tilde{\tau}_R(t) = \dfrac{2R_0}{c} + \dfrac{2\Delta R_0}{c} + \dfrac{2\Delta R(t)}{c}$ is substituted in. Here, ΔR_0 is the change in path length between the lidar system (with delay $\tau_R(t)$) and RSDH system caused by additional fiber delay etc. The phase is then given as

$$\phi_{\mathrm{RSDH}}(x,y,t) = 2\pi(f_s - f_{\Delta R_0})t - \varphi_b(t) + \varphi_{\Delta R_0}(t) + (\phi_{\mathrm{RX}}(x,y) - \phi_{\mathrm{LO}}(x,y))\,, \quad (101)$$

where $f_{\Delta R_0} = \frac{2\kappa\Delta R_0}{c}$. The term dependent on the path length differences between the systems is $\varphi_{\Delta R_0}(t) = -\frac{4\pi f_L \Delta R_0}{c} + \frac{4\pi\kappa(\Delta R_0)^2}{c^2} + \frac{8\pi\kappa R_0 \Delta R_0}{c^2} + \frac{8\pi\kappa\Delta R_0 \Delta R(t)}{c^2}$.

Phase of Stabilized RSDH

If the RSDH LO field is modulated by subtracting $\phi_{\mathrm{PFD}}(t)$, the phase of the corresponding stabilized RSDH is given as,

$$\phi_{\text{Stabilized RSDH}}(x,y,t) = 2\pi((f_s - f_{\Delta R_0} - f_{\mathrm{LO}})t + \phi_c + \frac{8\pi\kappa\Delta R_0}{c^2}\,\Delta R(t) + (\phi_{\mathrm{RX}}(x,y) - \phi_{\mathrm{LO}}(x,y))\,, \quad (102)$$

where ϕ_c is a constant phase defined as $\phi_c = -\phi_{\mathrm{LO}} - \frac{4\pi f_L \Delta R_0}{c} + \frac{4\pi\kappa(\Delta R_0)^2}{c^2} + \frac{8\pi\kappa R_0 \Delta R_0}{c^2}$. This results in a temporally stable hologram of a vibrating object as long as $(f_s - f_{\Delta R_0} - f_{\mathrm{LO}}) = 0$, and the term $\frac{8\pi\kappa R_0 \Delta R_0}{c^2}$ is negligible. To determine the limits on object velocity for which

this additional term can be neglected, we take the time derivative to compute the velocity. Adopting the washout criterion $|\phi_{\text{Stabilized RSDH}}(t)| = 1$ radian and solving for the critical velocity gives

$$|v|_{\text{crit}} = \frac{c^2}{8\pi\kappa\Delta R_0 \tau_{\text{int}}}, \tag{103}$$

which can be neglected, as it does not produce significant errors until velocities reach approximately $100\,\text{km}\,\text{s}^{-1}$ for $\Delta R_0 = 20\,\text{m}$, and $\tau_{\text{int}} = 200\,\mu\text{s}$.

Ultimately, the maximum object velocity that can be stabilized will depend upon the bandwidth of the PFD and the system filters. For a system bandwidth of $BW_{\text{PFD}} = 10$ MHz and a wavelength of $\lambda = 1550$ nm, the maximum measurable target velocity is given by the Doppler relation:

$$|v|_{\text{max}} = \frac{BW_{\text{PFD}}\,\lambda}{2} \approx 7.75 \text{ m/s}. \tag{104}$$

Integration of Lidar and stabilized Holographic Systems

In practice, to form an FMCW-lidar stabilized digital hologram, an object of interest is first chosen, and the gimbal is used to align the telescopic imaging system. The lidar system is then aimed at the oscillating object with the FSMs, where data is processed, providing an object range estimate f_{R_0}. The DH LO is then shifted my an amount f_s which will form a range-selective hologram at the computed object distance, after accounting for path length differences between the lidar the DH system. The lidar beat signal is also sent into the stabilization module where it is amplified with an automatic gain control to remove power oscillation before forming one input into the PFD. The second input is a tone from a signal generator at frequency f_{LO} chosen such that $(f_s - f_{\Delta R_0} - f_{\text{LO}}) = 0$.

Combining the FMCW lidar system with the RSDH system and the stabilization module enables the recording of digital holograms of vibrating objects. A schematic of the integrated

system is shown in Figure 45. In this configuration, the lidar system measures object vibrations as range-dependent beat frequency shifts. This information is then fed to the phase-frequency detector which creates an output voltage signal that is proportional to the instantaneous phase error and is used to modulate the DH LO beam, thereby compensating for phase shifts caused by motion.

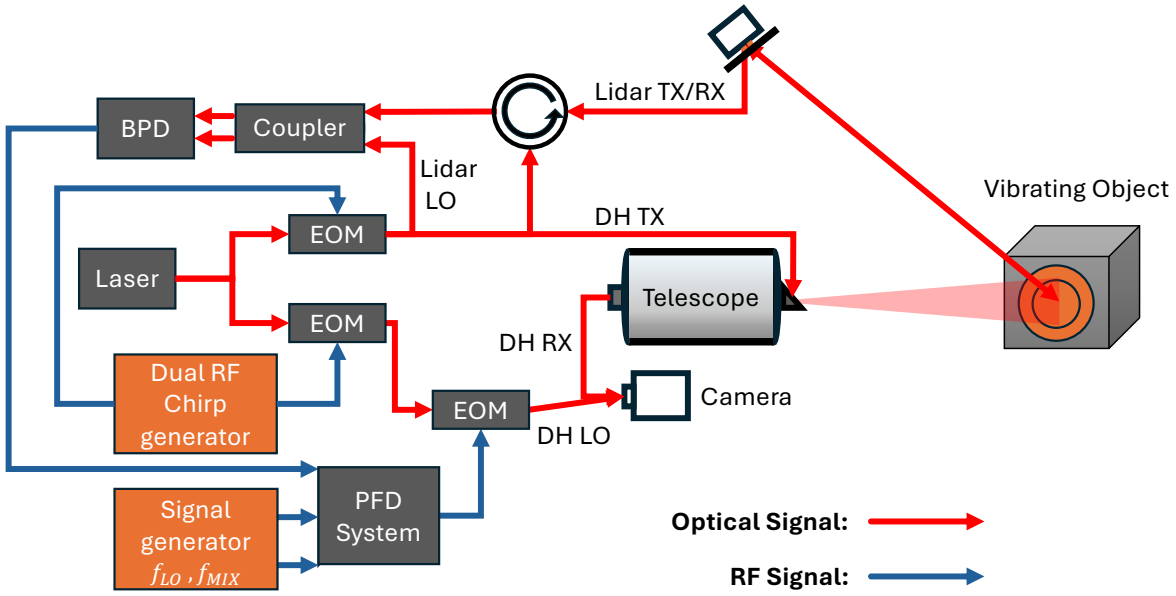


Figure 45: Schematic of the combined FMCW lidar and RSDH system when performing stabilized RSDH of a vibrating speaker.

A close up of the free-space optics for both the lidar and RSDH system is shown in Figure 46.

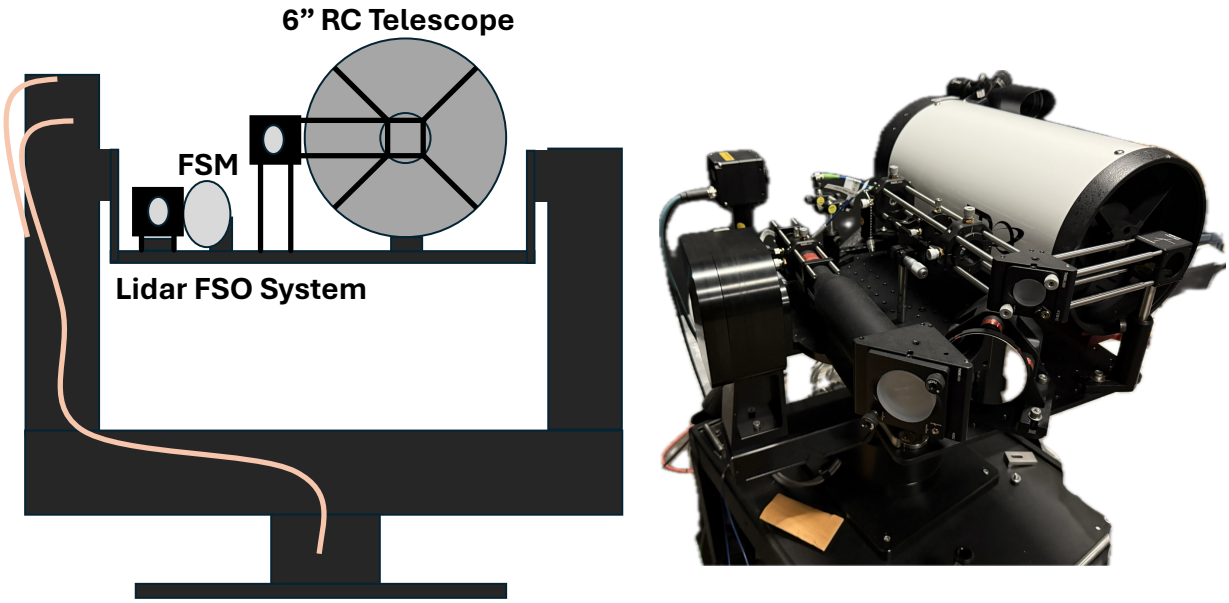


Figure 46: Illustration of the combined FMCW lidar and RSDH system.

FMCW LIDAR STABILIZED RANGE SELECTIVE DIGITAL HOLOGRAPHY FOR IMAGING VIBRATING OBJECTS

Manuscript Introduction

The primary objective of the dual FMCW lidar and range-selective imaging system is to provide wide field-of-view lidar scans of an object scene, enabling the identification of objects of interest and subsequent holographic recording using a gimbal-mounted digital holographic imaging system. Once the gimbal is correctly positioned, range-selective holograms of the chosen object can be recorded by shifting the DH LO frequency by an amount set by the object range. When the object is moving or vibrating, axial displacements approaching $\lambda/2$ during the integration time causes the hologram to wash out. To address this limitation, the stabilization subassembly is introduced.

In this approach, the lidar beam is directed at the object of interest by steering the fast-scanning mirrors. The lidar system detects object vibrations as changes in the range-dependent beat frequency and the stabilization system uses this information to modulate the digital holographic LO by an amount proportional to the phase differences induced by the motion.

The result is an FMCW lidar-enabled stabilization system capable of preserving range-selective holographic images of vibrating objects. We demonstrate this capability by presenting stabilization results for objects mounted on a subwoofer speaker at distances of 95 meters where axial displacements exceeded 18 wavelengths during integration. The results are presented in the following manuscript which is being prepared for publication.

Contribution of Authors and Co-Authors

Manuscript in following chapter

Author: Cole Hammond

Contributions: Design of combined lidar and RSDH system, Design of stabilization system, Data Collection, Initial Analysis, Software and post processing, Writing - original draft.

Author: Zachery Lakin

Contributions: Design of combined lidar and RSDH system, Writing - review and editing

Author: R. Krishna Mohan

Contributions: Conceptualization, Funding, Methodology, Resources, Supervision, Writing - review and editing

Author: Wm. Randall Babbitt

Contributions: Conceptualization, Funding, Methodology, Resources, Supervision, Writing - review and editing

Manuscript Information

Cole Hammond, Zachery Lakin, R. Krishna Mohan, Wm Randall Babbitt

Status of Manuscript:
____ Prepared for submission to a peer-reviewed journal
_X_ Officially submitted to a peer-reviewed journal
____Accepted by a peer-reviewed journal
____ Published in a peer-reviewed journal

OSA (Optical Society of America)
Submitted: 1 December 2025

FMCW Lidar-Enabled Stabilization for Range-Selective Digital Holographic Imaging of Vibrating Objects

COLE HAMMOND,[1,*] ZACHERY LAKIN,[1] R.KRISHNA MOHAN,[1] AND WM RANDALL BABBITT [1]

[1]*Spectrum Lab, Montana State University, Box 173510, Bozeman, Montana 59717, USA*
[*]*Colehammond2@montana.edu*

Abstract: Range-Selective Digital Holography (RSDH) is a coherent imaging technique that enables the reconstruction of digital holograms at tunable distances while suppressing the contributions from objects at other ranges. This selectivity is achieved by combining digital holography with Frequency-Modulated Continuous-Wave (FMCW) signals commonly found in lidar to produce a temporally modulated interference pattern. By tuning the local-oscillator (LO) frequency according to the object distance, a temporally stable hologram is formed at the desired range, which can then be recorded on a sensor array. The resulting range resolution can be substantially finer than the non–diffraction-limited depth of field. However, holographic systems are inherently sensitive to object motion and vibration, which introduce phase variations that can degrade the quality of the hologram. In particular, radial motion exceeding half the optical wavelength during the sensor integration time can induce phase shifts that lead to signal washout, requiring the use of short integration times that degrade the image signal-to-noise ratio (SNR). We demonstrate an FMCW-lidar-enabled stabilization system that preserves high-fidelity holographic reconstructions outdoors at distances up to 90 meters, with long integration times and significantly higher SNR, even when the object displacement exceeds 18 optical wavelengths during integration. The developed RSDH architecture enables a theoretical holographic imaging range window of multiple kilometers while providing stabilization over a similarly broad range of object distances.

1. Introduction

1.1. Digital Holography

Digital holography is a coherent imaging technique that reconstructs the complex optical field of an object through digital post-processing. In a typical holographic setup, the optical source is divided into two paths: one forms the transmit field (TX) that illuminates the object, while the other serves as a local oscillator (LO) reference for coherent detection. The reflected return field (RX) from the object interferes with the LO field at the sensor, producing an intensity pattern recorded on a sensor array. Digital post-processing of the recorded intensity enables retrieval of both the amplitude and phase of the target field.

Digital holograms can be recorded in an off-axis geometry, where a small angle between the LO and RX fields shifts the interference terms in the spatial frequency domain for easier separation, or in an on-axis configuration, where multiple recordings with known phase shifts of the LO are used to isolate the desired signal components [1, 2].

1.2. FMCW Lidar

Frequency Modulated Continuous-Wave (FMCW) lidar is a coherent lidar technique where a laser source is modulated with a linear frequency sweep in time (an optical chirp) and is divided into a LO and TX beam. The transmitted light reflects from the target and returns as the RX field, which interferes with the LO to produce a beat frequency recorded by a photodetector.

Motion of the object along the lidar line of sight produces a time-varying range, expressed as $R(t) = R_0 + \Delta R(t)$, where R_0 denotes the nominal line-of-sight distance to the object, and $\Delta R(t)$ represents its time-dependent displacement. This motion introduces a corresponding time-dependent round-trip propagation delay between the LO and RX optical fields, given by

$$\tau_R(t) = \frac{2(R_0 + \Delta R(t))}{c}, \tag{1}$$

with c being the speed of light. Eq. 1 assumes that changes in object range during the round-trip can be ignored. The conditions on $\Delta R(t)$ will be discussed below.

The photodetector output voltage for a moving or vibrating target can be written as

$$V_b(t) \propto \cos\left(\phi_b(t)\right), \tag{2}$$

where

$$\phi_b(t) = 2\pi\left(\left[\frac{2\kappa R_0 t}{c}\right] + \left[\frac{2R_0}{\lambda} - \frac{2\kappa R_0^2}{c^2}\right] + \left[\frac{2\kappa\Delta R(t)t}{c} + \frac{2\Delta R(t)}{\lambda} - \frac{4\kappa R_0\Delta R(t)}{c^2} - \frac{2\kappa\Delta R(t)^2}{c^2}\right]\right). \tag{3}$$

The first bracketed term is the range-dependent beat frequency at range R_0, the second bracketed term is the static phase contribution from the nominal range R_0, and the third bracketed term represents the time-dependent motion-induced phase. Here, $\kappa = B/\tau_c$ is the chirp rate (in Hz/s), B is the chirp bandwidth, τ_c is the chirp duration, $\lambda = c/f_L$ is the wavelength of the optical carrier, and f_L is the carrier frequency.

The time derivative of the total phase in Eq. (3) defines the instantaneous beat frequency observed at the photodetector. This beat frequency contains contributions from both the nominal range R_0 and the target's motion. The instantaneous beat frequency can be approximated as

$$f_b \approx f_{R_0} + \frac{2\kappa\Delta R(t)}{c} + \frac{2v(t)}{\lambda}, \tag{4}$$

where $f_{R_0} = \frac{2\kappa R_0}{c}$ denotes the range-dependent beat frequency corresponding to the nominal range R_0, and $v(t) = \frac{d\,\Delta R(t)}{dt}$ is the radial velocity of the object. The first two terms represent the range-dependent beat frequency determined by the FMCW chirp, while the third term corresponds to the Doppler shift arising from the object motion. This simplification neglects higher-order chirp–motion coupling effects proportional to $(2\kappa t/c)v(t)$, which are typically small for short chirp durations and moderate object speeds (100 m/s, for $B = 3$ GHz and $\tau_c = 1$ ms).

The range resolution of an FMCW lidar system is $\Delta R_{res} = c/2B$. The velocity resolution of an FMCW lidar system is determined by the optical wavelength and the duration over which the signal is coherently integrated. In most cases, this corresponds to the duration of the chirp τ_c and the velocity resolution can be expressed as

$$\Delta v = \frac{c}{2\tau_{int} f_L}, \tag{5}$$

where τ_{int} is the coherent integration time [3,4].

1.3. Range-Selective Digital Holography

Range-selective digital holography (RSDH) integrates digital holography with the principles of FMCW lidar by employing chirped optical waveforms for both the TX and LO beams,

enabling holograms to be reconstructed at user-selected distances [5–7]. Similar to FMCW lidar, interference between the LO and RX fields produces a beat frequency f_{R_0} for a stationary object at range R_0. Normally, this is undesired since a temporally modulated hologram would wash out during integration. However, if the LO field is frequency-shifted by an amount f_s to compensate for the range-dependent beat f_{R_0}, such that $|f_b| = |f_s - f_{R0}| \ll 1/\tau_{int}$, the interference pattern for a stationary object at range R_0 becomes sufficiently stable to allow coherent integration on a sensor array. In contrast, holograms from objects at other distances, outside of the system's range resolution, are temporally modulated and average out during integration. Holograms of objects that are moving with constant velocity v_0 at range R_0 can also be coherently integrated if $|f_s - (f_{R_0} + 2v_0/\lambda)| < 1/\tau_{int}$ [8]. The range resolution for both FMCW lidar and FMCW RSDH systems has been shown to be equivalent [5, 7]. The procedure of shifting the LO to cancel the range-dependent beat for a stationary object is shown in Figure 1. Here, the LO field is shown to be shifted downward by f_s to cancel the range-dependent beat f_{R_0}. It should be noted that the frequencies are relative, and shifting the LO (versus shifting the TX) is purely a matter of convention.

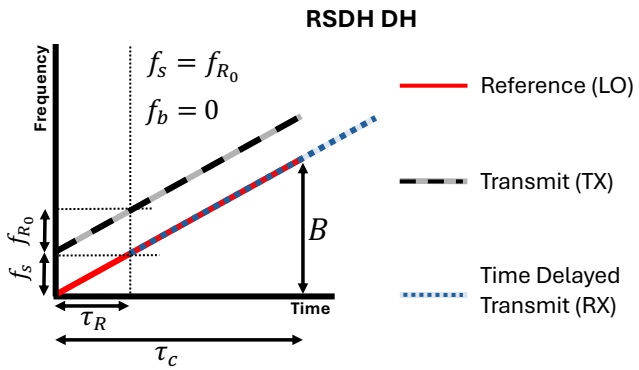


Fig. 1. Conceptual illustration of range-selective digital holography. Under the assumption of a stationary object, if the applied frequency shift f_s equals the range-dependent beat frequency f_{R0}, the resulting hologram will no longer be temporally modulated ($f_b = 0$).

1.4. Holography of Moving or Vibrating Objects

Holography has been extensively employed to detect and analyze the vibrations of objects, including stabilizing or correcting the reconstructed image quality in the presence of motion. A well-studied challenge in this domain is the compensation of motion-induced phase fluctuations, which can significantly degrade holographic reconstructions.

Early approaches addressed random object motion by attaching mirrors to the object and reflecting the reference beam off these mirrors to appropriately phase-modulate the local oscillator field [9–11]. A foundational contribution came from Powell and Stetson, who introduced the method of time-average holography [12]. In their technique, a hologram is recorded while the object undergoes harmonic vibration, and upon reconstruction, fringe patterns emerge that correspond to the vibration amplitudes across the surface, revealing the object's vibrational modes through interference effects. Building on this, later studies combined time-average holography with vibrating or modulated LO fields to extract not only amplitude but also relative phase information of vibrating points [13, 14].

Heterodyne holography techniques, where each path can be frequency shifted using an acousto-

optical frequency shifter (AOFS), have allowed object vibrations at specific tunable frequencies to be canceled, allowing constructive integration of vibrating objects [15]. More recently, an FMCW lidar-based RSDH stabilization system was demonstrated in a controlled laboratory setting with object distances of only a few meters and a limited field of view (FOV) of less than a few centimeters [8]. This technique relied on isolating and filtering the beat frequency from a lidar system and using it to directly modulate an AOFS in the DH LO path to compensate for object-induced Doppler shifts.

We have developed an alternative approach to a combined FMCW lidar and RSDH system that can stabilize digital holograms for coherent integration at demonstrated distances of up to 90 meters in outdoor conditions. This is achieved even when object motion exceeds multiple optical wavelengths during a single integration period by using an FMCW lidar-enabled stabilization system based on phase-frequency detectors (PFD). Phase stabilization is achieved by directly measuring the instantaneous phase of the lidar beat signal and applying a compensating modulation to the RSDH LO. Our novel technique also avoids the use of AOFS, whose limited bandwidth restricts the range window of RSDH. Instead, the developed chirp generation system produces two RF chirps that can be frequency-shifted relative to each other by f_s. This allows the RSDH LO chirp to be offset by up to 480 MHz from the TX chirp before optical modulation, significantly increasing the maximum range window over which RSDH images can be recorded to a hypothetical imaging range window of multiple kilometers.

2. Theory

2.1. Range-Selective Holographic Interference Signals from a Vibrating Target

To account for additional static path differences between the lidar and RSDH beams, such as fiber length or system offsets, we define an additional round-trip delay

$$\tilde{\tau}_R(t) = \tau_R(t) + \frac{2\Delta R_0}{c}, \tag{6}$$

where $2\Delta R_0$ represents the effective static round-trip offset. For a moving or vibrating object, the optical fields for the RSDH LO and RX beams are written as follows.

$$E_{\mathrm{LO}}(x,y,t) = A_{\mathrm{LO}}(x,y)\cos\Big(2\pi(f_L - f_s)t + \pi\kappa t^2 + \phi_{\mathrm{LO}}(x,y)\Big), \tag{7}$$

$$E_{\mathrm{RX}}(x,y,t) = A_{\mathrm{RX}}(x,y)\cos\Big(2\pi f_L\big(t - \tilde{\tau}_R(t)\big) + \pi\kappa\big(t - \tilde{\tau}_R(t)\big)^2 + \phi_{\mathrm{RX}}(x,y)\Big). \tag{8}$$

where f_s is the frequency shift used for nominal range selection, $A_{\mathrm{LO}}(x,y)$ and $A_{\mathrm{RX}}(x,y)$ and $\phi_{\mathrm{LO}}(x,y)$ and $\phi_{\mathrm{RX}}(x,y)$ are the spatial amplitudes and phases of the RSDH LO and RX fields.

The intensity recorded at the sensor array results from interference between the two fields and is given as:

$$I(x,y,t) \propto |A_{\mathrm{LO}}(x,y)|^2 + |A_{\mathrm{RX}}(x,y)|^2 + A_{\mathrm{LO}}(x,y)A_{\mathrm{RX}}(x,y)\cos\left(\phi_{\mathrm{RSDH}}(t) + \Delta\phi(x,y)\right), \tag{9}$$

where

$$\phi_{\mathrm{RSDH}}(t) = 2\pi\left(f_s - f_{\Delta R_0}\right)t - \phi_b(t) + \phi_{\Delta R_0}(t), \tag{10}$$

and $\Delta\phi(x,y) = \phi_{\mathrm{RX}}(x,y) - \phi_{\mathrm{LO}}(x,y)$, and $\phi_{\Delta R_0}(t) = -\frac{4\pi\Delta R_0}{\lambda} + \frac{4\pi\kappa(\Delta R_0)^2}{c^2} + \frac{8\pi\kappa R_0\Delta R_0}{c^2} + \frac{8\pi\kappa\Delta R_0\Delta R(t)}{c^2}$. The range-dependent beat contribution from the additional path length is defined as $f_{\Delta R_0} = \frac{2\kappa(\Delta R_0)}{c}$.

A temporally stable range-selective hologram is obtained for an object at distance R_0 if the RSDH LO frequency shift f_s is tuned such that $|f_s - f_{R_0} - f_{\Delta R_0}| \leq 1/\tau_{\mathrm{int}}$, where τ_{int} is the

sensor integration time. To preserve coherence over the integration, the time-dependent phase contributions must remain $\ll 2\pi$, corresponding to a radial displacement much smaller than $\lambda/2$ for one-way propagation or λ for a round-trip.

However, rapid phase fluctuations on the order of π or less can still reduce fringe contrast and degrade the reconstructed hologram. Active compensation of the time-dependent phase is therefore essential, particularly when the object displacement spans multiple wavelengths during the integration period. In such cases, destructive interference between temporally varying fringes leads to fringe washout and severe image degradation.

2.2. FMCW Lidar Enabled Stabilization

To mitigate the time-dependent phase in the RX field of the digital holographic system, we implement a stabilization scheme in which the RSDH LO field is phase-modulated to compensate for the motion-induced phase shifts in the RSDH RX field. This modulation effectively cancels the object-induced, time-varying phases in Eq. 9, thereby preserving optical coherence throughout the integration period.

The compensating phase is derived from an FMCW lidar subsystem that shares the same RF chirp as the digital holography system. Interference between the lidar LO and RX beams produces an optical beat signal that is detected by a photodetector, producing an output voltage given by Eq. 2. The photodetector output is then mixed with a signal at frequency f_{MIX} and initial phase ϕ_{MIX} from a signal generator. After filtering to suppress the difference-frequency component and amplification, the resulting waveform serves as an input to a phase-frequency detector and is given by

$$V_{\mathrm{RX}}(t) \propto \cos\left(2\pi f_{\mathrm{MIX}} t + \phi_b(t) + \phi_{\mathrm{MIX}}\right). \tag{11}$$

A second RF signal, generated at a tunable frequency f_{LO}, provides the other PFD input:

$$V_{\mathrm{LO}}(t) \propto \cos\left(2\pi f_{\mathrm{LO}} t + \phi_{\mathrm{LO}}\right), \tag{12}$$

where ϕ_{LO} is the initial phase of the signal generator. Up-mixing is required because it shifts the object-dependent beat frequencies from multiple ranges into the optimal frequency band for the PFD input, ensuring peak performance.

The output voltage of the PFD after filtering is proportional to the instantaneous phase difference between the two inputs. In an open-loop configuration, the output of the stabilization system is given as

$$V_{\mathrm{PFD}}(t) \propto \phi_{\mathrm{PFD}}(t) = 2\pi(f_{\mathrm{MIX}} - f_{\mathrm{LO}})t + \phi_b(t) + \phi_{\mathrm{MIX}} - \phi_{\mathrm{LO}}. \tag{13}$$

This error signal drives an electro-optical phase modulator that modulates the RSDH LO in Eq. 7, subtracting the phase of the PDF output ($\phi_{\mathrm{PFD}}(t)$) from the RSDH LO. Finally, the phase of the stabilized RSDH is calculated as the sum of the phases between the RSDH signal given in Eq. 10 and the output of the PFD in Eq. 13 given as

$$\phi_{\text{Stabilized RSDH}} = \phi_{\mathrm{RSDH}}(t) + \phi_{\mathrm{PFD}}(t) = 2\pi\left(f_s + f_{\mathrm{MIX}} - f_{\mathrm{LO}} - f_{\Delta R_0}\right)t + \phi_c + \frac{8\pi\kappa\Delta R_0}{c^2}\,\Delta R(t), \tag{14}$$

where ϕ_c is a constant phase defined as $\phi_c = \phi_{\mathrm{MIX}} - \phi_{\mathrm{LO}} - \frac{4\pi f_L \Delta R_0}{c} + \frac{4\pi\kappa(\Delta R_0)^2}{c^2} + \frac{8\pi\kappa R_0 \Delta R_0}{c^2}$.

The constant phase terms are inconsequential, since only time-varying phase fluctuations affect the holographic coherence and lead to hologram degradation. If the frequencies are chosen such that $(f_s + f_{\mathrm{MIX}} - f_{\mathrm{LO}} - f_{\Delta R_0}) = 0$, the phase contribution of the remaining term due to path length differences becomes negligible unless ΔR_0 is extremely large (many hundreds of

kilometers) or the velocity of the object is significant (km/s scale). This stability limit is obtained by differentiating Eq. 14 and finding the velocity that yields a one radian phase accumulation over the integration time:

$$|v_{\text{crit}}| = \frac{c^2}{8\pi\kappa\Delta R_0 \tau_{\text{int}}}, \tag{15}$$

which represents the critical maximum target velocity before path length differences introduce a one-radian phase shift between the lidar and RSDH systems. Substituting the experimental parameters ($\Delta R_0 \approx 20$ m) yields a critical velocity of approximately 100 km/s, indicating that the path length difference between the lidar and RSDH system is negligible. Also not that although Eq. 15 defines a theoretical velocity limit based on the phase-stability condition, the more practical constraint arises from the PFD input bandwidth and the dynamics of the loop filter. Although PFDs with gigahertz input bandwidths are commercially available, their performance is ultimately limited by the rate at which they can process successive 2π phase wraps through the loop filter without distortion or loss of modulation depth. Consequently, the maximum velocity of the object corresponds to the maximum rate of 2π phase wraps that the PFD and filter chain can resolve. This operational limit defines an effective bandwidth and thus the highest velocity for which stable reconstruction is maintained:

$$|v_{\text{crit}}| = \frac{\lambda}{2}\,\text{BW}_{\text{PFD}}, \tag{16}$$

where BW_{PFD} denotes the maximum resolvable phase-wrapping rate of the PFD and filter chain. The latency of the PFD detection and modulation of the RSDH LO (defined as τ_{PFD}), also comes into play, by introducing an acceleration limit on the object as $|a_{crit}| = \lambda/(2\tau_{int}\tau_{\text{PFD}})$.

Finally, in the above theory, the time-of-flight back from the object was ignored in our expression for $\Delta R(t)$. This time difference would introduce phase shifts that would be common to the lidar and RSDH return signals, and therefore be canceled by the stabilization, as least to first order.

In summary, when the object is stationary, $V_{\text{PFD}}(t)$ produces a constant output voltage, resulting in a fixed bias on the electro-optic phase modulator (EOPM) in the digital holography LO path. For a sinusoidally vibrating object, the PFD output varies sinusoidally (modulo 2π) and is proportional to the time-dependent phase of the RSDH RX field. By phase-modulating the RSDH LO with a signal proportional to this measured phase variation, the time-dependent phase $\phi_b(t)$ in the holographic interference term (Eq. 10) is effectively canceled, thereby stabilizing the interference fringes. As a result, the system preserves coherence over long integration periods, even when the object displacement during integration spans many optical wavelengths. Even under complex or non-linear motion (e.g., oscillatory vibrations or acceleration), the PFD output continues to provide an accurate representation of the time-varying phase.

3. Experimental Procedure

We constructed a combined scanning FMCW lidar and RSDH imaging system using a 6-inch Ritchey-Chrétien telescope mounted on a motorized gimbal [16]. A fast steering mirror (FSM) is used to steer the lidar beam (Optics in Motion OIM 3300). A schematic illustrating the integration of the FMCW lidar, the RSDH system, and the stabilization subsystem is shown in Fig. 2.

The optical source is a narrow-linewidth 1550 nm RIO diode laser (< 15 kHz), which is split into two main optical paths. One path is used exclusively for the digital holography LO, while the other serves as the shared source for the lidar TX, lidar LO, and DH TX beams. Each path is independently modulated with a 1.8 GHz linear frequency chirp using separate electro-optical intensity modulators (EOIMs), creating double-sideband optical signals, resulting in a lidar and RSDH range resolution of $\Delta R_{res} \approx 8.3$ cm.

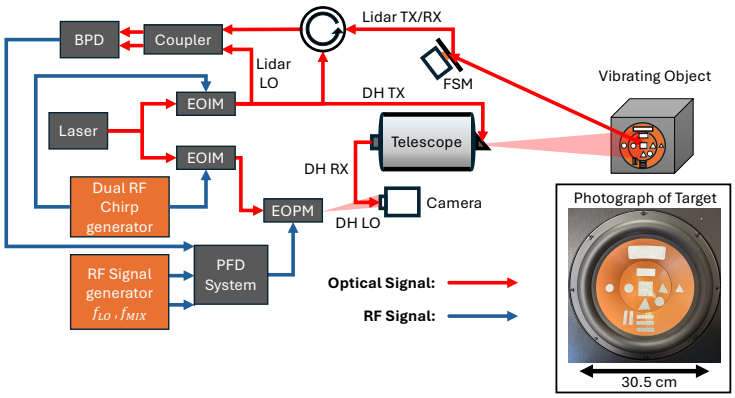


Fig. 2. Scanning FMCW Lidar and RSDH subsystems. The object is a subwoofer speaker with retroreflective tape attached to form a spatial pattern. The speaker is placed 90 meters away from the lidar and RSDH system.

The chirp waveforms that drive the EOIMs (Optilab Intensity Modulators) are generated using a Euvis DDS309 direct digital synthesizer (DDS), whose output is split into two RF lines and frequency-multiplied to increase the chirp bandwidth before driving the EOIMs. The RF output of the dual RF chirp generator that modulated the DH LO can be frequency-shifted relative to the other output. This configuration allows the frequency shift f_s to be easily implemented for RSDH. Because this method directly frequency-shifts the RF chirp rather than using AOFS, the system supports frequency offsets between RF chirps of up to 480 MHz, significantly exceeding what is typically achievable with AOFS. This extended tuning capability enables range-selective holographic reconstructions over a much larger range window, exceeding one kilometer in the current system.

3.1. Target Construction

A 12-inch diameter subwoofer loudspeaker (Klipsch R-12SWI) was used as the target because of its ability to produce controlled repeatable vibrations at known frequencies and amplitudes. The speaker also had the advantage that the center portion of the cone (orange section in the bottom-right image of Figure 2) was rigid and mostly moved in unison. Holograms were recorded while the speaker was powered off (stationary) and while the speaker was driven with a 101 Hz sine wave. The subwoofer amplitude was kept constant between all vibrational experiments. To enhance optical visibility and ensure strong return signals in both the digital holography and FMCW lidar channels, retroreflective tape was applied to the speaker surface, providing spatial features visible in the DH reconstructions.

The target was positioned outdoors at a distance of 90 meters from the combined lidar and RSDH system and tested under full daylight conditions. An image of the target is shown in Figure 2.

3.2. Data Acquisition and Integration

To evaluate stabilization performance, holographic recordings were taken under three conditions. This included continuous-wave (CW) holograms where the FMCW modulation was disabled both with and without target vibration, range-selective digital holograms with and without target vibration, and finally range-selective digital holograms of the vibrating target with the stabilization system enabled.

Holograms are captured using a LUCID InGaAs camera (Atlas IP67) with a resolution of

1280 x 1024 pixels. The chirp source and analog to digital converter (ADC) are triggered simultaneously, providing continuous lidar data over the approximately one-second experiment recording. The camera is externally triggered at 10 Hz and phase-locked to the chirp generation, ensuring that each integration period aligned with the start of a chirp. This also maintained temporal synchronization between the camera integrations and the lidar time-domain signal. Digital holograms are recorded in an off-axis configuration with the DH LO angled onto the sensor array. Hologram processing involved computing a 2-dimensional Fourier transform of the recorded intensity, spatial filtering in the Fourier domain with a mask, and taking an inverse Fourier transform of the masked data to reconstruct the hologram. The same mask was used for all holographic data. The integration time for each camera frame was set to 200 μs for both CW and RSDH recordings, matching the duration of the chirp used for RSDH. The FMCW lidar beam was optically focused near the edge of the speaker to minimize camera saturation while remaining close enough to the center to capture the dominant surface vibrations. All optical signal power levels, including the transmit beams, were kept constant throughout the different RSDH recordings.

The lidar optical beat signal is split into in-phase (I) and quadrature (Q) components using an optical hybrid (Kylia 90° hybrid) and detected on two balanced photodetectors (WeiserLabs). These analog I and Q signals were recorded simultaneously on two input channels of the ADC card (Vitrek GaGe). This configuration allows the range-Doppler ambiguity to be resolved and enables the Doppler frequency to be directly extracted from the lidar data [17–19]. During stabilized RSDH operation, the output from one of the photodetectors is split off and used as the input to the custom-built stabilization system. The phase is detected using an HMC439 phase-frequency detector in combination with a custom loop filter and associated circuitry, as shown in Figure 3. A one-time amplitude adjustment is made so that the peak-to-peak amplitude of the PFD output, $V_{\mathrm{PFD}}(t)$, matched twice the v_π value of the EOPM in the RSDH LO path before being used to drive the modulator.

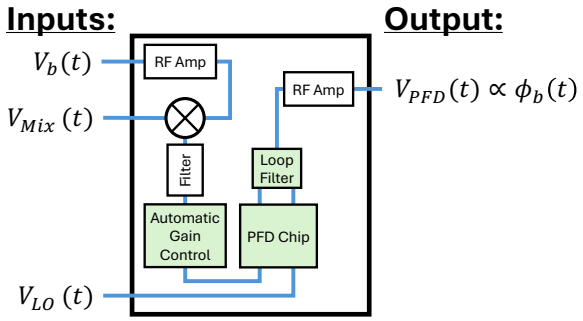


Fig. 3. Schematic the constructed stabilization system. The three inputs are $V_b(t)$, obtained from the photodetector measuring the lidar system's beat frequency, and $V_{\mathrm{MIX}}(t)$ and $V_{\mathrm{LO}}(t)$, which are tones generated from a signal generator. The output signal $V_{\mathrm{PFD}}(t)$ is proportional to the time-varying phase of the RSDH RX field.

Because both the camera and the Gage ADC are triggered in parallel, each recorded frame is aligned in time with a corresponding segment of the lidar Doppler signal. This enabled precise temporal correlation between the recorded holograms and the instantaneous motion of the vibrating target.

The speaker was driven at 101 Hz when vibrating, while the camera was triggered at 10 Hz. This ensured that each frame captured the target in a different phase of its vibration and when 10 frames are captured over 1 second, the system samples the full range of the vibration in equal steps. The amplitude of the vibration was kept constant between measurements.

4. Results

4.1. Quantifying Target Displacement

The speaker's velocity during each holographic recording is computed from the Doppler frequency shifts measured in the lidar data. The instantaneous radial velocity is obtained from the Doppler frequency $f_D(t)$ using

$$v(t) = \frac{f_D(t)\lambda}{2}. \tag{17}$$

In practice, the data are discrete because a single Doppler frequency is computed for each lidar chirp. By concatenating these values over time, a velocity profile of the speaker can be obtained and compared to the frame time stamps. The displacement during each frame can then be estimated by multiplying the object velocity by the sensor array's integration time (assuming that the velocity remains approximately constant over the integration time). Figure 4 shows the Doppler velocity of the speaker when vibrating. A maximum velocity of 0.145 ± 0.004 m/s was recorded, corresponding to a maximum displacement of approximately 18.7λ during the 200 μs integration time, assuming negligible frame-to-frame timing jitter in the 10 Hz camera acquisitions.

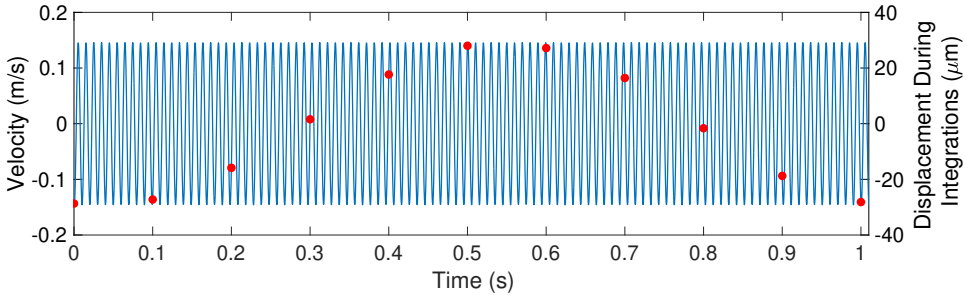


Fig. 4. Measured target Doppler velocity (blue line) and an illustrative example of the speaker displacement during the integration times (red dots) from the lidar system. This example assumes that the first frame is recorded at $t = 0$, with 10 frames recorded per second, each corresponding to a different phase of the speaker vibration.

4.2. Continuous-Wave Digital Holograms of Stationary and Vibrating Targets

To establish a baseline, CW holograms were recorded with FMCW modulation disabled. Figure 5 shows single frame reconstructions of the hologram intensity while the speaker was turned off and when vibrating at 101 Hz. The stationary target produces a clear holographic reconstruction of the object in every frame, whereas the motion of the vibrating target washes out the hologram. The bright spot in both figures is the lidar beam, which is used to monitor the vibration, and is also used for the stabilization system. These results highlight the sensitivity of coherent holographic imaging to radial target motion, as multiple wavelength displacement washed out the holographic reconstruction. The maximum displacement of the target during any single integration could be as large as 18.7λ, depending on where in the vibration cycle the integration occurred.

4.3. Range-Selective Digital Holograms of Stationary and Vibrating Targets

Next, RSDH recordings were performed with FMCW modulation enabled and the stabilization system disabled. This was achieved by measuring the target's range-dependent beat frequency f_{R_0} using the lidar system. The RSDH LO was then shifted by an amount f_s to cancel the range dependent beat for the target distance, R_0, after compensating for constant path length

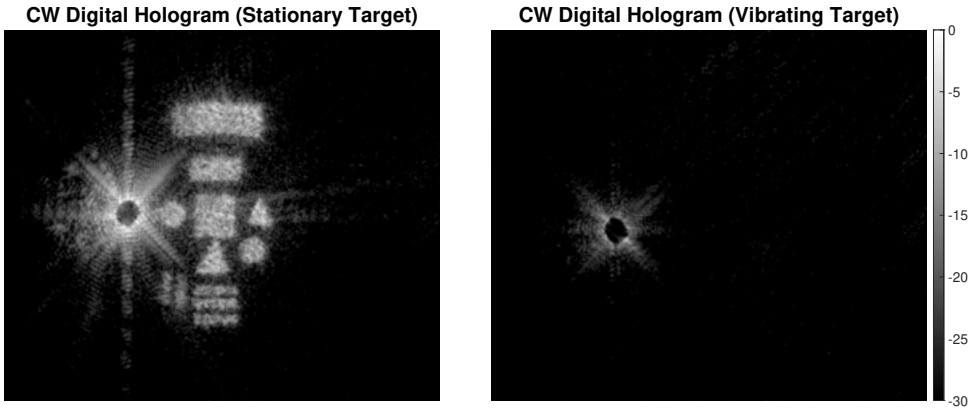


Fig. 5. Reconstructed CW hologram of the speaker when stationary (left) and vibrating (right). Target vibration causes the hologram to wash out during reconstruction. The bright disc near the center left of both images corresponds to the lidar beam. The scale is in dB, normalized to the strongest return in the left image.

differences between the lidar and holography system, ΔR_0. The constant path-length difference serves as a one-time calibration constant for the system. Once correctly shifted, holograms originating from the distance of the speaker will remain temporally stable, whereas return light from objects at ranges outside the chirp range resolution (ΔR_{res}) around R_0 will average to zero. RSDH recordings were taken again with the speaker turned off (stationary) and when vibrating at 101 Hz. Figure 6 shows ten consecutively recorded range-selective digital holograms of the stationary target (labeled A1-A10) and ten consecutively recorded range-selective holograms of the vibrating target (labeled B1-B10).

4.4. Stabilized Range-Selective Digital Holograms of Vibrating Targets

Finally, RSDH holograms of the vibrating speaker were recorded with the stabilization system active. This was carried out by adjusting the frequency of f_{MIX} so that $f_{\mathrm{MIX}} = f_{\mathrm{LO}} - f_{R_0}$, and applying the scaled output voltage of the stabilization system $V_{\mathrm{PFD}}(t)$ to the electro-optical phase modulator in the RSDH LO path. If the modulation voltage is not correctly scaled, even a small percentage error introduces a phase error each cycle. Over many cycles, these errors can accumulate into a phase shift that washes out the hologram, making accurate calibration essential. Figure 6 shows ten consecutive frames to illustrate the effect of real-time phase compensation (labeled C1-C10). The hologram of the speaker reappears in all frames, despite vibration over the full amplitudes and velocity excursions of the speaker. This demonstrates that the stabilization system effectively compensates for time-dependent phase shifts caused by motion, enabling coherent integration even for target displacements that span many optical wavelengths.

However, stabilization of a vibrating hologram does not result in the same holographic strength as when the object is stationary. This is likely due to small calibration errors in the EOPM drive voltage, as well as system inefficiencies such as energy in undesired sidebands of the EOPM, or even a loss of modulation depth in the output modulo 2π signal from the PFD.

5. Conclusion

We have demonstrated a novel stabilization technique for RSDH in which a phase-frequency detector measures the time-dependent phase of an FMCW lidar signal from an object of interest and modulates the RSDH LO phase to compensate for these phase variations in the RSDH return light. By extracting the phase of the lidar beat signal and applying a corresponding modulation

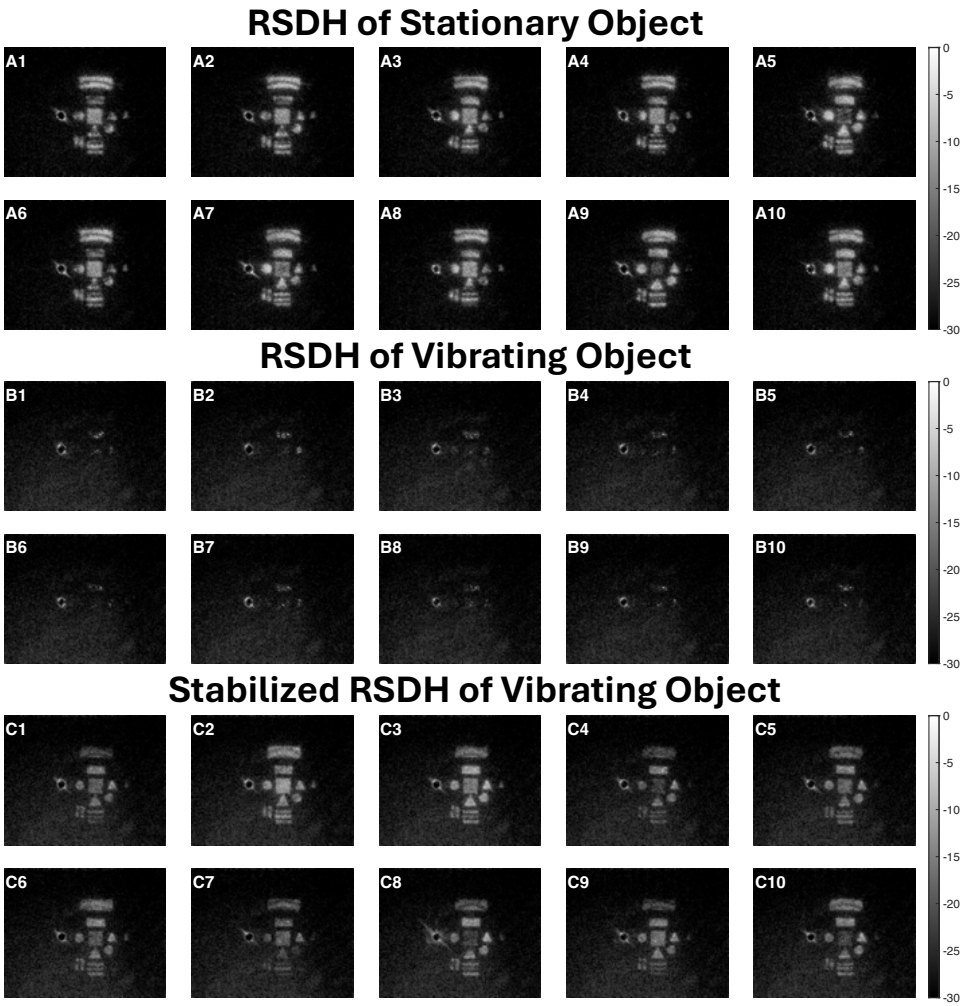


Fig. 6. Ten consecutive RSDH images of the non-vibrating speaker labeled A1-A10 (top). Ten consecutive RSDH images of the vibrating speaker labeled B1-B10 (center). Stabilized RSDH images of the vibrating speaker labeled C1-C10 (bottom). The intensity of the holograms is plotted in a dB scale which is normalized to the range-selective results for the stationary object.

to the RSDH LO, the system effectively corrects vibration-induced phase shifts during coherent integration that would otherwise degrade or blur the reconstructed hologram.

Using this approach, we have successfully imaged vibrating objects with radial displacements exceeding 18 optical wavelengths within a single camera integration period. Unlike previous methods that rely on AOFS, this implementation supports LO frequency shifts up to 480 MHz, extending the operational range window of our stabilized RSDH system potentially beyond a kilometer, assuming the optical powers are significantly increased. In addition, the effective stabilization range window, which is centered on a selected target range, is limited by the bandwidth of the PFD and supporting circuitry. Future work could explore techniques to track f_{R_0} and automatically set f_s and f_{MIX} so the system can stabilize targets as they move over the full RSDH range window.

Funding. Office of Naval Research (N00014-20-1-2260)

Acknowledgments. We gratefully acknowledge funding from the Office of Naval Research. This work relates to Department of Navy award N00014-20-1-2260 issued by the Office of Naval Research. The United States Government has a royalty-free license throughout the world in all copyrightable material contained herein. Any opinions, findings, and conclusions or recommendations expressed in this material are those of the author(s) and do not necessarily reflect the views of the Office of Naval Research.

Disclosures. The authors declare no conflicts of interest.

Data Availability. Data underlying the results presented in this paper are not publicly available at this time but may be obtained from the authors upon reasonable request.

References

1. T.-C. Poon and J.-P. Liu, *Introduction to Modern Digital Holography: With Matlab* (Cambridge University Press, 2014).
2. J. W. Goodman, *Introduction to Fourier Optics* (W. H. Freeman, 2017), hardcover ed.
3. V. Winkler, "Range doppler detection for automotive fmcw radars," in *2007 European Radar Conference,* (2007), pp. 166–169.
4. S. Crouch, "Velocity measurement in automotive sensing: How fmcw radar and lidar can work together," IEEE Potentials **39**, 15–18 (2020).
5. M. A. Goodman, R. K. Mohan, and W. R. Babbitt, "Range selective digital holographic imaging using fmcw lidar," Appl. Opt. **61**, B255–B261 (2022).
6. C. Hammond, W. R. Babbitt, and R. K. Mohan, "Range selective phase-shifting frequency-modulated digital holography with temporal-heterodyning," Appl. Opt. **62**, D157–D162 (2023).
7. C. A. Pearson, R. K. Mohan, and W. R. Babbitt, "Range-selective digital holography for three-dimensional imaging of a complex object," Appl. Opt. **64**, 9169–9177 (2025).
8. M. A. Goodman, R. K. Mohan, and W. R. Babbitt, "Range selective digital holographic imaging of vibrating objects using fmcw lidar," Appl. Opt. **63**, 5642–5652 (2024).
9. F. M. Mottier, "Holography of randomly moving objects," Appl. Phys. Lett. **15**, 44–45 (1969).
10. I. Grant and J. Wang, "Use of reference beam self-feedback phase modulation in the holographic detection of debonding," Appl. Opt. **29**, 1403–1405 (1990).
11. H. Kreitlow, T. Kreis, and W. Jüptner, "Holographic interferometry with reference beams modulated by the object motion," Appl. Opt. **26**, 4256–4262 (1987).
12. R. L. Powell and K. A. Stetson, "Interferometric vibration analysis by wavefront reconstruction," J. Opt. Soc. Am. **55**, 1593–1598 (1965).
13. D. B. Neumann, C. F. Jacobson, and G. M. Brown, "Holographic technique for determining the phase of vibrating objects," Appl. Opt. **9**, 1357–1362 (1970).
14. F. M. Mottier, "Time-averaged holography with triangular phase modulation of the reference wave," Appl. Phys. Lett. **15**, 285–287 (1969).
15. M. Gross, "Heterodyne holography with full control of both the signal and reference arms," Appl. Opt. **55**, A8–A16 (2016).
16. Z. Lakin, C. Pearson, M. Goodman, *et al.*, "Design and implementation of a long range FMCW lidar system in combination with a telescopic FMCW digital holographic imaging system," in *Practical Holography XXXVIII: Displays, Materials, and Applications,* vol. PC12910 P.-A. J. Blanche and S.-H. Lee, eds., International Society for Optics and Photonics (SPIE, 2024), p. PC1291008.
17. S. Suyama, H. Ito, R. Kurahashi, *et al.*, "Doppler velocimeter and vibrometer fmcw lidar with si photonic crystal beam scanner," Opt. Express **29**, 30727–30734 (2021).

18. F. Al-Shaikhli, A. Lamsal, G. Moreira, *et al.*, "Self-homodyne coherent lidar system for range and velocity detection," Opt. Express **32**, 22625–22633 (2024).
19. Y. Zhi, Y. Sun, Y. Zou, *et al.*, "Symmetrical dual-sideband oppositely chirped differential fmcw lidar," Opt. Express **31**, 38114–38131 (2023).

ADDITIONAL MATERIAL

This chapter presents additional experimental and analytical work conducted that supports or extends the main findings, but was not included in the core chapters or related publications. This included FMCW lidar vibrometry techniques, lidar point clouds, and Doppler point clouds. While not all components were published, they provide valuable context and serve as a foundation for potential future work.

FMCW Lidar Vibrometry

As demonstrated earlier in this thesis, the stabilization system was constructed using an FMCW lidar subassembly to measure the vibrations of a target and stabilize the local oscillator in the digital holography system. A natural question that arises is: beyond stabilization, what standalone information about object motion or vibration can be extracted from the FMCW lidar data alone?

One of the advantages of the integrated FMCW lidar and range-selective digital holography system is that each subsystem can be operated independently. In this section, we focus on the vibrometry capabilities of the FMCW lidar alone, without the use of holography.

In the FMCW lidar system, Doppler information is obtained by passing the interference signal through a 90-degree optical hybrid to produce in-phase (I) and quadrature (Q) components. These are then used to construct a complex-valued time-domain signal, as described in the background section. A key question addressed here is whether vibrational signatures can be extracted from this complex signal when it is recorded continuously over many chirps. Additionally, if the vibration frequency changes over time, can this system resolve those changes?

To evaluate the vibrometry performance, a loudspeaker was placed approximately 90 meters from the lidar system and driven to emit constant tonal vibrations at fixed frequencies.

The lidar's IQ time-domain signal was recorded continuously, and the data were segmented in time to analyze the Doppler shift in each segment. For each segment, the instantaneous velocity was computed from the Doppler frequency using:

$$v_D(t) = \frac{f_D(t)\lambda}{2}. \tag{105}$$

Although the velocity is shown here as a continuous function, in practice it is obtained from discrete Doppler frequency values. These estimates are generated by processing successive time windows across the IQ data. Because the sampling rate is much higher than the vibrational frequencies, the discrete velocity series is well approximated as continuous. The temporal resolution, Δt, of the resulting velocity trace was determined by the chosen window (segment) length. To estimate the target's displacement, the Doppler-derived velocity signal can either be numerically integrated over time, or approximated by multiplying each velocity sample by the duration of its corresponding time segment. An example of the time domain segmented data and the subsequent Doppler velocity computed over each chunk is shown in Figure 47. In this example, the time domain data is segmented into 30 chunks, shown in different colors, where each chunk is the beat signal between a single chirp. Only the real part of the complex time domain signal (I only) is shown in the plots. To illustrate the principle, only a short time period is shown to demonstrate the procedure. In practice, many seconds of data can be recorded and processed to determine the doppler frequency or position as a function of time over this longer duration.

Finally, to extract the vibrational frequency content, a Fourier Transform is applied to the time-domain position signal. Figure 48 shows the velocity and frequency spectra for a speaker vibrating at 101 Hz. The segment size used in this analysis was approximately equal to the duration of a single chirp, providing high temporal resolution while preserving

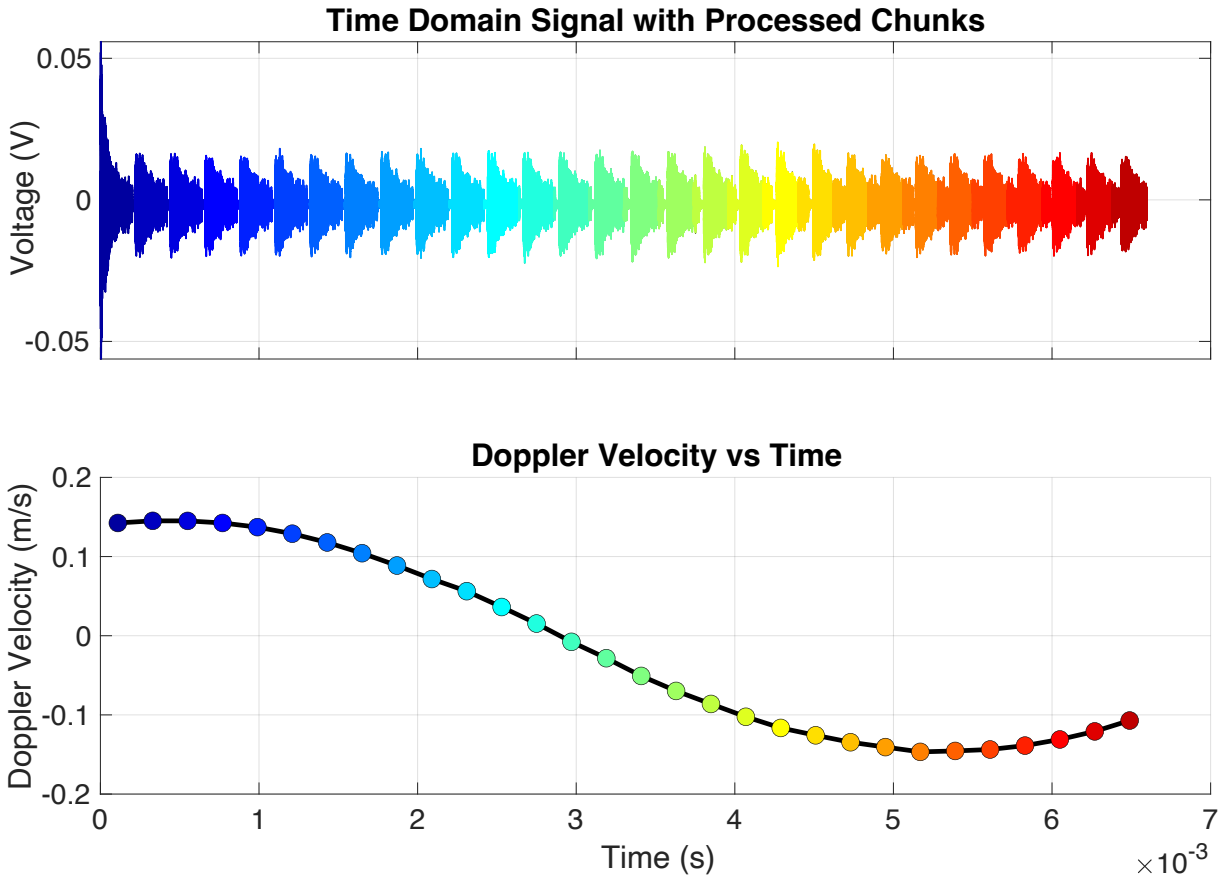


Figure 47: Segmented time-domain data where each segment is shown as a different color and is the recorded beat signal over a single chirp (top). Doppler velocity computed for each segment (bottom). The doppler frequency color is computed from the matching time domain data. Only the real part of the time-domain spectrum is plotted.

spectral accuracy.

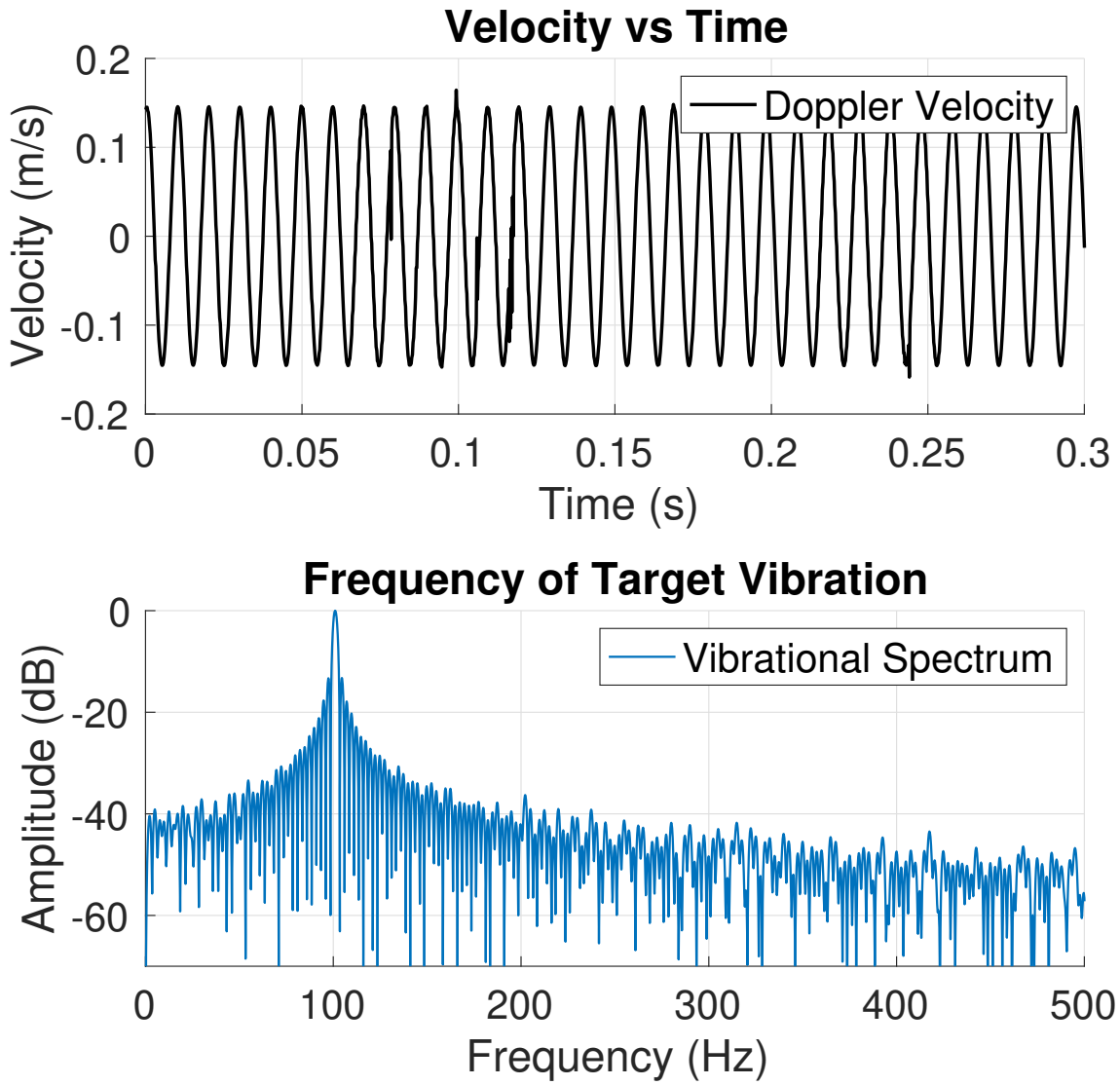


Figure 48: Doppler frequency vs time for 101 Hz speaker (top). Frequency spectrum of the target vibrations (bottom).

The results from the single-tone experiment demonstrate that the dominant vibrational frequency of the speaker can be accurately reconstructed using only the Doppler data from the FMCW lidar. This confirms the system's ability to extract precise vibrational information from a distant target.

A natural extension of this test is to explore how the system performs under more complex, time-varying vibrational inputs. Specifically, can a signal composed of multiple frequencies such as a musical recording be reconstructed from the lidar data?

To investigate this, a second experiment was conducted in which the speaker played a song containing dynamic frequency content over time. The same processing pipeline was applied where IQ data were recorded, segmented, and processed to extract velocity and position. The results of this experiment are presented in the following figures and demonstrate the system's potential for remote acoustic sensing and even coarse audio recovery. Playing the position data as an audio signal reconstructs the original song, opening up the possibility for long range FMCW lidar enabled listening devices, which can be made range selective.

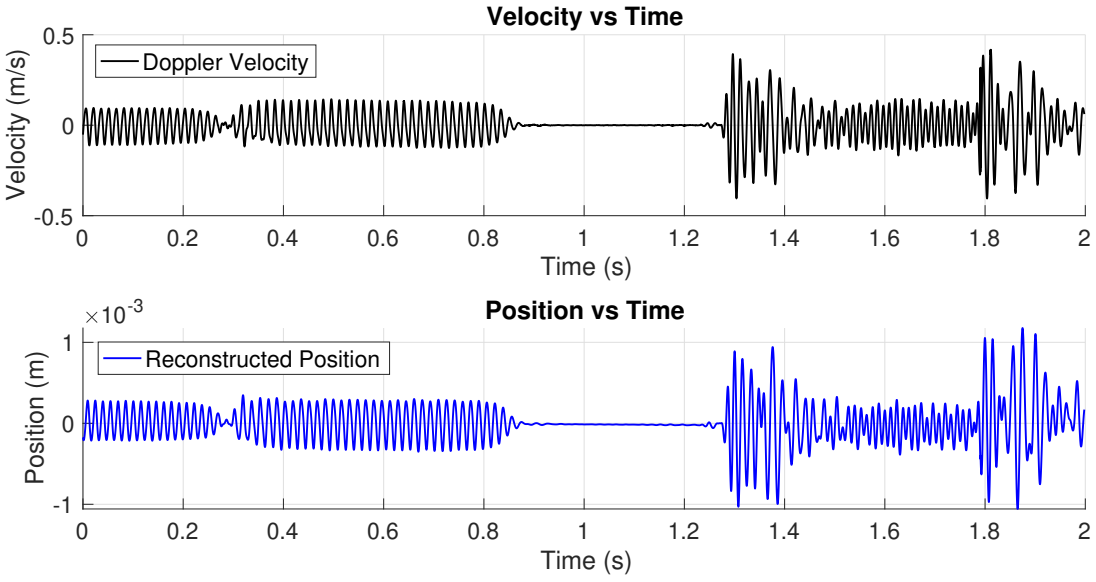


Figure 49: Doppler frequency vs time (top) and position vs time (bottom) of the speaker data when playing a song.

Lidar Point Clouds with Doppler Information

As outlined in a previous section, the hybrid FMCW-lidar and digital holographic system can be operated using only the lidar capabilities to create 3D point cloud images of targets at distances up to a quarter of a kilometer. This can be extended to provide not only the positional information of the target scene but also the Doppler shifts of moving objects. In order to achieve this, the Doppler frequency shift must be computed from the double-sided spectrum matrix $\widehat{\mathbf{P}}_{\mathrm{dB}}[n, i]$, where each row represents the two-sided frequency-domain spectrum of the received signal for the n^{th} mirror position. Because the Doppler frequency of a moving object affects the positive and negative frequency sidebands differently in IQ data, the Doppler velocity can be extracted by comparing these two sidebands. This separation enables the range-dependent beat frequency (which determines range) to be distinguished from the Doppler frequency shift (which determines velocity). For each mirror position, the positive and negative frequency peaks are paired, with their average providing the Doppler estimate and their difference yielding the range-dependent beat. Only pairs with Doppler differences below a doppler threshold are retained which simplified processing. Although true correlation between the positive and negative frequencies can be used to measure Doppler frequency shifts, it requires processing the full frequency spectrum which is computationally intensive and significantly slower than peak-based matching.

Figure 50 presents a 3D point cloud of two people standing in front of a vehicle, with trees in the background. The same data, processed to extract doppler frequency information, is shown below. In this representation, motion relative to the lidar is indicated by color. Red indicates a redshift of the return signal, which corresponds to motion away from the sensor, while blue indicates a blueshift corresponding to motion toward the system. In the figure, the two people are spinning in opposite directions, which is not apparent from the lidar point cloud but becomes obvious in the Doppler point cloud.

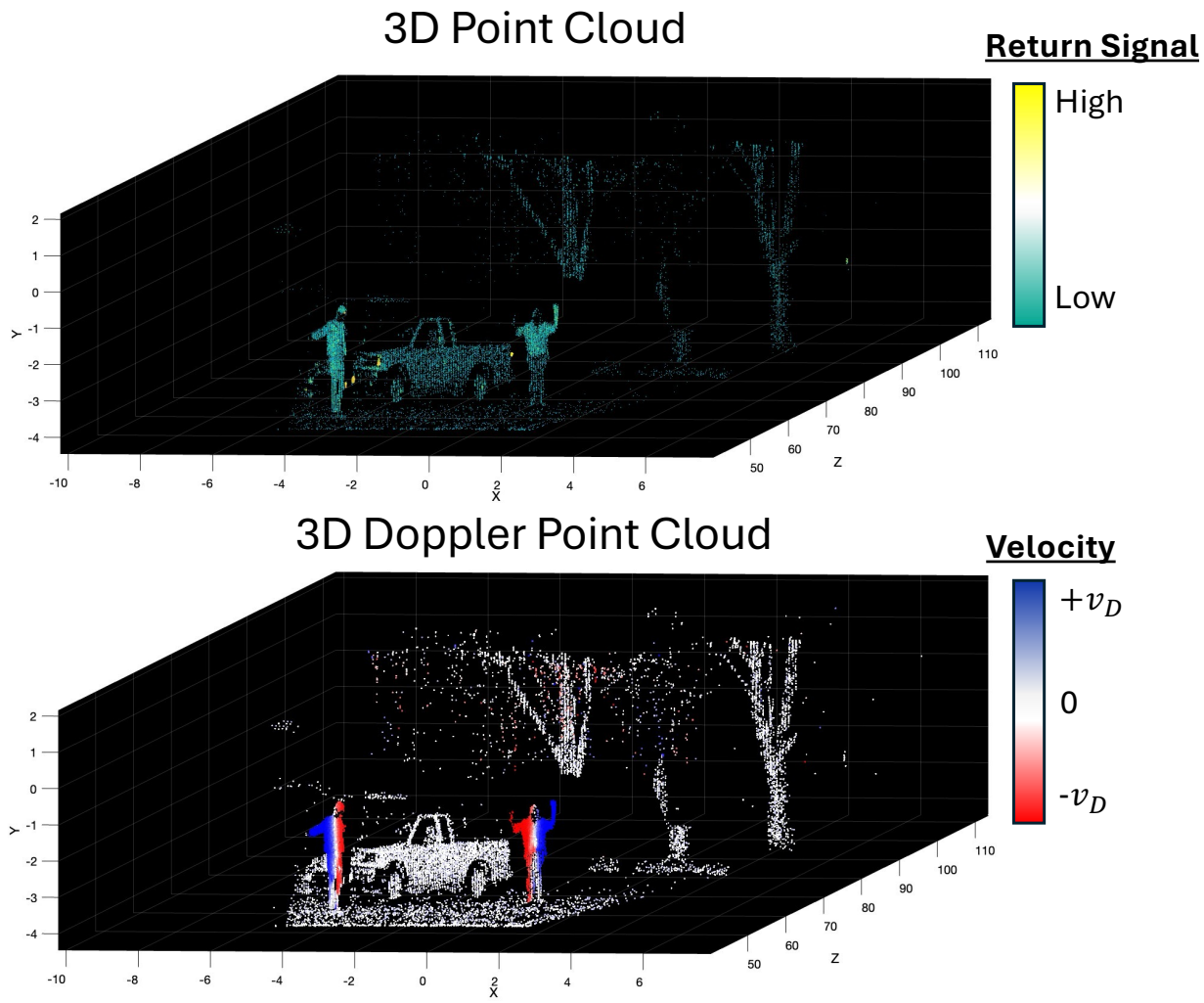


Figure 50: 3D lidar point cloud depicting two people, a vehicle, and trees (top). The same data processed for Doppler information (bottom) shows the two people rotating in opposite directions, while the vehicle and trees remain stationary. The color bars indicate signal strength (top) and object velocity (bottom), with red and blue chosen to represent red and blue shifts, respectively.

CONCLUSION

This thesis investigated advance range-selective digital holography techniques. A key result is the demonstration of a novel on-axis RSDH method that used TH RSDH, and the development of a theoretical model of the detuning effects inherent to RSDH systems when integration occurs over multiple chirps. A second key achievement was the construction of a combined FMCW lidar and RSDH imaging system designed for operations at distances over a kilometer. This system was used to demonstrate, for the first time, stabilized RSDH in outdoor conditions when imaging vibrating objects that move multiple wavelengths during integration.

Research Problem and Objectives

Coherent imaging systems are uniquely capable of producing range-selective, high-resolution 3D reconstructions by exploiting interference between a reference beam and the light scattered from an object. However, conventional off-axis range-selective digital holography suffers from reduced spatial resolution and inefficient sensor usage. This is because the off-axis geometry necessitates spatial filtering in the frequency domain to separate the hologram from background signals. This inefficiency is especially problematic when using high-speed imaging arrays, which benefit from maximizing the use of available pixels. To address this, the research pursued the development of an on-axis technique that leverages temporal heterodyning, allowing for range selectivity without sacrificing spatial resolution.

Additionally, holography is particularly sensitive to object motion, vibration, or phase changes caused by turbulence. These issues are especially pronounced in outdoor imaging, where such disturbances are more prevalent. Consequently, a novel stabilization system, specifically designed for long-range applications, was developed to mitigate these effects and

enable coherent imaging in dynamic environments.

Key Findings and Contributions

This thesis presents several key findings that advance the field of digital holography, particularly in the context of range-selective imaging. The work not only demonstrates new experimental capabilities but also introduces theoretical models and practical techniques that extend the application of holography beyond traditional static or laboratory settings and into outdoor environments. Three key findings have been achieved in this thesis.

- **Temporal Heterodyne On-Axis Holography:** A novel method for range-selective digital holography was developed and demonstrated using temporal heterodyning in an on-axis configuration. This approach enables high frame rates and maximizes sensor bandwidth utilization by avoiding the spatial frequency shifting inherent in off-axis systems and the necessary masking. This represents a significant contribution to the field by demonstrating more efficient and compact holographic imaging techniques. The findings have been presented and published in a peer-reviewed journal [71, 85].

- **Detuning Behavior in Multi-Chirp Systems:** The thesis provides a theoretical and experimental investigation into the effects of local oscillator detuning in holographic systems that integrate over multiple chirped signals. A mathematical framework was developed for temporal-heterodyne RSDH to characterize how detuning influences signal fidelity and range selectivity. These insights are valuable for designing robust holographic systems that operate under imperfect synchronization or when integration occurs over multiple chirps. These results are also applicable to other range-selective holographic techniques that integrate over multiple chirps and has been published in a peer-reviewed journal [86].

- **FMCW Lidar-Enabled Stabilization for Range-Selective Holographic Imaging:** A combined scanning lidar and RSDH system was constructed which included a lidar-enabled phase stabilization system to enable coherent holographic imaging of vibrating objects in outdoor environments. This work demonstrates, for the first time, that range-resolved phase stabilization is feasible over long distances (demonstrated up to 95 meters), opening the door to practical field deployment of digital holography for dynamic scenes. This contribution is particularly impactful by demonstrating coherent imaging systems can still operate in conditions of objects vibration and air turbulence, which would normally prove unfeasible. The results have been compiled into a manuscript which is pending submission.

Together, these findings advance both the theoretical and applied frontiers of digital holography. The methods and models developed in this thesis extend the capabilities of coherent imaging, making it more viable for real-world, long-range, and vibration-prone scenarios.

Implications, Limitations, and Future Work

On-axis holographic systems are easier to align than off-axis systems, use simpler geometries, and most importantly, don't require spatial filtering which reduces the effective resolution. The demonstration of a novel on-axis range selective holographic system which uses temporal-heterodyning is significant because it introduces an easy to align and manufacture range-selective holographic method.

While on-axis holography improves sensor efficiency, it remains more sensitive to object motion due to the additional recordings required for a single reconstruction. ToF detectors generally have much lower pixel counts than CCD sensor arrays, and as ToF arrays scale to higher pixel counts, designers increasingly adopt advanced modulation and demodulation

schemes to manage pixel-to-pixel crosstalk and maintain depth accuracy. These more complex schemes are designed, in part, to limit crosstalk between detectors, but they also complicate the adoption of such cameras for holographic applications. Additionally, while many commercially available ToF detectors use silicon-based sensors, high-pixel-count arrays at longer, more eye-safe wavelengths (e.g., > 1 μm or 1550 nm) remain less prevalent.

While the demonstrated lidar-enabled stabilization technique extends the applicability of digital holography to moving or vibrating objects which are more realistic in outdoor uncontrolled settings, the stabilization system is inherently point-based, as it stabilizes the holography system based on motion at a single spot on the object. For large or non-rigid objects exhibiting non-uniform motion, this approach can introduce errors, since the lidar beam cannot measure the velocity of the entire object. Portions of the object moving or vibrating outside the lidar spot may experience uncorrected phase shifts, resulting in residual image blur or decoherence.

Future research in stabilized RSDH may focus on addressing current limitations through a multi-faceted approach. One potential direction is combining point-based stabilization with advanced post-processing techniques designed to minimize residual phase errors across the object. Alternatively, multi-point stabilization systems could be explored, where multiple lidar beams are used to assess the vibration as well as rotation of the object at different locations.

Tangentially, the lidar-derived vibrometry techniques developed here could potentially be integrated into 3D point-cloud systems, enabling the measurement of vibrational signatures alongside spatial geometry.

In summary, this thesis contributes both theoretical and practical advancements to the field of digital holography, particularly in enabling high-resolution, range-selective imaging under motion. It sets the groundwork for broader use of coherent imaging technologies outside laboratory environments, pushing the boundary of what is possible in remote sensing

and 3D imaging.

REFERENCES CITED

[1] C Maher, Al Naboulsi, H Sizun, and F de Fornel. Fog attenuation prediction for optical and infrared waves. *Opt Eng*, 43(2):319–329, 2004.

[2] Maher Al Naboulsi. Fog attenuation prediction for optical and infrared waves. *Optical Engineering*, 43(2):319, 2004. ISSN 0091-3286. doi: 10.1117/1.1637611. URL https://dx.doi.org/10.1117/1.1637611.

[3] Swapnesh Panigrahi. *Real-time imaging through fog over long distance*. Thesis, 2016.

[4] Luc R. Bissonnette. Imaging through fog and rain. *Optical Engineering*, 31(5):1045, 1992. ISSN 0091-3286. doi: 10.1117/12.56145. URL https://dx.doi.org/10.1117/12.56145.

[5] John D. van der Laan, Brian J. Redman, Jacob W. Segal, Karl Westlake, Jeremy B. Wright, and Brian Z. Bentz. Increased range and contrast in fog with circularly polarized imaging. *Applied Optics*, 62(10):2577–2586, 2023. doi: 10.1364/AO.479271. URL https://opg.optica.org/ao/abstract.cfm?URI=ao-62-10-2577.

[6] Daiki Kijima, Takahiro Kushida, Hiromu Kitajima, Kenichiro Tanaka, Hiroyuki Kubo, Takuya Funatomi, and Yasuhiro Mukaigawa. Time-of-flight imaging in fog using multiple time-gated exposures. *Opt. Express*, 29(5):6453–6467, Mar 2021. doi: 10.1364/OE.416365. URL https://opg.optica.org/oe/abstract.cfm?URI=oe-29-5-6453.

[7] A. W. Lohmann and C. A. Shuman. Image holography through convective fog. *Optics Communications*, 7(2):93–97, 1973. ISSN 0030-4018. doi: https://doi.org/10.1016/0030-4018(73)90075-8. URL https://www.sciencedirect.com/science/article/pii/0030401873900758.

[8] Andrew M Wallace, Abderrahim Halimi, and Gerald S Buller. Full waveform lidar for adverse weather conditions. *IEEE transactions on vehicular technology*, 69(7):7064–7077, 2020. ISSN 0018-9545.

[9] Steven M. Beck, Joseph R. Buck, Walter F. Buell, Richard P. Dickinson, David A. Kozlowski, Nicholas J. Marechal, and Timothy J. Wright. Synthetic-aperture imaging laser radar: laboratory demonstration and signal processing. *Appl. Opt.*, 44(35):7621–7629, Dec 2005. doi: 10.1364/AO.44.007621. URL https://opg.optica.org/ao/abstract.cfm?URI=ao-44-35-7621.

[10] Stephen Crouch, Brant M. Kaylor, Zeb W. Barber, and Randy R. Reibel. Three dimensional digital holographic aperture synthesis. *Opt. Express*, 23(18):23811–23816, Sep 2015. doi: 10.1364/OE.23.023811. URL https://opg.optica.org/oe/abstract.cfm?URI=oe-23-18-23811.

[11] Samuel T. Thurman and James R. Fienup. Phase-error correction in digital holography. *J. Opt. Soc. Am. A*, 25(4):983–994, Apr 2008. doi: 10.1364/JOSAA.25.000983. URL https://opg.optica.org/josaa/abstract.cfm?URI=josaa-25-4-983.

[12] P. Memmolo, Marco Leo, Silvio Montrésor, Cosimo Distante, Melania Paturzo, Pascal Picart, Bahram Javidi, and Pietro Ferraro. Strategies for reducing speckle noise in digital holography accepted article preview. 07 2018. doi: 10.1038/s41377-018-0050-9.

[13] M.C. Roggemann, B.M. Welsh, and B.R. Hunt. *Imaging Through Turbulence*. Laser & Optical Science & Technology. Taylor & Francis, 1996. ISBN 9780849337871. URL https://books.google.com/books?id=nuIC-MkOR4UC.

[14] Joseph W. Goodman. *Statistical Optics*. Wiley, Hoboken, NJ, 2nd edition, 2015. ISBN 978-1-119-00945-0.

[15] Larry C. Andrews and Ronald L. Phillips. *Laser Beam Propagation through Random Media*. SPIE Press, 2nd edition, 2005. ISBN 978-1510643703.

[16] Mark F. Spencer, Robert A. Raynor, Matthias T. Banet, and Dan K. Marker. Deep-turbulence wavefront sensing using digital-holographic detection in the off-axis image plane recording geometry. *Optical Engineering*, 56(3):031213, 2016. doi: 10.1117/1.OE.56.3.031213. URL https://doi.org/10.1117/1.OE.56.3.031213.

[17] Richard A. Muller and Andrew Buffington. Real-time correction of atmospherically degraded telescope images through image sharpening. *J. Opt. Soc. Am.*, 64(9):1200–1210, Sep 1974. doi: 10.1364/JOSA.64.001200. URL https://opg.optica.org/abstract.cfm?URI=josa-64-9-1200.

[18] Joseph C. Marron, Richard L. Kendrick, Nathan Seldomridge, Taylor D. Grow, and Thomas A. Höft. Atmospheric turbulence correction using digital holographic detection: experimental results. *Opt. Express*, 17(14):11638–11651, Jul 2009. doi: 10.1364/OE.17.011638. URL https://opg.optica.org/oe/abstract.cfm?URI=oe-17-14-11638.

[19] Samuel T. Thurman. Phase-error correction in digital holography using single-shot data. *J. Opt. Soc. Am. A*, 36(12):D47–D61, Dec 2019. doi: 10.1364/JOSAA.36.000D47. URL https://opg.optica.org/josaa/abstract.cfm?URI=josaa-36-12-D47.

[20] Abbie E. Tippie and James R. Fienup. Multiple-plane anisoplanatic phase correction in a laboratory digital holography experiment. *Opt. Lett.*, 35(19):3291–3293, Oct 2010. doi: 10.1364/OL.35.003291. URL https://opg.optica.org/ol/abstract.cfm?URI=ol-35-19-3291.

[21] Cameron J. Radosevich, Casey J. Pellizzari, Samuel Horst, and Mark F. Spencer. Imaging through deep turbulence using single-shot digital holography data. *Opt. Express*, 28(13):19390–19401, Jun 2020. doi: 10.1364/OE.395674. URL https://opg.optica.org/oe/abstract.cfm?URI=oe-28-13-19390.

[22] Casey J. Pellizzari, Mark F. Spencer, and Charles A. Bouman. Imaging through distributed-volume aberrations using single-shot digital holography. *J. Opt. Soc. Am. A*, 36(2):A20–A33, Feb 2019. doi: 10.1364/JOSAA.36.000A20. URL https://opg.optica.org/josaa/abstract.cfm?URI=josaa-36-2-A20.

[23] Atsushi Wada and Yoko Miyamoto. Wavelength scanning digital holography using temporal fourier transform. pages 1–2. IEEE, 2015. doi: 10.1109/WIO.2015.7206911.

[24] Jing Gao, N. Anantrasirichai, and David Bull. Atmospheric turbulence removal using convolutional neural network, 2019. URL https://arxiv.org/abs/1912.11350.

[25] Casey J. Pellizzari, Timothy J. Bate, Kevin P. Donnelly, Gregery T. Buzzard, Charles A. Bouman, and Mark F. Spencer. Coherent plug-and-play artifact removal: Physics-based deep learning for imaging through aberrations. *Optics and Lasers in Engineering*, 164: 107496, 2023. ISSN 0143-8166. doi: https://doi.org/10.1016/j.optlaseng.2023.107496. URL https://www.sciencedirect.com/science/article/pii/S0143816623000258.

[26] Casey J. Pellizzari, Timothy J. Bate, Maya G. Mandyam, Cameron J. Radosevich, Samuel Horst, and Mark F. Spencer. Speckle-free coherent imaging through deep turbulence. *Opt. Lett.*, 49(12):3508–3511, Jun 2024. doi: 10.1364/OL.520540. URL https://opg.optica.org/ol/abstract.cfm?URI=ol-49-12-3508.

[27] Zeb W. Barber, Wm. Randall Babbitt, Brant Kaylor, Randy R. Reibel, and Peter A. Roos. Accuracy of active chirp linearization for broadband frequency modulated continuous wave ladar. *Appl. Opt.*, 49(2):213–219, Jan 2010. doi: 10.1364/AO.49.000213. URL https://opg.optica.org/ao/abstract.cfm?URI=ao-49-2-213.

[28] Peter A. Roos, Randy R. Reibel, Trenton Berg, Brant Kaylor, Zeb W. Barber, and Wm. Randall Babbitt. Ultrabroadband optical chirp linearization for precision metrology applications. *Opt. Lett.*, 34(23):3692–3694, Dec 2009. doi: 10.1364/OL.34.003692. URL https://opg.optica.org/ol/abstract.cfm?URI=ol-34-23-3692.

[29] Louis Cuellar, Sami Shakir, David Voelz, Mark Spencer, and John Vera Cruz. Digital holography three-dimensional imaging using frequency chirping of a laser. In Jean J. Dolne and Mark F. Spencer, editors, *Unconventional Imaging and Adaptive Optics 2020*, volume 11508, page 115080H. International Society for Optics and Photonics, SPIE, 2020. doi: 10.1117/12.2570395. URL https://doi.org/10.1117/12.2570395.

[30] Atsushi Wada and Yoko Miyamoto. Wavelength scanning digital holography using temporal fourier transform. In *2015 14th Workshop on Information Optics (WIO)*, pages 1–2, 2015. doi: 10.1109/WIO.2015.7206911.

[31] Louis Cuellar, Sami A. Shakir, David Voelz, Mark F. Spencer, and John Vera Cruz. Digital holography three-dimensional imaging using frequency chirping of a laser. SPIE. doi: 10.1117/12.2570395. URL https://dx.doi.org/10.1117/12.2570395.

[32] Brian W. Krause, Bruce G. Tiemann, and Philip Gatt. Motion compensated frequency modulated continuous wave 3d coherent imaging ladar with scannerless architecture. *Appl. Opt.*, 51(36):8745–8761, Dec 2012. doi: 10.1364/AO.51.008745. URL https://opg.optica.org/ao/abstract.cfm?URI=ao-51-36-8745.

[33] M. Yokota, T. Ishikawa, and N. Aoki. Polarization analysis of the object wave using FMCW-digital holography. In Peter Lehmann, Wolfgang Osten, and Armando Albertazzi Gonçalves, editors, *Optical Measurement Systems for Industrial Inspection XI*, volume 11056 of *Society of Photo-Optical Instrumentation Engineers (SPIE) Conference Series*, page 110563R, June 2019. doi: 10.1117/12.2525698.

[34] Hikaru Hamada and Masayuki Yokota. Two-wavelength digital holography using frequency-modulated continuous-wave technique for multiplexing in the time–frequency domain. *Optical Review*, 30(6):595–605, December 2023. doi: 10.1007/s10043-023-00840-w.

[35] Stephen Crouch and Zeb W. Barber. Laboratory demonstrations of interferometric and spotlight synthetic aperture ladar techniques. *Opt. Express*, 20(22):24237–24246, Oct 2012. doi: 10.1364/OE.20.024237. URL https://opg.optica.org/oe/abstract.cfm?URI=oe-20-22-24237.

[36] Matthew A. Goodman, R. Krishna Mohan, and Wm. Randall Babbitt. Range selective digital holographic imaging using fmcw lidar. In *Digital Holography and 3-D Imaging 2022*, page W7A.2. Optica Publishing Group, 2022. doi: 10.1364/DH.2022.W7A.2. URL https://opg.optica.org/abstract.cfm?URI=DH-2022-W7A.2.

[37] Corey Pearson. *Frequency-modulated continuous-wave digital holography for outdoor three-dimensional imaging*. Thesis, 2025.

[38] Matthias Germann, Tatiana Latychevskaia, Conrad Escher, and Hans-Werner Fink. Pulsed electron holography. *Applied Physics Letters*, 102(20), May 2013. ISSN 1077-3118. doi: 10.1063/1.4807661. URL http://dx.doi.org/10.1063/1.4807661.

[39] Ian Grant and Jianmin Wang. Use of reference beam self-feedback phase modulation in the holographic detection of debonding. *Appl. Opt.*, 29(10):1403–1405, Apr 1990. doi: 10.1364/AO.29.001403. URL https://opg.optica.org/ao/abstract.cfm?URI=ao-29-10-1403.

[40] Horst Kreitlow, Thomas Kreis, and Werner Jüptner. Holographic interferometry with reference beams modulated by the object motion. *Appl. Opt.*, 26(19):4256–4262, Oct 1987. doi: 10.1364/AO.26.004256. URL https://opg.optica.org/ao/abstract.cfm?URI=ao-26-19-4256.

[41] François M Mottier. Holography of randomly moving objects. *Applied Physics Letters*, 15(2):44–45, 1969.

[42] James P. Waters. Object motion compensation by speckle reference beam holography. *Appl. Opt.*, 11(3):630–636, Mar 1972. doi: 10.1364/AO.11.000630. URL https://opg.optica.org/ao/abstract.cfm?URI=ao-11-3-630.

[43] R.M Galloway. Coherent imaging via temporal heterodyne and spatial shearing methods. Master's thesis, Montana State University, 2018.

[44] Matthew A. Goodman, R. Krishna Mohan, and Wm. Randall Babbitt. Range selective digital holographic imaging of vibrating objects using fmcw lidar. *Appl. Opt.*, 63(21): 5642–5652, Jul 2024. doi: 10.1364/AO.528983. URL https://opg.optica.org/ao/abstract.cfm?URI=ao-63-21-5642.

[45] Paul Mcmanamon. *LiDAR Technologies and Systems*. 07 2019. ISBN 9781510625396. doi: 10.1117/3.2518254.

[46] Jesse Zheng. Analysis of optical frequency-modulated continuous-wave interference. *Appl. Opt.*, 43(21):4189–4198, Jul 2004. doi: 10.1364/AO.43.004189. URL https://opg.optica.org/ao/abstract.cfm?URI=ao-43-21-4189.

[47] Jesse Zheng. *Optical frequency-modulated continuous-wave (FMCW) interferometry*. Springer Series in Optical Sciences. Springer, New York, NY, 2005 edition, January 2005.

[48] *Semiconductor Photon Detectors*, chapter 17, pages 644–695. John Wiley & Sons, Ltd, 1991. ISBN 9780471213741. doi: https://doi.org/10.1002/0471213748.ch17. URL https://onlinelibrary.wiley.com/doi/abs/10.1002/0471213748.ch17.

[49] Bengt Edlén. The refractive index of air. *Metrologia*, 2(2):71, apr 1966. doi: 10.1088/0026-1394/2/2/002. URL https://doi.org/10.1088/0026-1394/2/2/002.

[50] Philip E. Ciddor. Refractive index of air: new equations for the visible and near infrared. *Appl. Opt.*, 35(9):1566–1573, Mar 1996. doi: 10.1364/AO.35.001566. URL https://opg.optica.org/ao/abstract.cfm?URI=ao-35-9-1566.

[51] A. Voronin and A. Zheltikov. The generalized sellmeier equation for air. *Scientific Reports*, 7:srep46111, 08 2017. doi: 10.1038/srep46111.

[52] *Electro-Optics*, chapter 18, pages 696–736. John Wiley & Sons, Ltd, 1991. ISBN 9780471213741. doi: https://doi.org/10.1002/0471213748.ch18. URL https://onlinelibrary.wiley.com/doi/abs/10.1002/0471213748.ch18.

[53] A. Loayssa, D. Benito, and M. J. Garde. Single-sideband suppressed-carrier modulation using a single-electrode electrooptic modulator. *IEEE Photonics Technology Letters*, 13 (8):869–871, 2001. ISSN 1041-1135. doi: 10.1109/68.935831. URL https://dx.doi.org/10.1109/68.935831.

[54] Colton Richard Stiffler, Scott Henry Bekker, Kristian D Merkel, Randy R Reibel, William R Babbitt, and Krishna Mohan Rupavatharam. Techniques for single sideband suppressed carrier (ssbsc) optical signals that scale to bandwidths over 20 gigahertz, 2015.

[55] Jesse Zheng. Optical frequency-modulated continuous-wave interferometers. *Applied Optics*, 45(12), 4 2006. ISSN 0003-6935. doi: 10.1364/AO.45.0. URL https://www.osti.gov/biblio/20779327.

[56] Fatima Al-Shaikhli, Anjana Lamsal, Gustavo Moreira, Maurice O'Sullivan, and Rongqing Hui. Self-homodyne coherent lidar system for range and velocity detection. *Opt. Express*, 32(13):22625–22633, Jun 2024. doi: 10.1364/OE.523198. URL https://opg.optica.org/oe/abstract.cfm?URI=oe-32-13-22625.

[57] Yanan Zhi, Yujiao Sun, Yu Zou, Bijun Xu, and Kehan Tian. Symmetrical dual-sideband oppositely chirped differential fmcw lidar. *Opt. Express*, 31(23):38114–38131, Nov 2023. doi: 10.1364/OE.501555. URL https://opg.optica.org/oe/abstract.cfm?URI=oe-31-23-38114.

[58] Joseph W Goodman and RW Lawrence. Digital image formation from electronically detected holograms. *Applied physics letters*, 11(3):77–79, 1967. ISSN 0003-6951.

[59] Ting-Chung Poon and Jung-Ping Liu. *Introduction to Modern Digital Holography: With Matlab*. Cambridge University Press, 2014.

[60] Augustin Jean Fresnel. Memoire sur la diffraction de la lumiere. *Memoires de l'Academie des sciences, serie 5*, V, 1826. Presented 29 July 1818; awarded Grand Prix de Physique 1819.

[61] Joseph W Goodman. Introduction to fourier optics. *Introduction to Fourier optics, 3rd ed., by JW Goodman. Englewood, CO: Roberts & Co. Publishers, 2005*, 1, 2005.

[62] Adam Konijnenberg and Arthur Urbach. 6.6: Fresnel and fraunhofer approximations. In Adam Konijnenberg and Arthur Urbach, editors, *Scalar Diffraction Optics*. LibreTexts, 2022. URL https://phys.libretexts.org/Bookshelves/Optics/BSc_Optics_(Konijnenberg_Adam_and_Urbach)/06%3A_Scalar_diffraction_optics/6.07%3A_Fresnel_and_Fraunhofer_Approximations. Accessed: 2025-10-30.

[63] Emmett N. Leith and Juris Upatnieks. Reconstructed wavefronts and communication theory∗. *J. Opt. Soc. Am.*, 52(10):1123–1130, Oct 1962. doi: 10.1364/JOSA.52.001123. URL https://opg.optica.org/abstract.cfm?URI=josa-52-10-1123.

[64] Emmett N. Leith and Juris Upatnieks. Wavefront reconstruction with continuous-tone objects∗. *J. Opt. Soc. Am.*, 53(12):1377–1381, Dec 1963. doi: 10.1364/JOSA.53.001377. URL https://opg.optica.org/abstract.cfm?URI=josa-53-12-1377.

[65] Dennis Gabor. A new microscopic principle. 1948.

[66] Ichirou Yamaguchi and Tong Zhang. Phase-shifting digital holography. *Opt. Lett.*, 22 (16):1268–1270, Aug 1997. doi: 10.1364/OL.22.001268. URL https://opg.optica.org/ol/abstract.cfm?URI=ol-22-16-1268.

[67] Lingfeng Yu and Myung K. Kim. Wavelength-scanning digital interference holography for tomographic three-dimensional imaging by use of the angular spectrum method. *Opt. Lett.*, 30(16):2092–2094, Aug 2005. doi: 10.1364/OL.30.002092. URL https://opg.optica.org/ol/abstract.cfm?URI=ol-30-16-2092.

[68] Louis Cuellar, Sami Shakir, David Voelz, Mark Spencer, and John Cruz. Digital holography three-dimensional imaging using frequency chirping of a laser. page 16, 08 2020. doi: 10.1117/12.2570395.

[69] Wada Atsushi and Miyamoto Yoko. Wavelength scanning digital holography using temporal fourier transform. *2015 14th Workshop on Information Optics (WIO)*, 06 2015. doi: 10.1109/wio.2015.7206911. URL https://cir.nii.ac.jp/crid/1873116917978581376.

[70] Atsushi Wada, Makoto Kato, and Yukihiro Ishii. Multiple-wavelength digital holographic interferometry using tunable laser diodes. *Appl. Opt.*, 47(12):2053–2060, Apr 2008. doi: 10.1364/AO.47.002053. URL https://opg.optica.org/ao/abstract.cfm?URI=ao-47-12-2053.

[71] Cole Hammond, Wm. Randall Babbitt, and R. Krishna Mohan. Range selective phase-shifting frequency-modulated digital holography with temporal-heterodyning. *Appl. Opt.*, 62(10):D157–D162, Apr 2023. doi: 10.1364/AO.478525. URL https://opg.optica.org/ao/abstract.cfm?URI=ao-62-10-D157.

[72] Corey A. Pearson, R. Krishna Mohan, and Wm. Randall Babbitt. Range-selective digital holography for three-dimensional imaging of a complex object. *Appl. Opt.*, 64 (31):9169–9177, Nov 2025. doi: 10.1364/AO.573746. URL https://opg.optica.org/ao/abstract.cfm?URI=ao-64-31-9169.

[73] Reinhard W. Meier. Depth of focus and depth of field in holography. *J. Opt. Soc. Am.*, 55(12), Dec 1965. doi: 10.1364/JOSA.55.1693_1. URL https://opg.optica.org/abstract.cfm?URI=josa-55-12-1693_1.

[74] Harold Merklinger. *The ins and outs of focus: an alternative way to estimate depth-of-field and sharpness in the photographic image*. Seabord Printing Limited, Nova Scotia, 1992. ISBN 0-9695025-0-8. URL http://www.trenholm.org/hmmerk/.

[75] Larry Li. Time-of-flight camera - an introduction. White Paper, Texas Intruments, 2014. URL: https://www.ti.com/lit/wp/sloa190b/sloa190b.pdf.

[76] *SentisToF - M100 Time-of-Flight Smart Sensor*. Bluetechnix GmbH, Waidhausenstrabe 3/19, 1140 Wien, Austria, 2016.

[77] Bluetechnix GmbH. *Sentis-ToF-M100 Software User Manual, Version 10*. Waidhausenstraße 3/19, 1140 Vienna, Austria, February 2016. URL https://datasheets.becom-group.com/goto/Sentis/ToF/M/100/Sentis-ToF-M100_SUM_V10.pdf. Document No.: 900-308 / A; Publication date: 11 February 2016.

[78] Texas Instruments Incorporated. *OPT8241 3D Time-of-Flight Sensor Datasheet (Rev B)*. Dallas, TX, USA, Oct 2015. URL https://www.mouser.com/ds/2/405/opt8241-1141069.pdf. SBAS704B – June 2015, revised October 2015.

[79] LUCID Vision Labs. *Helios2+ Time-of-Flight (ToF) IP67 3D Camera — Specification Sheet*, 2025. URL https://www.1stvision.com/cameras/Lucid-Vision-Labs/dataman/Lucid%20Vision%20Labs%20Helios2%2B%20Specifications.pdf. Spec sheet; accessed 2025-10-30.

[80] Euvis, Inc. *DDS Based Arbitrary Chirping Module - DSM309*. Euvis, Newbury Park, CA, USA. URL https://www.euvis.com/products/mod/dsm/dsm309/index.html. Product Information Page.

[81] Jaime Neeley. Opto-mechanical design and analysis for coherent active imaging. Master's thesis, Montana State University, 2022.

[82] Optics In Motion, LLC. *OIM3300G Specification Sheet*, 2019. URL https://opticsinmotion.org/wp-content/uploads/2019/09/OIM3300G-Specification-Sheet-3-20-2014.pdf. Version 3-20-2014.

[83] Floyd M. Gardner. *Phaselock Techniques*. John Wiley & Sons, Hoboken, NJ, USA, 3 edition, 2005.

[84] Analog Devices, Inc. *HMC439 - Phase/Frequency Detector*. Analog Devices, Norwood, MA, USA, 2015. URL https://www.analog.com/media/en/technical-documentation/data-sheets/hmc439.pdf.

[85] Cole Hammond, Wm. Randall Babbitt, and R. Krishna Mohan. Range selective frequency-modulated digital holography with temporal-heterodyning. In Pierre-Alexandre J. Blanche and Seung-Hyun Lee, editors, *Practical Holography XXXVIII: Displays, Materials, and Applications*, volume 12910, page 1291008. International Society for Optics and Photonics, SPIE, 2024. doi: 10.1117/12.3003276. URL https://doi.org/10.1117/12.3003276.

[86] Cole Hammond, R. Krishna Mohan, and Wm. Randall Babbitt. Frequency detuning analysis in multi-chirp range-selective digital holography with temporal heterodyning. *Appl. Opt.*, 64(27):8077–8087, Sep 2025. doi: 10.1364/AO.571313. URL https://opg.optica.org/ao/abstract.cfm?URI=ao-64-27-8077.

APPENDIX

EXPERIMENTAL SETUPS AND COMPONENTS

This appendix presents figures for all experimental setups used in this work, along with a list of the key components employed in each system.

Temporal-Heterodyne Holographic System

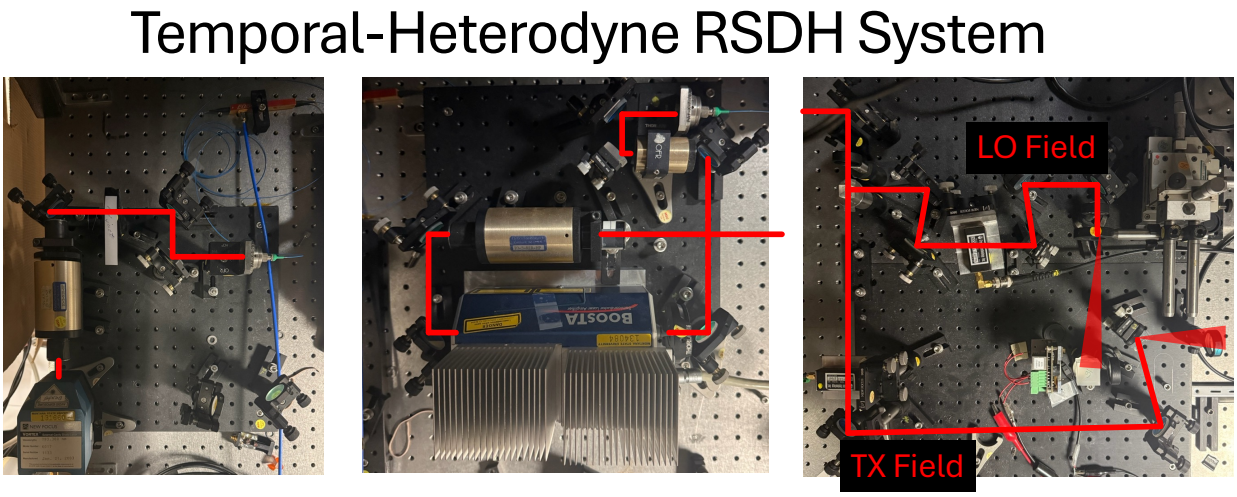


Figure 51: Range-Selective Temporal Heterodyne Digital Holography System.

Table 1: Key components used in the Temporal-Heterodyne RSDH System.

Component	**Description / Model**
Laser	793 nm Vortex Diode, 19 mW output
Electro-optical Phase Modulator	EOspace Phase Modulator
Free-space Amplifier	Boosta 2 W Optical Amplifier
Acousto-optical Frequency Shifters	Crystal Technologies AOMs
Time-of-flight Camera	Sentis M100 ToF Detector
Signal Generators (LO)	Hewlett Packer (E4432B)
Signal Generator (RX)	TPI Synthesizer (TPI-1001-A)

Combined Lidar and RSDH imaging System

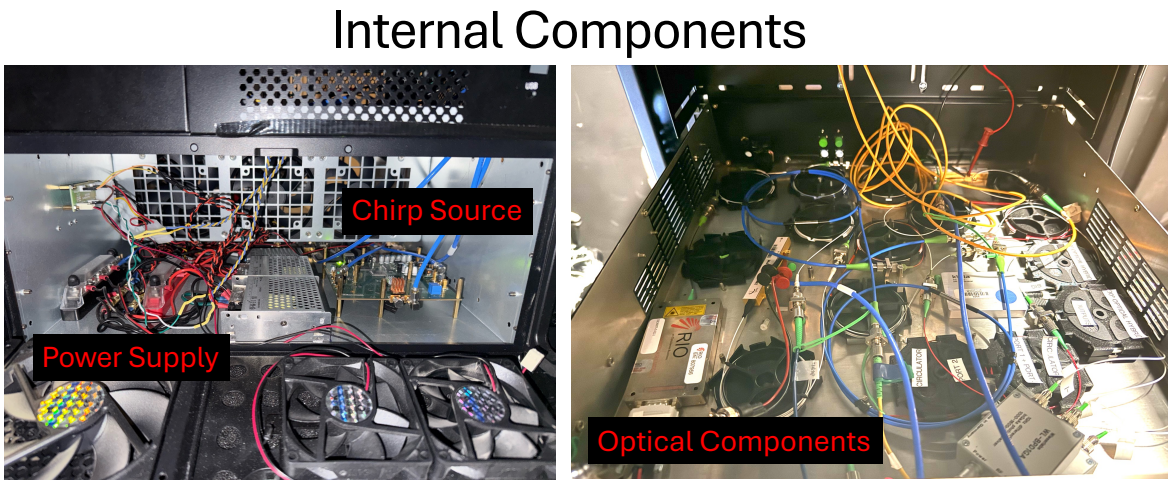


Figure 52: Internal components of the combined lidar and RSDH system.

Table 2: Key components used in the Chirped-RSDH System.

Component	**Description / Model**
Laser	1550 nm RIO Diode Laser
Chirp Source	Euvis 309 DSM Chirp Board
Signal Generator (Lidar)	TPI Synthesizer (TPI-1001-A)
Signal Generator (RSDH LO)	Hewlett Packer (E4432B)
Electro-optical Modulators	Optilab Phase Modulator and Optilab Intensity Modulator

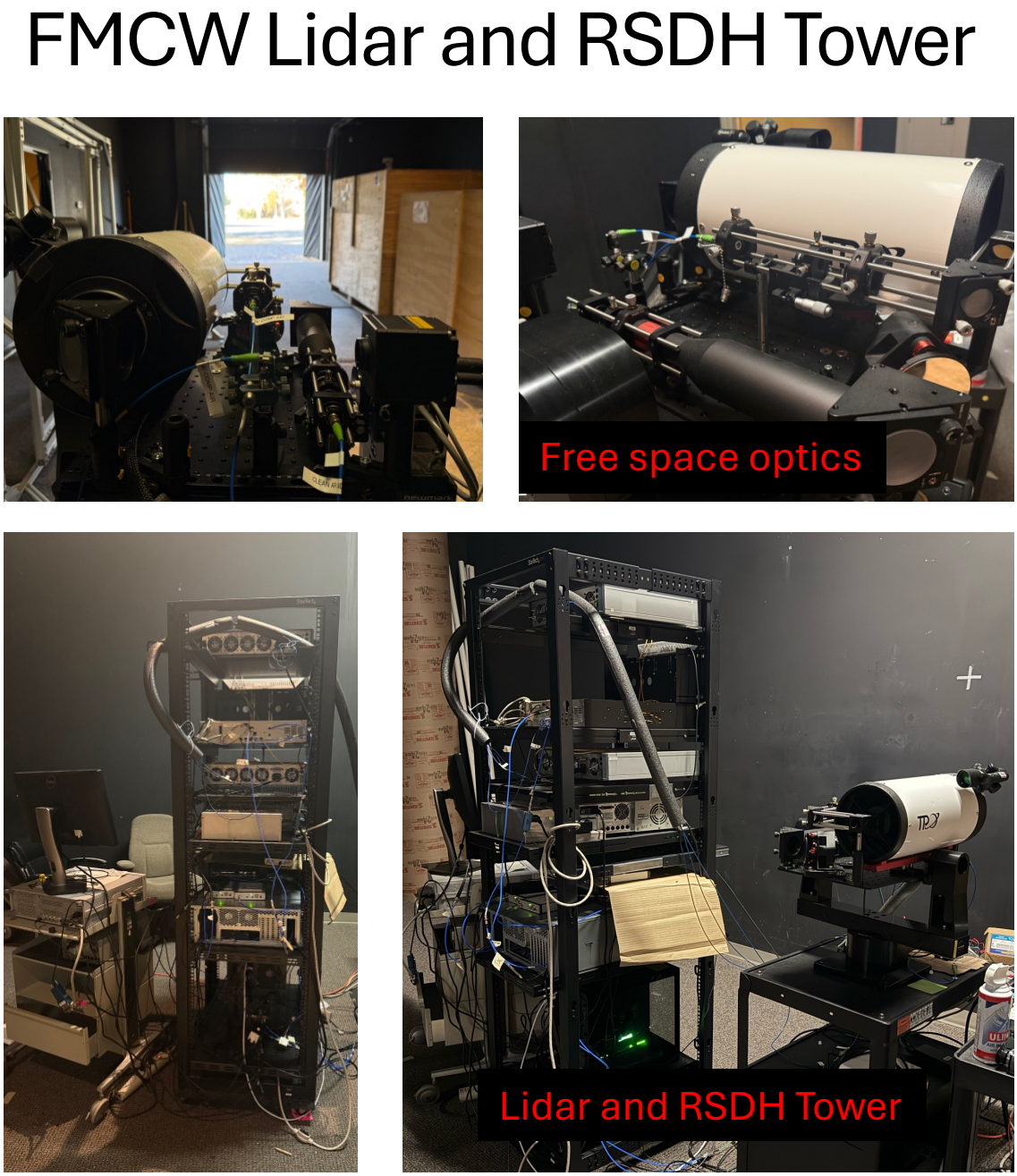


Figure 53: Lidar and RSDH tower.